

DIFFUSE OPTICAL TOMOGRAPHY TO STUDY THE ISCHEMIC STROKE IN RAT MODELS

by

ZI-JING LIN

Presented to the Faculty of the Graduate School of
The University of Texas at Arlington in Partial Fulfillment
of the Requirements
for the Degree of

DOCTOR OF PHILOSOPHY

THE UNIVERSITY OF TEXAS AT ARLINGTON

May 2013

Copyright © by ZI-JING LIN

All Rights Reserved

ACKNOWLEDGEMENTS

With deepest gratitude, I would like first to thank my supervisor, Dr. Hanli Liu. Throughout my doctoral work, she encouraged me to be an independent thinker and develop my research skills. I am grateful to her for supporting me with assistantships and fellowships throughout these years.

I would like to thank Dr. Shao-Hua Yang for helping me with the animal measurements and giving me all the information and support that was required. I also express my thanks to Dr. Jianzhong Su for all his guidance and great collaboration. I am very grateful to Dr. Georgios Alexandrakis and Dr. Digant Davé for serving on my dissertation committee and providing valuable suggestions. I would like to extend my gratitude to Dr. Yuan Bo Peng, for his suggestions and help in animal measurements. Especially, I would like to take this opportunity to thank Dr. Liping Tang, for all his valuable suggestion and help in life and career.

I would like to thank Dr. Ren Ming and Dr. Wenjun Li for their great help in animal surgery. My appreciation also goes to Drs. Yueming Liu and Natee Pantong for helping me in data processing and analysis. I would like to express my thanks to Dr. Haijing Niu, for her support and friendship. I am also grateful for the support, assistance and friendship from all the current and previous members of Biomedical Optical Laboratory.

Finally and always the most important part, I would like to thank my father, older brother, my wife and my son, for without their continuous support, I would not have been able to achieve much. The dissertation is dedicated to my mother who passed away during my course of study. I believe that she is always around to support me. I thank her and this dissertation is dedicated to her.

December 03, 2012

ABSTRACT

DIFFUSE OPTICAL TOMOGRAPHY TO STUDY THE ISCHEMIC STROKE IN RAT MODELS

Zi-Jing Lin, PhD

The University of Texas at Arlington, 2013

Supervising Professor: Hanli Liu

Stroke, including ischemic stroke and hemorrhagic stroke, is the major leading cause of death in the United States. More than 80 percent of stroke patients are diagnosed with ischemic stroke, which usually results from blockage of artery in the brain by thrombosis or arterial embolism. Animal Models, which permit powerful genetic and molecular approaches, provide an essential tool to study and understand the basic processes and potential therapeutic interventions for this disease. Significant efforts have been made to closely mimic the changes that occur in humans during and after stroke using animal models.

Recent development on near infrared (NIR) diffuse optical tomography (DOT) has been made to non-invasively image the changes of hemoglobin concentrations in human and animal brains. DOT is an attractive approach for evaluating and investigating stroke physiology. It can provide hemodynamic images of animal stroke with a potential for continuous, non-invasive monitoring at different stages of ischemic stroke.

My research focuses on examining continuous wave (CW) DOT to study cerebral ischemia in rat models. This work consists two main parts. In the first part, a CCD-camera-based DOT system was built for animal measurements. The system was calibrated and validated by computer simulations as well as by the laboratory tissue-like phantoms. The

recently developed depth compensation algorithm was introduced to help the depth localization and image quality in three dimensional diffuse optical image reconstructions. Another image reconstruction method, globally convergent method developed by a group of our collaborators, was briefly introduced. Laboratory phantom measurements showed the ability of CCD-camera-based DOT to image small perturbation in tissue-mimic phantoms, demonstrating that the system has a great potential to image heterogeneity in biological tissues, such as ischemic stroke in the rat brain. However, this CCD-camera-based DOT failed to produce good-quality images when being used in actual rat ischemic stroke models; this failure may result from the non-contact CCD-camera approach, which is more sensitive or weighted toward surface reflection signals with a smaller portion of diffuse light detected.

In the second part of my work, a fiber-based CW DOT system was alternatively utilized to investigate two commonly-used rat ischemic stroke models, suture and embolism models. Volumetric images of changes in oxy-hemoglobin concentration due to ischemic stroke were successfully reconstructed, with improved spatial resolution, using a rat brain atlas. Also, quantification of changes in cerebral blood flow (CBF) during and after cerebral ischemia is crucial because ischemic tissues may be recovered or dead depending on different levels of blood perfusion. Since CW DOT measures only changes of hemoglobin concentrations, an Indocyanine green (ICG) tracking technique was introduced to determine corresponding CBF. Results from the two rat stroke models show that with an interleaved approach, changes of hemoglobin concentrations and of CBF, during as well as after stroke, can be simultaneously determined using the fiber-based DOT system. In this way, I was able to show and identify therapeutic outcomes of a thrombolytic treatment given to the embolism-induced ischemic model. Furthermore, resting-state functional connectivity (RSFC) was also investigated to reveal lesion-induced neuronal connection disruption during stroke and tissue recovery after stroke. Final analysis shows loss of bilateral RSFC after cerebral ischemia, followed by partial RSFC recovery during the reperfusion phase.

TABLE OF CONTENTS

ACKNOWLEDGEMENTS	iii
ABSTRACT	iv
LIST OF ILLUSTRATIONS.....	xi
LIST OF TABLES	xix
Chapter	Page
1. INTRODUCTION.....	1
1.1 Stroke	1
1.2 Modern medical imaging techniques in diagnosis of ischemic stroke.....	2
1.3 Non-invasive optical imaging of ischemic stroke	3
1.4 The use of animal models in stroke research	4
1.5 Specific aims and outline of the study.....	5
2. PRINCIPLES OF NEAR INFRARED SPECTROSCOPY AND DIFFUSE OPTICAL TOMOGRAPHY	9
2.1 Background	9
2.2 Light interaction with biological tissues and optical window	9
2.3 Near infrared spectroscopy	10
2.4 Diffuse optical tomography.....	12
2.4.1 Forward problem: Modeling light propagation in biological tissues	13
2.4.2 Inverse problem: reconstruction of tissue optical properties in spatial domain	18
2.4.3 Reconstruction of spatial distribution of changes of hemoglobin concentration	19
2.5 Instrumentation of continuous wave DOT	20

3. VOLUMETRIC THREE DIMENSIONAL RECONSTRUCITON WITH DEPTH COMPENSATION	24
3.1 Introduction.....	24
3.2 Formation of DCA	25
3.3 Previous study of DCA with laboratory phantom in simple geometry	29
3.4 Application in model-based FEM	32
3.4.1 Modeling of standard rat head template	32
3.4.2 Image reconstruction and implementation of DCA	35
3.4.3 Total sensitivity analysis.....	37
3.4.4 Setup of computer simulations.....	39
3.4.5 Results	40
3.5 Conclusion.....	44
4. VOLUMETRIC DIFFUSE OPTICAL TOMOGRAPHY USING CCD-CAMERA-BASED IMAGING SYSTEM.....	47
4.1 Introduction.....	47
4.2 Instrumentation	48
4.2.1 Calibration of CCD camera	49
4.2.2 Stability and linearity of the CCD camera system.....	55
4.3 Optode geometry for CCD-camera based DOT.....	58
4.4 Computer simulation in evaluation the CCD-camera based DOT	59
4.4.1 Setup of optode array arrangement.....	59
4.4.2 Image reconstruction of DOT	60
4.4.3 Metrics of reconstruction performances.....	61
4.4.4 Setup of computational simulation	61
4.4.5 Results	63

4.5 Optimization of number of sources based on computer simulation	64
4.6 Phantom experiment	66
4.6.1 Experimental setup	66
4.6.2 Results	67
4.7 Comparison of conventional image reconstruction versus globally convergent method (GCM) in small geometry phantom study.....	68
4.7.1 Globally convergent method (GCM)	68
4.7.2 Experimental setup of phantom study.....	71
4.7.3 Results	73
4.8 Study of suture-induced ischemic stroke model using CCD-camera based DOT	77
4.8.1 Methods.....	77
4.8.2 Results	82
4.9 Summary and conclusion.....	83
5. FIBER-BASED CONTINUOUS WAVE DIFFUSE OPTICAL TOMOGRAPHY TO STUDY THE CEREBRAL ISCHEMIC IN PRE-CLINICAL RAT MODEL	86
5.1 Introduction.....	86
5.2 Methods.....	89
5.2.1 Animal Preparation.....	89
5.2.2 Suture-induced and embolism-induced MCAO model.....	89
5.2.3 Experimental setup	90
5.2.4 Study design	93
5.2.5 Forward light modeling and Image reconstruction.....	96
5.2.6 Calculation of ICG Kinetics and Data Analysis	97
5.2.7 Interleaved data acquisition and volumetric images for hemodynamics and BFI	98

5.2.8 Statistical consideration	99
5.3 Results	100
5.3.1 Rat brain atlas-guided DOT of cerebral hemodynamics in ischemic rats	100
5.3.2 Changes of cerebral hemodynamic for suture-induced ischemic stroke model	102
5.3.3 Changes of cerebral hemodynamic for embolism-induced ischemic stroke model	108
5.3.4 Dynamic response of ICG bolus measured by NIRS	110
5.4 Discussion	115
5.4.1 Rat brain atlas-guided, volumetric DOT	115
5.4.2 Effects of baseline optical properties and mesh densities on reconstructed DOT images	116
5.4.3 Two types of MCAO rat models	119
5.4.4 Advantages of Interleaved Data Acquisition and Analysis	120
5.4.5 Weakness of the study	122
5.5 Conclusion	123
6. DIFFUSE OPTICAL TOMOGRAPHY TO STUDY THE BILATERAL FUNCTION CONNECTIVITY AFTER CEREBRAL ISCHEMIA WITH RESTING-STATE FUNCTIONAL CONNECTIVITY	125
6.1 Introduction	125
6.2 Materials and Methods	126
6.2.1 Animal Preparation	126
6.2.2 Middle cerebral artery occlusion (MCAO) models	126
6.2.3 Experimental groups	127
6.2.4 Experimental setup	127
6.2.5 Data pro-processing and correlation analysis	129
6.3 Results	130

6.3.1 Validation of methodology by normal and sham rats	130
6.3.2 Resting-state functional connectivity for suture-induced MCAO model	133
6.3.3 Resting-state functional connectivity for embolism-induced MCAO model	134
6.4 Discussion and Conclusion	136
7. SUMMARY AND FUTURE WORK	140
7.1 Summary	140
7.2 Future work	142
APPENDIX	
A. HUMAN HEAD ATLAS-GUIDE DOT	145
B. MATLAB CODE FOR CONVERTING COORDINATES IN RW SPACE TO MNI SPACE	172
C. RECIPE OF GELATIN PHANTOM	174
REFERENCES	176
BIOGRAPHICAL INFORMATION	184

LIST OF ILLUSTRATIONS

Figure	Page
1.1 Illustration of two major types of stroke, (a) ischemic stroke and (b) hemorrhagic stroke. Figure was modified and reprinted from Ref [2]	2
2.1 A Hand Covering a Flashlight Beam in a Dark Room.....	9
2.2 Absorption coefficients for the main absorbing chromophores in biological tissues, including oxygenated hemoglobin, deoxygenated hemoglobin, and water	10
2.3 Illustration of diffuse optical tomography. D1 to D3 represent detector fibers located at three different positions with 3 different separations with source fibers (d1 to d3).....	13
2.4 Schematic of forward problem of DOT. Light intensities measured by detectors are unknown but optical properties of the medium of tissue inside the boundary are known	14
2.5 Models of light propagation in (a) infinite and (b) semi-infinite medium	15
2.6 Schematic of inverse problem of DOT. Light intensities measured by detectors are known but optical properties of the medium of tissue inside the boundary are unknown	19
2.7 Front (left) and back (right) view of the DYNOT instrument. Figure was reprinted from Ref. [35]	21
2.8 Block Diagram of the DYNOT instrument. LD: laser diodes, LDD: laser diode driver, TECD: thermo-electric cooler driver, f 1,2: laser modulation frequencies, DPS: digital phase shifter, OS: optical time-division multiplexer. Figure was reprinted from Ref. [35].	22
3.1 Relationship between the adjustable power γ versus the depth of reconstructed object. (a) to (c) show the CNR for 0.5%, 1% and 2% of random noise added. (d) to (e) demonstrate the CNR for 0.5%, 1% and 2% of random noise	27
3.2 Relationship of (a) CNR and (b) PE on adjustable power γ and regularization parameter α	29
3.3 Reconstructed DOT images of a single embedded object placed in the center of x-y plane and at z=-3 cm, as marked by the dashed circle. (a) and (c) are obtained with $\gamma=0$ for the x-y and x-z plane, respectively; (b) and (d) obtained with $\gamma=1.6$ for the same respective planes.	30

3.4 Reconstructed images of two objects placed symmetrically around the center of x-y plane and z=-3 cm (dashed circles). (a) and (c) are with $\gamma=0$, while (b) and (d) with $\gamma=1.6$	31
3.5 Reconstructed DOT images of two objects (dashed circles), placed -2 cm and -3 cm in depth with a center-to-center separation of 4.1 cm in x-z plane. (a) It is formed with $\gamma=0$, while (b) is obtained with $\gamma=1.3$	32
3.6 (a) T2-weighted MR image. 3D surface rendered rat head tissue models showing (b) skin/muscle (colored in green), (c) skull (colored in yellow), and (d) brain (colored in light blue).....	33
3.7 3D meshes of (a) skin/muscle, (b) skull and (c) brain.	33
3.8 Optodes projection on 3D rendering rat head model.	35
3.9 (a) 3D surface rendered plot represents cortical (colored with yellow) and subcortical (colored with gray) region of cerebrum. The distributions of different threshold levels of measurement sensitivities at three locations shown in (b) while DCA was not (c) or was (d) applied.	37
3.10 Setup of computer simulation for (a) S-1, (b) S-II, and (c) S-III. Panel on the bottom display the corresponding coronal sections of S-I to S-III.....	40
3.11 (a) Figure shows the coronal section of S-I. The coronal-sectioned reconstructed image of S-I (b) without and (c) with DCA was adopted. (d) The posterior view and (e) top view of 3D reconstruction. The reconstructed objects were defined as the voxels with reconstructed value larger than 50% of the maximum value.	41
3.12 (a) Figure shows the coronal section of S-II. The coronal-sectioned reconstructed image of S-I (b) without and (c) with DCA was adopted. (d) The posterior view and (e) top view of 3D reconstruction. The reconstructed objects were defined as the voxels with reconstructed value larger than 50% of the maximum value.	42
3.13 (a) Figure shows the coronal section of S-III. The coronal-sectioned reconstructed image of S-I (b) without and (c) with DCA was adopted. (d) The posterior view and (e) top view of 3D reconstruction. The reconstructed objects were defined as the voxels with reconstructed value larger than 50% of the maximum value.....	43
4.1 Schematic diagram of a CCD-camera-based DOT system for laboratory measurement.....	49
4.2 (a) Surface graphics of dark image taken from our CCD camera with 500ms integration time. (b) The cross section profiles along X axis of images taken with different integration times	50

4.3 (a) Surface graphics of flat field image taken from our CCD camera with 500ms integration time. (b) The cross-section profile of intensity from a flat field image along X axis.....	51
4.4 (a) A tissue phantom which was sitting on a phantom supporter with the illumination light coming from the bottom. (b) Schematic illustration of the procedure of flat filed correction	52
4.5 The cross-section profiles of intensity from a raw and corrected image along (a) X axis and (b) Y axis.....	53
4.6 (a) Computer simulated image and (b) image taken from CCD camera and the n corrected with flat filed correction. Both images were meshed into 13x9 grids. (c) Surface graphic depicts the ratio between the intensity from corrected object image and simulated image.....	54
4.7 Top row: pictures showing the four different light source locations, which are upper left corner, upper right corner, lower left corner and lower right corner, respectively. Bottom row: figures on left shows the raw CCD images taken with the four respective light source locations while figures on right shows the corrected CCD images taken with the four respective light source locations	55
4.8 Ratio of the intensities (IM/IB) for a 1% Intralipid solution (a) at different times of measurement, and (b) with different light intensities. The relationships between $\log(I_0/I)$ and (c) the volume of ink added into the testing solution for a 1% Intralipid solution, and (d) the concentration of Intralipid. Dashed line in (d) shows the linear relationship for Intralipid concentrations between 1% and 2.5%	57
4.9 Optode geometry for CCD-camera-based DOT system. The dimension of FOV was $m \times n$ in mm^2 . "X" represents possible locations of source fibers	59
4.10 Scheme of optode geometries used in the simulation study. (a) to (c) are corresponded to G-I to G-III. Notice that the dimension of all dashed unit squares is 10×10 mm^2 . (x: source fibers; o: detector fibers; : bifurcated fibers).....	59
4.11 Schematic diagram of setups used in simulation study. (a) Setup I: The inclusion was located right below the center of measurement plane. (b) Setup II: The inclusion was located close to the right side corner of the measurement volume	62
4.12 Reconstructed DOT images of a single object in X-Z plane: (a) and (c) with DCA ($\gamma=1.3$), and (b) and (d) without DCA. Top to bottom rows were obtained from G-I to G-III (Figure 4.8). Black dashed circles represent the actual location and size of simulated absorbers. Images here were normalized between minimum (0) to maximum (1)	63
4.13 Profiles of reconstructed $\Delta\mu_a$ values along x-axis for (a) experimental setup I and (b) experimental setup II. Dashed lines represent the actual location of the inclusion in X axis	65

4.14 Schematic illustration of the experimental setup for phantom study.....	66
4.15 Three dimensional plots of reconstructed images for (a) one inclusion with DCA ($\gamma = 1.6$) and without DCA (i.e. $\gamma = 0$), and (b) two inclusions with DCA ($\gamma = 1.6$) and without DCA ($\gamma = 0$). Voxels with the reconstructed absorption values above 80% of the maximum value are selected as reconstructed objects.	67
4.16 The domains used in GCM calculations. (a) The physical domain Ω with a triangular mesh. (b) The background domain Ω_0 with a mixed mesh which contains the physical domain Ω and the computational domain Ω_1 both with triangular meshes for the forward calculation purpose (c) the computational domain Ω_1	70
4.17 Schematic of layout of GCM	71
4.18 Schematic of physical setup of GCM	71
4.19 (a) Schematic illustration of the experimental setup for phantom study. (b) Photograph shows the setup of phantom. Four source fibers were placed on four sides of the square phantom. One side of source fiber was connected to the rail system (indicated by white arrow) which allowed moving to different locations along one side	72
4.20 (a) A spherical gelatin phantom used as an inclusion for the laboratory experiment. (b) Illustration of an inclusion embedded in the cubic tissue- mimicking phantom.....	73
4.21 Reconstructed images of one inclusion with a contrast level in absorption of (a) 2:1, (b) 3:1, and (c) 4:1 when DCA was applied. Reconstructed images of one inclusion at a contrast level of (d) 2:1, (e) 3:1, and (f) 4:1 without DCA applied	74
4.22 (a) A 3-D schematic drawing showing the data acquisition process of $\varphi(x,y,s)$ on the boundary of the physical domain Ω (reprinted from Su et al.). (b) Schematic illustration of the lateral plane for image reconstruction.	75
4.23 Reconstructed images by using GCM for (a) 2:1, (b) 3:1, and (c) 4:1 contrast levels relative to background. Circled areas represent actual location of absorber.	76
4.24 Reconstructed images of two absorbers (a) without DCA, (b) with DCA, and (c) with GCM.	77
4.25 Illustration of cranial circulatory system (circle of Willis) of the rat and middle cerebral artery occlusion induced by endovascular suture on left hemisphere. The left branches of OA, STA, and the ECA were cauterized and left PPA was temporally clipped. The monofilament silicon-coated suture was introduced into the lumen of ECA and then advanced to MCA bifurcation. The abbreviation from top to bottom: ACA: anterior cerebral artery; MCA: middle cerebral artery, BA: basilar artery; ICA: internal carotid	

artery; PPA, pterygopalatine artery; ECA: external carotid artery; STA: superior thyroid artery; OA, occipital artery; CCA, common carotid artery.	79
4.26 (a) Photograph of the experimental setup rat MCAO measurement. Upper panel of figure shows that four fibers were placed around the FOV of CCD camera. (b) Schematic illustration of experimental setup for rat MCAO experiment.	81
4.27 Images acquired from CCD camera for (a) 720nm and (b) 820nm in three different time periods."L" represents left and "R" represents right side of brain. (c) and (d) display the cross-section profiles of images obtained from CCD camera for (a) 720nm and (b) 820nm.	82
5.1 (a) Photograph shows clots in PE-50 catheter. (b) Photograph displays the clots injection via small hole on ECA through PE-50 catheter. The abbreviations in Figure 5.3b: ICA: internal carotid artery; PPA, pterygopalatine artery; ECA: external carotid artery; STA: superior thyroid artery; CCA: common carotid artery. Figures were provided by Dr. Ming Ren.....	90
5.2 Recombinant tissue plasminogen activator (rtPA) was administrated throughout Jugular vein. Figure on the right was provided by Dr. Ming Ren	90
5.3 Illustration of optode arrangement of bifurcated probes. The nearest inter-optode distance is 5 mm	91
5.4 (a) Photograph of home-made platform which allowed measuring rat in supine position. Plastic skews indicated by arrow were used to fix skin/muscle hooks for surgery. Optical fiber bundles came from the bottom of the platform. (b) Photograph of home-made probe holder which consisted two material, including silicone rubber and lead metal.	92
5.5 Catheter was implemented in femoral vein in advance for ICG injection	93
5.6 Schematic drawings of measurement protocols in: G-I and G-II for suture-induced ischemic model and G-III and G-IV for embolism-induced ischemic model. G-II was used to study the interference of ICG injection to changes of hemodynamic as well as changes of cerebral blood flow via ICG kinetics. G-III was administrated saline only after embolization while G-IV was administrated the rtPA 60-min after embolization.....	94
5.7 Curve displays the change of optical density (ΔOD) measured by 760nm following an ICG bolus and the definition of ICG kinetics. Blood flow index (BFI) is calculated by maximal light absorption change after intravenous bolus of ICG divided by the rise time.	98
5.8 (a) Illustration of where the section was cut. The coronal views of reconstructed ΔHbO_2 images during the MCAO while (b) DCA was not applied and (c) DCA was adopted. Black dashed line outlines the cortical region and red dashed line outlines the sbcortical region.	100

5.9 (a) Volumetric hemodynamic reconstruction for rat brain during MCAO. Left column displays the Iso-surface rendering of ΔHbO_2 , ΔHbR and ΔHbT . Color represent the concentration changes in micromolar (μM). Column on the right displays the multiple coronal sections of hemodynamic changes during MCAO. Each section is 0.5mm thickness. (b) 2,3,5-triphenyltetrazolium chloride stain of the infarct region of brain sample. (c) Diagram represents the coronal sections of rat brain. The hatched area represents the most common pattern of ischemic damage. Figure is reprinted from A. Tamura et al.	102
5.10 Two region of interest (ROIs) in rat brain and dimensions of two ROIs. ROI-1 located in contralateral control hemisphere and ROI-2 represents ipsilateral ischemic hemisphere. Figure on the right shows the dimension of ROI.....	103
5.11 Left column shows the time tracers of (a) ΔHbO_2 , (b) ΔHbR and (c) ΔHbT in two ROIs for G-I. Every data point is presented as mean plus SD. Right column display the corresponding coronal reconstructed images at three time points, which are baseline, during occlusion, and after reperfusion, respectively. Cortical region in Figure is marked with black dashed line while subcortical region is marked with red dashed line.	104
5.12 Two region of interest (ROIs) in rat brain and dimensions of two ROIs. ROI-1 located in contralateral control hemisphere and ROI-2 represents ipsilateral ischemic hemisphere. Figure on the right shows the dimension of ROI.	106
5.13 Scatter plots for comparison of (a) ΔHbO_2 , (b) ΔHbR and (c) ΔHbT between G-I and G-II in two ROIs.....	107
5.14 Left column shows the time tracers of (a) ΔHbO_2 , (b) ΔHbR and (c) ΔHbT in two ROIs for G-III (control group) and G-IV (treatment group). Every data point is presented as mean plus SD. Right column display the corresponding coronal reconstructed images at three time points, which are baseline, after embolization, and after rtPA/saline administration, respectively. Cortical region in Figure is marked with black dashed line while subcortical region is marked with red dashed line.	109
5.15 Profiles of ICG kinetics.....	110
5.16 Coronal sectioned images of spatial distribution maps of ΔICG , RT, and BFI from (a) normal rats, and (b) rats during MCAO. Color scale for ΔICG and BFI are normalized between minimum (0) and maximum (1). Color in RT maps represent in second.....	111
5.17 Time tracers of ratio of BFI between ROI-1 and ROI-II in G-II. Every data point represent mean plus SD. Bottom row show cornoal section of BFI images during MCAO and after suture was withdrawn (reperfusion).	113

5.18 Time tracers of ratio of BFI between ROI-1 and ROI-II in G-III and G-IV. Every data point represent mean plus SD. Bottom row displays corneal section of BFI images after embolization and after rtPA (G-IV) or saline (G-III) administration	114
5.19 Reconstructed images of coronal sections of ΔHbO_2 from (a) to (d) are reconstructed by different sets of optical properties. Figures (c) and (d) were used the same optical properties but (d) was modeled with only one-layer. (e) Scatter plots for comparison of ΔHbO_2 among four sets of optical properties in ROI-2.	118
5.20 Brain sample removed from G-IV. Small breaking-down clot was found at peripheral branch of MCA (indicated by arrow).	120
6.1 (a) Rat was positioned in supine position during the NIR measurement. (b) Optode array arrangement for NIR measurement.	128
6.2 3D rendered plot of ischemic (red) and control (blue) side of hemispheres. Seed was located on outer right side of cortical area, as shown in figure in the right.	130
6.3 (a) Data analysis was performed on one slice of coronal-sectioned image which cut along the location at MCA territory. (b) Normalized temporal profiles from seed, mirror and central regions.	131
6.4 Resting-state functional connectivity correlation maps for (a) normal rats (n = 12) and (b) sham-operated rats (n = 2). Correlation maps showing here were averaged maps.	131
6.5 Two ROIs located on both outer side of brain.....	132
6.6 Comparison of functional connectivity between ROI-1 and ROI-2 for normal rats (n=12). Error bar represents the standard deviation of z.....	132
6.7 Resting-state functional connectivity correlation maps for (a) $G-I_{\text{lesion}}$ (n = 10) and (b) $G-I_{\text{no_lesion}}$ (n = 7). Correlation maps showing here were averaged maps. Notice that color shown here presents the correlation coefficient r and ranges between -0.2 and 1	133
6.8 Comparison of functional connectivity between ROI-1 and ROI-2 for $G-I_{\text{lesion}}$ (n = 10) and $G-I_{\text{no_lesion}}$ (n = 7). Error bar represents the standard deviation of z.	134
6.9 Resting-state functional connectivity correlation maps for (a) $G-II_{\text{rtPA}}$ (n = 4) and (b) $G-II_{\text{control}}$ (n = 7) obtained from different time point measurements. Correlation maps showing here were averaged maps. Notice that color shown here presents the correlation coefficient r. Figures in upper panel are scaled within range between 0 and 1 and -0.2 to 1 for bottom panel.	135

6.10 Time tracer of functional connectivity between ROI-1 and ROI-2 for G-I _{rIPA} (n = 4) and G-II _{control} (n = 3). Measurements were performed before MCAO surgery and also 1 day, 2 day, 3 day, and 5 day after MCAO. Each point represents the functional connectivity averaged for ROI. Error bar represents the standard deviation of z.	136
6.11 Resting-state functional connectivity correlation maps obtained by different hemodynamic contrast, which are (a) ΔHbO_2 , (b) ΔHbO_2 and (c) ΔHbT	139

LIST OF TABLES

Table	Page
3.1 Optical properties of rat head tissue	33
3.2 Overlapping ratio between the MS volume cut at the three chosen threshold levels and cortical/subcortical volume, calculated using compensated (with DCA) and uncompensated (without DCA) approaches	39
3.3 Summary of the CNR and location error and VR values for three simulation setup.....	44
4.1 Summary of the CNR and PE values for three geometries.....	64
4.2 Summary of the CNR, PE and CPU time for different numbers of sources.....	65
4.3 Comparison of CNR and AR between reconstructions with and without DCA applied.....	75
4.4 Summary of quantifications (reconstructed by GCM)	76
5.1 Correlation coefficients of the comparison between G-I and G-II in ROI-1 and ROI-II for ΔHbO_2 , ΔHbR , and ΔHbT	107
5.2 Optical properties of 3-layer and 1-layer homogeneous rat head model.....	117
6.1 Measurement protocol of resting-state NIRS measurement.....	129

CHAPTER 1
INTRODUCTION

1.1 Stroke

Stroke is a cerebrovasculature deficit and the major leading cause of death in the United States. Some quick facts about stroke are: (1) it is the fourth leading cause of death, killing over 137,000 people each year [1], and a leading cause of serious, long-term adult disability; (2) approximately more than 700,000 strokes will occur this year, one occurring every 40 seconds, and taking a life approximately every four minutes; (3) starting from 1998, the annual stroke death rate fell approximately 35 percent and kept increasing; (4) stroke can happen to anyone at any time, regardless of race, sex or age.

There are two types of stroke:

1. Ischemic stroke: Ischemic stroke (Figure 1.1a) occurs when arteries which supply oxygen and nutrients to brain tissues are blocked by blood clots or by the gradual build-up of plaques, causing severe reduction of blood flow.
2. Hemorrhagic stroke: Hemorrhagic stroke (Figure 1.1b) occurs when blood vessel bursts inside the brain and bleeds into surrounding tissues.

More than 80 percent (~87%) of stroke patients are diagnosed with ischemic stroke. Stroke patients must not only survive the acute stages of infarction, but also cope with serious physical, psychological, emotional and financial consequences due to neurological impairment. The estimated direct and indirect cost of managing stroke in the United States is more than 75 billion annually. The high cost, loss of life, physical and mental disability necessitates effective therapeutic interventions.

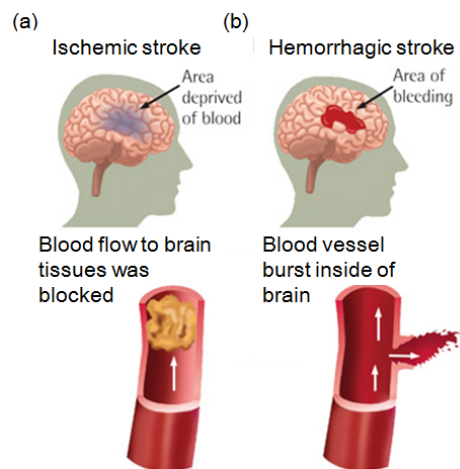


Figure 1.1 Illustration of two major types of stroke, (a) ischemic stroke and (b) hemorrhagic stroke. Figure was modified and reprinted from Ref. [2].

1.2 Modern medical imaging techniques in diagnosis of ischemic stroke

While it is important to determine whether the patient has stroke, it is equally important to determine the type of stroke each type may require different treatments. Current imaging techniques which can be used to diagnose the type of stroke are described as follows.

- Magnetic resonance imaging (MRI) and magnetic resonance angiography (MRA): MRI and MRA use the response of water molecules to generate a detailed image of the brain and its arteries. MRI is more accurate in the diagnosis of acute ischemic stroke and its cause. MRI and MRA can assess brain damage and its reversibility as well as the risk of complications from the stroke.
- Computed tomography (CT): CT scan uses X-rays to produce a 2-dimensional or 3-dimensional picture of the brain. Based on the type of stroke, CT can be more specific:
 - Computed tomography angiography (CTA) scan uses intravenous contrast fluid to visualize the arteries in the brain; it can help diagnose ischemic stroke by determining its cause (such as a clot in an artery) and can provide guidance for treatment.

- A non-contrast CT scan is very fast (less than 1 min) and can accurately detect blood, so it is used to quickly diagnose hemorrhagic stroke.
- Ultrasonography uses high-frequency sound waves to investigate the blood flow as well as the structure of blood vessel. There are several ultrasonographic techniques, such as:
 - Carotid ultrasound: Ultrasound transducer, placed on neck close to the location of common carotid artery (CCA), can examine the arteries in the neck that provide blood to the brain. It can show blood clots, atherosclerotic plaques, and other problems which may cause ischemic stroke.
 - Transcranial Doppler (TCD): TCD mainly measures the direction and speed of blood flow in arteries in the brain. It can be used to find the position of a clot in the artery or the narrowing of an artery.
- Cerebral angiography: Use of cerebral angiography requires surgical insertion of a catheter into an artery. This method is the most accurate test for problems with brain arteries. However, it plays a limited role in acute stroke diagnosis because it is riskier, takes a longer time, and requires more equipment and professional personnel than other imaging modalities. Digital cerebral angiography is mostly used for a direct intravascular removal of an embolus, widening the artery with a balloon, putting in a stent, or injecting thrombolytic drugs to dissolve a clot.

1.3 Non-invasive optical imaging of ischemic stroke

To date, a large number of studies using optical imaging to investigate ischemic stroke have been done and reported in three stages of stroke, including stroke prevention [3-5], monitoring acute and sub-acute stage of ischemic stroke [6-8], and most importantly, guiding and evaluating rehabilitation after ischemic stroke [9-11]. Optical imaging does not allow assessing the changes of structure. However, optical imaging is able to provide several parameters, such as changes in hemoglobin concentration, blood and tissue oxygenation,

cerebral blood flow and perfusion, which can be used to characterize and explore the ischemic stroke.

Most of the studies were mainly achieved by channel-wise near infrared spectroscopy (NIRS) measurements; or, based on the principles of NIRS, studying topographic images with spatial resolution in centimeter range. While topographic imaging can provide images of parts of surface of brain, diffuse optical tomographic (DOT) imaging has ability to image brain activity with depth information. DOT is an attractive approach for evaluating and investigating stroke physiology. It provides hemodynamic or metabolic images with potential for continuous, non-invasive monitoring in different stages of ischemic stroke, including prevention, acute or sub-acute stages, or rehabilitation guidance after ischemic stroke. Results have been demonstrated in humans [12, 13] as well as in animals [14, 15].

1.4 The use of animal models in stroke research

Given the facts that stroke is the major cause of death and disability in the United States, it is a major public health issue requiring urgent development of effective therapies. The experimental animal models, which permit more powerful genetic and molecular approaches, provide an essential tool to study and understand the basic processes or potential therapeutic interventions in this disease. This knowledge can improve medical treatment for human ischemic stroke.

As described in previous section, more than 80% of human stroke are ischemic stroke; thus, large amounts of experimental models of focal cerebral ischemia have been developed in order to closely mimic the physiological changes during and after cerebral ischemia. Middle cerebral artery (MCA) ischemic stroke models have been established in different animal species mostly through occlusion of MCA using either craniotomy or endovascular approach because ischemic stroke is often caused by occlusion of the middle cerebral artery (MCA) and its branches in human (approximately 80% of all ischemic stroke patients). With all different species of animals, rats are the mostly commonly used animals due to the following reasons: 1)

the similarity to human in cerebral anatomy and physiology; 2) their low cost and small size; and 3) greater public and institutional ethical acceptability of use relative to larger animals

Rat middle cerebral artery occlusion (MCAO) model can be categorized into two groups: which are permanent ischemia and transient ischemia, respectively. Between two types of ischemia models, transient ischemia model provides the platform which allows researchers to manipulate different experimental conditions, such as duration of occlusion, and generate different degree of ischemic damages. Many MCAO rat models have been developed and can be divided into two major categories, Intraluminal MCAO model and thromboembolic model. Intraluminal MCAO model is the most commonly-used rodent MCAO model due to its relative simplicity. This model provides relatively consistent outcome and is suitable for neuroprotection drug experiments. Another MCAO model - thromboembolic model, is more complicated as compared to Intraluminal MCAO model. The outcome of this model is harder to expect, such as diffuse and inhomogeneous infarction, due to different sizes and locations of clots. However, this model more closely mimics the human ischemic stroke and suitable to investigate the thrombolytic drug and evaluate the effect of thrombolytic therapy.

1.5 Specific aims and outline of the study

In humans, ischemic stroke is often caused by occlusion of the middle cerebral artery (MCA) and its branches. Many ischemic stroke models have been established (although in rodents) mostly through occlusion of MCA using either craniotomy or endovascular approach. Although different imaging techniques have been used in experimental studies and clinically with great success, portable, non-invasive imaging tools are highly desirable so as to be able to provide real-time, cerebral functional images for better diagnosis and prognosis of ischemic stroke. While less cost-intensive optical imaging has a limitation in the penetration depth for humans, it has promising potential to serve as an imaging tool in development of anti-stroke therapies using the well-developed rodent MCAO model. Although DOT enables imaging of hemodynamic changes of brain with depth information, few studies have focused on DOT of

cerebral ischemia induced microvasculature dysfunction, especially in animal ischemic stroke models. Therefore, considering all the information mentioned above, the overall goals of this project are:

- i. To refine and validate the proposed image reconstruction algorithms with laboratory phantoms and animal measurements by using CCD (charged-coupled-device)-camera-based and fiber-based DOT system.
- ii. To investigate whether proposed algorithms can be used to study the widely-used rodent MCAO model.
- iii. To explore the difference and effect of therapeutic intervention of ischemic stroke.

To accomplish the goals, the fundamental hypothesis is that recently developed image reconstruction algorithms in combination with CCD-camera-based or fiber-based NIR measurements can provide three-dimensional (3D) tomographic imaging tool to explore and investigate the cerebral ischemia in rodent ischemic stroke models. The specific aims for this work are listed as follows:

Specific Aim 1: To develop and optimize the CCD-camera-based diffuse optical tomographic system to study cerebral ischemia in animal model: We will use CCD-camera-based DOT to monitor the hyper-acute cerebral ischemia and study the treatment effect in well-developed pre-clinical animal models based on the newly developed tomographic image reconstruction algorithms.

Specific Aim 2: To refine and validate the newly developed image reconstruction algorithms to study the cerebral ischemia in animal model using fiber-based diffuse optical tomographic system: We will measure hemodynamic changes due to cerebral ischemia in animals using fiber-based DOT system. Newly developed tomographic image reconstruction algorithms will be utilized and validate with animal data.

Specific Aim 3: To monitor and investigate the hemodynamic changes and ICG kinetics for embolism-induced middle cerebral artery occlusion model before and after treatment in: We will perform NIR measurements in combination with light-absorbing dye to study the hemodynamic changes and reduction of cerebral blood flow in rats with acute embolic ischemic stroke.

Specific Aim 4: Monitor resting-state functional connectivity to investigate the treatment effect and recovery after cerebral ischemic stroke: While fNIRS has been demonstrated having ability in study the resting-state functional connectivity, we will perform resting-state fNIR measurements for longitudinal monitoring to evaluate the recovery and treatment effect for ischemic rodent models based on the resting-state functional connectivity in acute or sub-acute stage of stroke.

The progresses towards these aims are detailed in the outline below:

Chapter 2 details the basic principle of near infrared spectroscopy (NIRS) and the background theory of continuous wave (CW) NIRS measurement. The variant of NIRS diffuse optical tomography (DOT) is introduced.

Chapter 3 describes the recently developed state-of-the-art depth compensation algorithm (DCA) which can effectively improve the depth localization and resolution in three dimensional volumetric reconstructions. The approach toward the rodent study is introduced.

Chapter 4 details the development of CCD camera-based DOT system. Computer simulations and laboratory phantom experiments were performed to optimize and validate the proposed system. Moreover, another state-of-the-art image reconstruction globally convergent method (GCM) is introduced and experimental phantom study for validation of GCM is presented. In the last part of this chapter, the system is moved towards the suture-induced MCAO rat model and the results and discussion are described.

Chapter 5 provides the experimental results in study the cerebral ischemia using fiber-based CW DOT system. Two ischemic models, which are Intraluminal (suture-induced) MCAO model and thromboembolic (embolism-induced) MCAO model, were measured. This chapter consists of two parts. First part of the chapter demonstrates the results of changes of hemoglobin concentration before, during, and after rat MCAO. Second part of this chapter describes the study of changes of cerebral blood flow by introducing the Indocyanine Green (ICG)-tracking techniques.

Chapter 6 details the study of tissue recovery after MCAO using resting-state functional connectivity. This chapter is more toward the study of sub-acute or chronic stage of ischemic stroke.

Chapter 7 summarizes my work and future work toward this project is described.

CHAPTER 2
PRINCIPLES OF NEAR INFRARED SPECTROSCOPY AND DIFFUSE OPTICAL
TOMOGRAPHY

2.1 Background

This chapter describes how light in near-infrared region can potentially investigate tissue heterogeneity and its physical and mathematical background. Section 2.3 summarizes the principle of near infrared spectroscopy and theory of continuous wave near infrared spectroscopy measurements. Section 2.4 briefly describes the principle of diffusion optical tomography. The affiliated subsection describes the forward problem of diffuse optical tomography which model light propagation in high scattering medium and also the inverse problem which aims to recover optical properties in spatial domain.

2.2 Light interaction with biological tissues and optical window

When light propagates in biological tissues, it will interact with different tissue compounds. The two fundamental interactions are elastic scattering and absorption which are responsible for determining the photon distribution within the medium. Fluorescence will be emitted followed absorption of light by tissue chromophore or fluorophore. Fluorescence will not be addressed here as this study mainly focuses on the changes of absorption properties.



Figure 2.1 A Hand Covering a Flashlight Beam in a Dark Room

Figure 2.1 shows the photograph of a blocked flashlight beam (which is considered as light with broadband range) by human hand. Only red light is observed to be coming out. This example demonstrates that most of the visible light is absorbed by biological tissues except red light. More specifically, Figure 2.2 shows the absorption spectrum of the main absorbing chromophores in biological tissues; including hemoglobin (can be oxygenated hemoglobin (HbO_2) or deoxygenated hemoglobin (HbR)), and water (up to 70% of body weight). Light within near-infrared (NIR) wavelength portion (650nm -900nm, shown in Figure 2.2, highlighted with pink block) has relatively lower absorption coefficients (μ_a) than the wavelengths outside this range. Light in this region or so-called “optical window” has unique property of somehow being transparent in biological tissues. This feature ensures photons can penetrate deeply into biological tissues (up to several centimeters depending on tissue optical properties).

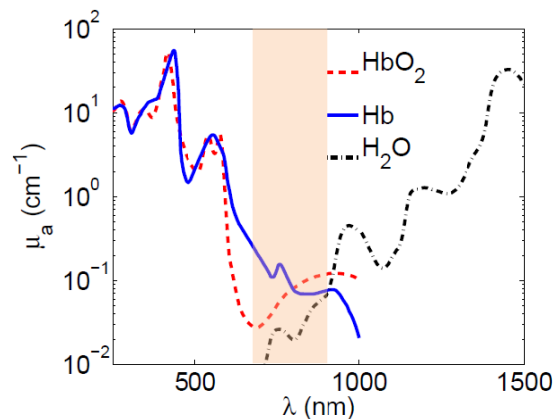


Figure 2.2 Absorption coefficients for the main absorbing chromophores in biological tissues, including oxygenated hemoglobin, deoxygenated hemoglobin, and water.

2.3 Near infrared spectroscopy

As mention in section 2.1, oxygenated and deoxygenated hemoglobin are two main chromophores in biological tissues. Near infrared spectroscopy (NIRS) is the non-invasive spectroscopic technique that uses light with NIR range to investigate hemoglobin concentration, specifically for oxygenated and deoxygenated hemoglobin. Based on the types of sources,

there are three types of NIRS- time-resolved system, frequency system, and continuous wave (CW) system. In this chapter, only CW system is introduced, since our lab mainly focuses on CW measurements. Compared to first two systems, CW system uses continuous wave light at constant amplitude for measurement, which is relatively easy to build and acquires data fast. However, CW system cannot provide absolute quantifications of concentration due to lack of temporal information, instead, providing only relative changes.

CW measurement measures the changes in light intensity due to change in absorption. Traditionally, modeling the relationship of measured light intensity after passing through a pure absorption medium with source intensity can be expressed using Beer-Lambert law (BLL), as:

$$OD = \text{Log}\left(\frac{I}{I_0}\right) = \varepsilon cd \quad (2.1)$$

where OD is the optical density, I_0 represents the intensity of incident light, I is the intensity of transmitted light, ε is the extinction coefficient of hemoglobin, c is the concentration of hemoglobin, and d is the actual length of light path through solution. For the medium which consists of more than one absorbing agents, Equation 1.1 can be written as superposition of individual contribution:

$$OD = \text{Log}\left(\frac{I}{I_0}\right) = (\varepsilon_1 c_1 + \varepsilon_2 c_2 + \dots + \varepsilon_n c_n) d \quad (2.2)$$

However, when light is shot into high scattering medium, such as biological tissue, it no longer directly pass through the medium. Light propagates into medium or tissue and return to the surface after multiple scattering, which causes the changes in light path. To modify this kind of scenario, the modified Beer-Lambert law (MBLL) was proposed and Equation 1.1 is rewritten as:

$$OD = \text{Log}\left(\frac{I}{I_0}\right) = \varepsilon \cdot c \cdot d \cdot \text{DPF} + G = \varepsilon \cdot c \cdot L + G \quad (2.3)$$

where DPF is the differential path length factor, G is the constant term to compensate for the losses due to scattering and L is the optical path length. Since absorption coefficient can be expressed as $\mu_a(\lambda) = \varepsilon(\lambda)c$, Equation 1.3 can then be rewritten:

$$OD = \text{Log}\left(\frac{I}{I_0}\right) = \mu_a \cdot L + G \quad (2.4)$$

In case of relative measurement, measurement can measure what happens within blood flow and neglect the effect from the surrounding tissues. Collecting data from baseline condition and transient condition, the changes of OD can be calculated from Equation 2.4 and expressed as:

$$\Delta OD = OD_{\text{transient}} - OD_{\text{baseline}} = \Delta\mu_a \cdot L \quad (2.5)$$

Since HbO₂ and HbR are two major chromophores in NIR region, with dual wavelengths measurements, Equation 1.5 can be extended as:

$$\begin{aligned} \Delta OD^{\lambda_1} &= \left(\varepsilon_{\text{HbO}_2}^{\lambda_1} \Delta \text{HbO}_2 + \varepsilon_{\text{HbR}}^{\lambda_1} \Delta \text{HbR} \right) \cdot L \\ \Delta OD^{\lambda_2} &= \left(\varepsilon_{\text{HbO}_2}^{\lambda_2} \Delta \text{HbO}_2 + \varepsilon_{\text{HbR}}^{\lambda_2} \Delta \text{HbR} \right) \cdot L \end{aligned} \quad (2.6)$$

Here ΔHbO_2 and ΔHbR represent the concentration changes of HbO₂ and HbR. The change of absorption coefficients can be derived from Equations 2.5 and 2.6 as:

$$\begin{aligned} \Delta\mu_a^{\lambda_1} &= \varepsilon_{\text{HbO}_2}^{\lambda_1} \Delta \text{HbO}_2 + \varepsilon_{\text{HbR}}^{\lambda_1} \Delta \text{HbR} \\ \Delta\mu_a^{\lambda_2} &= \varepsilon_{\text{HbO}_2}^{\lambda_2} \Delta \text{HbO}_2 + \varepsilon_{\text{HbR}}^{\lambda_2} \Delta \text{HbR} \end{aligned} \quad (2.7)$$

It is clearly shown that ΔHbO_2 and ΔHbR can be obtained if dual wavelengths relative measurements were performed.

2.4 Diffuse optical tomography

Diffuse optical tomography (DOT) is a variant of NIRS. As shown in Figure 2.3, with multiple source-detector pair measurements, the spatial distribution of tissue heterogeneity can be reconstructed. DOT consists of two parts: (1) the forward model, which represents the light propagation to the medium or tissue being imaged; and 2) the inverse model, which retrieves

the optical properties of the imaged medium or tissue. The forward and inverse problems are described in the following sub-section.

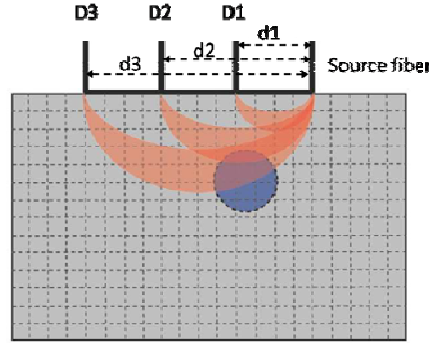


Figure 2.3 Illustration of diffuse optical tomography. D1 to D3 represent detector fibers located at three different positions with 3 different separations with source fibers (d1 to d3).

2.4.1 Forward problem: Modeling light propagation in biological tissues

Figure 2.4 shows the schematic illustration of the forward problem. Basically, with known tissue optical property distribution, one predicts the light propagation in biological tissues based on some physical or mathematical model. The fundamental forward model for photon transport through diffuse medium such as biological tissues is the radiative transport equation (RTE). However, in high-albedo (predominately scattering) medium, the RTE can be simplified to diffusion equation which is the diffusion approximation of RTE [16] and can be expressed as:

$$-\nabla \cdot D(r) \nabla \phi(r, \omega) + \mu_a(r) \phi(r, \omega) + \frac{i\omega}{c} \phi(r, \omega) = q_0(r, \omega) \quad (2.8)$$

where $\phi(r, \omega)$ is the fluence at position r modulated by frequency ω , D is the diffusion coefficient which is expressed as:

$$D = \frac{1}{3(\mu_a + \mu'_s)} \quad (2.9)$$

Here μ_a is the absorption coefficient and $\mu'_s = \mu_s (1 - g)$ is the reduced scattering coefficient and g is the anisotropy factor. q_0 is isotropic source located at $1/\mu'_s$.

Modeling using diffusion equation can produce valid and reliable results and nowadays is the most widely used forward model in DOT field. Large amount of studies have been presents such as prostate cancer [17, 18], breast cancer detection [19, 20], and imaging the human brain activity [21, 22].

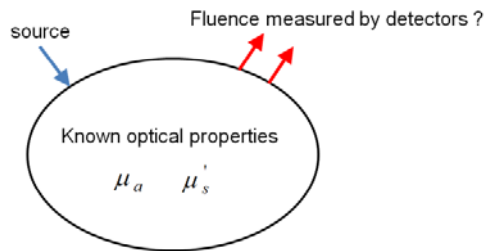


Figure 2.4 Schematic of forward problem of DOT. Light intensities measured by detectors are unknown but optical properties of the medium of tissue inside the boundary are known.

Solving the diffusion equation allows prediction of light propagation in tissues. There are three major ways to solve the diffuse equation based on the known optical properties, which are Monte Carlo model, analytical solution of diffuse equation, and finite element method (FEM), respectively. In Monte Carlo method the process which can occur in diffuse equation are considered as stochastic processes. The simulations of light propagation using Monte Carlo method are available in both simple geometries [23, 24] as well as the three-dimensional heterogeneous mediums [25]. Details are not addressed in this section since only FEM and analytical solution of diffuse equation were used in this study.

2.4.1.1 Analytical solution of diffusion equation

Analytical solution of Equation 2.5 exists for homogenous medium with simple geometries, such as infinite homogenous (shown in Figure 2.5a) or semi-infinite homogenous media [26, 27] (Figure 2.5b). Consider a semi-infinite geometry (Figure 2.5b), where source and detector are placed on same side of surface of medium with separation of d . The source is simulated as the isotropic source located at $z = z_0 = \frac{1}{\mu_s}$ [27]. At an index-matched boundary no photon current is allowed back into the medium. In the case of an index-mismatched boundary the only inward directed current is due to the reaction at the boundary. This boundary condition

can approximately be described by placing a source with negative strength at a distance

$$z = z_0 = \frac{1}{\mu_s}$$

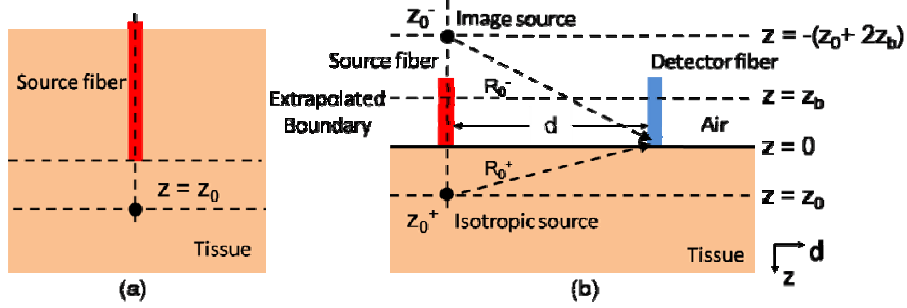


Figure 2.5 Models of light propagation in (a) infinite and (b) semi-infinite medium

This boundary condition is called extrapolated boundary condition (EBC) as it artificially generate a virtual boundary at $z = z_b$ where the fluence rate at this extrapolated boundary is zeros. By applying the EBC, the fluence rate at the detector can be calculated as the sum of the infinite solution from two the isotropic sources (one is isotropic and another is its negative imaging source) and can be expressed as:

$$\phi(r) = \frac{P}{4\pi D} \left(\frac{\exp(-\mu_{eff} R_0^+)}{R_0^+} - \frac{\exp(-\mu_{eff} R_0^-)}{R_0^-} \right) \quad (2.10)$$

where $R_0^+ = \sqrt{d^2 + (z - z_0^+)^2}$ and $R_0^- = \sqrt{d^2 + (z - z_0^-)^2}$. μ_{eff} represents the effective attenuation coefficient and can be defined as:

$$\mu_{eff} = \sqrt{\frac{\mu_a}{D}} \quad (2.11)$$

2.4.1.2 Perturbation model with Rytov approximation

As DOT mainly measures absorption and scattering heterogeneities within tissue, a simple way to model heterogeneities is to consider a linear perturbation to the homogeneous case. The perturbation due to the heterogeneous variation of optical properties from the background is approximated by a Born or Rytov [28, 29] expansion. With the Rytov approximation, the detected fluence can be written as:

$$\phi(r_s, r_d) = \phi_0(r_s, r_d) \exp(\phi_s(r_s, r_d)) \quad (2.12)$$

where $\phi_0(r_s, r_d)$ is the fluence from the background without perturbation, $\phi_s(r_s, r_d)$ represents the perturbations due to the heterogeneity of optical properties. In most of cases, especially in the study of brain activity, the change in optical property is due to the changes of oxy- and deoxy- hemoglobin concentrations. Assuming for simplicity that the changes in scattering were slow and negligible, $\phi_s(r_s, r_d)$ can be written in matrix form as:

$$\phi_s(r_s, r_d) = \ln\left(\frac{\phi(r_s, r_d)}{\phi_0(r_s, r_d)}\right) = -\frac{vh^3}{D} \frac{G(r_{si}, r_d)G(r_j, r_{di})}{G(r_{si}, r_{di})} \Delta\mu_a(r_j) \quad (2.13)$$

where r_{si} and r_{di} the positions of i^{th} source and i^{th} detector. G is the Greens function of the photon diffusion equation for the given boundary conditions and optical properties.

Equation 2.13 can then be broken down into discrete components and expressed as:

$$y = A x \quad (2.14)$$

where y represents the measured changes of light intensity due to the perturbation which contain $N \times 1$ measurements (source-detector pairs). x is the reconstructed volume or space in changes of absorption coefficients which contains $M \times 1$ voxels. "A" links the perturbation of absorption in the voxel in volume to be reconstructed to the particular source-detector measurement pair or physically represents the measurement sensitivity matrix. This physically describes the information pertaining to a large effect due to a small perturbation, in our case, changes of absorption, will have on the measurements.

2.4.1.3 Finite element method for diffusion equation

The finite element method (FEM) is a numerical method used to solve ordinary and partial differential equations and is extensively applied to several different engineering fields. The method is based on the integration of the terms in the equation to be solved. The advantage of FEM is that method can be applied to heterogeneous medium and the arbitrary geometry. With the modeling of light propagation, the FEM is utilized to give the solution of diffusion equation. The key feature of FEM analysis is to consider the problem only for each

element instead of whole geometry. In the discretized geometry, the solution of diffusion equation can be approximated by:

$$\phi^h(r) = \sum_{i=1}^V \phi_i u_i(r) \Omega^h \quad (2.15)$$

where Ω^h is the finite dimensional subspace spanned by basis functions $u_i(r)$. The diffusion equation in the FEM analysis can be replaced by a system of linear algebraic equations [30]:

$$\phi = \left[K(D) + C \left(\mu_a + \frac{i\omega}{c_m} \right) + \frac{1}{2A} F \right]^{-1} q_0 \quad (2.16)$$

where

$$K_{i,j} = \int_{\Omega} D(r) \nabla u_i \cdot \nabla u_j d^n r$$

$$C_{i,j} = \int_{\Omega} \left[\mu_a(r) + \frac{i\omega}{c_m(r)} \right] u_i(r) u_j d^n r$$

$$F_{i,j} = \int_{\partial\Omega} u_i(r) u_j d^{n-1} r, \text{ and}$$

$$q_{0_i} = \int_{\Omega} u_i(r) q_0(r) d^n r$$

Several FEM packages exist in order to solve the diffusion equation for light propagation in diffuse media. In this work, the MATLAB-based FEM solver NIRFAST [31] was used. In NIRFAST, at the boundary, the Robin-type boundary condition is used to represent the boundary condition between air and tissue. This boundary condition describes that the fluence at the tissue boundary exits but does not return. The flux leaving the external boundary is equal to the fluence rate at the boundary weighted by a factor that accounts for the internal reflection of light back into the tissue. The Robin-type boundary condition can be expressed as:

$$\phi(\xi, \omega) + 2 \hat{A} n \cdot \kappa(\xi) \nabla \phi(\xi, \omega) = 0 \quad (2.17)$$

where ξ is the point on the external boundary of geometry, \hat{n} is the outward pointing normal and \tilde{A} depends on the relative refractive index mismatch between the tissue and air. Since the matrices K , C and F in Equation 2.16 are sparse, the solution can be obtained by standard methods such as bi-conjugate gradient in the complex case. The details of the FEM formulation of the forward model are given in Refs. [30, 32, 33].

Referring the Ref [34], the forward model in FEM framework can also be simplified as:

$$y = Jx \quad (2.18)$$

Here y is the corresponding change in amplitude of the measured signal, i.e. $y = y_t - y_o$, where y_o is the baseline measurement and y_t is the measurement after a change in absorption. x represents the small changes in absorption coefficient. J is the Jacobian matrix which also represents the measurement sensitivity as same definition as notation A in Equation 1.x and is expressed as:

$$J_{rh} = \begin{bmatrix} \frac{\partial \ln I_1}{\partial \mu_{a1}} & \frac{\partial \ln I_1}{\partial \mu_{a2}} & \dots & \frac{\partial \ln I_1}{\partial \mu_{aN}} \\ \frac{\partial \ln I_2}{\partial \mu_{a1}} & \frac{\partial \ln I_2}{\partial \mu_{a2}} & \dots & \frac{\partial \ln I_2}{\partial \mu_{aN}} \\ \vdots & \vdots & \ddots & \vdots \\ \frac{\partial \ln I_M}{\partial \mu_{a1}} & \frac{\partial \ln I_M}{\partial \mu_{a2}} & \dots & \frac{\partial \ln I_M}{\partial \mu_{aN}} \end{bmatrix}_{M \times N} \quad (2.19)$$

where N represents number of nodes, M is number of measurements, I is the amplitude measured from detectors. It is that using the natural logarithm of amplitude changes, that is, $y = \log(y_t) - \log(y_o) = \log(y_t/y_o)$ also leads to the Rytov approximation, as described in section 2.4.1.2.

2.4.2 Inverse problem: reconstruction of tissue optical properties in spatial domain

Figure 2.6 shows the schematic illustration of the forward problem of DOT. Basically, with known measurement signals or light intensity, one retrieves the spatial distributions of optical properties or perturbation in biological tissues. Thus, in our case, the aim of solving inverse problem is the recovery of the changes of absorption coefficient using the detected

changes in optical density. Given the Equation 2.14, the changes of absorption can be obtained by solving the equation.

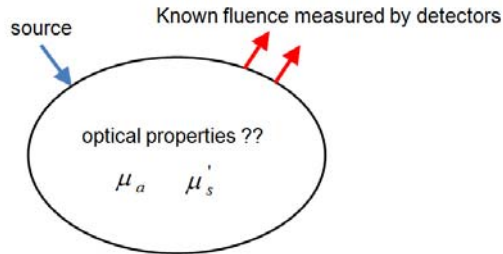


Figure 2.6 Schematic of inverse problem of DOT. Light intensities measured by detectors are known but optical properties of the medium inside the boundary are unknown.

To solve the Equation 2.14, the sensitivity matrix A must be inverted. However, it is noteworthy that to reconstruct the perturbation for each pixel/voxel/node, the number of measurements must be equal to the number of pixel/voxel/node. However, measurements can only obtain from the surface of the tissues or medium, resulting $N \gg M$ in Equation 2.14. This kind of situation makes inverse problem of DOT become ill-posed, as well as under-determined (sensitivity matrix A is not equal). The common way to solve such problems is through regularization. The Moore-Penrose generalization [28] is implemented and Equation 2.14 can be solved as:

$$x = A^T (AA^T + \alpha s_{\max} I)^{-1} y \quad (2.20)$$

where I represents the identity matrix, s_{\max} is the maximum eigenvalue of AA^T , and α is the regularization parameter. Equation 2.18 can also be solved by same regularization and the solution is:

$$x = J^T (JJ^T + \alpha s_{\max} I)^{-1} y \quad (2.21)$$

2.4.3 Reconstruction of spatial distribution of changes of hemoglobin concentration

Solving inverse problem of DOT provide the spatial distribution of changes of optical density (ΔOD). Following the principle of CW-NIRS, to reconstruct the spatial distribution of changes of hemoglobin concentration, specifically for oxygenated and deoxygenated

hemoglobin in this work, data from two wavelengths must be acquired. According on Equations 2.5 and 2.6, the changes of oxygenated and deoxygenated hemoglobin concentrations can be written in matrix form as:

$$\begin{bmatrix} \Delta HbO_2 \\ \Delta HbR \end{bmatrix} = \begin{bmatrix} \varepsilon_{HbO_2}^{\lambda_1} & \varepsilon_{HbR}^{\lambda_1} \\ \varepsilon_{HbO_2}^{\lambda_2} & \varepsilon_{HbR}^{\lambda_2} \end{bmatrix}^{-1} \begin{bmatrix} \Delta OD^{\lambda_1} \\ \Delta OD^{\lambda_2} \end{bmatrix} / L \quad (2.22)$$

Here ΔOD^{λ_1} and ΔOD^{λ_2} represent the spatial distribution of ΔOD for wavelength λ_1 and λ_2 . ΔHbT and ΔHbT are also the spatial distributions changes of hemoglobin. Changes of total hemoglobin concentration can then be calculated by:

$$\Delta HbT = \Delta HbO_2 + \Delta HbR \quad (2.23)$$

2.5 Instrumentation of continuous wave DOT

Similar with CW-NIRS, CW-DOT uses the CW light as to a source for measurement. CW light source emitted photons into the scattering medium or tissues and light which have propagated inside the medium/tissues was then detected by the detector. Detectors can be arranged on the same side as incident light source (reflectance) or the opposite side of the light source (transmittance). Depend upon the different types of detector; measurements can be divided by contact or non-contact measurements. For non-contact measurement, CCD camera is used to image the region-of-interest (ROI). Every pixel of CCD camera can be treated as small detectors, which provides a large amount of data for each measurement. CCD-camera-based DOT system was developed in this dissertation work for tissue-mimic phantom studies and animal measurement. Details are described in the later chapter (Chapter 4). Regarding the contact measurement, multiple optical fibers are arranged on the surface of the target tissues/medium to receive the reflected light, which also allow interrogating the region covered by the optical fiber array. CCD-camera-based DOT systems are mostly used for phantom or animal measurements, while fiber-based DOT systems are more extensively applied to all kinds of the approaches, including animal and human measurements.

To date, several fiber-base CW-DOT systems are commercially available. In our

laboratory, there are three major systems currently used, which are NeuroDot (Cephalogics[®]), dynamic near-infrared optical tomographic instrument, DYNOT (NIRx Medical Technologies, LLC, NY, USA), and CW-6 (TechEn Inc, Milford, MA), respectively. In this work, DYNOT was used for animal measurements and is briefly introduced in this section. NeuroDot was used to perform the human measurements and will be introduced in the Appendix A.

The DYNOT system uses a noninvasive functional imaging method that employs low-energetic laser radiation to probe highly scattering media, such as tissue (Figure 2.7). The term dynamic is used because multiple optical tomographic data sets are acquired in a continuous fashion at high repetition rates (several images per second), thus allowing the study of physiologic changes inside the target. In our current system, two wavelengths (760 nm and 830 nm) are provided by two laser diodes, whose light is coupled sequentially into 32 different fiber bundles that deliver the light to different positions on the surface of the tissue to be studied. Each laser is operated at an output power of about 100 mW; about 25 mW of which reaches the target. The laser intensity is a sine-wave modulated at a frequency in 4-11 kHz range. Each source fiber bundle forms one branch of a bifurcated fiber bundle that joins another branch.



Figure 2.7 Front (left) and back (right) view of the DYNOT instrument. Figure was reprinted from Ref. [35]

This second branch is used for light detection. Each detector fiber bundle terminates on a single silicon photodiode of a multi-channel detection module [35]. The computer controls the communication between the various system hardware components and data acquisition. The DYNOT system is operated using a LabView-based GUI, which provides an interactive virtual control panel on the computer [35].

The front and back view of the DYNOT system is shown in Figure 5.3, with labels for the various subsections. The labels are:

- 1 – Power supply,
- 2 – Motor controller,
- 3 – PMD (programmable multi-channel detector) with detection fibers,
- 4 – Laser diode controller,
- 5 – PC with monitor/keyboard,
- 6 – Fiber optic cables,
- 7 – Optical switch,
- 8 – Optics shielding cover,
- 9 – Laser diodes (covered).

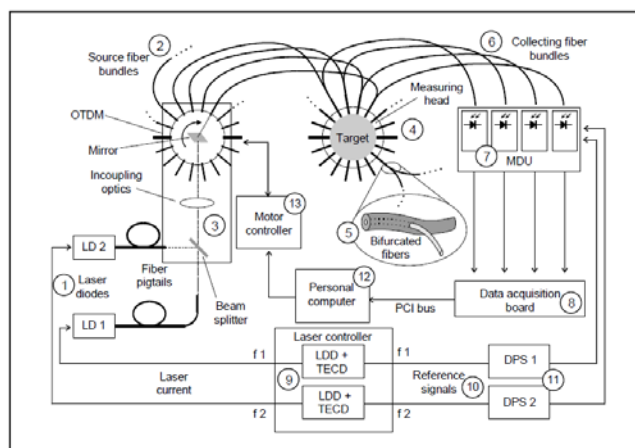


Figure 2.8 Block Diagram of the DYNOT instrument. LD: laser diodes, LDD: laser diode driver, TECD: thermo-electric cooler driver, f 1,2: laser modulation frequencies, DPS: digital phase shifter, OS: optical time-division multiplexer. Figure was reprinted from Ref. [35].
 In Figure 2.8, block diagram of DYNOT is shown where the following stands for, LD:

laser diodes, LDD: laser diode driver, $f_1, 2$: laser modulation frequencies, TECD: thermo-electric cooler driver DPS: digital phase shifter, OS: optical time-division multiplexer. Initially light from two laser diodes (1) is combined and focused into an optical switch (3). Light is sequentially deflected on to each of the source fiber with the help of a rotating mirror within the optical switch (3). The DC servo motor controls the mirror movement under the control of a computer operated motor controller (13). Fiber bundles (6) consists of 32 bifurcated fibers, which serves the purpose of guiding the source light to the target and the back reflected light from the target to a programmable multi-channel detector (PMD) (7). The data acquisition board (8) digitizes the output from PMDs. Laser controller (9) controls the operation and temperature-stabilization of the laser diodes.

CHAPTER 3
VOLUMETRIC THREE DIMENSIONAL RECONSTRUCTION WITH DEPTH COMPENSATION
ALGORITHM

3.1 Introduction

In recent years, near infrared (NIR) diffuse optical tomography (DOT) has been intensively used to investigate the tissue heterogeneity non-invasively. Different approaches of using DOT have been presented, such as functional human brain imaging [21, 22] and cancer detection (e.g. breast [19, 20], prostate [17, 18, 30], etc.). Although DOT has the ability to recover the distribution of tissue heterogeneity in three dimensional (3D) space/volume, due to the intrinsic diffuse nature of photons in biological tissues, the sensitivity of DOT decreases dramatically with increase in depth. The high sensitivity at the superficial layer results in the reconstruction of deep object towards the surface of imaging field, leading to poor depth localization [36].

Significant efforts have been made by several research groups to improve spatial resolution and depth accuracy in DOT. Recently, researchers have used hybrid image systems, which combine DOT with other image modalities, such as magnetic resonance imaging (MRI) and computed tomography (CT), to improve the accuracy of depth localization and spatial resolution. This kind of combination provides prior anatomical information which can overcome the depth limitation in DOT [37].

From the aspect of image reconstruction algorithm, Pogue et al. [38] introduced spatially variant regularization (SVR) to compensate the decrease in measurement sensitivity with increased radial depth. This is based on the frequency-domain technique and a circular probe geometry which is often used for breast cancer imaging. Furthermore, Culver et al. [14] also presented a similar approach for CW-based DOT with reflectance probe geometry for a rat

brain model. Both methods have modified the penalty term of regularization along depth, and thus benefiting the image quality of DOT.

Recently, layer-based depth compensation algorithm (DCA), based on maximum singular values (MSVs) of layered sensitivity, to effectively improve depth localization of DOT in deep tissue, has been developed by our laboratory [39]. Specifically, DCA can compensate the severely decreased sensitivity in the deep layers by creating a balancing weight matrix that improves measurement sensitivity with increased depth. This weighted matrix is made by inversely arranging MSVs to generate a pseudo-exponential matrix which allows counterbalancing the reduced measurement sensitivity in deep layers. In this chapter, the formation of DCA and its experimental validation using laboratory tissue-mimic phantoms and its approach in complex geometry with finite element method (FEM) for rat head model is presented. The quantitative results of computer simulations are demonstrated.

3.2 Formation of DCA

Following the conventional DOT forward and inverse problem, the Rytov formulation of the scattered field is written in discrete form as $y = Ax$ and x can be solved through regularization as shown in Equation 2.20. Here A represents the measurement sensitivity and the measurement sensitivity of DOT in deep tissue is significantly lower than that in superficial tissue because of the severe attenuation in light intensity as increase of propagation depth. In order to overcome this problem, DCA has been recently developed [39] by introducing a weighted matrix M , which has a pseudo-exponential magnitude with depth to counterbalance the loss of sensitivity of A in deep layers. The weighted matrix M is formed as:

$$M = \begin{bmatrix} \max(A_L) & & & \\ & \max(A_{L-1}) & & \\ & & \ddots & \\ & & & \max(A_1) \end{bmatrix}^\gamma \quad (3.1)$$

where $\max(A_i)$ represents the maximum singular values for measurement sensitivities within the particular layer i which is decomposed from forward matrix A , where $i = 1 \dots L$, γ is an

adjustable power and can be varied between 0 and 3. The detailed derivation and validation of DCA can be found in references [39]. The key component in DCA is the formation of a transformation matrix $A^\#$, as defined by $A^\# = AM$. Then $A^\#$ is used to replace the original sensitivity matrix, A , in Equation 2.20. The reconstructed image to be obtained using DCA can be written:

$$\hat{x}_{DCA} = (AM)^T (AM(AM)^T + \alpha S_{\max} I)^{-1} y \quad (3.2)$$

where S_{\max} is the maximum eigenvalue of $AM(AM)^T$.

As demonstrated in our recent publications [39], the power of depth compensation is controlled by the exponent parameter of γ in M . The larger the γ value is, the larger the weight is to compensate the measurement sensitivity toward a deeper layer, and vice versa. An inappropriate selection of γ could lead to over-compensation and give rise to inaccurate results. Our previous studies have suggested an optimal range of γ to be 1.0-1.6 for accurate depth localization and better reconstructed image quality.

The selection of optimal range of γ was based on the value of position error (PE) and contrast-to-noise ratio (CNR). PE is the distance from the center of actual object to the center of the reconstructed object. CNR [30] indicates whether the reconstructed object can be clearly distinguished from the background. A reconstructed image was divided into two regions: volume of interest (VOI) and volume of background (VOB). VOI was defined by the location and size of the reconstructed object. VOB was defined by the remaining volume of the image. CNR can be calculated by:

$$CNR = \frac{\mu_{VOI} - \mu_{VOB}}{\left[w_{VOI} \sigma_{VOI}^2 + w_{VOB} \sigma_{VOB}^2 \right]^{1/2}} \quad (3.3)$$

where w_{VOI} and w_{VOB} are the weight factors of the VOI and VOB relative to the entire volume (i.e., VOI or VOB divided by the entire volume), μ_{VOI} and μ_{VOB} are the mean values of object and background volumes in a 3D reconstructed image, and σ_{VOI} and σ_{VOB} are the respective standard deviations. Niu et al. [30] have found that the optimal range of γ is still held with

changing background optical properties, including absorption and scattering coefficients and concluded that DCA can be effectively applied for multispectral DOT.

Besides changing background optical properties, several different percentages of random noise (0.5%, 1% and 2%) were added in simulations to investigate the influence of noise versus adjustable power. Figure 3.1 shows the simulative CNR and PE results which represent the function of adjustable power γ and the depth of reconstructed object. Figures 3.1a to 3.1c demonstrate the CNR values for different level of noise, which are 0.5%, 1% and 2%, respectively. Figures 3.1d to 3.1f show the PE for 0.5%, 1% and 2% of random noise.

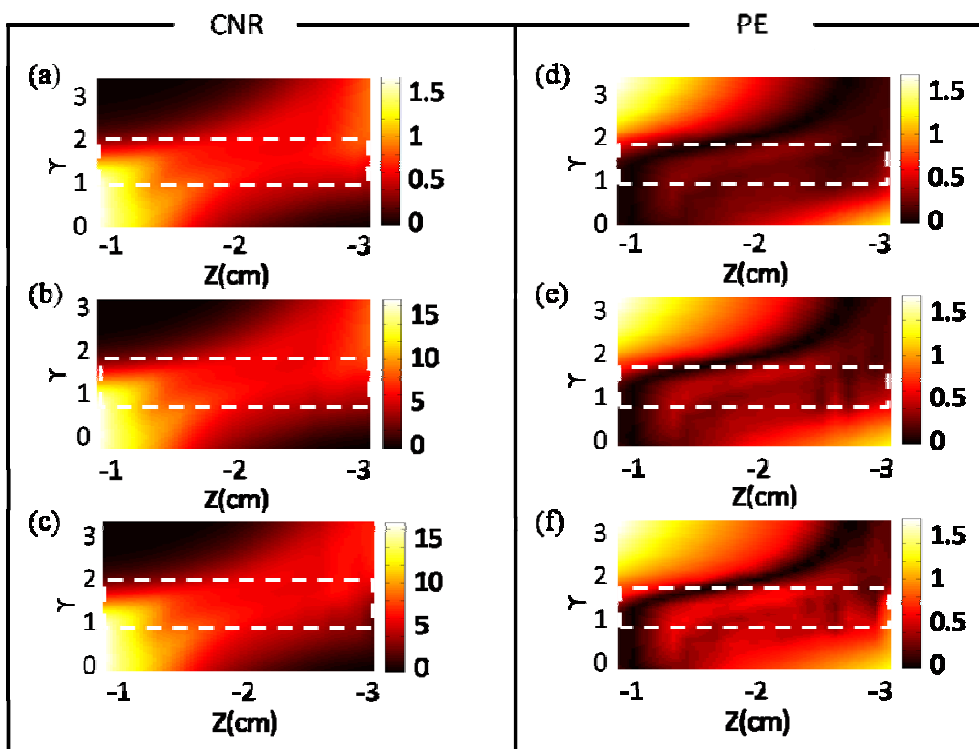


Figure 3.1 Relationship between the adjustable power γ versus the depth of reconstructed object. (a) to (c) show the CNR for 0.5%, 1% and 2% of random noise added. (d) to (f) demonstrate the PE for 0.5%, 1% and 2% of random noise.

From Figures 3.1a to 3.1c, it can be clearly seen that adjustable power γ is within the range of 1.0 to 2.0 (marked by dashed boxes), the CNR values are relatively high as compared to the remaining area. In terms of the PE, from Figure 3.1d to 3.1f, it can be noticed that the PE

values decrease as the γ increase, suggesting that better selection of γ should be the function of the depth of absorber. However, since the depth of absorbers are unknown in real measurements, there is an optimal range of γ between 1.0 to 1.6 (marked by dashed boxes) which provides relatively better quality of reconstructed image and depth localization. Moreover, these figures clearly indicate that the optimal range of γ is still held as the level of random noise increase from 0.5% to 2%. Therefore, it can be concluded that the optimal range of adjustable power γ is still effective for different level of noise, which reduced the selection of empirical parameters in practical use.

Furthermore, from Equation 3.2, it can be noticed that in image reconstruction of DCA, there are two parameters which can highly affect the quality of reconstructed images, which are adjustable power γ and regularization parameter α . It has been reported that parameter α used in Tikhonov regularization can stabilize and optimize the solution of ill-posed inverse problem by suppressing the noise. The selection of α is highly relative to the noise level of measurements. Our previous studies have suggested that appropriate selection of γ can improve the quality of reconstructed images by enhancing the spatial resolution as well as the depth localization [39]. To investigate the relationship between adjustable power γ and regularization parameter α , computer simulations, with the same setup presented in Niu et al. [39], were performed.

Figures 3.2a and 3.2b show the relationship of CNR and PE on adjustable power γ and regularization parameter α . From Figure 3.2a, it was found that within the optimal range of γ (1.0 to 1.6), CNR values are relatively higher with whole range of α , meaning quality of reconstructed images are relatively stable and consistent. In terms of PE, it is noticed that there is a small diagonal range of PE which has relatively lower PE values, as shown in Figure 3.2b. The smaller the α was selected, the larger the γ should be used. The same scenario can be seen in case of CNR plot shown in Figure 3.2a. As be known that the purpose of regularization parameter α is to stabilize the solution of ill-posed inverse problem by suppressing the noise. Hence, from Figures 3.2a and 3.2b, it can be concluded that DCA is also effective on noise

suppression as well as stabilize the solutions of ill-posed inverse problems with the appropriate selection of γ (1.0 to 1.6) even the too large or small γ were selected, that is, provide stable qualities of reconstructed images.

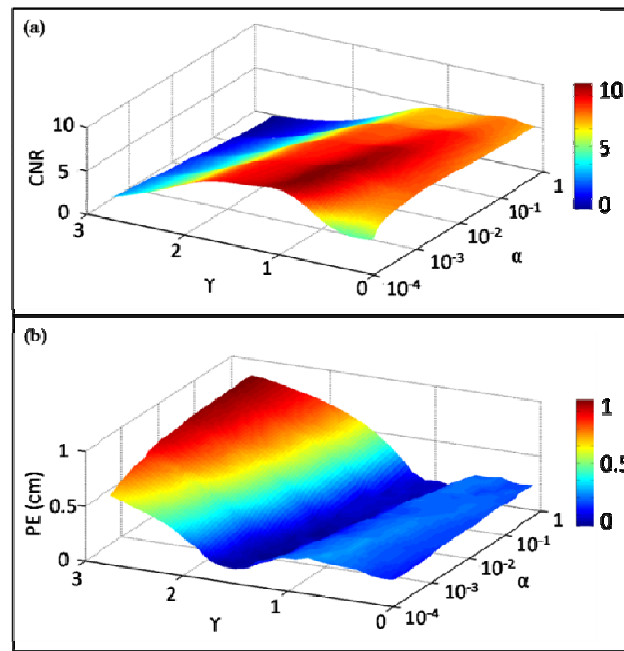


Figure 3.2 Relationship of (a) CNR and (b) PE on adjustable power γ and regularization parameter α

3.3 Previous study of DCA with laboratory phantom in simple geometry

Validation of DCA using laboratory tissue-mimic phantom have been performed and presented in Refs. [39]. Here, I briefly introduced the procedures and experimental results for reconstruction of embedded absorber in 3D space.

Multi-channel, continuous-wave near infrared tomographic imager was utilized to perform the experiments with a plastic container of 10 cm \times 10 cm \times 7 cm filled with a 1% Intralipid solution as a homogeneous medium. The background medium had a μ_a of 0.06 cm⁻¹ and a μ_s' of 8.2 cm⁻¹. The probe geometry was positioned on the surface of the container with 5x5 bifurcated fibers with inter-optode separation of 1.5cm. In experiment I, a 1-cm, spherical absorber ($\mu_a = 0.3$ cm⁻¹, recipe shown in Appendix C) was placed in the center of the x-y plane

and 3 cm below the surface of the phantom (i.e., $z=-3$ cm). The measured DOT data with and without the absorber were respectively acquired to generate the changes in optical signals seen by all the channels. In experiment II, keeping the experimental setup and parameters unchanged, two 1-cm-diameter absorbers were placed at $z=-3$ cm with a center-to-center separation of 3 cm along x axis.

Figure 3.3 shows the reconstructed images of one embedded object in both x-y and x-z planes using $\gamma=0$ and $\gamma=1.6$. It clearly demonstrates that the reconstructed image in z direction is pulled towards the superficial surface when $\gamma=0$ (Figure 3.3c) without applying DCA, while the lateral location of the absorber in x-y plane is relatively accurate (Figure 3.3a). The reconstructed object is located accurately at the expected depth (Figure 3.3d) when DCA was applied.

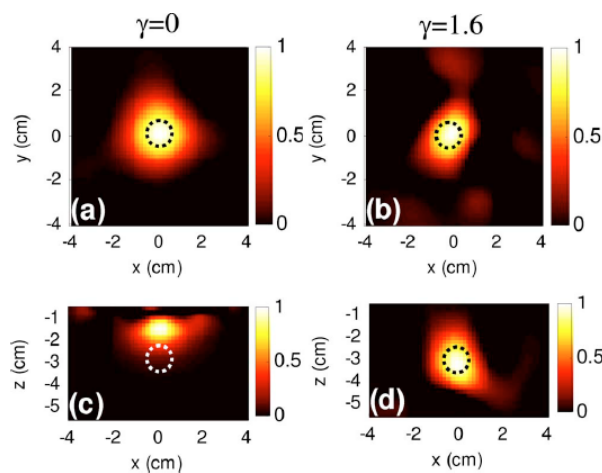


Figure 3.3 Reconstructed DOT images of a single embedded object placed in the center of x-y plane and at $z=-3$ cm, as marked by the dashed circle. (a) and (c) are obtained with $\gamma=0$ for the x-y and x-z plane, respectively; (b) and (d) obtained with $\gamma=1.6$ for the same respective planes. Figures were reprinted from Niu et al [39].

Similarly, reconstruction with DCA adopted ($\gamma=1.6$) shows the improvement in depth localization even when two absorbers are embedded (Figure 3.4). It is noteworthy that DCA with an optical γ ($=1.6$) has greatly improved the lateral contrast and localization of the two imaged absorbers, as compared between Figures 3.4a and 3.4b.

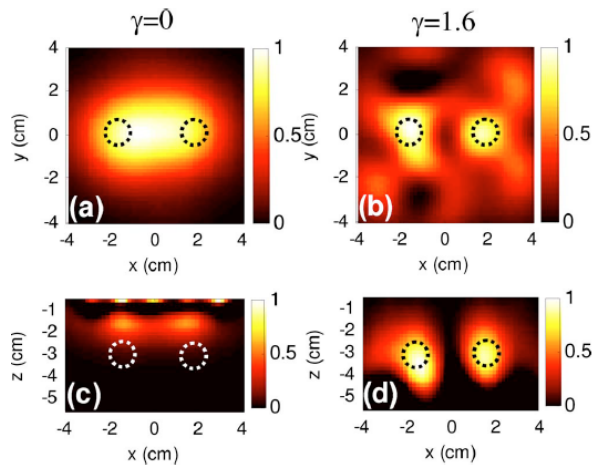


Figure 3.4 Reconstructed images of two objects placed symmetrically around the center of x-y plane and z=-3 cm (dashed circles). (a) and (c) are with $\gamma=0$, while (b) and (d) with $\gamma=1.6$. Figures were reprinted from Niu et al [39].

Another phantom experiment was performed using the same continuous-wave near infrared tomographic imager and optode geometry. An Intralipid solution of 1% with $\mu_a=0.08 \text{ cm}^{-1}$ and $\mu_s'=8.8 \text{ cm}^{-1}$ was used to fill a container of $15 \times 10 \times 10 \text{ cm}^3$ as a homogeneous medium. Two spherical absorbers of around 1 cm in diameter and $\mu_a = 0.3 \text{ cm}^{-1}$ were simultaneously placed at the depths of -2 cm and -3 cm below the surface of the phantom with a center-to-center separation of about 4.1 cm.

Figure 3.5 shows the reconstructed images of the two inclusions in x-z plane. It can be observed that both of these reconstructions can provide accurate localizations in lateral direction along x-axis. However, it is also found that the reconstructed inclusions by $\gamma=0$ are pulled towards the superficial layers. Also, the two inclusions are projected at almost the same depth. For the reconstruction with DCA adopted, the reconstruction with $\gamma=1.3$ leads to improved accuracy in depth for the two inclusions. Also, the depth difference between them can be easily observed on top of the background.

The laboratory experiment demonstrates that reconstruction with DCA can significantly improve the depth localization and also the lateral resolution in reconstruction of one or two embedded inclusions.

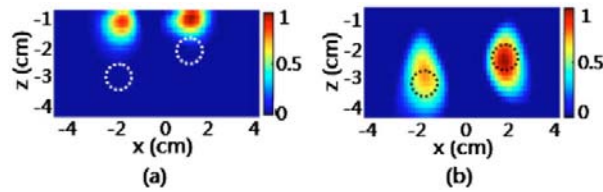


Figure 3.5 Reconstructed DOT images of two objects (dashed circles), placed -2 cm and -3 cm in depth with a center-to-center separation of 4.1 cm in x-z plane. (a) It is formed with $\gamma=0$, while (b) is obtained with $\gamma=1.3$. Figures were reprinted from Niu et al [39].

3.4 Application in model-based FEM

As described in previous section, the light propagation can be analytically modeled and solved while model the tissue or space to be reconstructed as semi-medium. However, for more complicated tomography cases, which reconstructs spatially varied optical property distribution, numerical methods such as finite element method (FEM) is used. FEM can deal with most of the complicated geometry and also take advantage of providing spatial information compared to modeling the volume as semi-infinite medium. Although FEM in DOT is relatively computation intensive compared to analytically solved light propagation in tissue, great emphasis has been placed in DOT field since it allows spatial characterization of the optical properties of tissue objectively. In this section and subsection, approaches of model-based FEM combined with DCA are presented, including rat and human head model (Appendix A).

3.4.1 Modeling of standard rat head template

In order to generate the three dimensional rat head model, the T2-weighted MRI sequence (Figure 3.6a) was used to obtain the anatomical structure of rat head [40]. This template set of rat head atlas was constructed by 30 rats with the body weight range from 214 to 364g. Three ROIs, which were skin/muscle, skull and brain, respectively, can be segmented based on multi-level Otsu's thresholding techniques [41]. The segmented two dimensional image sequences were then stacked together to form three dimensional volume model, as shown in Figures 3.6b to 3.6d.

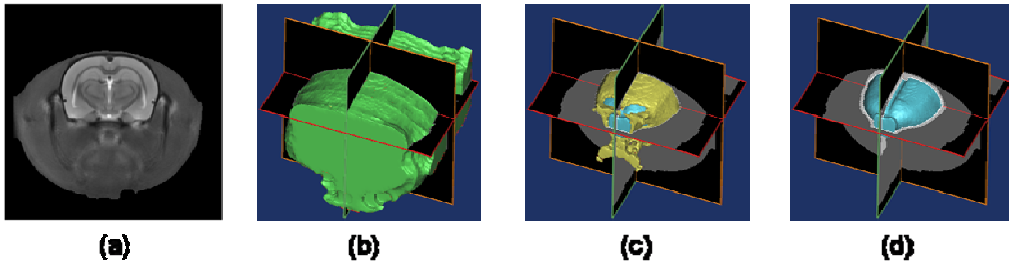


Figure 3.6 (a) T2-weighted MR image. 3D surface rendered rat head tissue models showing (b) skin/muscle (colored in green), (c) skull (colored in yellow), and (d) brain (colored in light blue).

Three dimensional finite element model (FEM) meshes (Figure 3.7) were then generated by MATLAB-based mesh generator iso2mesh (<http://iso2mesh.sourceforge.net/cgi-bin/index.cgi>), as shown in Figure 3.7. The model contained 16118 nodes corresponding to 96389 linear tetrahedral elements. Each node was labeled by one of three ROIs and the node locations were assigned the particular tissue optical properties [42]. The optical properties of rat head tissues are listed in Table 3.1.

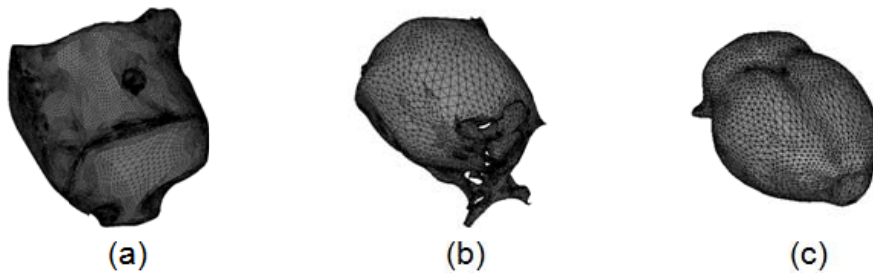


Figure 3.7 3D meshes of (a) skin/muscle, (b) skull and (c) brain.

Table 3.1 Optical properties of rat head tissue [42]

	Skin/Muscle	Skull	Brain tissue
μ_a (mm ⁻¹)	0.02	0.015	0.015
μ_s (mm ⁻¹)	0.68	2.2	2.2

To project the optode locations onto three dimensional rat head model for modeling light propagation within model, the projection procedure was similar as described in section

3.4.1.2. The optode geometry used here was rectangular array which consisted of 4 rows times 5 columns. The optode geometry using in this section was the bifurcated fiber array which was used in the actual animal measurements and will be addressed in the later chapter.

To achieve a geometric transformation of the rat head coordinates so that the optode locations measured in the real-world coordinates can be read and projected on the MRI coordinates. To do so, four landmarks were selected on the rat head (i.e., two eyes and two ears) as references to compute the transformation matrix, W . Specifically, the optode locations in a real-world (RW) coordinates system were measured by a 3D magnetic space digitizer. Using the coordinates of the rat's eyes and ears as reference points, the affine transformation matrix W can be obtained by:

$$P_{MRR} = W P_{RWR} \quad (3.5)$$

and

$$P_{RWR} = \begin{bmatrix} x_{RW_eyel} & y_{RW_eyel} & z_{RW_eyel} & 1 \\ x_{RW_eyer} & y_{RW_eyer} & z_{RW_eyer} & 1 \\ x_{RW_earl} & y_{RW_earl} & z_{RW_earl} & 1 \\ x_{RW_erarr} & y_{RW_erarr} & z_{RW_erarr} & 1 \end{bmatrix}, P_{MRR} = \begin{bmatrix} x_{MR_eyel} & y_{MR_eyel} & z_{MR_eyel} & 1 \\ x_{MR_eyer} & y_{MR_eyer} & z_{MR_eyer} & 1 \\ x_{MR_earl} & y_{MR_earl} & z_{MR_earl} & 1 \\ x_{MR_erarr} & y_{MR_erarr} & z_{MR_erarr} & 1 \end{bmatrix} \quad (3.5)$$

where P_{RWR} represents the reference coordinates matrix for the animal's eyes and ears measured by the 3D digitizer using the real world (RW) coordinate system, and P_{MRR} represents the reference coordinates of the same four points in the MRI (MR) coordinate system. The subscripts of 'r' and 'l' represent right side and left side, respectively. After the transformation matrix, W , was obtained through Equations 3.4 and 3.5, the optode locations matrix measured by the digitizer and expressed in the RW coordinates, P_{RWO} , can then be projected onto the surface in the 3D (MRI) rat head model, as written by:

$$P_{MRO} = W P_{RWO} \quad (3.6)$$

where P_{MRO} represents the coordinates of the optodes in the rat head model given by the MRI coordinates system. However, points after affine transformation were quite close to the surface of head model but not exactly located on surface of head model in most cases. In order

to assure optodes were exactly projected on the surface, the norms of closest surface patches were calculated and optodes were then projected along the averaged norm of those patches. The optode projected onto the surface of rat head model is shown in Figure 3.8.

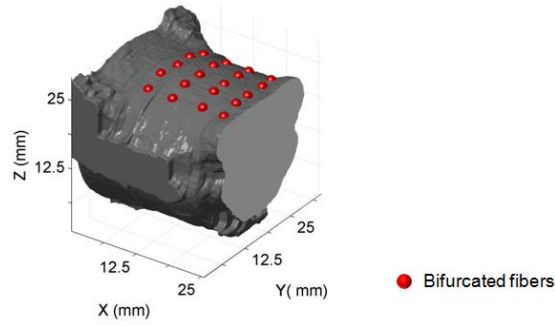


Figure 3.8 Optodes projection on 3D rendering rat head model.

Forward light modeling in rat head model was performed using finite element method based (FEM) MATLAB package NIRFAST [31] to obtain Jacobian matrix (also called sensitivity matrix) J , which represents changes in measured boundary data due to the small absorption perturbations. Given the Equation 2.18, the forward problem for rat head model can then be written as:

$$\Delta y = J_{rh} \Delta x \quad (3.7)$$

where Δy represents the measured changes of optical density between initial baseline and after changes of absorption due to focal cerebral ischemia, J_{rh} is the Jacobian matrix derived from rat head model and Δx represents change of absorption for each node.

3.4.2 Image reconstruction and implementation of DCA

To recover the change of absorption for each node, the inverse problem was solved using (Tikhonov regularization) Moore-Penrose generalized inverse (Equation 2.21):

$$\Delta x = J_{rh}^T (J_{rh} J_{rh}^T + \lambda I)^{-1} \Delta y \quad (3.8)$$

DCA, with modified sensitivity matrix J by counterbalancing the measurement sensitivity for deeper layer tissue, was then adopted. To implement DCA in the FEM-based rat brain atlas

geometry, we needed to determine the distances from scalp to inside tissue (which is the L in Equation 3.1) to be compatible with the rat brain atlas. Numerically, the following steps were taken in order to adapt DCA and to form volumetric DOT within the rat brain model:

- a. Calculate the total un-compensated sensitivity J_{rh}^{total} at node n by:

$$J_{rh_n}^{total} = \sum_{m=1}^{NM} J_{rh_{m,n}} \quad (3.9)$$

where $J_{rh_n}^{total}$ represents the total un-compensated sensitivity at node n , NM is the total number of measurements (or of source-detector pairs), and $J_{rh_{m,n}}$ is the un-compensated sensitivity at node n due to the measurement m .

- b. Find or quantify each L within the rat head atlas, we grouped all of the nodes which were located on the scalp of the rat head model as group Ω_0 , and grouped the rest of the nodes below the scalp as Ω . The distances from an individual node in Ω to all of the nodes in Ω_0 were calculated; the minimum of all these distances was used to define the distance between the respective nodes to the scalp. All the nodes having an equal distance to the rat scalp facilitated a layer within the rat head model to be used in DCA.
- c. Divide the distances into different depths with respect to the surface of the head model. Generate weighting matrix M by calculating the maximum singular values within respective depths or layers.
- d. Modify sensitivity matrix $J_{rh}^{\#} = J_{rh} M$.

Computation compensated $J_{rh}^{\#}$ took 10s on 3.30 GHz Intel i5-processor with 16 gigabytes memory. $J_{rh}^{\#}$ was calculated once for each rat data and then applied to entire time series measurement. $\gamma = 1.3$ was used in this study. The image reconstruction with DCA by replacing J_{rh} with $J_{rh}^{\#}$ can be expressed:

$$\hat{\Delta x}_{DCA} = J_{rh}^{\#} \left(J_{rh}^{\#} J_{rh}^{\# T} + \lambda I \right)^{-1} \Delta y = M J_{rh} \left(J_{rh} M^2 J_{rh}^T + \lambda I \right)^{-1} \Delta y \quad (3.10)$$

3.4.3 Total sensitivity analysis

Unlike the human head structure, the NIRS measurement can basically cover whole rat brain since light within NIR range can penetrate several centimeters in depth. Considering the volumetric distributions of DOT sensitivities, we compared the depth-compensated and depth-uncompensated measurement sensitivities (MS), namely, $J_{rh}^{\#}$ versus J_{rh} , within cortical (shown by yellow 3D surface rendered plot in Figure 3.9a) and subcortical (shown by gray 3D surface rendered plot in Figure 3.9a) areas.

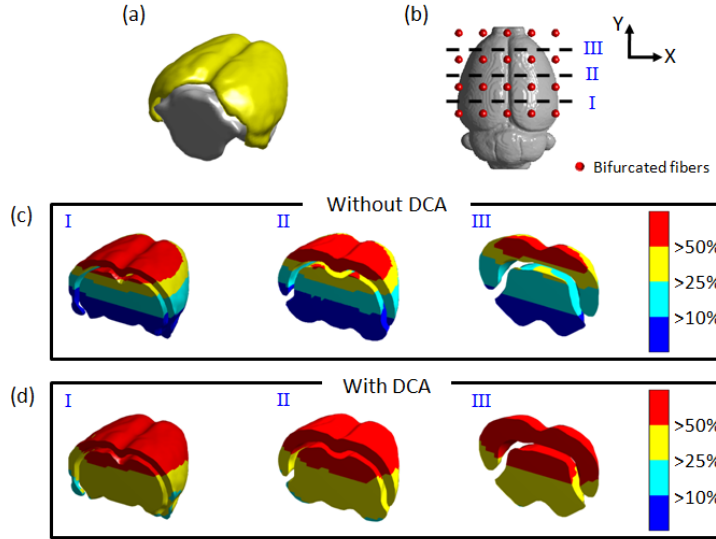


Figure 3.9 (a) 3D surface rendered plot represents cortical (colored with yellow) and subcortical (colored with gray) region of cerebrum. The distributions of different threshold levels of measurement sensitivities at three locations shown in (b) while DCA was not (c) or was (d) applied.

Moreover, since the distributions of MS depend highly on the arrangement of optodes, we chose three coronal cross sections to see volumetric sensitivity distributions, as marked by three dashed lines in Figure 3.9b ~2 mm above the bottom row (cross-section I), central line (cross-section II), and ~2 mm below the top row (cross-section III) of the optode array, respectively. Figures 3.9c and 3.9d depict the corresponding coronal views of spatial

distributions of un-compensated and compensated MS. Both sets of these figures reveal that the upper cortical and subcortical areas/volumes (red colored) have a MS higher than MS_{high} ($MS_{high} = 50\% S_{max}$, where S_{max} is the maximum sensitivity). Without using DCA, Figure 3.9c shows that approximate one-third of the cross-sectional cerebral area have a MS lower than MS_{low} ($MS_{low} = 10\% S_{max}$), mainly located at the bottom of the subcortical area. After utilizing DCA, Figure 3.9d illustrates that almost all the cortical and subcortical areas/volumes have a MS above a MS_{medium} ($MS_{medium} = 25\% S_{max}$), demonstrating improved MS in depth for imaging deeper tissues.

To quantitatively evaluate spatial distributions of measurement sensitivity (MS) in each of the coronal cross sections, we calculated an overlapping ratio between the MS areas, thresholded at different levels (i.e., $MS_{max} = 50\% S_{max}$; $MS_{medium} = 25\% S_{max}$; $MS_{low} = 10\% S_{max}$), and cortical and subcortical areas, as summarized in Table 1. The overlapping ratio can be defined by:

$$Overlapping\ ratio = \frac{|R_{th} \cap R_{area}|}{R_{area}} \quad (3.11)$$

where R_{th} represents the area region of MS above a chosen threshold, and R_{area} is the total area of cortical or subcortical regions. From Table 3.2, I observed that 55% of the cortical volume MS having higher than 50% of S_{max} , compensated sensitivities have approximate 55% of overlapping with cortical area and 22% with subcortical area while there are 46% and 5% of overlapping with cortical and subcortical areas in terms of un-compensated sensitivity. Moreover, both cortical and subcortical areas have measurement sensitivities larger than 10% of maximum sensitivity (only approximate 5% areas with measurement sensitivities less than 25% of maximum sensitivity) for compensated sensitivities compared to un-compensated sensitivities (55% and 28% for sensitivities larger than 25% of maximum sensitivity; 87% and 71% for sensitivities larger than 10% of maximum sensitivity). Results indicated that DCA has great potential to reconstruct changes of hemodynamic in deeper cerebrum tissues with better

localizations and resolutions.

Table 3.2 Overlapping ratio between the MS volume cut at the three chosen threshold levels and cortical/subcortical volume, calculated using compensated (with DCA) and uncompensated (without DCA) approaches.

Selected threshold	Compensated (DCA)		Uncompensated (without DCA)	
	Cortical volume	Subcortical volume	Cortical volume	Subcortical volume
$MS_{max}=50\%S_{max}$	0.55	0.22	0.46	0.05
$MS_{medium}=25\%S_{max}$	0.93	0.97	0.55	0.28
$MS_{low}=10\%S_{max}$	1	1	0.87	0.71

3.4.4 Setup of computer simulations

This section presents results based on computer simulations, which allowed me to quantify the performance of reconstructed images with and without DCA adoption. The real animal experiment results are described and demonstrated in Chapter 5. As previously stated, the main focus areas in the study of animal brain activities are the cortical and subcortical areas. Simulations were performed with three different setups:

1. S-I: The simulated absorptive perturbation was assigned to simulate the focal changes due to cerebral ischemia. The XY plane was located at the center of the optode array along the Y direction (Figure 3.10). S-I was simulated while the hemodynamic change occurred at the cortical area (approximate 2 mm below the skin surface) closer to the midline of the brain. The simulated perturbation had a 2:1 contrast in absorption and 1% Gaussian random noise was added in simulation.
2. S-II: Since the purpose of this simulation was to study hemodynamic changes due to cerebral ischemia, and since literature has identified the territory of the middle cerebral artery (MCA) as the most common location of embolic infarction, this occlusion model represents the outer side of brain hemisphere. For this reason, S-II simulated perturbation located on the outer right side of the brain. The perturbation was placed on the outer cortical area approximately 6 mm below the skin surface,

as shown in Figure 3.10b. It is also noteworthy that the overlapping measurement at this location is less than that at the S-I location, which may cause the effect of reconstructed image quality. The simulated perturbation had a 2:1 contrast in absorption and 1% Gaussian random noise was added in simulation.

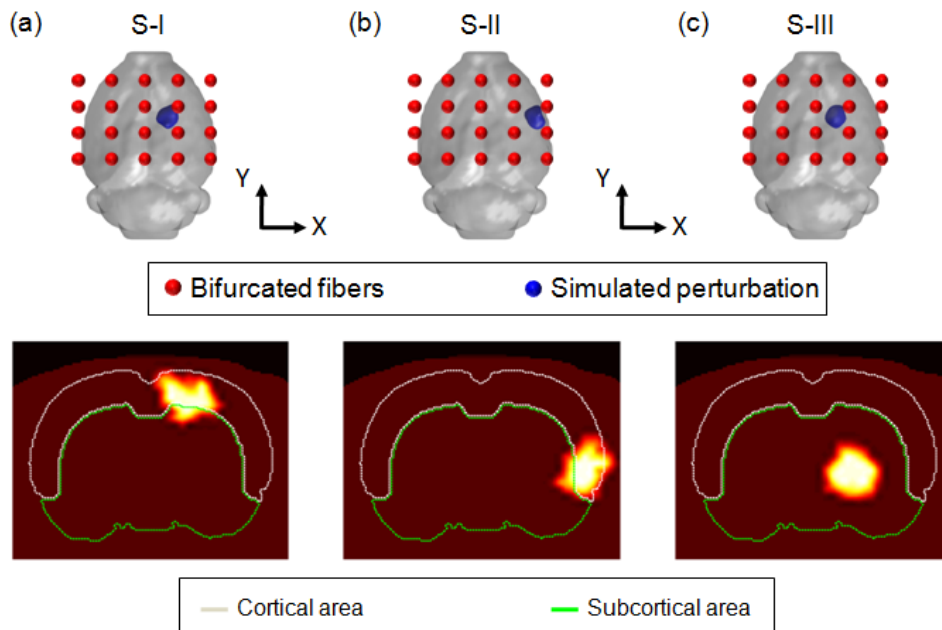


Figure 3.10 Setup of computer simulation for (a) S-I, (b) S-II, and (c) S-III. Panel on the bottom display the corresponding coronal sections of S-I to S-III.

3. S-III: S-III simulated the hemodynamic change, which occurred in the subcortical area. The location on the XY plane was the same as that found in S-I except the simulated perturbation was placed deeper (Figure 3.10c, approximately 6 mm below the skin surface). Similar to S-I and S-II, this simulated perturbation had a 2:1 contrast in absorption and 1% Gaussian random noise was added in simulation.

Figure 3.10 illustrates setups for three computer simulations.

3.4.5 Results

Figure 3.11 shows the simulation results for S-I. Comparing Figure 3.11a to 3.11b, the depth location of the reconstructed object in 3.11b is more accurate than in 3.11a although the

reconstructed perturbation was moved slightly toward the surface of skin. Figure 3.11c shows similar depth localization compared to Figures 3.11b but slightly improved depth localization was observed when DCA was applied. Moreover, Figures 3.11d and 3.11e display three dimensional rendered surface plots of the actual and reconstructed objects. The reconstructed objects were defined as voxels with values larger than 50% of the maximum value. Figure 3.11e clearly shows that the depth localization of reconstructed objects are slightly higher compared to the location of actual objects (blue) but the objects reconstructed with DCA (green) reside at a relatively correct location. The locations of reconstructed objects along the XY plane for both cases are matched with actual objects, as shown in Figure 3.11e.

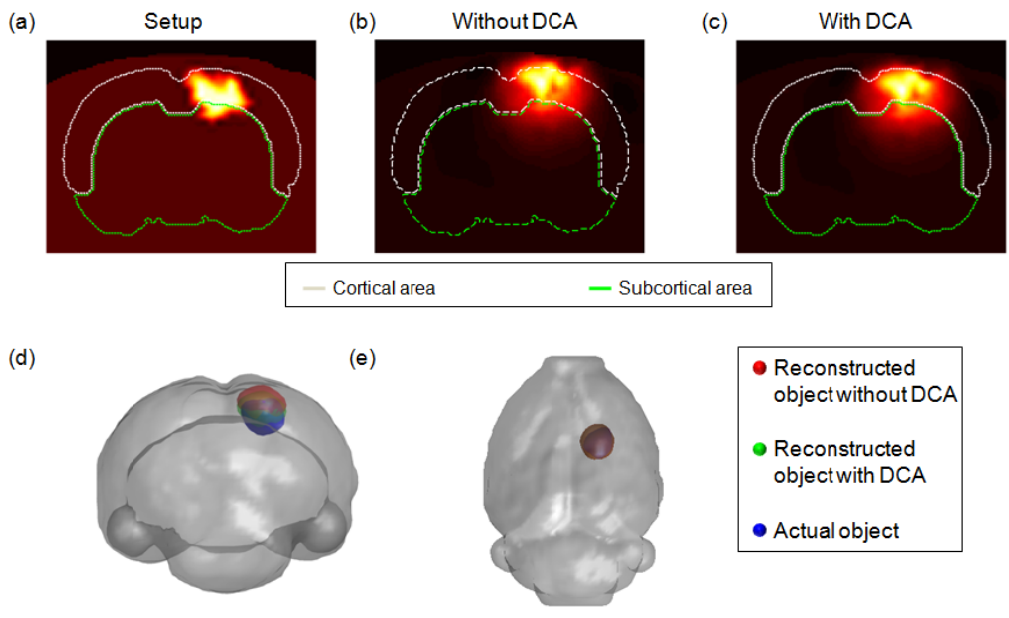


Figure 3.11 (a) Figure shows the coronal section of S-I. The coronal-sectioned reconstructed image of S-I (b) without and (c) with DCA was adopted. (d) The posterior view and (e) top view of 3D reconstruction. The reconstructed objects were defined as the voxels with reconstructed value larger than 50% of the maximum value.

In terms of results for S-II, Figure 3.12b shows a larger localization error, especially in depth localization, since the reconstructed perturbation was pulled toward the surface of the skin/muscle without DCA application. With DCA application, the reconstructed object exhibited a large improvement in depth localization as compared to the actual depth shown in Figure 3.12a.

Moreover, Figures 3.12d and 3.12e show a slight displacement toward the midline of the brain, which was observed for the perturbation reconstruction without DCA (red). A good performance in both depth and lateral localization can be found for objects reconstructed with DCA (green). Figure 3.13 demonstrates the reconstructed results in S-III. The absorber is located in a deeper localization of the brain model, which represents the hemodynamic change that occurs in the subcortical area. Similar to S-II, the object reconstructed without DCA adoption shows a larger error in depth localization (Figure 3.13b) as compared to the actual location of the simulated perturbation (Figure 3.13a). Figure 3.13c also shows the best localization in depth after DCA was applied. Furthermore, Figure 3.13e shows a relatively accurate localization on the XY plane. The object reconstructed without DCA (red) resides outside the actual object (blue) while objects reconstructed with DCA are shown covering the actual object (Figure 3.13d). Results show that DCA also demonstrates an improvement in depth localization in S-III.

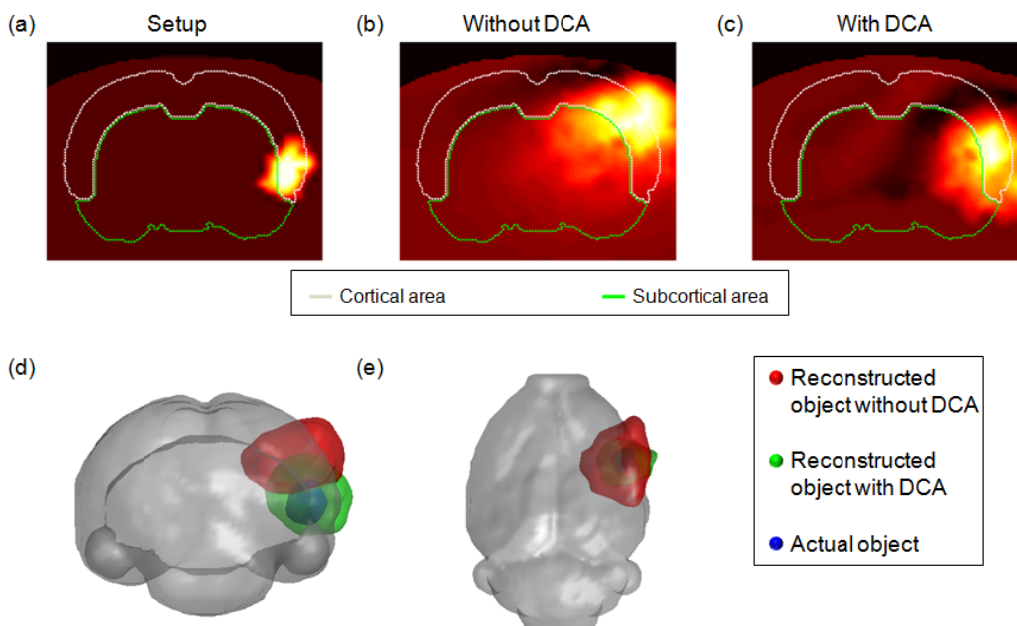


Figure 3.12 (a) Figure shows the coronal section of S-II. The coronal-sectioned reconstructed image of S-I (b) without and (c) with DCA was adopted. (d) The posterior view and (e) top view of 3D reconstruction. The reconstructed objects were defined as the voxels with reconstructed value larger than 50% of the maximum value.

Quantitatively, the reconstruction performances were evaluated by CNR (Equation 3.3) and location error. The location error was defined as:

$$location\ error = \sqrt{(x_{recon} - x_{actual})^2 + (y_{recon} - y_{actual})^2 + (z_{recon} - z_{actual})^2} \quad (3.12)$$

where the x_{recon} , y_{recon} , and z_{recon} are the xyz coordinates of the centroid of reconstructed objects and x_{actual} , y_{actual} , and z_{actual} are the centroid coordinates of simulated perturbation. Also, the volume ratio (VR), which was defined by the ratio between actual object and reconstructed object, was also compared. The summary is listed in Table 3.3.

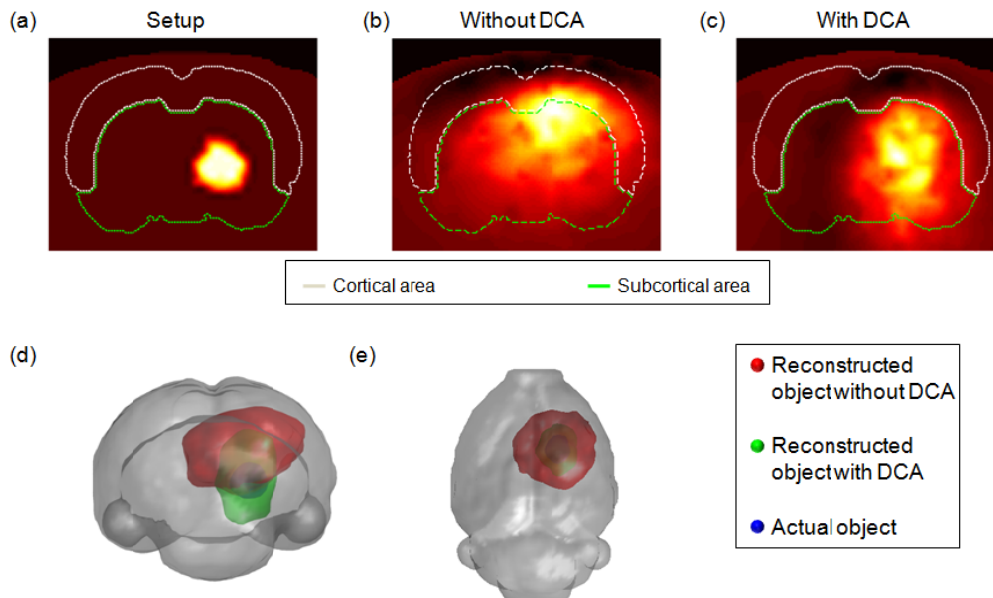


Figure 3.13 (a) Figure shows the coronal section of S-III. The coronal-sectioned reconstructed image of S-I (b) without and (c) with DCA was adopted. (d) The posterior view and (e) top view of 3D reconstruction. The reconstructed objects were defined as the voxels with reconstructed value larger than 50% of the maximum value.

In S-I, the location error for both reconstructions were similar and relatively small (0.22 mm and 0.38 mm). CNR and VR also show similar results for both cases. Results imply that DCA does not really improve localization when the simulated perturbation is located in a relatively superficial layer. In S-II, the values of CNR (4.65 versus 3.12) do show an

improvement when DCA was applied. Although VRs for both reconstructions are approximately four times larger than actual object (3.73 and 4.22) due to the low depth resolution of diffuse optical tomography (DOT), DCA also showed better performance in VR. Location error exhibited an improvement that was more than four times larger when DCA was applied. In S-III, the use of DCA also improved reconstructed image quality because of the larger CNR (4.73 versus 3.58). Location error also showed more than 4 times improvement with DCA (0.81) compared to no DCA (3.27). Overall, based on the computer simulation, reconstruction with DCA provided better performances in reconstructed image quality as well as localization (especially in depth) when the same optode geometry was used. Simulation results also suggest that using DOT to study cerebral ischemia in rat models benefits with DCA application. The improvement will be demonstrated in a later chapter (Chapter 5).

Table 3.3 Summary of the CNR and location error and VR values for three simulation setups

	S-I		S-II		S-III	
	W	W/O	W	W/O	W	W/O
CNR	6.63	6.47	4.65	3.12	4.73	3.58
Location error (mm)	0.22	0.38	0.89	3.49	0.81	3.27
VR	1.11	1.07	3.73	4.22	3.52	4.01

* W: With DCA

* W/O: Without DCA

3.5 Conclusion

This chapter presents the feasibility of generating volumetric diffuse optical tomography together with a depth compensation algorithm (DCA). DCA was initially developed in simple voxel-based geometry where the homogenous background optical properties and the optimization of adjusted power selection was done using computer simulation. Convincing results in improvement of depth localization were demonstrated based on computer simulations and laboratory phantom experiments.

DCA allows depth localization correction for 3D-DOT image reconstruction; however, it is well-known that conventional 3D diffuse optical tomographic images lack structure and anatomical information, which may cause inaccurate of target region localization estimates. To

solve this problem, DOT researchers recently began merging DOT images with other image modalities, such as CT, MRI and ultrasound, to provide anatomical structure or so-called “*prior*” information. Using “*prior*” information from other image modalities, researchers were able to perform 3D DOT image reconstruction in arbitrary geometry utilizing heterogeneous background optical properties. In the fNIRS community, researchers are accustomed to either subject-specific [21, 43] or standard template head [44] anatomical structures from MRI, which are used to study brain activities and response to different brain tasks. Combined with the structural information from transrectal ultrasonography, DOT can provide the optical information needed to benefit prostate cancer detection [18]. Moreover, structure-guided DOT has also been used to detect breast cancer [45, 46]. Even though structure-guided DOT has the capability of better visualization as well as lateral localization, large errors in depth localization still exist because the sensitivity of DOT exponentially attenuates with the increase of penetration depth. This chapter combines the structure-guided 3D-DOT with DCA to overcome the lack of anatomical structure and poor depth localization in DOT. The proposed methodology can facilitate the study of hemodynamic changes during cerebral ischemia in rat models (will describe in Chapter 5). Also, this same methodology can be extended to study brain activity in human subjects (will describe in Appendix A).

Overall, this chapter presents the development of a depth compensation algorithm and its applications in complex geometry with FEM approaches. A rat head model was generated from a template of MR image sequences. Based on the rat head model, total sensitivity analysis showed that image reconstruction with DCA has great potential in imaging deep tissue with better depth localization and resolution. Since the latter phase of this study focused on measuring cerebral ischemia in rat MCAO models, computer simulations with different setups were used to simulate different location of hemodynamic changes during cerebral ischemia. These simulations also demonstrated the improvement of depth localization and reconstructed image quality when DCA was applied. Results shown in this chapter suggest that this

methodology should be utilized in future physiology studies focusing on cerebral ischemia in rat MCAO models.

CHAPTER 4
VOLUMETRIC DIFFUSE OPTICAL TOMOGRAPHY USING CCD-CAMERA-BASED IMAGING
SYSTEM

4.1 Introduction

The last decade has witnessed the emergence of diffuse optical tomography (DOT) medical imaging modality [47, 48], which permits near infrared (NIR) light (650-900 nm) to penetrate deep tissues in several centimeters noninvasively. This technique has been investigated for several clinical applications, particularly for monitoring of functional brain activities [16, 43, 49] and detection of breast cancer [46, 50]. The fundamental principle of DOT is that the detected NIR signals reflect optical properties of underlying biological tissues [17], and the spatial distribution of such measured optical properties can be used to reconstruct optical tomographic images.

In the meantime, small animal models have been often utilized in preclinical research in order to investigate a variety of human diseases. Commonly used small animal imaging modalities include magnetic resonance imaging (MRI) [51], computed tomography (CT) [52], positron emission tomography (PET) [30] and single photon emission computed tomography (SPECT) [53]. As compared to MRI and CT, DOT is able to provide functional sensitivity. It is also radiation free unlike CT, PET and SPECT. In fact DOT has become a commonly used imaging methodology in preclinical studies for diseases, such as stroke [54] and cancer [55].

To date, fiber-based and CCD (charge-coupled-device)-camera-based DOT techniques are well developed and widely performed in both human and animal studies. A fiber-based DOT system has several advantages, namely, being compatible with different geometry and shape of a measured organ and having low noise because of direct contact of fibers on the tissue surface. However, limited surface area on small animals places a constraint on placement of many fiber

optodes. This in turn, restricts the spatial resolution of reconstructed images. A CCD-camera-based DOT system eliminates such a problem since the CCD camera can serve as a detector array with possibly thousands of virtual detectors and cover a wide field of view (FOV). Moreover, such a DOT system is simpler and more portable with lower cost, as compared to a fiber-based DOT system.

While DOT is a promising tool to image diseases non-invasively, one major limitation exists due to scattering of photons traveling in tissue. Namely, the strong scattering of biological tissue causes the detection sensitivity of DOT to attenuate exponentially with increased depth, resulting in poor depth localization in DOT. A number of different research groups have strived to improve the accuracy of in-depth localization. A layer-based sigmoid adjustment (LSA) method was introduced to balance the sensitivity contrast in depth by directly adjusting the forward sensitivity matrix [56]. Spatially variant regularization (SVR) [38] was also introduced to compensate the decrease in measurement sensitivity with increase of depth by modifying the penalty term of regularization along depth. SVR has been utilized in the frequency-domain and CW-based DOT techniques for imaging human breast cancer and brain functions. Recently, we have developed a depth compensation algorithm (DCA) to significantly improve the accuracy of DOT in depth localization, as demonstrated by both laboratory phantom and human brain measurements [39], using fiber-based DOT systems.

In this chapter, efforts have been focused to demonstrate the feasibility and improvement of three-dimensional (3D) volumetric DOT for small animal imaging by using CCD-camera-based DOT in combination with DCA. Our results are based on computer simulations and laboratory phantom experiments, confirming that the combination of a CCD camera and DCA is an effective approach for 3D volumetric images to be utilized in preclinical research.

4.2 Instrumentation

A CCD-camera-based, NIR spectroscopic imaging system, which consisted of a broadband light source, a multiplexer, a 6-filter wheel, and a high-speed CCD camera (Figure

4.1) with a pixel matrix of 496×656 was implemented. Such a system allowed acquisition of transmitted/reflected NIR signals from living tissues at specific wavelengths so as to obtain hemodynamic signals within a time scale of a hundred milliseconds. CCD-camera was calibrated by utilizing laboratory tissue-like phantoms in order to (a) calibrate the CCD camera for its non-uniformity and to (b) examine the stability and linearity of the calibrated camera. The procedures are described in the following section.

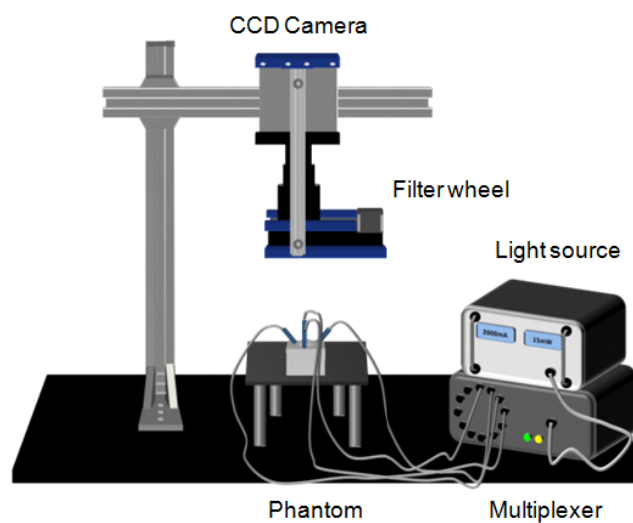


Figure 4.1 Schematic diagram of a CCD-camera-based DOT system for laboratory measurement

4.2.1 Calibration of CCD camera

Numbers of factors affect the results of a CCD image. These factors include (1) small electric signals seen by the camera without any optical input, or dark current, (2) pixel-to-pixel sensitivity variations, and (3) non-uniform illumination of the CCD chip due to vignetting and dust. Flat field correction is a common technique [57] that can be used to obtain improved quality of CCD images. The flat field technique removes the effects due to dark current, pixel-to-pixel sensitivity variations, uneven illumination, and non-uniformity caused by vignetting and dust.

During the process of correction, we collected two types of images besides taking raw object images: (1) dark images without any optical input and (2) reference images (flat field images) with planer illumination. The dark images were needed to correct the electric current that flows through each pixel of the CCD array without any optical input. Figure 4.2a depicts the dark images taken from our CCD camera with 500ms integration time. It clearly shows higher intensity on right side of image compared to left side. Also, an approximate 300 in intensity was detected for each pixel of CCD array even without any optical input. Figure 4.2b shows the cross section profiles cut along X axis of images taken with different integration times. It reveals the intensity of dark current increased as integration time increased but the patterns of intensity distribution were similar. Figure 4.2b suggests that the dark image for flat field correction should be taken with the same integration time as the raw object images

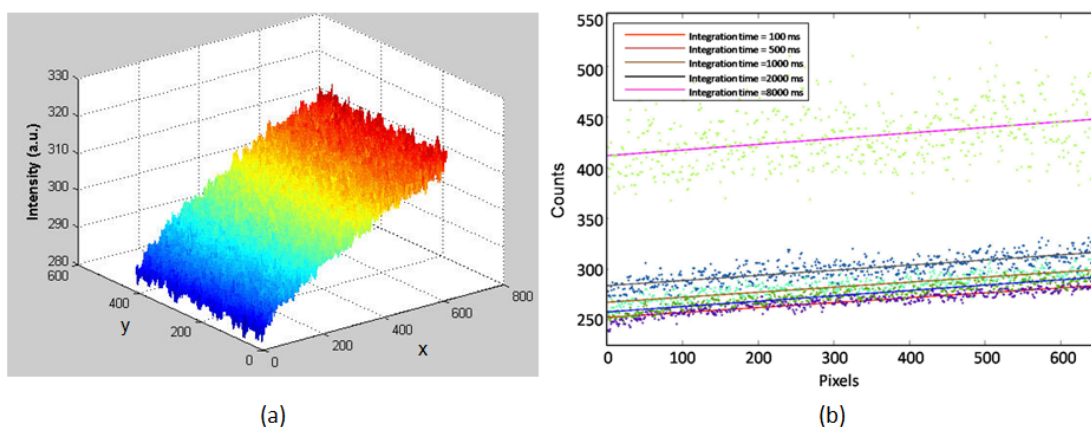


Figure 4.2 (a) Surface graphics of dark image taken from our CCD camera with 500ms integration time. (b) The cross section profiles along X axis of images taken with different integration times.

In terms of reference images, the planer-illuminated reference images were obtained by uniformly illuminating a highly-reflecting reference plate, which has a reflectivity of 98% and a dimension of $200 \times 200 \text{ mm}^2$. To approximately achieve a planar illumination, we used a white light lamp and placed it 1.5 meters away from the measurement site, with a good amount of light intensity, without saturating the camera. Figure 4.3a shows the flat filed image acquired by

our CCD camera and the corresponding cross section profile (Figure 4.3b). It can be observed that center part of CCD array has higher sensitivity while the sensitivity decreases from center toward the edge part of CCD array. Similar intensity distribution is found as dark image since right side of image has higher intensity compared to left side of image.

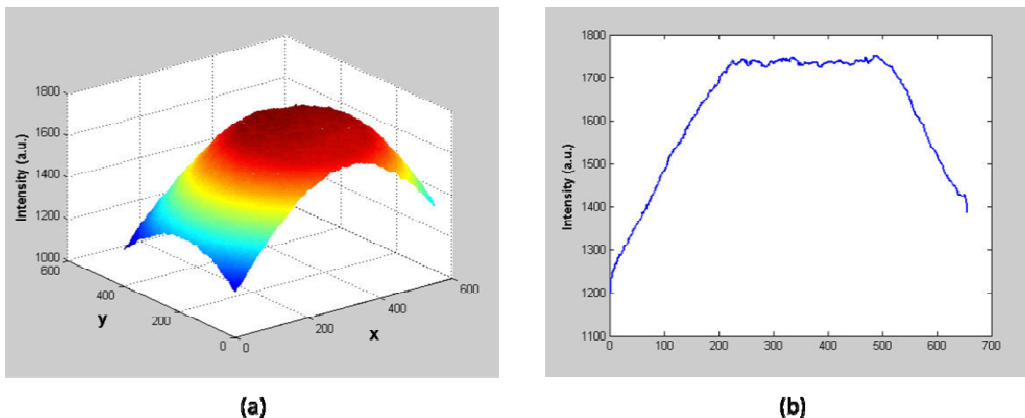


Figure 4.3 (a) Surface graphics of flat field image taken from our CCD camera with 500ms integration time. (b) The cross-section profile of intensity from a flat field image along X axis

To demonstrate the procedures used to perform flat field correction and the necessity of correcting a raw image, the phantom experiment was performed with transmission setup in which object image was taken with a point-source illumination from one side of the objects (Figure 4.4a). The phantom was made with 1% homogenous intralipid (Baxter Healthcare Corporation, Deerfield, IL) solution. The procedures used to perform flat field correction in this study are depicted in Figure 4.4b and are described below: first, take a dark image by blocking the camera's entrance completely, followed by taking object images. The integration times were kept the same for both situations. Second, take a reference image with a planar illumination followed by the corresponding dark image, also using the same integration time for both. Then, corrected object images can be obtained with the following equation:

$$I = K \frac{O - D_o}{R - D_R} \quad (4.1)$$

where I represents the corrected image, R is the reference image from the reference plate, O is the raw object image, D_O and D_R represent dark images taken with the corresponding integration times for the object and reference plate, respectively; K is a constant and usually is equal to the intensity averaged over the area of reference image.

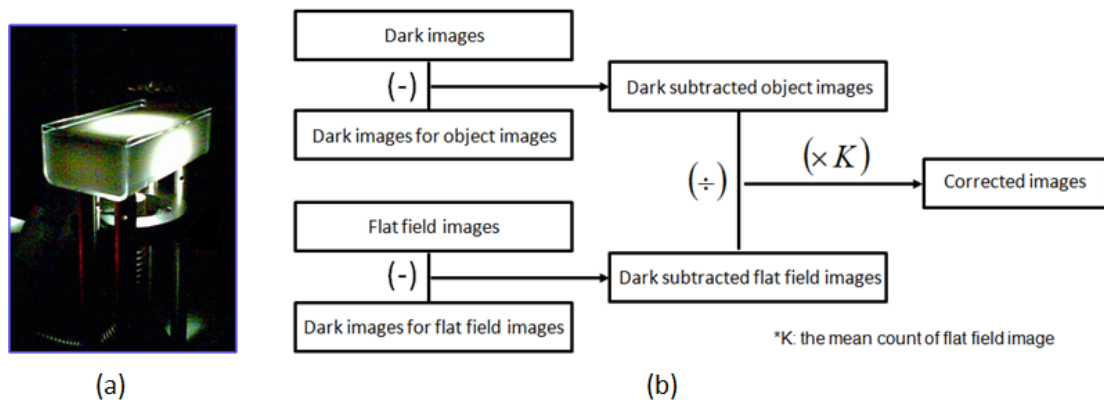


Figure 4.4 (a) A tissue phantom which was sitting on a phantom supporter with the illumination light coming from the bottom. (b) Schematic illustration of the procedure of flat filed correction.

Figure 4.5 shows the cross-section profiles along X axis and Y axis of a CCD image before and after flat field correction. It is noticed that the center of field of view (FOV) detects much higher light intensity than the edges before correction. After the correction, it is clearly shown that the uniformity on the edges is much improved. For quantitative comparison, maximal relative deviations between the central intensity and the intensity at the edge of the images for both the raw and corrected images were calculated, using the following expression:

$$\text{relative deviation} = \frac{\text{central intensity}}{\text{intensity at the edge}} \quad (4.2)$$

The estimated maximal values of relative deviations were 40% and 10% for the raw image and corrected image, respectively. In most of the image regions, such deviations in the corrected images were less than 10%.

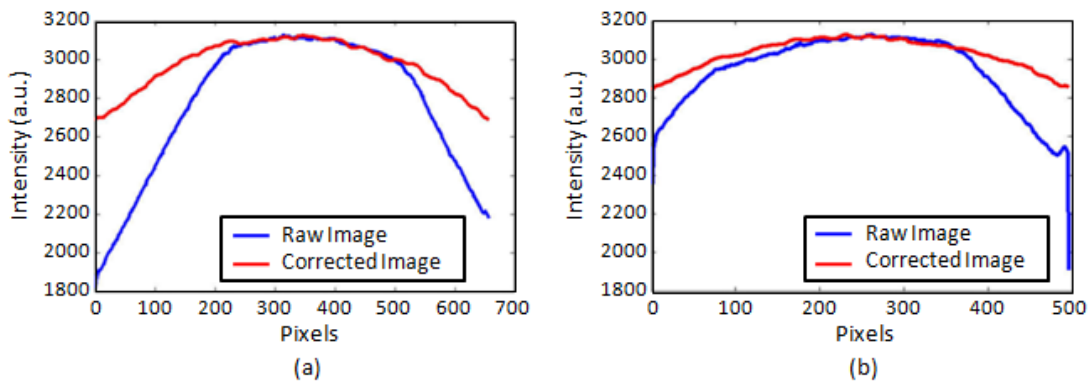


Figure 4.5 The cross-section profiles of intensity from a raw and corrected image along (a) X axis and (b) Y axis.

Moreover, the results from corrected image and image from computer simulation which is considered as the ideal case of light distribution without considering photon loss while traveling before hitting the CCD array were compared to estimate the quantum efficiency of CCD camera. The ratios between corrected image and simulated image were calculated. The corrected image and simulated images were rescaled to peak value of images for comparison. Also, both images were then meshed into 13x9 grids, as shown in upper row of Figure 4.6. Inter-point distance was approximate 1mm. Figure 4.6c depicts the ratio between the intensity from corrected object image and simulated image. It is clearly shown that at center part of images the ratios are pretty close to 1, meaning two images are pretty matched around central. Also, the intensity differences around the edge are reduced from approximate 35% difference (ratio between uncorrected and simulated images, not shown) to 5% difference.

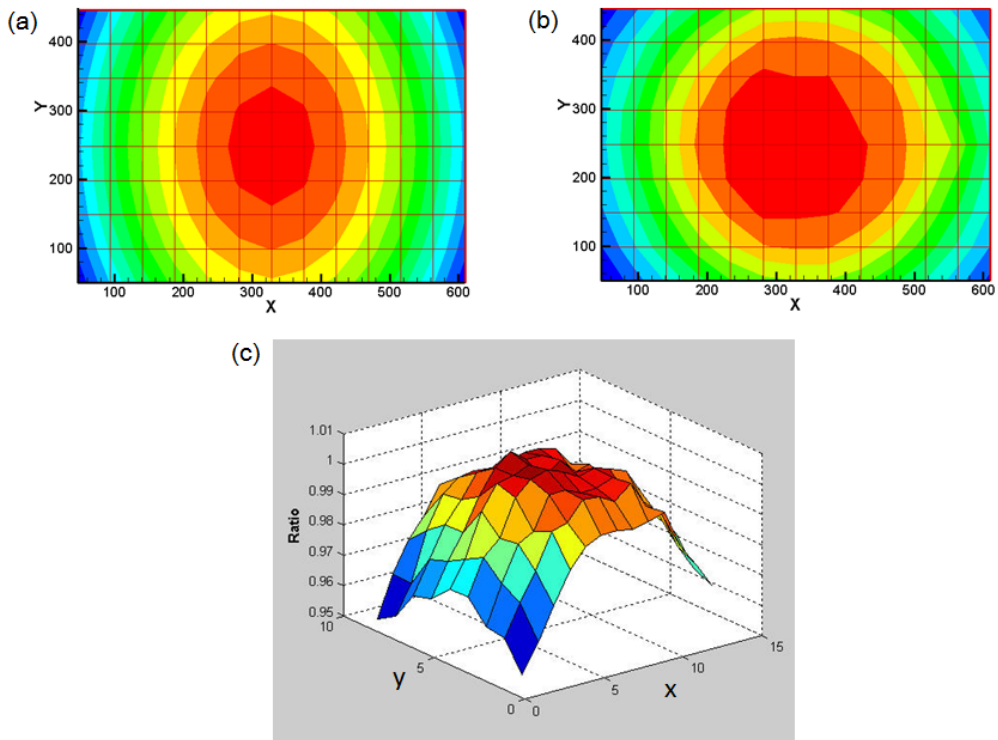


Figure 4.6 (a) Computer simulated image and (b) image taken from CCD camera and the n corrected with flat filed correction. Both images were meshed into 13x9 grids. (c) Surface graphic depicts the ratio between the intensity from corrected object image and simulated image.

Another phantom experiment was performed to demonstrate the improvement of the light intensity distribution. The experimental and phantom setup was the same as Figure 4.4a beside the light source was moved to four different corners of FOV of CCD camera. The photographs for respective raw images where light source moved to different corners are shown in upper row of Figure 4.7. Left column of bottom row of Figure 4.7 shows the images taken from CCD camera. It shows that the area containing the higher light intensities moves toward the center of FOV regardless of the position of the light source. This is due to higher sensitivity of photon detection around the central part of CCD camera. After performing the flat field correction, as described above, right column of bottom row of Figure 4.7 shows the images after correction, where the highest intensities are located at the locations of the light sources near

four corners of the FOV, proving the accuracy of the corrected images and necessity for image correction.

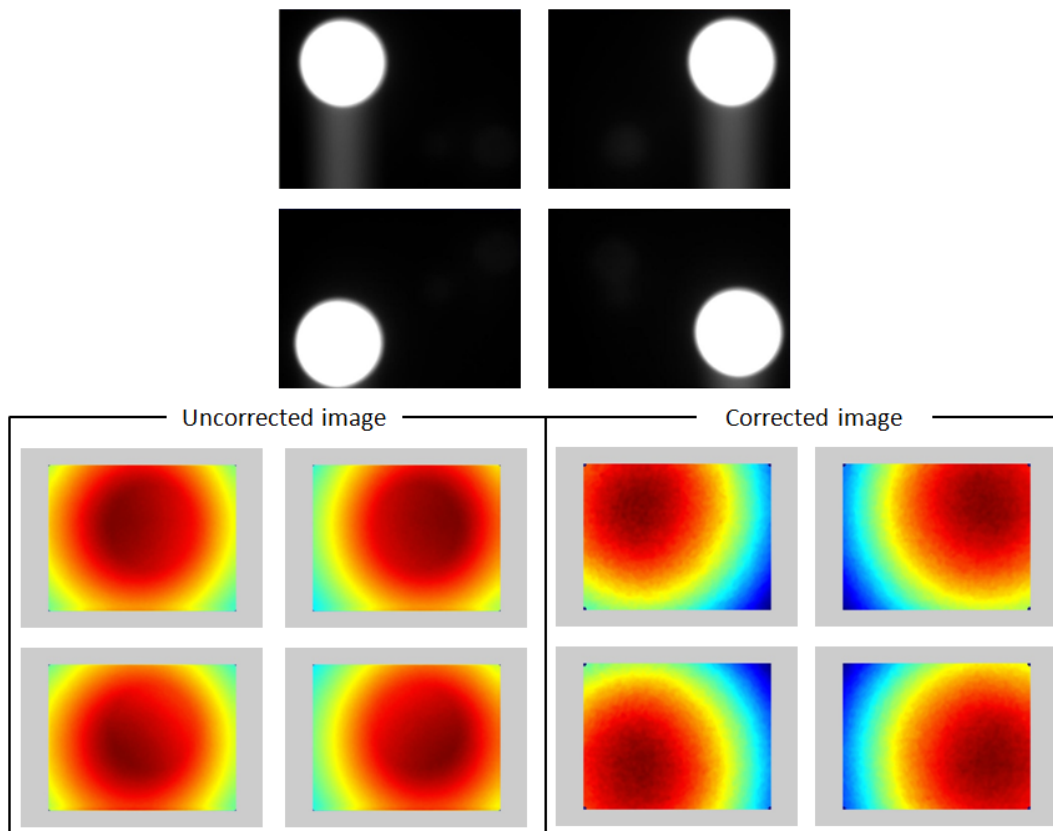


Figure 4.7 Top row: pictures showing the four different light source locations, which are upper left corner, upper right corner, lower left corner and lower right corner, respectively. Bottom row: figures on left shows the raw CCD images taken with the four respective light source locations while figures on right shows the corrected CCD images taken with the four respective light source locations.

4.2.2 Stability and linearity of the CCD camera system

To check the stability of the CCD camera system, repeated measurements were taken at different times. A 1% Intralipid solution was utilized as a testing medium and optical readings were taken as the baseline images (I_B) at time '0', followed by other images (I_M) taken 1 minute, 5 minutes, 10 minutes, 30 minutes, 1 hour and 1 day after the baseline measurement using the same experimental conditions (i.e., the same integration time). Each of the images was calibrated or corrected with the flat field correction and averaged over all the pixels per image to

obtain an averaged light intensity for each respective image. Then, a ratio between the averaged intensity from each set of I_M and the averaged intensity from I_B (the baseline image) were obtained for all cases, as shown in Figure 4.8a. It is very clear that the image intensities taken at different time intervals are fluctuated less than 1% of that of the baseline image, confirming a good stability of the CCD camera system. Similar experiments were repeated using a 1.5% Intralipid solution to increase the light scattering property of the testing medium. The results are very consistent with the results from 1% Intralipid solution, demonstrating that a CCD camera has high stability with a fluctuation of intensity less than 1%.

In addition, we checked whether the intensity of light source could affect the results. We took numerous images using the same Intralipid concentration, but with different intensities of the light source. The averaged intensity of an image taken at light source level 5 was selected as the baseline, I_B ; the ratios between the averaged intensities from other images, I_M , with different light source levels to the chosen baseline, I_M/I_B , are shown in Figure 4.8b. This set of tests confirms that the level of the light source does not significantly affect the relative changes of our CCD camera output. Namely, the camera provides stable output images, independent of variable light levels.

Furthermore, to test the linearity of the CCD camera system, two experiments were performed: (1) one was to determine the image intensity changes versus absorption changes within the testing medium, and (2) the other one was to obtain the relationship between the image intensity measured versus changes in light scattering property within the testing medium. The tissue-mimic intralipid solution was held in an acrylic box, which had a dimension of 10 cm × 5 cm × 3 cm (length × width × height). The acrylic box was wrapped by black tape except the top side of the box to prevent light from passing through the box wall.

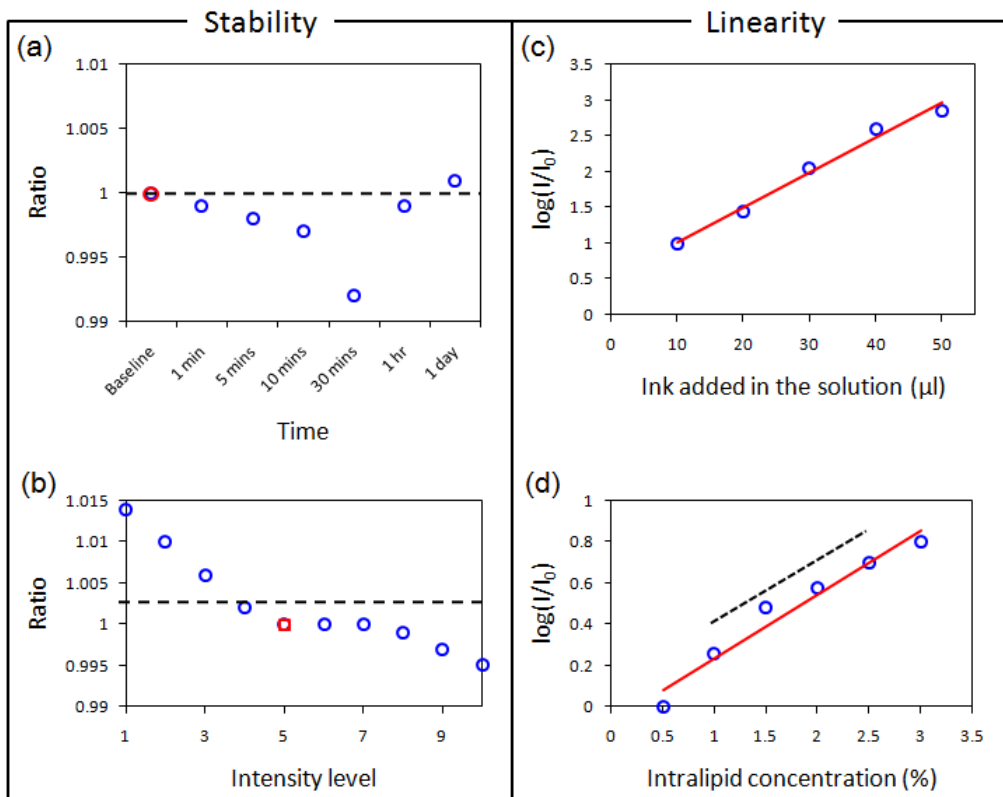


Figure 4.8 Ratio of the intensities (I_M/I_B) for a 1% Intralipid solution (a) at different times of measurement, and (b) with different light intensities. The relationships between $\log(I/I_0)$ and (c) the volume of ink added into the testing solution for a 1% Intralipid solution, and (d) the concentration of Intralipid. Dashed line in (d) shows the linear relationship for Intralipid concentrations between 1% and 2.5%.

For absorption changes, the image experiments were taken at 1% Intralipid solutions with addition of 10 μl , 20 μl , 30 μl , 40 μl , and 50 μl of diluted ink. The CCD camera readings were taken throughout these Intralipid solutions, using the same integration time. We further plotted values of $\log(I_0/I)$ versus the volume of the ink added in the solution, where I_0 and I represented the averaged image intensities taken from the Intralipid solutions without ink and with different concentrations of ink. As seen in Figure 4.8c, the data can be fitted well by a linear line. A similar behavior was seen for the 1.5% Intralipid case, confirming that a CCD camera has high-quality performance in its linearity with respect to light absorption.

For light scattering changes, the experiments were taken from multiple Intralipid solutions with concentrations of 0.5%, 1%, 1.5%, 2%, 2.5%, and 3% (using the same integration time). A plot of $\log(I_0/I)$ versus concentration of Intralipid is given in Figure 4.8d, where I_0 and I represent the averaged image intensities taken from the Intralipid solutions at 0.5% and other concentrations. A good linear relationship is seen when Intralipid concentrations are between 1% and 2.5% (shown by the dashed line in the figure). While changes of image intensity due to light scattering may non-linearly depend on the Intralipid concentration [58], such non-linearity is relatively small and can be non-significant within the scattering property range for biological tissues [59, 60]. Thus, the optical density measured from the CCD camera is linearly proportional to the light scattering changes, at the first-order approximation.

4.3 Optode geometry for CCD-camera based DOT

Instrument noise may appear during the measurements with a CCD camera that serves as multiple detectors. Dark noise and non-uniformity of CCD chip sensitivity are two noise sources. Another common problem is associated with the limited dynamic range of a CCD camera. When an individual pixel of the CCD array reaches its maximal intensity, the individual pixel well is occupied by electrons which can also overflow into the neighboring pixel wells. Such an overspill of electrons thereby distorts the actual signals not only at the saturated pixel but also several adjacent pixels. In order to minimize the problem of signal saturations, the source fibers in this study were arranged around the field of view (FOV) of the CCD camera, as shown in Figure. 4.9. Such geometry can also be utilized while keeping the source fibers within the FOV.

As shown in Figure 4.9, the dimension of FOV of the CCD camera was $m \times n \text{ mm}^2$. Instead of using physical detectors, virtual detectors were used in this non-contact CCD camera imaging system. Virtual detectors refer to groups of CCD pixels within FOV of the CCD camera combined. The signal-to-noise ratio (SNR) at selected locations can be enhanced by averaging the signals of all pixels selected. For example, if we selected 10x10 pixels to be binned as a

virtual detector, the entire FOV would have a total number of $\sim 50 \times 66$ virtual detectors for the DOT measurements. This implies that a CCD-camera-based DOT system may serve as a high-density imaging device with an easy-to-change detector array by grouping the pixels in different ways as detectors.

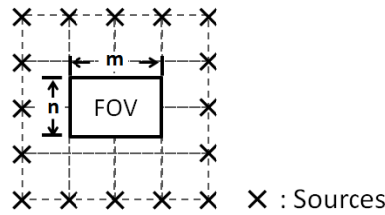


Figure 4.9 Optode geometry for CCD-camera-based DOT system. The dimension of FOV was $m \times n$ in mm^2 . "X" represents possible locations of source fibers.

4.4 Computer simulation in evaluation the CCD-camera based DOT

4.4.1 Setup of optode array arrangement

To evaluate reconstruction performances using the source-camera geometry given in Figure 4.9 (also replotted in Figure 4.10a and denoted as G-I), computer simulations were performed and the results were compared with those that were derived using the source-

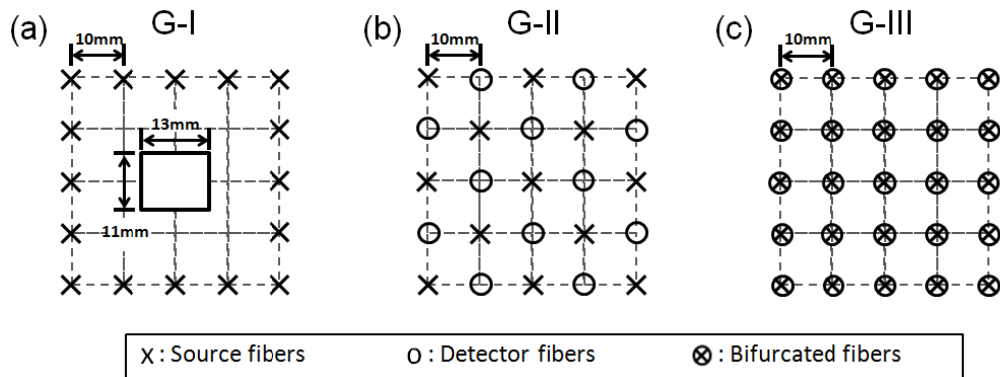


Figure 4.10 Scheme of optode geometries used in the simulation study. (a) to (c) are corresponded to G-I to G-III. Notice that the dimension of all dashed unit squares is $10 \times 10 \text{ mm}^2$. (x: source fibers; o: detector fibers; ⊗: bifurcated fibers).

detector geometries commonly seen in the fiber-based DOT system (shown in Figure 4.8b and Figure 4.8c). Several sets of simulations were carried out under the conditions of (1) using different numbers of sources and virtual detectors, (2) without and (3) with utilization of DCA.

As shown in Figure 4.10a, sixteen sources were used in G-I. In terms of the number of virtual detectors, we defined the dimension of FOV to be $13 \times 11 \text{ mm}^2$ and the dimension of each virtual detector to be 1 mm^2 . Therefore, there were a total of $13 \times 11 = 143$ virtual detectors used in the simulations. The geometry shown in Figure 4.10b (G-II) is commonly used optode geometry with sources and detectors being alternately placed. The geometry given in Figure 4.10c (G-III) exhibits the optode setup with bifurcated fibers, i.e., each fiber can serve as a source and detector.

4.4.2 Image reconstruction of DOT

The photon propagation in a highly scattering medium follows the diffusion equation, and the analytic solution of the diffusion equation can be utilized to study optical signal changes due to absorption perturbation, as given by:

$$\Delta OD = -\log\left(\frac{\Phi_{pert}}{\Phi_0}\right) = -\frac{1}{2.3} \ln\left(\frac{\Phi_{pert}}{\Phi_0}\right) = \frac{1}{2.3} \int \Delta\mu_a(r)L(r)dr \quad (4.3)$$

where ΔOD is the change in optical density. Φ_0 is the photon fluence in a semi-infinite, homogeneous medium, and Φ_{pert} is the photon fluence with absorbers embedded. L is the effective pathlength of light through the tissue experiencing the absorption change. While eq. (3) is known as the modified Beer-Lambert law, it can be generalized in a matrix form and written as $y=Ax$, where matrix y represents measured changes in optical density from all the measurements, matrix x corresponds to a volumetric vector of the unknown perturbation in absorption coefficient in the volume under study, and matrix A describes the sensitivity of measurements to the change in absorption within each voxel in the medium.

However, solving $y=Ax$ is non-trivial, involving an under-determined, ill-posed inverse problem because the number of measurements is much fewer than the number of unknowns

(i.e., voxels) to be reconstructed. In the current research field, to reconstruct a DOT image, the Tikhonov regularization [28] method has been employed; an image of \mathbf{x} can be given by:

$$\hat{\mathbf{x}} = A^T (AA^T + \alpha S_{\max} I)^{-1} \mathbf{y} \quad (4.4)$$

where $\hat{\mathbf{x}}$ is the reconstructed image of absorption perturbation; I is the identity matrix; S_{\max} is the maximal singular value of matrix AA^T , and α is the regularization parameter. DCA can then be adopted by introduced the weighted matrix M which is described in section 3.2 and Equation 4.4 can be rewritten as:

$$\hat{x}_{DCA} = (AM)^T (AM(AM)^T + \alpha S_{\max} I)^{-1} \mathbf{y} \quad (4.5)$$

4.4.3 Metrics of reconstruction performances

The reconstruction performances were evaluated by two parameters: (1) the position error (PE) and (2) Contrast-to-Noise ratio (CNR) [61]. PE is the distance from the center of actual object to the center of the reconstructed object. The reconstructed object was defined by the pixels with values above half of the maximum value. CNR indicates whether the reconstructed object can be clearly distinguished from the background. A reconstructed image was divided into two regions: volume of interest (VOI) and volume of background (VOB). VOI was defined by the location and size of the reconstructed object. VOB was defined by the remaining volume of the image. CNR can be calculated by:

$$CNR = \frac{\mu_{VOI} - \mu_{VOB}}{\left[w_{VOI} \sigma_{VOI}^2 + w_{VOB} \sigma_{VOB}^2 \right]^{1/2}} \quad (4.6)$$

where w_{VOI} and w_{VOB} are the weight factors of the VOI and VOB relative to the entire volume (i.e., VOI or VOB divided by the entire volume), μ_{VOI} and μ_{VOB} are the mean values of object and background volumes in a 3D reconstructed image, and σ_{VOI} and σ_{VOB} are the respective standard deviations.

4.4.4 Setup of computational simulation

In the simulation, a homogeneous semi-infinite medium with a volume of $40 \times 40 \times 30$

mm³ was considered (Figure 4.11). The origin of the coordinates was set at the center of top surface, as marked in the figure; this surface was also chosen to be the measurement surface in the simulation. As commonly used, a set of absorption and reduced scattering coefficients of $\mu_a=0.1 \text{ cm}^{-1}$ and $\mu'_s=10 \text{ cm}^{-1}$ were selected to simulate the background tissue.

Two different setups were utilized to evaluate the performances of optode geometries: Setup 1: is shown in Figure 4.9a, where a spherical absorber with an 8-mm diameter was placed at $(X,Y,Z)=(0,0,-20)$ (in mm), with a 3:1 contrast ratio in μ_a relative to the background μ_a . Observation of the optode geometry of the CCD-camera-based DOT imaging system revealed fewer overlapping measurements near four corners of FOV of the camera, as compared to the center of FOV. This is because more overlapping measurements occur near the center of FOV when we pair most of the virtual detectors with given light sources in the current source-camera setup. It has also been shown that a higher measurement density does not necessarily improve the spatial resolution significantly [62]. Thus, to evaluate and compare the effect of the number of overlapping measurements at the four corners, in setup 2, one spherical absorber was placed near the right corner of the medium with respect to the setup 1, as shown in Figure 4.11b. A random Gaussian noise of 1% in amplitude was added to the simulated measurement data. DCA was employed with a compensation power of $\gamma=1.3$.

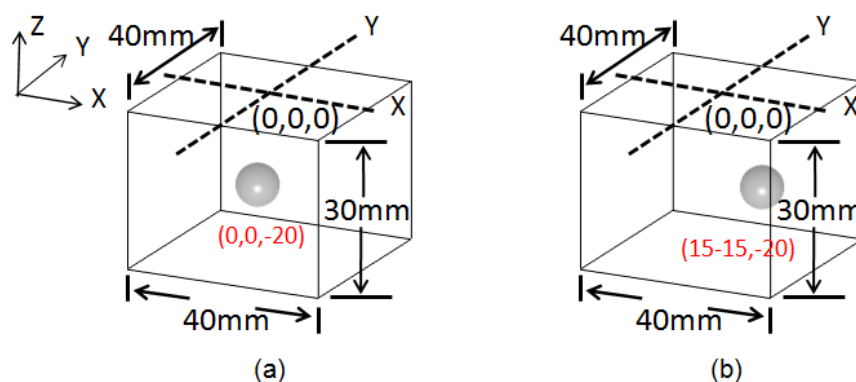


Figure 4.11 Schematic diagram of setups used in simulation study. (a) Setup I: The inclusion was located right below the center of measurement plane. (b) Setup II: The inclusion was located close to the right side corner of the measurement volume.

4.4.5 Results

The reconstructed images in the X-Z plane from both setups are shown in Figure 4.12: Figures 4.12a and 4.12b are obtained from Setup 1 with the absorber placed at the center of measurement plane, while Figures 4.12c and 4.12d result from Setup 2. Also, the three rows from top to bottom in the figure correspond to the fiber-camera or fiber-fiber geometry of G-I to G-III, respectively. Figures 4.12b and 4.12d clearly show that the reconstructed images for all geometries are pulled towards the superficial surface along Z direction when DCA is not used or $\gamma = 0$. After DCA was employed with $\gamma = 1.3$, the reconstructed object was reconstructed at the expected depth (Figure 4.12a and 4.12c). By comparing the reconstructed images using the three geometries of G-I to G-III, we can see that the overall qualities of DOT images are all similar. However, in Figure 4.12c, it is noticed that the DOT images with G-II and G-III exhibit a relatively better shape for the reconstructed objects, while G-I leads to a little distorted profile (tilted to the center) when the absorber was close to the edge of the imaging medium.

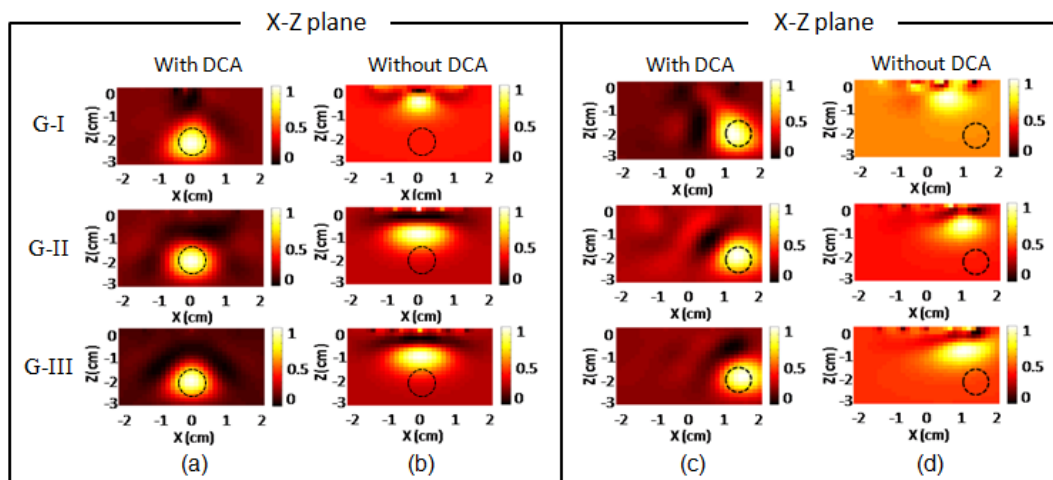


Figure 4.12 Reconstructed DOT images of a single object in X-Z plane: (a) and (c) with DCA ($\gamma=1.3$), and (b) and (d) without DCA. Top to bottom rows were obtained from G-I to G-III (Figure 4.8). Black dashed circles represent the actual location and size of simulated absorbers. Images here were normalized between minimum (0) to maximum (1).

To further quantify the comparison among the three geometries, respective values of CNR and PE from each geometry (Figure 4.10) and for two simulation setups (Figure 4.11), has

been calculated and the corresponding values are listed in Table 4.1. It is clearly seen that there are significant improvements of PE values with DCA, as we expected, for both setups, while the overall PE values in Setup 1 are better than those in Setup 2. Next, we focused on only the data with DCA: by close inspection on G-I to G-III for setup 1, we observed that CNR values from all three optode geometries are not greatly different although G-III has a little higher CNR. A similar trend can be seen for Setup 2. Regarding PE values obtained only with DCA, no noticeable difference appeared for all three geometries (less than 1 mm) in either of the setups.

Table 4.1 Summary of the CNR and PE values for three geometries

	Setup 1 (absorber at center)						Setup 2 (absorber on side)					
	G-I		G-II		G-III		G-I		G-II		G-III	
	W	W/O	W	W/O	W	W/O	W	W/O	W	W/O	W	W/O
CNR	5.66	4.39	5.65	4.12	5.73	4.58	5.45	5.46	5.61	5.62	6.47	4.72
PE(cm)	0.20	0.82	0.20	0.75	0.20	0.72	0.36	0.81	0.35	0.79	0.35	0.78

* W: With DCA; W/O: Without DCA

Overall, the computer simulation results confirm that the geometry of G-I, which can be utilized as a CCD-camera-based DOT system, was able to deliver excellent DOT images at the same quality level as the other two fiber-based DOT systems do. Given the simplicity, low-cost, and portability of such a system, it may be preferred in pre-clinical, small animal studies.

4.5 Optimization of number of sources based on computer simulation

It is known the limited space around animals serves as a deterrent for the placement of several optodes. Thus, we further investigated a possible optimal number of optodes that could still permit a reasonably good DOT image. In geometry G-I, only source fibers need to be arranged around the FOV of CCD camera. Therefore, several computer simulations were performed based on both setups (Figure 4.11) used in Section 4.3 in order to optimize the numbers of sources and virtual detectors. Specifically, the light sources were placed symmetrically around the origin to prevent the distortion of reconstructed images.

Figure 4.13 shows several cross-section profiles of the reconstructed $\Delta\mu_a$ values along

x-axis with different numbers of sources while the absorber was placed at center (Figure 4.11a) and close to the edge of medium (Figure 4.11b). It is clear from this figure that an increase in number of the sources can lead to an enhanced reconstructed contrast, and thus resulting in a clearer DOT image. However, no substantial difference was observed in absorption contrast while the number of sources increased from 8 to 12 and further to 16 in both cases.

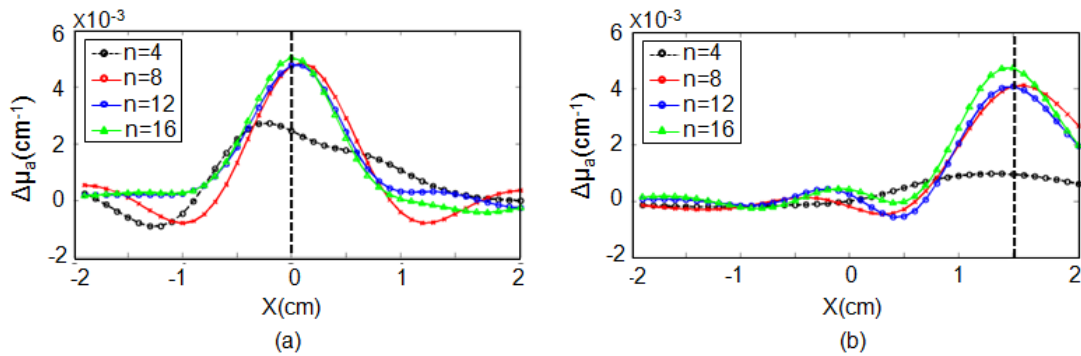


Figure 4.13 Profiles of reconstructed $\Delta\mu_a$ values along x-axis for (a) experimental setup I and (b) experimental setup II. Dashed lines represent the actual location of the inclusion in X axis.

More quantitatively, we calculated CNR and PE values for all four cases with the number of sources of $n=4, 8, 12,$ and 16 . The respective values are given in Table 4.2. It shows unambiguously that no difference in PE and CNR appears when n has changed from 8 to 16. However, the computational time for $n=16$ is ~ 2.5 times longer than that for $n=8$. Hence, for practical use, we would suggest to utilize eight sources instead of twelve or more, which offer the same quality of DOT images but have less complexity of a DOT system.

Table 4.2 Summary of the CNR, PE and CPU time for different numbers of sources

Numbers of Source	<i>Setup I</i> (absorber at center)				<i>Setup II</i> (absorber on side)			
	4	8	12	16	4	8	12	16
CNR	4.27	5.66	5.67	5.83	1.24	4.42	4.51	4.58
PE (cm)	0.41	0.20	0.20	0.20	0.88	0.35	0.32	0.32
CPU time(sec)	27.1	102.1	209.4	289.2	27.1	102.1	209.4	289.2

4.6 Phantom experiment

4.6.1 Experimental setup

Besides the computational investigation given above, laboratory phantom studies were performed to confirm the findings. A broad-band white light source (Illumination Technologies, Inc. Model 3900, quartz-tungsten halogen lamp, Figure 4.14) was used, and a 12-bit CCD camera (SamBa Q34 with Navitar Zoom 7000 lens, Figure 4.14) was employed as the detector. An automatic filter wheel, consists of 6 different filters, was mounted in front of CCD camera. The FOV of the camera was $13 \times 11 \text{ mm}^2$, the same dimension as used in the simulations. The total FOV was divided into 143 (13×11) virtual detectors, meaning that each virtual detector had 38×38 pixels. In this study, 8 light sources were connected to and controlled by a multiplexer (Avantes Inc. Multiplex Channels 1x16, Figure 4.14). 8 fibers were placed around the FOV of CCD camera and sequentially delivered the light to tissue-like phantom. The images were then taken by CCD camera.

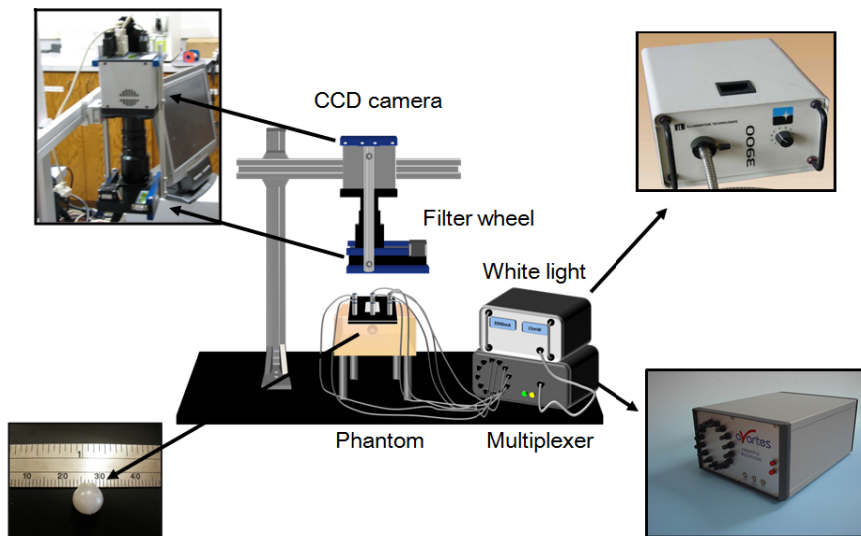


Figure 4.14 Schematic illustration of the experimental setup for phantom study.

A total of 8×143 source-detector (virtual) pairs were pooled to perform DOT image reconstructions with utilization of DCA. The total volumetric imaging space was $40 \times 40 \times 30 \text{ mm}^3$.

A 1% Intralipid solution was used to generate the liquid tissue phantom with background optical properties of $\mu_a=0.1 \text{ cm}^{-1}$ and $\mu'_s=10 \text{ cm}^{-1}$. A spherical gelatin inclusion of 8 mm in diameter (lower left corner, Figure 4.14, recipe shown in Appendix C) was embedded 20 mm below the liquid surface, with a 2.5:1 contrast ratio in absorption between the inclusion and background. Moreover, another similar experiment was repeated with two identical inclusions embedded at 20mm depth.

4.6.2 Results

Three dimensional (3D) reconstructed images are shown in Figures 4.15a and 4.15b for the phantom experiments described above. To obtain 3D plots, we have selected the reconstructed absorption values at 80% of its maximum as a volume threshold in order to form the imaged object. From both Figures 4.15a and 4.15b, it is clear that the embedded objects can be successfully reconstructed at a relatively accurate depth when DCA was applied. However, because of the diffuse nature of light in tissues, the volume ratio between the reconstructed and real object is around 2:1, which also depends on the threshold value selected and the depth of the embedded inclusion.

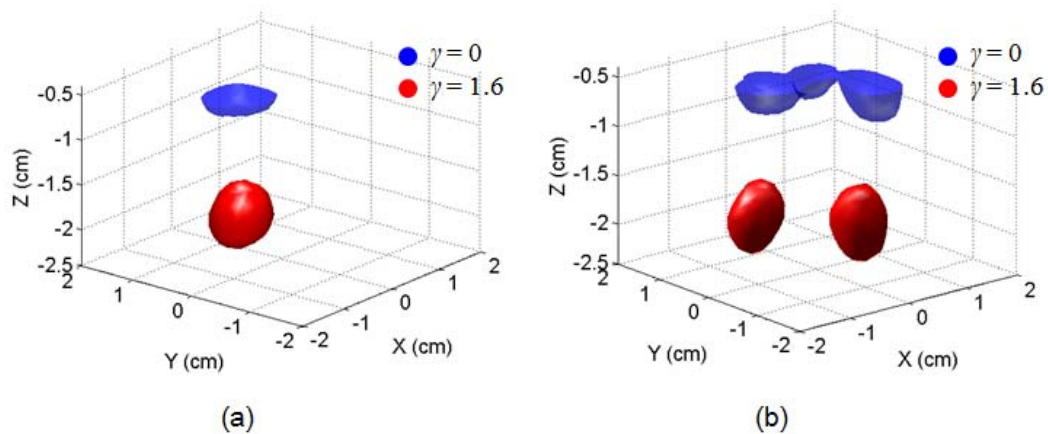


Figure 4.15 Three dimensional plots of reconstructed images for (a) one inclusion with DCA ($\gamma = 1.6$) and without DCA (i.e. $\gamma = 0$), and (b) two inclusions with DCA ($\gamma = 1.6$) and without DCA ($\gamma = 0$). Voxels with the reconstructed absorption values above 80% of the maximum value are selected as reconstructed objects.

4.7 Comparison of conventional image reconstruction versus globally convergent method (GCM) in small geometry phantom study

In this section and subsection, the idea of new reconstruction method, globally convergent method (GCM), is introduced. The comparisons among the images reconstructed by GCM, conventional image reconstruction (L2-regularization), and image reconstruction with DCA applied are also demonstrated. Images reconstructed with GCM were provided by Dr. Yueming Liu.

4.7.1 Globally convergent method (GCM)

In this subsection, the globally convergent method is briefly described. The details for GCM can be found in Refs [63-65]. For the convenience of readers, major ideas and mathematical processes are reviewed here. The development of a GCM was initiated by Klivanov et al [66]. Mathematically, diffuse optical tomography deals with a coefficient inverse problem (CIP) for an elliptic equation with an unknown potential. GCM has been developed to solve this problem since it is mathematically guaranteed to converge or have a global minimum regardless of the errors between an initial guess and the final solution.

Given the diffusion equation:

$$\nabla \cdot (D(x, y) \nabla w(x, y, s)) - \mu_a(x, y) w(x, y, s) = -\delta(x - x_m, y - s), (x, y) \in \Omega_0 \quad (4.7)$$

$$\frac{\partial w(x, y, s)}{\partial n} + w(x, y, s) = 0, (x, y) \in \partial\Omega_0 \quad (4.8)$$

where $w(x, y, s)$ represents the photon fluence rate and $\delta(x, y)$ represents the light source; μ_a represents the absorption coefficient and D represents diffusion coefficient and can be expressed as:

$$D = \frac{1}{3(\mu_a + \mu'_s)} \quad (4.8)$$

where μ'_s is the reduced scattering coefficient. In diffusion regime, the scattering coefficient is much larger than absorption coefficient so that the Equation 4.8 can be simplified as:

$$D = \frac{1}{3\mu'_s} \quad (4.9)$$

The locations of light sources (x_m, s) can be chosen at several points with different s . Equation 4.8 is commonly known as Robin Boundary condition. Here three domains were determined and shown in Figure 4.16. The forward problem domain/background domain Ω_0 is the two dimension domain which contains entire plane. Ω is the physical domain which we are interested to reconstruct. Ω_1 is the computational domain for inverse problem of GCM.

For the source located outside the physical domain Ω , the right hand side of Equation 4.7 can be set as 0 and Equation 4.7 can be rewritten as:

$$\nabla \cdot (D(x, y) \nabla w(x, y, s)) - \mu_a(x, y) w(x, y, s) = 0, \quad (x, y) \in \Omega \quad (4.10)$$

$$w(x, y, s) = \phi(x, y, s), \quad (x, y) \in \partial\Omega \quad (4.11)$$

where $\phi(x, y, s)$ represents light intensities that can be measured on the boundary of domain Ω . Photon fluence $w(x, y, s)$ can be changed to $\tilde{w}(x, y, s)$ and Equations 4.11 and 4.12 can be expressed as:

$$\Delta \tilde{w}(x, y, s) - a(x, y) \tilde{w}(x, y, s) = 0 \quad (x, y) \in \Omega \quad (4.12)$$

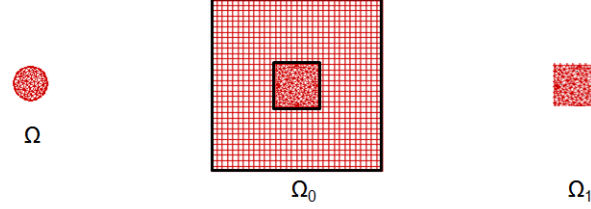
$$\tilde{w}(x, y, s) = \tilde{\phi}(x, y, s), \quad (x, y) \in \partial\Omega \quad (4.13)$$

where $a(x, y)$ is a new unknown coefficient and need to be reconstructed, defined as:

$$a(x, y) = \frac{1}{2} \Delta(\ln D(x, y)) + \frac{1}{4} \nabla(\ln D(x, y)) \cdot \nabla(\ln D(x, y)) + \frac{\mu_a(x, y)}{D(x, y)} \quad (4.14)$$

Notice that $a(x, y)$ contains two unknown optical properties in space, which are absorption coefficient μ_a and reduced scattering coefficient μ'_s , respectively. Absorption coefficient is the major unknown need to be reconstructed since it is more related to HbO₂ and HbR. Assuming that μ'_s is uniform and unchanged in space, Equation 4.14 can be simplified as:

$$a(x, y) = \frac{\mu_a(x, y)}{D(x, y)} = 3\mu_a(x, y)\mu'_s(x, y) \quad (4.15)$$



- Ω : the physical domain, representing a cross section of the hemisphere in the phantom
- Ω_0 : the forward problem domain, for forward problem simulation
- Ω_1 : the computational domain, used to perform inverse problem calculations

Figure 4.16 The domains used in GCM calculations. (a) The physical domain Ω with a triangular mesh. (b) The background domain Ω_0 with a mixed mesh which contains the physical domain Ω and the computational domain Ω_1 both with triangular meshes for the forward calculation purpose (c) the computational domain Ω_1 . Figure was modified from Su et al. [63].

We change variable as $u = \ln \tilde{w}(x, y, s)$. Equation 4.12 can be rewritten as the nonlinear elliptic equation as:

$$\Delta u(x, y, s) + \nabla u(x, y, s) \cdot \nabla u(x, y, s) - \alpha(x, y) = 0 \quad (4.16)$$

where $\alpha(x, y) = 3(\mu_a \mu_s')(x, y)$.

In order to solve Equation (4) to obtain $\alpha(x, y)$, the convexification method was used with several light sources along a straight line, that is, add an extra term of $u = u(x, y, r)$, where r is the location of the light source, in both equations and solutions. Let $v = \frac{\partial u}{\partial r}$, and $u_\infty(x, y)$ be the limiting solution as the source is far away. Then, $\alpha(x, y)$ can be eliminated by differentiating Equation (4) with respect to r . Function v then satisfies an integral differential equation, which is:

$$\Delta v(x, y, r) + 2\nabla v(x, y, r) \cdot \nabla \left(\int_{-\infty}^r v(x, y, r) dr + u_\infty(x, y) \right) = 0 \quad (4.17)$$

Once Equation (5) is solved, u can be calculated by integration since $v = \frac{\partial u}{\partial r}$. Coefficient $\alpha(x, y)$ then can be derived from Equation 4.17 since function $u(x, y)$ will be known.

The complete steps of GCM to reconstruct image is shown in Figure 4.17.

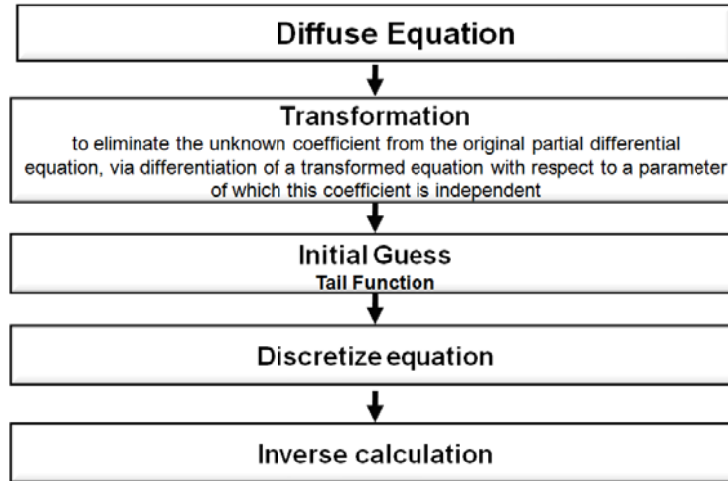


Figure 4.17 Schematic of layout of GCM

4.7.2 Experimental setup of phantom study

The laboratory tissue-mimic phantom experiment was performed. The purpose of this phantom study was to evaluate the feasibility of using DCA and GCM to study the ischemic stroke in rodent model. To simulate the scheme of ischemic areas in rat brain, the phantom and absorber/inclusion was made in relatively small dimension. Notice that the current development of GCM, the data measured with transmitted setup is needed (Figure 4.18). To satisfy the mathematic setup of GCM, the phantom experiment was designed as follows.

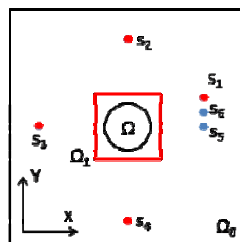


Figure 4.18 Schematic of physical setup of GCM

A diode laser (Coherent Inc. wavelength at 808 nm) was used as the light source, and a fast-speed, 12-bit CCD camera (SamBa Q34 with Navitar Zoom 7000 lens) with a matrix of $496 \times 656 \text{ pixel}^2$ was employed as the detector; the field of view (FOV) of the camera was 13×11

mm². In this study, 4 light sources were connected to and controlled by a multiplexer (Avantes Inc. Multiplex Channels 1x16). The multiplexer was utilized to deliver light at multiple locations by multiple fibers. The experimental setup is depicted in Figure 4.19a. One side of source fiber was connected to the rail system which allowed movement to different locations along one side and simulated multiple light sources on one side to generate the initial gauss (tail function) (Figure 4.19b).

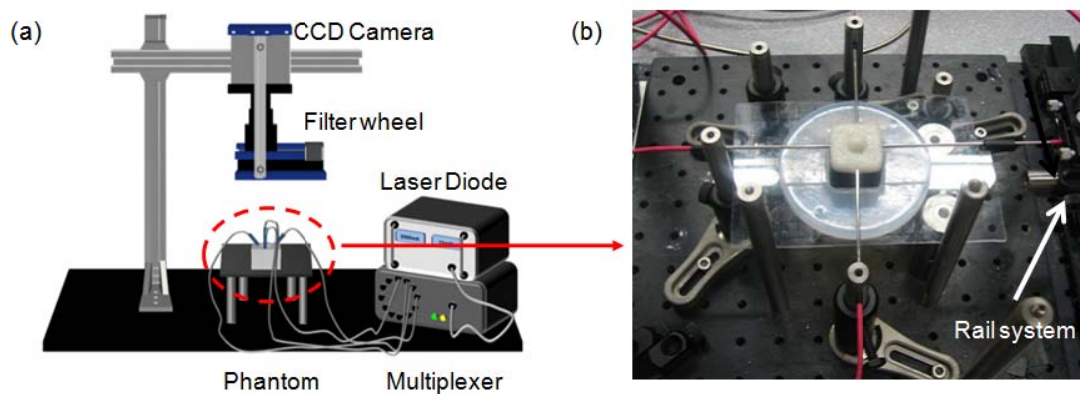


Figure 4.19 (a) Schematic illustration of the experimental setup for phantom study. (b) Photograph shows the setup of phantom. Four source fibers were placed on four sides of the square phantom. One side of source fiber was connected to the rail system (indicated by white arrow) which allowed moving to different locations along one side

Appropriate tissue phantoms were made by mixing gelatin powder with intralipid solution. After the gelatin-intralipid mixture was cooled down within a solid mold, it formed a shape of rectangular box with a hemispherical contour on top of the surface, as shown in Figure 4.19b. The hemisphere had a diameter of 13 mm and was made to emulate a rat head. The cubic block was a solid gelatin phantom of 30x30x30 mm³ and was planned to emulate an optical mask or a matching cap that will be utilized in our animal studies to reduce the effect of refractive index mismatch between the animal head and possible air space. The optical properties of tissue phantom were $\mu_a = 0.09 \text{ cm}^{-1}$ and $\mu_s' = 9 \text{ cm}^{-1}$, which were measured by oximeter (Oxiplex, ISS Inc.).

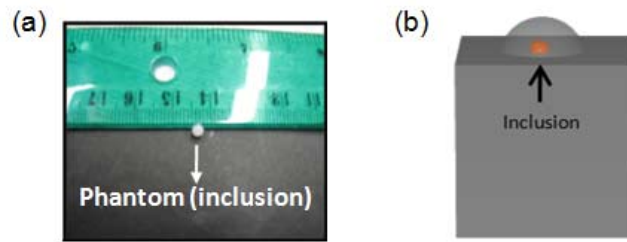


Figure 4.20 (a) A spherical gelatin phantom used as an inclusion for the laboratory experiment. (b) Illustration of an inclusion phantom embedded in the cubic tissue-mimicking phantom.

For the absorbers to simulate blood clotting or trauma in the rat brain, several spherical gelatin inclusions with 3-mm diameter (Figure 4.20a) were made, having several different contrast levels in absorption relative to the background phantom. In the laboratory experiments, one of the spheres was chosen and embedded in the hemispherical top of the cubic tissue phantom, as depicted in Figure 4.20b. According to the anatomical structure of rat head, the depth from rat scalp to its cortex is approximate 4-5 mm. Therefore, in this phantom study, inclusions were placed 5-7 mm below the surface of the hemispherical top; this depth should be reasonable to mimic animal experiments for future rat ischemic stroke study.

4.7.3 Results

In this section and affiliated subsection, the results for DCA and GCM are described.

4.7.3.1 DCA study

Since the CCD camera was used as the detecting system, instead of using fiber-based detectors, virtual multiple detectors were thought in this experiment. The virtual detectors were formed by grouping several pixels within field-of-view (FOV) of the CCD camera. In this study, the total FOV was divided into 143 (13×11) virtual detectors, meaning that each virtual detector was formed by grouping 38×38 pixels together. The total volumetric imaging space was 20×20×20 mm³. The baseline was measured by using the spherical gelatin inclusion which had the same optical properties as the background tissue phantom. In the perturbation

measurements, spherical gelatin inclusions having contrast levels in absorption from 2:1 to 4:1 with respect to the background were embedded in the spherical top on the cubic phantom (Figure 4.19b) and measured by the CCD camera to emulate the case of blood vessel occlusion or reperfusion.

Figures 4.21a, 4.21b and 4.21c show reconstructed lateral images from contrast 1:2 to 1:4 with DCA applied ($\gamma=1.3$); Figures 4.21d, 4.21e and 4.21f show the images reconstructed by using the conventional DOT reconstruction method. Notice that the volumetric images were reconstructed with and without DCA adopted first and then sliced at 5mm depth. By comparing the top and bottom row of Figure 4.21, we clearly see that the qualities of reconstructed images are improved by DCA since the reconstructed contrasts are much enhanced. Moreover, DCA helps improve the shapes of the reconstructed object, which are more concentrated and relatively more circular.

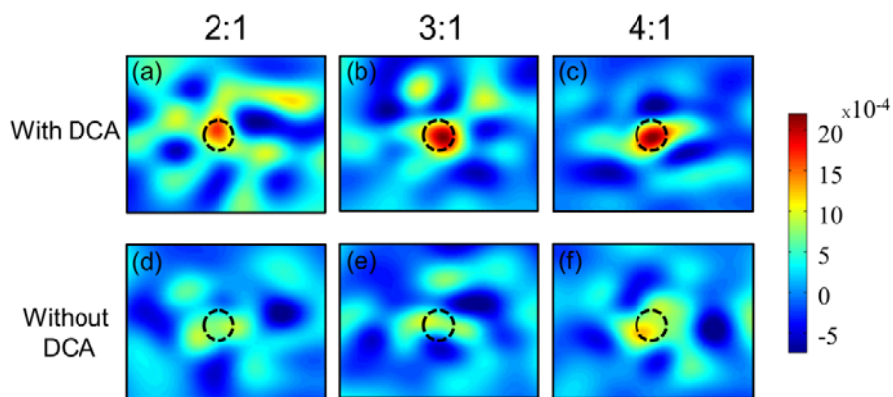


Figure 4.21 Reconstructed images of one inclusion with a contrast level in absorption of (a) 2:1, (b) 3:1, and (c) 4:1 when DCA was applied. Reconstructed images of one inclusion at a contrast level of (d) 2:1, (e) 3:1, and (f) 4:1 without DCA applied.

Furthermore, to quantify the reconstruction performances of DCA, two parameters were introduced: they are CNR (Equation 4.6) and area ratio (AR), respectively. Area ratio is the ratio between the area of reconstructed object and the area of actual object. CNR can be defined as Equation 4.6. Notice that the reconstructed object was defined by the pixels with value above

the 50% of the maximum value. From Table 4.3, it can be seen that with DCA applied, the AR values are smaller, while the CNR values are higher, which is considered having the better qualities for reconstructed images.

Table 4.3 Comparison of CNR and AR between reconstruction with and without DCA applied

	1:2		1:3		1:4	
	<i>W</i>	<i>WO</i>	<i>W</i>	<i>WO</i>	<i>W</i>	<i>WO</i>
<i>CNR</i>	3.25	2.16	4.13	3.27	4.62	3.29
<i>AR</i>	3.31	3.78	3.05	4.11	3.03	4.07

**W*: with DCA applied; *WO*: without DCA applied

4.7.3.2 GCM study

To implement the GCM with CCD camera data, phantom geometry was firstly input to generate the finite element unstructured meshes. During the measurements, the CCD camera was focused on the hemispherical top of the cubic phantom (Figure 4.19b). The 3-mm spherical gelatin inclusions were placed near the center of this plane. Light intensity data from the image acquired by CCD camera was extracted only at the boundary of 2D cross-section of the presumed "animal head" as depicted in Figure 4.22a. The inverse reconstruction was performed in a 2D plane along the intersection between the hemispherical top and the cubic block of the phantom, as shown in Figure 4.22b.

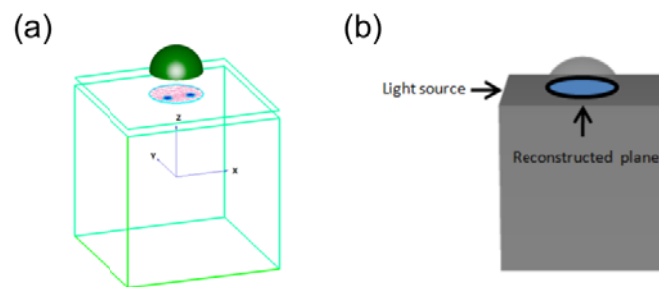


Figure 4.22 (a) A 3-D schematic drawing showing the data acquisition process of $\varphi(x, y, s)$ on the boundary of the physical domain Ω (reprinted from Su et al. [43]). (b) Schematic illustration of the lateral plane for image reconstruction

Using GCM, the locations of inclusion with different contrast levels in absorption were successfully reconstructed, as shown in Figure 4.23 (Figures were processed and provided by Dr. Yueming Liu). It must be mentioned that the reconstructed images shown here have different color scales. The relative errors in location for all three cases are within 10%, which is considered to be acceptable in a reasonable range of error.

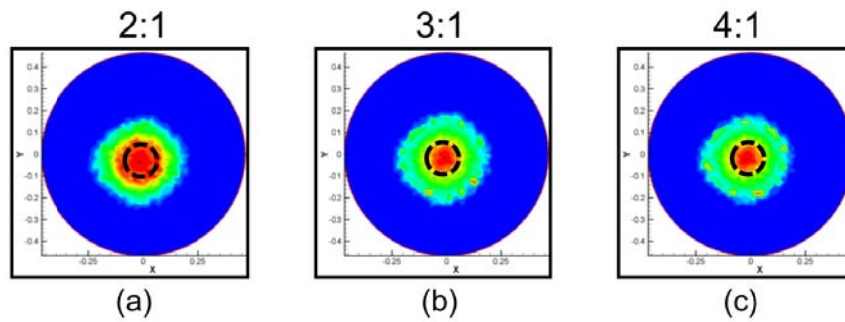


Figure 4.23. Reconstructed images by using GCM for (a) 2:1, (b) 3:1, and (c) 4:1 contrast levels relative to background. Circled areas represent actual location of absorber.

Furthermore, the distributions of $\alpha(x,y)$, which represent the changes in absorption in this study, were also reconstructed. Comparisons between the reconstructed α and actual α values are shown in Table 4.4. Since the inclusions are the homogenous gelatin spheres, the actual α values of inclusions are $3 \times \mu_a \times \mu_s'$, as defined in Section 4.6.1. The reconstructed α values were calculated using the peaks of the reconstructed images. Table 4.4 shows clearly that GCM gives rise to successful reconstruction of α values at all three contrast levels within a relative error range of 5-10% with respect to the actual α values.

Table 4.4 Summary of quantifications (reconstructed by GCM)

	Contrast level		
	2:1	3:1	4:1
Actual Alpha*	4.8	7.2	9.6
Reconstructed	4.31	6.98	10.16

* $Alpha = 3 \times \mu_a \times \mu_s'$

4.7.3.3 Two inclusion: DCA versus GCM

For further validation, two inclusions with an absorption contrast level of 3:1 relative to the background were placed at 5mm depth with an approximate separation of 4 mm. The reconstructed images are shown in Figure 4.24. As compared between Figures 4.24a and 4.22b, the spatial resolution is improved with DCA since two objects can be resolved. Moreover, Figure 4.22c (provided by Dr. Yueming Liu) demonstrates that GCM also has good performance among all three cases because the two objects were clearly resolved with much better spatial resolution and much smaller background noise.

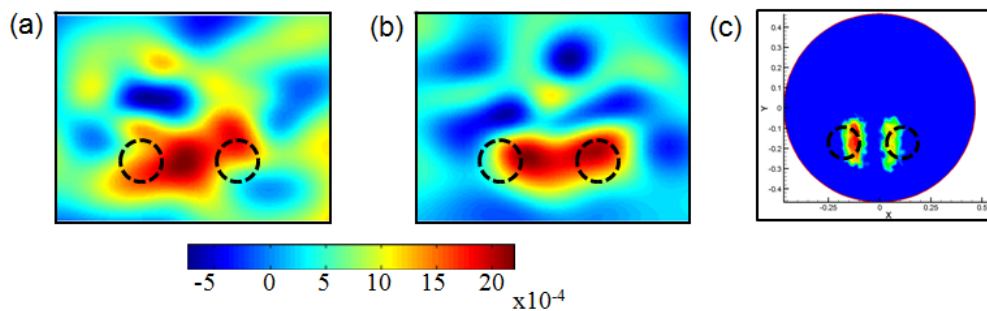


Figure 4.24 Reconstructed images of two absorbers (a) without DCA, (b) with DCA, and (c) with GCM.

4.8 Study of suture-induced ischemic stroke model using CCD-camera based DOT

The feasibility of using a CCD-camera-based DOT to study embedded inclusions in a tissue-mimicking medium in both computational simulations and real experimental phantom measurements has been demonstrated in previous sections. The whole CCD-camera-based DOT system then moved to real animal measurements to study cerebral ischemia in rat models.

4.8.1 Methods

In this section and affiliated subsection, the experimental setup, surgery for rodent model, data acquisition is described.

4.8.1.1 Animal preparation

Male Sprague-Dawley rats weighing 350-400 grams were purchased from Charles River (Wilmington, MA). The rats were housed in an environment providing 12 hr light and 12 hr dark cycle and had free access to water and food. All surgical procedures were approved by the Institutional Animal Care and Use Committee of the University of Texas at Arlington and the University of North Texas Health Science Center (UNTHSC) at Fort Worth.

4.8.1.2 Middle cerebral artery occlusion

Focal cerebral ischemia for rat was introduced by suture-induced middle cerebral artery occlusion (MCAO). This operation has been well-developed for years [67, 68]. Nowadays it is widely-used in investigating the mechanism and physiology of ischemic stroke throughout several methodologies, such as non-invasive imaging and histology [67-69]. Animal surgeries were performed by Dr. Ming Ren, a well-trained neurosurgeon and post-doctoral researcher at the UNTHSC Department of Pharmacology & Neuroscience at Fort Worth. The procedure included two parts which were occlusion of MCA and reperfusion (restoration of MCA blood flow), which is briefly described as follows.

Occlusion of MCA:

1. A midline cervical skin incision was made with the following arteries exposed under an operating microscope: the left branches of common carotid artery (CCA), external carotid artery (ECA) and its branches of superior thyroid artery (STA) and occipital artery (OA), internal carotid artery (ICA) and its pterygopalatine artery (PPA) branch.
2. The STA, ECA, OA were permanently cauterized, and other arteries were temporarily clipped including the PPA artery branch. A monofilament suture coated with silicone (CutterSil[®] Mucosa, Polysilicone material) on its front-end was introduced into the lumen of ECA through a small hole, and then Ren continued advancing the suture from the ECA to ICA lumen to the middle cerebral artery (MCA). The suture tip then blocked the entry to MCA.

3. After MCA was blocked by the monofilament suture, a timer was set for 60-min.

Reperfusion:

1. After 60-min of occlusion, the suture was smoothly withdrawn from the ICA but not completely off the hole of ECA.
2. The ICA was temporarily clipped and the suture completely removed.
3. After the suture was fully removed, the small hole in the ECA was cauterized and sealed. The clip was then removed from the ICA and PPA.
4. The incision was stitched according to the cervical skin incision closure procedure.

The diagram of the middle cerebral artery occlusion is depicted in Figure 4.25.

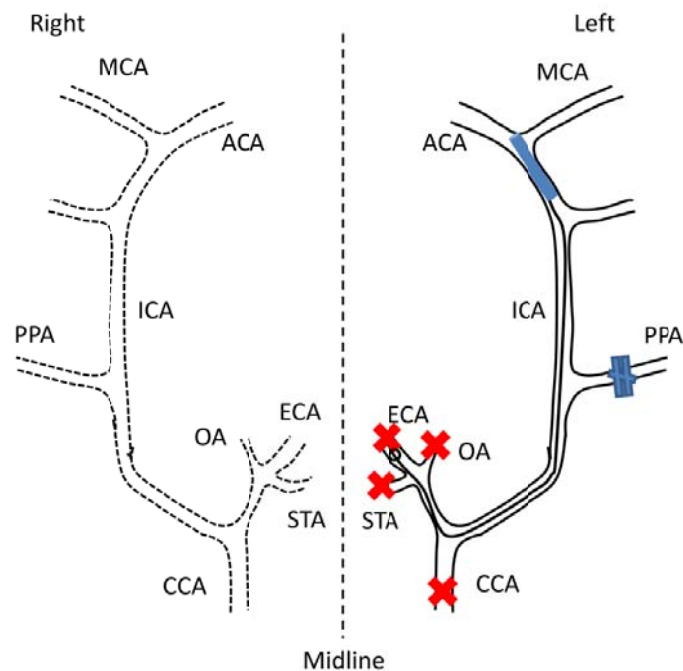


Figure 4.25 Illustration of cranial circulatory system (circle of Willis) of the rat and middle cerebral artery occlusion induced by endovascular suture on left hemisphere. The left branches of OA, STA, and the ECA were cauterized and left PPA was temporally clipped. The monofilament silicon-coated suture was introduced into the lumen of ECA and then advanced to MCA bifurcation. The abbreviation from top to bottom: ACA: anterior cerebral artery; MCA: middle cerebral artery; BA: basilar artery; ICA: internal carotid artery; PPA, pterygopalatine artery; ECA: external carotid artery; STA: superior thyroid artery; OA, occipital artery; CCA, common carotid artery. Figure is modified from M. J. O'Neill et al. [70].

4.8.1.3 Experimental Setup

A broad-band white light source (Illumination Technologies, Inc. Model 3900, quartz-tungsten halogen lamp) emitted light on the rat's head (Figure 4.26a). A total of four source fibers were used and switched by a multiplexer. Two fibers were positioned on the top of the scalp and the other two fibers were placed on the side of the rat's head (Figure 4.26a, upper panel). A CCD camera was used as the detector with a field of view (FOV) of $13 \times 11 \text{ mm}^2$. An automatic filter wheel with five filters, which were 720, 760, 780, 820, and 860 nm, respectively, was mounted in front of the CCD camera. For each light source, images were sequentially captured by one of the five filters according to the position of the light source, which was then switched by the multiplexer. Images captured by the CCD camera were then stored in the computer for further analysis.

During the measurements, the rats were anesthetized with isoflurane (2-2.5%) in 80% air and 20% O₂. Body temperature was monitored by a rectal probe and was maintained by a heating pad between 36.5° C and 37° C. Physiological parameters, including heart rate, breath rate, and arterial oxygen saturation, were measured and monitored by a pulse oximeter (MouseOx, STARR Life Sciences Corp, MN, USA). The measured flow is shown in Figure 4.26b.

Regarding the measurement protocol, background images (before stroke) were acquired by a CCD camera, and then the rat was removed for MCAO surgery. The MCAO surgery lasted approximately 10 to 15 mins. During the surgery, rats were also anesthetized with isoflurane. After surgery, rats were then moved back to their original housing and fibers were placed at the same locations as before. Images during MCAO were captured by the CCD camera for about 60 minutes, after which reperfusion was performed by smoothly withdrawing the suture back. Images for reperfusion were captured during the procedure which lasted about 30 minutes.

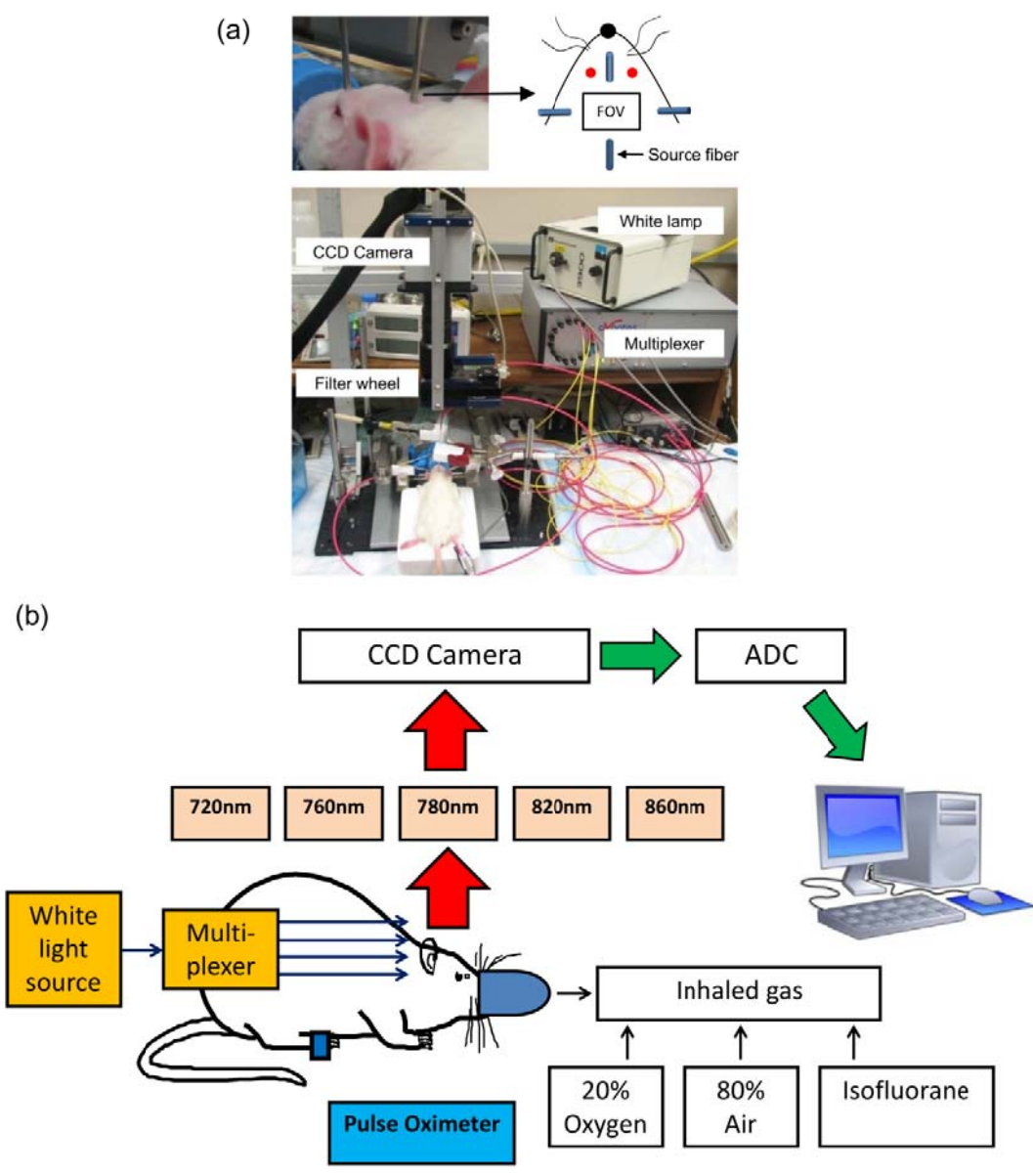


Figure 4.26 (a) Photograph of the experimental setup rat MCAO measurement. Upper panel of figure shows that four fibers were placed arranged the FOV of CCD camera. Two fibers were positioned on the top of scalp and the other two fibers were placed on side of the rat head (b) Schematic illustration of experimental setup for rat MCAO experiment.

4.8.2 Results

Figures 4.27a and 4.27b show images where the light source was located on the left side originating from two different wavelengths (720 nm and 820 nm). Images were acquired from three different periods which are baseline, MCAO, and reperfusion, respectively. The FOV of the CCD camera in this setup was 11 mm x 7.6 mm which corresponded to 656 x 496 pixels. Images in Figure 4.27 have same color scale. From Figure 4.27, it is clearly seen that there is no significant difference among the three images taken from three different time points (Figures 4.27a and 4.27b).

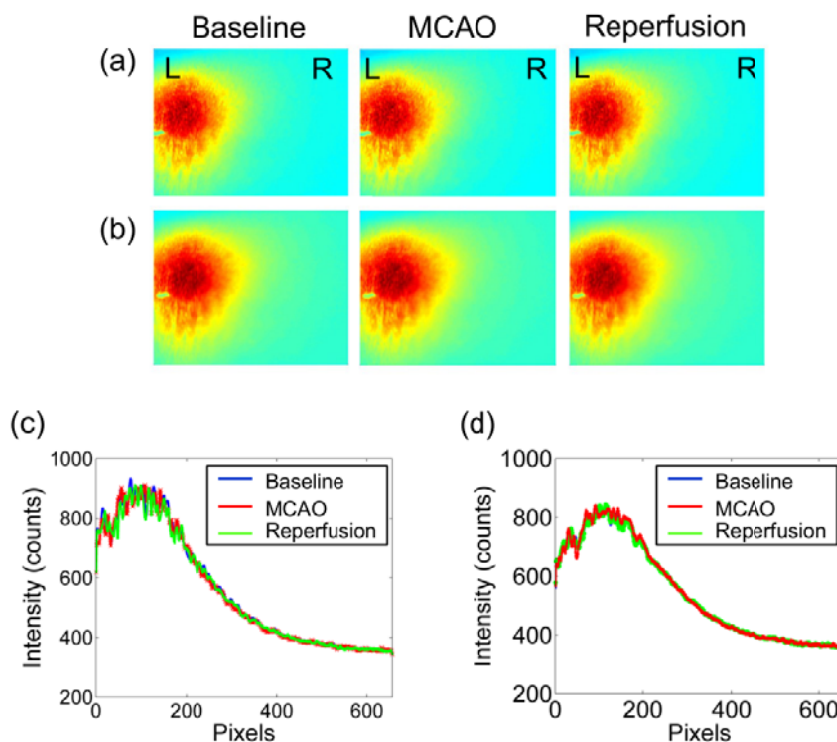


Figure 4.27 Images acquired from CCD camera for (a) 720nm and (b) 820nm in three different time periods. "L" represents left and "R" represents right side of brain. (c) and (d) display the cross-section profiles of images obtained from CCD camera for (a) 720nm and (b) 820nm.

Moreover, by comparing the cross-section profiles of images from three different time periods, we see no significant difference among curves from the three periods (Figures 4.27c

and 4.27d). Although the left side of MCA was occluded, no huge changes of optical density (baseline intensity ± 10 counts) on left side of curves could be found as we expected.

4.9 Summary and conclusion

In this chapter, the feasibility of using a CCD-camera-based DOT system to probe the embedded object in a tissue-mimicking phantom was presented. The first part of the chapter introduced the whole development of the CCD-camera-based DOT system. The calibration procedure shows a large improvement in correcting the uneven detection sensitivity of a CCD camera. A laboratory phantom experiment exhibited the difference between uncorrected and corrected images in terms of light intensity distribution, especially on the edge of the CCD camera's FOV. The linearity and stability of the data taken from the CCD camera was also evaluated. This was an important procedure which assured the reproducibility of data taken from the camera.

In order to maximize the available pixels which can serve as virtual detectors and also minimize the problem of signal saturations, the optode arrangement for this setup was designed in a way that arranged the light source around the FOV of the camera. The computer simulation demonstrated similar results while using this array geometry compared to the other widely-used optode geometry. Moreover, in combination with DCA which was introduced in Chapter 3, this optode geometry showed a large improvement in depth localization as well as image quality while doing the three dimensional (3D) volumetric image reconstructions.

Since the purpose of whole development was for animal study, and it is known that the small surface area around animals places a constraint on optode placement, computer simulations were performed to optimize the number of sources in this kind of optode geometry. Results suggested that 8 is a relatively good number of sources that can fit the whole system setup due to the trade-off among reconstructed image quality and computational expense as well as system complexity. Laboratory phantom study demonstrates the convincing 3D reconstruction results based on the whole system setup and methodology. Although only a 12-

bit CCD camera was utilized in our preliminary experiment setup, the optical signals from 20 mm depth could still be detected by grouping several pixels from the CCD-camera readings as virtual detectors. Overall, because of its simplicity, low-cost, and portability, a CCD-camera-based DOT may become a highly sought after imaging tool for pre-clinical small animal studies.

In the second part of this chapter, another newly-developed image reconstruction method, Globally Convergent Method (GCM), was introduced, which was developed by Dr. Jianzhong Su's group (UT Arlington - Mathematics Department). GCM has demonstrated convincing outcomes in diffuse optical tomographic image reconstruction based on a large amount of computational simulations. Especially, GCM allows recovery of the absolute values of optical properties using data acquired from continuous wave (CW) measurements. The experimental setup and phantom were designed for experimental proof of GCM. The dimension and geometry were relatively small since the whole methodology and systemic setup was proposed to facilitate the investigation of cerebral ischemia in a pre-clinical rodent model. In the meantime, DCA was also adopted in this phantom study in parallel. Reconstructed images from both methods show improvement of image quality and localization as compared to conventional DOT image reconstruction. However, DCA only provided better image quality and localization, but it did not improve the values of recovered optical properties. GCM demonstrated a good ability to recover absolute values. Results from the second part of this chapter demonstrate the feasibility of using a CCD-camera-based DOT system combined image reconstruction method, which uses DCA and GCM to image small inclusions in a turbid medium such as a biological tissue.

The third part of this chapter examines real animal measurement. The CCD-camera-based DOT system described in the first two sections of this chapter was utilized for measuring suture-induced MCAO model. Results shown in this chapter are not what we expected to observe. Although there is a trade-off between the detected signal and the size of FOV since FOV depends on the focal distance of the lens, further experiments are still needed to

investigate the reasons for experimental failure. A CCD camera has been successfully used as a detector of DOT in animal studies [71-74], which proved that a CCD camera is a suitable detector for reducing the complexity of system setup. For future measurements, the CCD camera should have a larger dynamic range, e.g. 16 bits, to maximize achievable signal. As the dynamic range of a device is increased, the ability to quantitatively measure the dimmest or small changes of intensities in an image is improved.

Overall, this chapter presents the development of a CCD-camera-based DOT system, which was designed for small animal measurement. Using a CCD camera as detector, more optical signals were obtained using one signal acquisition within a FOV which provided a lot of information. By grouping several pixels as a virtual detector, large amounts of source-virtual detector pairs were used for image reconstruction and numbers of virtual detectors were adjustable by changing the the dimension of the virtual detector, i.e., we grouped a small number of pixels to serve as detector. With the newly developed image reconstruction methods, DCA and GCM results demonstrated the improvement of depth localization, spatial resolution, and also quantification. In terms of rat MCAO model measurement, although negative results were presented and further modifications of the whole system are needed to fit the real condition of real animal measurements, this kind of non-contact DOT system still has great potential for different approaches of rat brain activity measurements due to its low complexity.

CHAPTER 5

FIBER-BASED CONTINUOUS WAVE DIFFUSE OPTICAL TOMOGRAPHY TO STUDY THE CEREBRAL ISCHEMIC IN PRE-CLINICAL RAT MODEL

5.1 Introduction

Middle cerebral artery (MCA) ischemic stroke models have been established in rats mostly through occlusion of MCA using either craniotomy or endovascular approach because ischemic stroke is often caused by occlusion of the middle cerebral artery (MCA) and its branches in human. Several types of non-invasive imaging techniques, such as computed tomography (CT) [75], magnetic resonance imaging (MRI), especially diffusion- and perfusion-weighted MRI [76], have been used in experimental studies and clinical use with great success. For the last decade, furthermore, researchers have been making efforts for non-invasive detection of cerebral hemodynamics using near infrared spectroscopy (NIRS) due to its portability, non-radiation, cost-effectiveness, and high temporal resolution. Since light in the Near-infrared (NIR) range (600-900 nm) can penetrate a few centimeters into brain tissues, it can probe changes in oxygenated (HbO₂) and deoxygenated (HbR) hemoglobin concentrations in the cerebral regions. Total hemoglobin concentrations can be quantified by $HbT = HbO_2 + HbR$, serving as another hemodynamic contrast in proportion to the cerebral blood volume. Compared to other imaging modalities, NIRS measurements have great potential for continuous, noninvasive monitoring in human and animals with high temporal resolution.

With single or limited source-detector pairs, several NIRS measurements were performed in investigating cerebral hemodynamics during cerebral ischemia [77, 78] using suture-induced rat MCA occlusion (MCAO) model. With multiple source-detector pairs measurements, researchers [79, 80] showed two dimensional (2D) topographic maps of HbT by spatial interpolation for the rats with MCAO. Their results exhibited good correlations with MR

images and histological brain slices of the animals. Moreover, diffuse optical tomography (DOT), which utilizes diffusion theory to reconstruct tomographic images of multi-channel NIRS with a relatively large number of source-detector pairs, has demonstrated the feasibility of three dimensional (3D) image reconstruction of cerebral hemodynamics during cerebral ischemia in rat MCAO [54] or common carotid artery (CCA) occlusion models [81].

Besides the study of concentration changes of hemoglobin, assessment of cerebral blood flow (CBF) is important and useful in subject with acute ischemic stroke, especially for embolism-induced ischemia. Continuous observations of regional CBF (rCBF) with patients receiving thrombolytic treatment is crucial because ischemic tissues may be dead, or dead due to different level of blood perfusion recovery. Latter may cause severe neurological deficit or can be fatal. Studies have shown the infarct volume highly depend on reduction of CBF during cerebral ischemia and perfusion recovery from cerebral ischemia [82]. There are several techniques providing rCBF measurement, including single photon emission tomography (SPECT) [83, 84], CT, positron emission tomography (PET) [85, 86], perfusion-weighted MRI, diffuse correlation spectroscopy (DCS) [87, 88], and Laser Doppler Flowmetry [78, 89]. All have been adopted in human and animals. Besides those techniques, measurements of rCBF by tracking the kinetics of an intravenous indocyanine green (ICG) using NIRS have been reported in evaluation of reduction of rCBF with patients with acute ischemic stroke [90]. ICG-tracking technique allows repetitive non-invasive (or minimally invasive due to the injection of ICG solution) measurements in very short period because of rapid clearance of ICG from the blood. Researchers have shown that blood flow index (BFI), derived from ICG kinetics, is significant correlated to cortical blood flow [91], and also allows to estimate rCBF with good reproducibility [92, 93]. Using NIRS tomographic technique, researchers showed the feasibility of generating 2D CBF images of infants with infarcts and hemorrhages with good correlation with SPECT images [94].

The aim of this work was to study changes of cerebral hemodynamics and CBF kinetics during and after ischemic stroke, with and without thrombolytic therapy for an embolic MCAO model, using three dimensional diffuse optical tomography (3D-DOT). We have achieved interleaved 3D imaging of hemispheric hemodynamic changes and CBF kinetics after integrating conventional DOT with our recently developed depth compensation algorithm (DCA). The novelty of this approach includes (1) design and implementation of an interleaved method to quantify two sets of changes in both hemoglobin concentrations and BFI during and after MCAO in rat; (2) integration of DCA with a volumetric mesh-based rat head model to generate volumetric DOT on a rat brain atlas; (3) longitudinal imaging and quantification of cerebral hemodynamics and CBF index before, during, and after a thrombolytic therapy for an embolic MCAO model.

This chapter provides details on several aspects of study in the following order: First, modification and combination of our recently developed DCA with a volumetric mesh-based rat head model to generate volumetric DOT on a rat brain atlas/template for improved depth localization and better visualization of MCAO effects in the rat brain will be done. Second, we will describe how a suture-induced MCAO rat model was achieved and measured by a high-density DOT system 1 hour during and 1 hour after MCAO. The suture-induced MCAO model was studied mainly for validation of our experimental setup, measurement methodology, and volumetric image reconstruction as this model has been well established and documented. Third, utilization and measurement of our newly established embolism-induced MCAO rat model will be done with the same experimental setup and procedures. Next, interleaved data analysis and volumetric image reconstruction will be described for longitudinal monitoring of cerebral hemodynamics and CBF index during and after MCA embolization as well as the effect of a thrombolytic treatment. This work wishes to demonstrate the feasibility and usefulness of using interleaved volumetric DOT to monitor longitudinal progresses of cerebral hemodynamics and

blood perfusion during and after cerebral ischemia, with and without therapeutic treatments, with high-quality 3D visualization and quantifications.

5.2 Methods

In this section and affiliated subsection, the instrumentation, experimental setup, surgery for rodent model, and data acquisition are described.

5.2.1 Animal Preparation

Male Sprague-Dawley rats weighing 350-400 grams were purchased from Charles River (Wilmington, MA) and housed in a 12 hr light and 12 hr dark cycle with free access to water and food. All surgical procedures were approved by the Institutional Animal Care and Use Committee of the University of Texas at Arlington and the University of North Texas Health Science Center.

5.2.2 Suture-induced and embolism-induced MCAO model

Two major types of ischemic stroke models were measured in this study, which were suture-induced MCAO model [77, 95] and embolism-induced MCAO model [96], respectively. Since procedure of suture-induced MCAO model is described in section 4.7.1.2, I briefly describe the procedures of embolism-induced MCAO model as follows.

1. Blood clots, mixed with thrombin, fibrinogen, and fresh blood withdrawn from donor rat, were made 24-hr before the stroke induction.
2. For surgery of embolic MCAO, rat was anesthetized with isoflurane (2-2.5%) and the left external carotid artery (ECA) was exposed through a midline cervical skin incision. Blood clots were then introduced into the lumen of ECA via the PE-50 (inner diameter = 0.58mm; outer diameter = 0.99mm) tubing (Figure 5.1a) with the tip of catheter close to the CCA bifurcation for delivering clots toward the brain (Figure 5.1b).

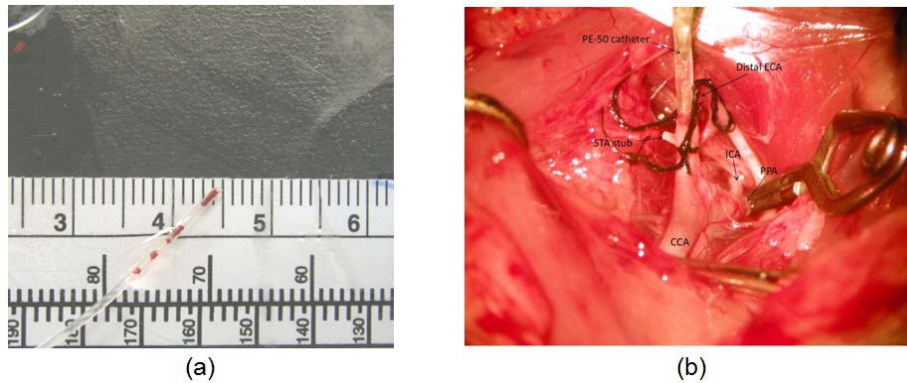


Figure 5.1 (a) Photograph shows clots in PE-50 catheter. (b) Photograph displays the clots injection via small hole on ECA through PE-50 catheter. The abbreviations in Figure 5.3b: ICA: internal carotid artery; PPA, pterygopalatine artery; ECA: external carotid artery; STA: superior thyroid artery; CCA: common carotid artery. Figures were provided by Dr. Ming Ren.

- One hour after embolization, rat was received thrombolysis, which recombinant tissue plasminogen activator (rtPA) was intravenously injected in the jugular vein (Figure 5.2) at a dose of 5mg/kg body weight with a 10% bolus and 90% continuous infusion for 30-mins.

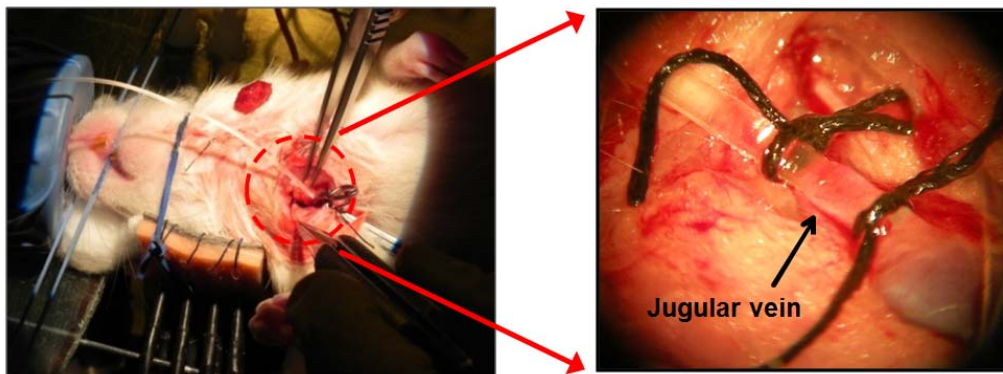


Figure 5.2 recombinant tissue plasminogen activator (rtPA) was administrated throughout Jugular vein. Figure on the right was provided by Dr. Ming Ren.

5.2.3 Experimental setup

DOT measurements on a rat head were performed non-invasively with DYNOT, as introduced in section 2.5. Laser light from each of two laser diodes, with wavelengths = 760nm

and 830 nm, was sequentially coupled into different fiber bundles, which deliver the laser light to various positions on the rat head. On rat scalp, fibers were arranged in rectangular shape. The fiber array consisted of 20 bifurcated source–detector probes (4 rows x 5 columns) that were placed symmetrically on the scalp above the region of cerebrum with a nearest inter-optode distance of 5 mm, as shown in Figure 5.3. The full tomographic dataset, involving 20 sources and 20 detectors, contained total 380 source-detector pairs/measurements (i.e., 20x19, ignoring the collocation fiber pairs). The system operated in continuous-wave mode with a frame rate of 1.81 Hz.

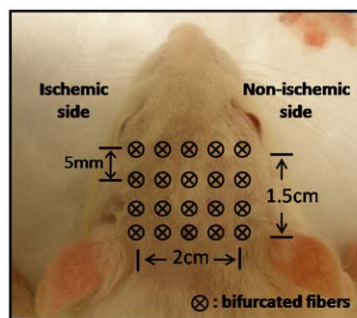


Figure 5.3 Illustration of optode arrangement of bifurcated probes. The nearest inter-optode distance is 5 mm

The rat hair was trimmed to ensure better fiber-skin contact. During the measurement, the animal was fixed in a rigid platform and kept in the supine position (Figure 5.4a). The platform was made by acrylic board with a rectangular hole which allowed fibers coming from the bottom. Several plastic skewers were attached on the board to fix the skin/muscle hooks for the purpose of MCAO surgery. Height can be adjusted by tuning the nuts. The reason for having the rats in the supine position was that it allowed us to have access to midline cervical structure for MCAO surgery without perturbing the DOT measurement and to keep the locations of optodes unchanged throughout the entire period of experiment.

All optodes were also hold by home-made holder. The holder consists of two materials, including silicone rubber and lead metal, as shown in Figure 5.6b. Silicone rubber (smooth-on

Inc, Easton, PA) with approximate 1mm thickness provides the strength to hold and fix the fiber bundles. Lead is soft, bendable and not too heavy which allow the holder to keep the curvature to fit the slight variations of size and curvature of rat heads. Notice that there are 7 columns of bifurcated source–detector probes in Figure 5.4b. The most outer left and right columns were used for image reconstructions by globally convergence method (GCM) and were not adopted in conventional image reconstruction procedure.

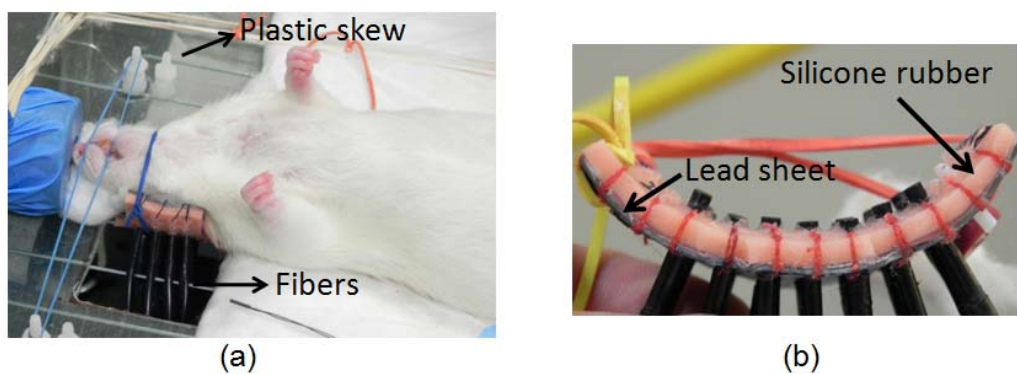


Figure 5.4 (a) Photograph of home-made platform which allowed measuring rat in supine position. Plastic skews indicated by arrow were used to fix skin/muscle hooks for surgery. Optical fiber bundles came from the bottom of the platform. (b) Photograph of home-made probe holder which consisted two material, including silicone rubber and lead metal.

During the measurements, rats were anesthetized with isoflurane (2-2.5%) in 80% of air/20% of O_2 . Notice that extra oxygen was provided in order to maintain spontaneous hemodynamic fluctuations at relative stable level and make sure the changes of hemodynamic mainly caused by cerebral ischemia. Body temperature was monitored by a rectal probe and was maintained by a heating pad between 36.5°C and 37°C. Physiological parameters, including heart rate, breath rate, and arterial oxygen saturation, were measured and monitored by pulse oximeter MouseOx (STARR Life Sciences Corp, MN, USA). NIRS data recorded by DYNOT were pre-processed for each source-detector pair measurement. A band-pass filter, with corner frequencies between 0.01 and 0.3 Hz, was applied to remove the high-frequency instrument noise and low-frequency baseline drift.

5.2.4 Study design

Based on how the ischemic stroke was generated, our experimental protocols were divided into two major groups: G-I was for the suture-induced ischemic model and G-II for embolism-induced ischemic model.

For both models, an ICG-tracking method was also utilized to study reduction of CBF due to focal cerebral ischemia. ICG powder (Sigma-Aldrich Co. LLC, St. Louis, Mo) was dissolved and diluted with saline, having a dosage of 1mg/kg, approximately 0.4 mg per rat. ICG solution was further separated into several (9) small volumes for multiple injections through the femoral vein at 9 different time points during the entire experiment (See Figure 5.6). For ICG injection, a catheter was replaced or imbedded (Figure 5.5) into the rat's skin incision in the groin in advance to minimize the leakage of ICG solution.

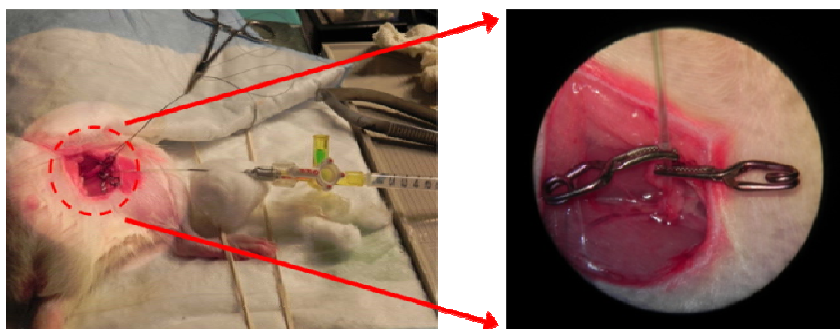


Figure 5.5 Catheter was placed or imbedded into the rat's skin incision in the groin for ICG injection

To determine the inter-injection period for ICG, we performed ICG kinetics measurements on normal rats (n=3). For each rat, the ICG solution with an appropriate concentration was injected 3 times every 30 min. We observed that the recovery time between the injection and the time when the optical signals returned to the pre-injection level was 2.2 ± 0.6 min (not shown). Based on this result, the inter-injection period was selected to be 10 min which allows enough time for ICG to be cleared from the animal's blood stream.

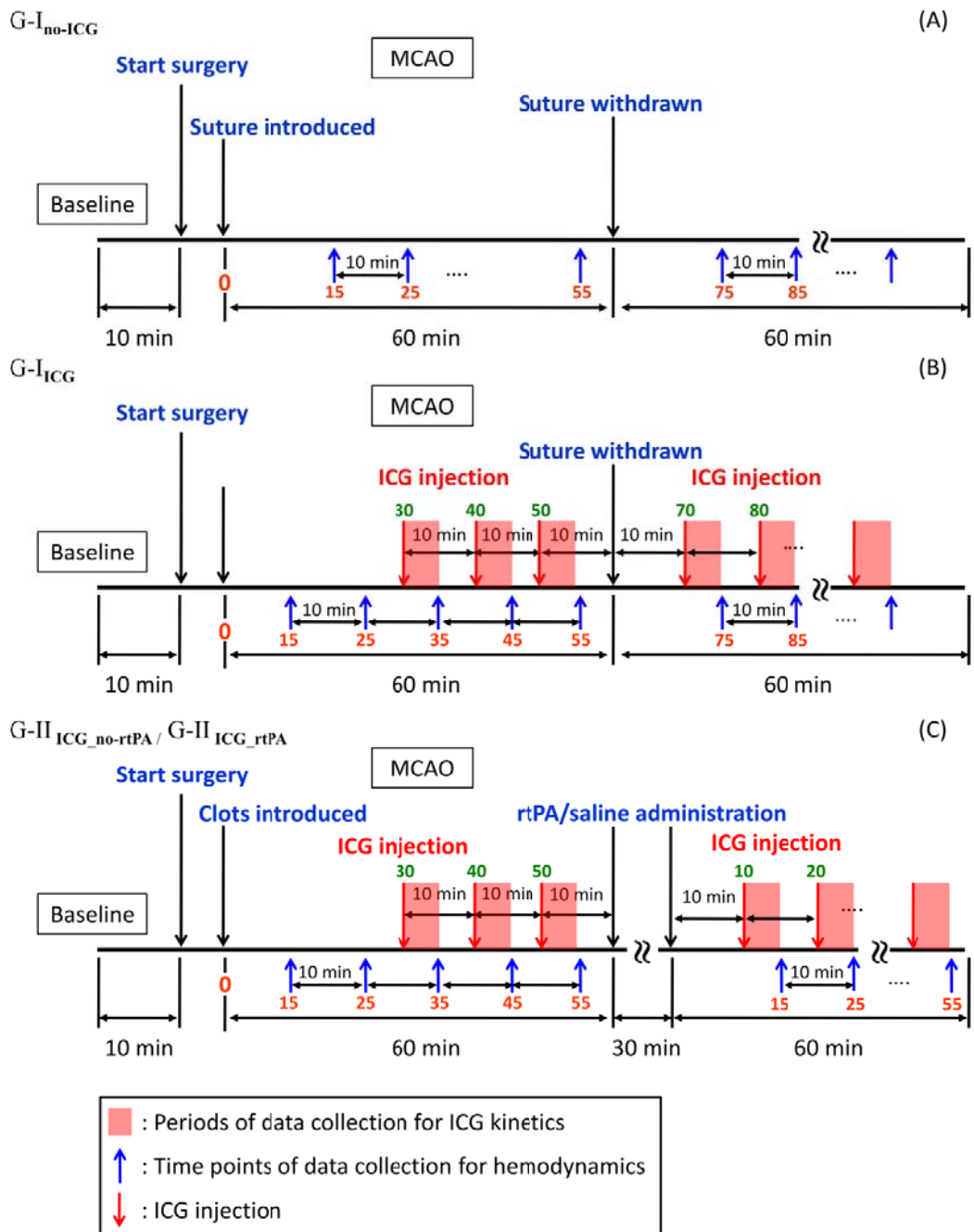


Figure 5.6 Schematic drawings of measurement protocols in: G-I_{no-ICG} and G-I_{ICG} for the suture-induced ischemic model and G-II_{ICG_no-rtPA} and G-II_{ICG_rtPA} for the embolism-induced ischemic model. The x-axis is not plotted in scale.

It is also noteworthy that the NIRS measurements would be interfered by ICG injections. In order to study the effect of ICG injections on the measured changes of hemodynamic signals during cerebral ischemia, we compared the hemodynamic measurements between two sub-groups that were with and without ICG injection. This comparison was carried out using only suture-induced ischemic rat models. The two sub-groups are described as follows.

1. G-I_{no-ICG} (n=9): Rats were performed for MCAO surgery; the left MCA was occluded by silicon-coated suture for 60 min, followed by reperfusion after smoothly withdrawing the suture. The NIRS measurements were not perturbed by ICG injection.
2. G-I_{ICG} (n=6): Rats were underwent MCAO surgery with the same procedures as that used in G-I_{no-ICG}. ICG solution was injected at following time points: 30, 40, 50 min after the suture was introduced, 10 min after withdrawal of the suture, and every 10 min thereafter for 1 hour.

Furthermore, 12 rats were used for the embolism-induced ischemia study. Six rats were treated with rtPA, while the other 6 rats were used as a control group, only having received saline injection instead. These two sub-groups are described as follows.

1. G-II_{ICG_no-rtPA} (permanent cerebral ischemia, control group; n=6): Rats were underwent MCAO surgery; the left MCA was occluded by embolic clots for 60 min. Saline was administrated for 30 min after 1hour occlusion. ICG solution was also injected at 30, 40, 50 min after embolization, 10 min after saline administration, and every 10 min thereafter for 1hour.
2. G-II_{ICG_rtPA} (temporary cerebral ischemia, treatment group; n=6): Rats were similarly prepared as G-II_{ICG_no-rtPA} but rtPA was administrated. Time points for ICG solution injections were also the same as those used for G-II_{ICG_no-rtPA} for appropriate comparison.

All of these four sub-groups of experimental protocols are depicted or outlined in Figure 5.6.

5.2.5 Forward light modeling and Image reconstruction

Forward light modeling in rat head model was performed using finite element method based (FEM) MATLAB package NIRFAST [31] to obtain Jacobian matrix (also called sensitivity matrix) J , which represents changes of measured boundary data due to the small absorption perturbations. As described in section 3.4.1, the forward problem for rat head model can then be written as:

$$\Delta y = J_{rh} \Delta x \quad (5.1)$$

where Δy represents the measured changes of optical density between initial baseline and after changes of absorption due to focal cerebral ischemia, J_{rh} is the Jacobian matrix derived from rat head model and Δx represents change of absorption for each node.

As described in previous section, changes of absorption can be solved using (Tikhonov regularization) Moore-Penrose generalized inverse [97]:

$$\Delta x = J_{rh}^T (J_{rh} J_{rh}^T + \lambda I)^{-1} \Delta y \quad (5.2)$$

where λ is the regularization factor and was chosen as 10^{-2} times the maximum of diagonal of the matrix $J_{rh} J_{rh}^T$ and I is the identity matrix. DCA can be then applied as:

$$\hat{\Delta x}_{DCA} = J_{rh}^{\#} (J_{rh}^{\#} J_{rh}^{\#T} + \lambda I)^{-1} \Delta y \quad (5.3)$$

where $J_{rh}^{\#}$ represents the compensated Jacobian matrix and λ was chosen as 10^{-2} times the maximum of diagonal of the matrix $J_{rh}^{\#} J_{rh}^{\#T}$. With dual wavelengths measurement, the changes of hemodynamic at different time points can be solved as:

$$\begin{bmatrix} \Delta HbO_2 \\ \Delta HbR \end{bmatrix} = \begin{bmatrix} \mathcal{E}_{HbO_2}^{760} & \mathcal{E}_{HbR}^{760} \\ \mathcal{E}_{HbO_2}^{830} & \mathcal{E}_{HbR}^{830} \end{bmatrix}^{-1} \begin{bmatrix} \Delta \mu_a^{760} \\ \Delta \mu_a^{830} \end{bmatrix} \quad (5.4)$$

Change of total hemoglobin concentration ΔHbT is then expressed as summation of ΔHbO_2 and ΔHbR .

5.2.6 Calculation of ICG kinetics and data analysis

Two wavelengths used in CW-DOT measurements are all close to the maximal absorption spectrum of ICG in blood/plasma [9]. I selected optical signals measured by 760nm for image reconstructions and further data analysis. From each temporal or longitudinal measurement set per animal, a time series of volumetric reconstructed images proportional to the ICG concentrations were obtained. ICG kinetics was then obtained by extracting the signals from each voxel along the time axis. Specifically, the optical signals were first corrected or calibrated to the 5-sec pre-injection baseline level and then de-trended to remove any signal drift due to either the instrument drift or slow hemodynamic drift in the rats during and/or after MCAO. Figure 5.9 shows the changes of optical density (ΔOD) following and ICG bolus. To quantify the ICG kinetics, several parameters were determined as follows [91].

1. Maximum changes of ICG concentration (ΔICG): For most of NIRS measurements, HbO_2 and HbR are two major chromophores contributed to the changes of optical signals. In this study, nevertheless, ICG was also utilized to study CBF or its index during and after MCAO. It is noticed that we were not capable to obtain the absolute concentration changes of ICG due to the limitation of used wavelengths for measurement. However, we observed significantly larger changes or increases in optical density (more than 10-fold) seen right after ICG injection in the animals as compared to the fluctuations of optical signals caused by changes of HbO_2 and HbR concentration. Hence, changes of optical density ($\Delta\text{OD}_{\text{ICG}}$) were defined as ΔICG in this study (see Figure 5.7).

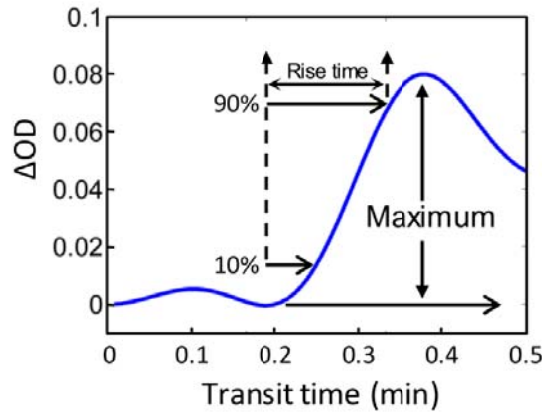


Figure 5.7 Curve displays the change of optical density (ΔOD) measured by 760nm following an ICG bolus and the definition of ICG kinetics. Blood flow index (BFI) is calculated by maximal light absorption change after intravenous bolus of ICG divided by the rise time.

2. Rise time (RT; Figure 5.11b): RT was defined as the time interval when ΔOD_{ICG} increased from 10% to 90% of maximum ΔICG , ΔICG_{max} ; this definition could avoid the exact temporal selection of start point of ICG bolus.
3. Blood flow index (BFI): BFI can be obtained by:

$$BFI = \frac{\Delta ICG}{RT} \quad (5.5)$$

As described in Section 5.2.5, changes in light absorption (due to either ischemia or ICG administration) can be reconstructed at each voxel or node in the rat head model. Then, we were able to reconstruct tomographic images of ΔOD_{ICG} at different time points when ICG was injected. Accordingly, volumetric ICG kinetics images were generated by calculating the corresponding values of ΔICG , RT , and BFI , at each voxel or mesh node.

5.2.7 Interleaved data acquisition and volumetric images for hemodynamics and BFI

While the data collection in our animal experiments by the multi-channel DYNOT system was temporally continuous before, during, and after MCAO, two different types of optical density changes (ΔOD), which reflected two types of physiological signals, were acquired in an interleaved format. In general, ΔOD values at a selected wavelength in our rat MCAO

measurement should be equal to $\Delta OD_{total} = \Delta OD_{ICG} + \Delta OD_{no-ICG}$, where ΔOD_{ICG} and ΔOD_{no-ICG} represent ΔOD values with and without ICG administration in the animal. As mentioned in Sections 2.3 and 2.6, the clearance time of ICG in the animal was about 2.2 ± 0.6 min, while an increase in ΔOD by ICG could be 10-fold bigger right after ICG injection in the animals.

Therefore, we designed an interleaved approach to obtain two phases of data selection/acquisition: One was to grasp the ΔOD values within 3-4 minutes right after ICG injection so that $\Delta OD_{total} \approx \Delta OD_{ICG}$; the other was to pick up the optical signals 5 minutes after ICG administration so that $\Delta OD_{total} \approx \Delta OD_{no-ICG}$ since most of ICG was cleared from the rat blood stream. The former measurement during $\Delta OD_{total} \approx \Delta OD_{ICG}$ allowed us to determine BFI readings as described in section 2.6, while the latter measurement during $\Delta OD_{total} \approx \Delta OD_{no-ICG}$ resulted in quantification of HbO₂, HbR, and HbT.

Specifically, the interleaved protocol is shown in Figure 5.6. For hemodynamic signal (HbO₂, HbR, HbT) analysis in all four animal groups (i.e., G-I_{no-ICG}, G-I_{ICG}, G-II_{ICG_no_rtPA}, and G-II_{ICG_rtPA}), data acquisition time points were selected at 15 min after suture was introduced, followed by every 10 min thereafter until 1 hour after the reperfusion to avoid large interference from ΔOD_{ICG} in the early phase of ICG clearance. Note that for G-II (i.e., embolism-induced MCAO), an extra period of 30 min was added 1 hour after MCAO to infuse the rtPA/saline solution for 30-min thrombolytic/sham treatment (see Figure 5.8). On the other hand, for BFI data acquisition in three groups (i.e., G-I_{ICG}, G-II_{ICG_no_rtPA}, and G-II_{ICG_rtPA}), ICG solution was injected at 30, 40, 50 min after the MCAO was introduced, 10 min after suture withdrawal or rtPA/saline infusion, and every 10 min thereafter for 1 hour (see Section 5.2.4 and Figure 5.6).

5.2.8 Statistical consideration

All data were expressed as mean \pm SD (standard deviation). The significance of differences between group means was determined using Student's paired t-test. The relationship of hemodynamic changes between G-I_{no-ICG} and G-I_{ICG} for each of HbO₂, HbR, and HbT at the same time points throughout the entire experiment (before, during, and after MCAO)

was examined by Pearson product-moment correlation. P value less than 0.05 was considered significant.

5.3 Results

5.3.1 Rat brain atlas-guided DOT of cerebral hemodynamics in ischemic rats

The comparison of the reconstructed images with and without DCA was adopted are demonstrated in the following subsection. Moreover, the comparison between reconstructed image and histological brain sample is described.

5.3.1.1 Comparison the reconstructed hemodynamic between DCA applied and conventional image reconstruction

As showed in section 3.4.3, total sensitivity analysis demonstrated higher measurement sensitivities (larger than 50%) covering cortical and subcortical regions. This reveals deeper measurement sensitivities coverage than regular DOT. Figure 5.8 displays the experimental results of reconstructed ΔHbO_2 images in coronal section view during MCAO. Figure 5.8b shows the image reconstructed by conventional way while Figure 5.8c shows the image reconstructed with DCA applied. The location where the section was cut is depicted in Figure 5.8a.

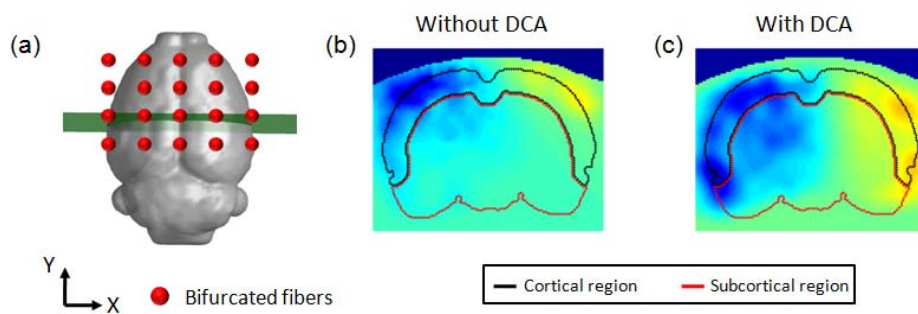


Figure 5.8 (a) Illustration of where the section was cut. The coronal views of reconstructed ΔHbO_2 images during the MCAO while (b) DCA was not applied and (c) DCA was adopted. Black dashed line outlines the cortical region and red dashed line outlines the subcortical region.

Figure 5.8c demonstrates the improvement of depth localization of hemodynamic changes which were mostly observed in cortical and subcortical regions. Changes of hemodynamic were mostly found toward superficial while DCA were not applied (Figure 5.8b).

Since adoption of DCA has been shown the improvement of depth localization in experimental data as well as the computer simulations (section 3.4.5), the following image reconstructions and data analysis were done with DCA applied.

5.3.1.2 Comparison the reconstructed volumetric images versus histological brain sample

Using the procedures given in section 3.4, we were able to obtain volumetric DOT images reconstructed on a rat brain atlas for studying cerebral hemodynamics in ischemic stroke rats. Figure 5.11 demonstrates such reconstructed images from G-I_{no-ICG} rats during MCAO. Left column of Figure 5.9a shows the isosurface plots or 3D rendered rat brains of changes in oxygenated (ΔHbO_2), deoxygenated (ΔHbR), and total hemoglobin (ΔHbT) concentrations, averaged across 9 rats. Column on the right shows coronal-sliced reconstructed tomographic images of ΔHbO_2 , ΔHbR and ΔHbT sliced along multiple locations at the middle cerebral artery (MCA) territory. The isosurface rendered plots in Figure 5.9a reveal decreases of ΔHbO_2 and ΔHbT and increases in ΔHbR during MCAO. These plots also demonstrate that major hemodynamic changes occurred on the outer side of the left hemispheres, which matched well near the MCA territory. The volumetric DOT results were confirmed by histological analysis [2,3,5-triphenyltetrazolium chloride (TTC) staining] of this suture-induced stroke rat model, as shown in Figure 5.9b. Furthermore, the coronal views of these images exhibit that major hemodynamic changes in our study took place on the left side of cortical as well as subcortical regions. This observation is consistent with a review report [98, 99], which documented that most of the animal stroke models produce substantial damage to many different brain regions, specially including those seen in Figure 5.9c.

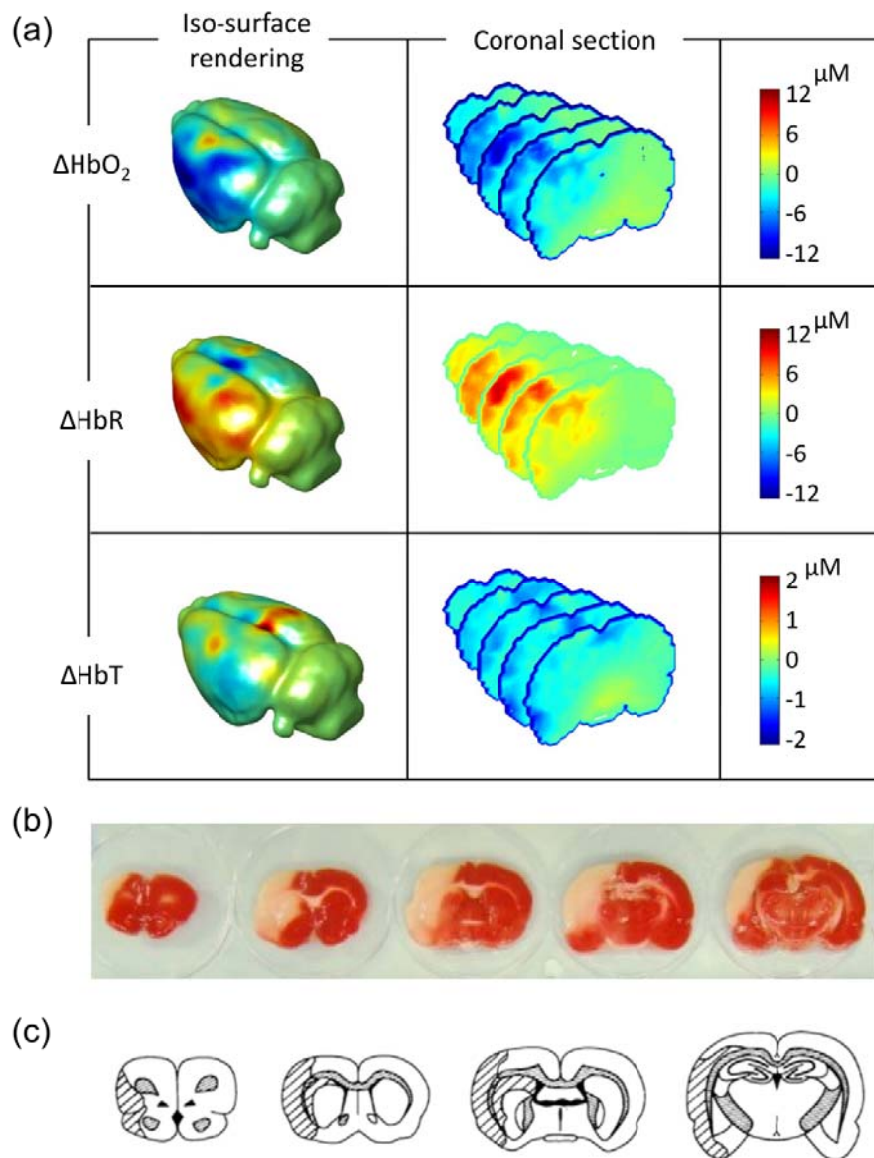


Figure 5.9 (a) Volumetric hemodynamic reconstruction for rat brain during MCAO. Left column displays the 3D surface rendered plots of ΔHbO_2 , ΔHbR and ΔHbT . Color represent the concentration changes in micromolar (μM). Column on the right displays the multiple coronal sections of hemodynamic changes during MCAO. Each section is 0.5mm thickness. (b) 2,3,5-triphenyltetrazolium chloride stain of the infarct region of brain sample. (c) Diagram represents the coronal sections of rat brain. The hatched area represents the most common pattern of ischemic damage. Figure is reprinted from A. Tamura et al. [99].

5.3.2 Changes of cerebral hemodynamic for suture-induced ischemic stroke model

To further investigate the hemodynamic changes during MCAO and reperfusion, we

compared the reconstructed DOT images between the ischemic and non-ischemic side of the rat brain. Two regions of interest (ROIs) within the reconstructed images were chosen to be outer right side (ROI-1, contralateral control region) and outer left side (ROI-2, ipsilateral ischemic region) of the rat brain, as shown in Figure 5.10 with correct dimensions and locations marked.

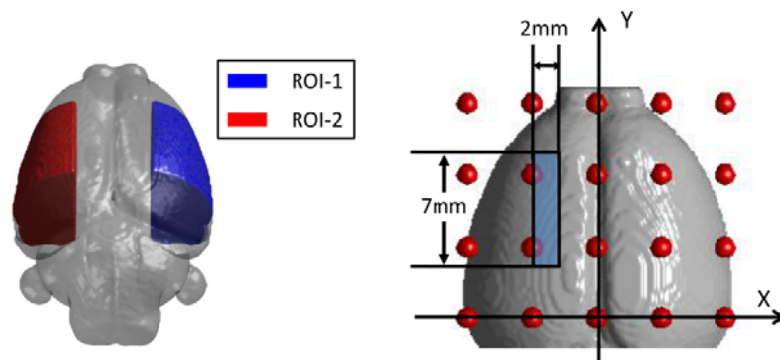


Figure 5.10 Two region of interest (ROIs) in rat brain and dimensions of two ROIs. ROI-1 located in contralateral control hemisphere and ROI-2 represents ipsilateral ischemic hemisphere. Figure on the right shows the dimension of ROI.

5.3.2.1 Temporal and spatial analysis

For temporal data analysis, all the FEM mesh nodes located within the two ROIs were extracted; the corresponding reconstructed parameters (e.g., ΔHbO_2 and ΔHbR) were spatially summed and averaged at each time point for each rat, followed by a grand average over 9 rats. Quantitative time traces of hemodynamic changes from these ROIs at different time periods are plotted in the left column of Figure 5.11. From Figure 5.11a, a significant decrease in ΔHbO_2 was observed in ROI-2 while the suture was introduced (0-min at start of occlusion). In the meantime, a dramatic increase of ΔHbR could be seen at the start of occlusion (Figure 5.11b).

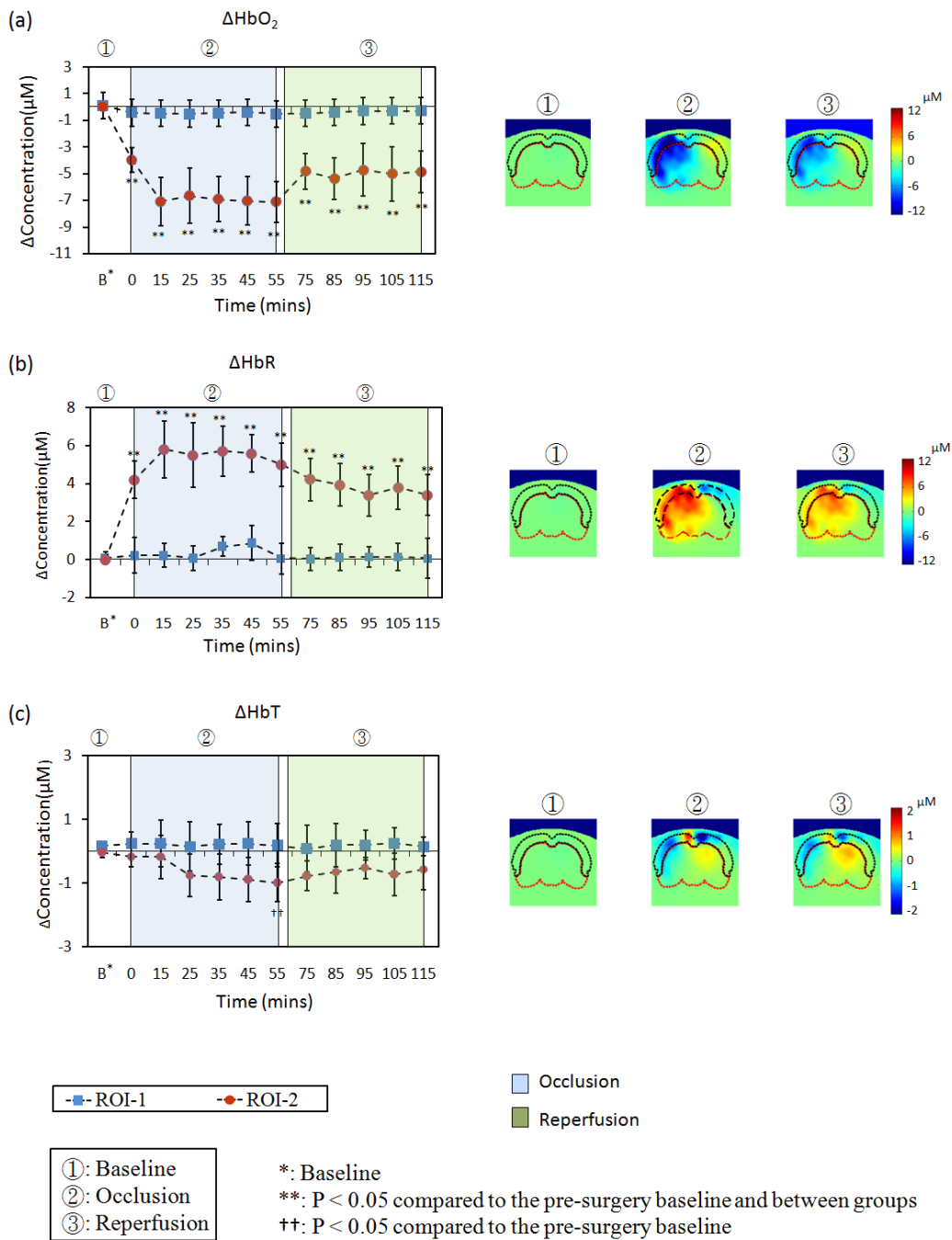


Figure 5.11 Left column shows the time tracers of (a) ΔHbO_2 , (b) ΔHbR and (c) ΔHbT in two ROIs for G-I. Every data point is presented as mean plus SD. Right column display the corresponding coronal reconstructed images at three time points, which are baseline, during occlusion, and after reperfusion, respectively. Cortical region in Figure is marked with black dashed line while subcortical region is marked with red dashed line.

As the suture was withdrawn 1 hour after MCAO, both ΔHbO_2 and ΔHbR values returned gradually toward the pre-MCAO baseline. However, both ΔHbO_2 and ΔHbR did not completely recover to the pre-surgery baseline. Regarding the non-ischemic side of the rat brain, small fluctuations were found in both ΔHbO_2 and ΔHbR , but there was no statistical significance in either of them as compared to the pre-surgery baselines, respectively.

Furthermore, statistical analysis was taken to compare respective hemodynamic parameters (i.e., ΔHbO_2 , ΔHbR , ΔHbT) between the two ROIs at selected time points (15 minutes right after MCAO, followed by every 10 min thereafter), as marked in the left column of Figure 5.11. The analysis results suggest that there exist significant differences in ΔHbO_2 and ΔHbR between the two ROIs during both periods of occlusion and reperfusion, respectively. Figure 5.11c shows that ΔHbT in ROI-2 exhibited a similar trend to ΔHbO_2 ; however, there was no statistical difference in ΔHbT between the two ROIs at respective time points, nor between the pre-MCAO baseline and ΔHbT signals before, during, and after MCAO surgery for each ROI.

For spatial data analysis, the right column of Figure 5.11 shows three characteristic, time-evolving coronal images averaged over 9 rats before, during, and after MCAO (i.e., baseline, 30 min and 90 min after the suture was introduced). This set of coronal images consistently reveals that ROI-2 had a much more decrease in ΔHbO_2 and an increase in ΔHbR throughout the most of ROI-2 during MCAO, and that the recoveries in both parameters started to occur after the suture was removed, but were only partial within ROI-2.

5.3.2.2 Study of influence of hemodynamic changes with ICG injection

Figure 5.12 shows the profiles of hemodynamic changes with two successive ICG injections (marked within light blue and light yellow blocks). As described in previous section, separating the concentration changes for three components (HbO_2 , HbR , and ICG) which affect the optical signals changes in this study is a challenge. This is due to the lack of one more wavelength measurement. However, Figure 5.12 clearly shows that curves of hemodynamic changes (ΔHbO_2 , ΔHbR and ΔHbT) were only contaminated by ICG bolus at the early period

after ICG injection (Figure 5.14, circled by dashed line). After approximate 2-3 mins, the curves return to the level before ICG injection and remain relatively stable as presented in section 5.3.2.1. Result demonstrates the feasibility of study hemodynamic changes and ICG kinetics together with same measurement and setup.

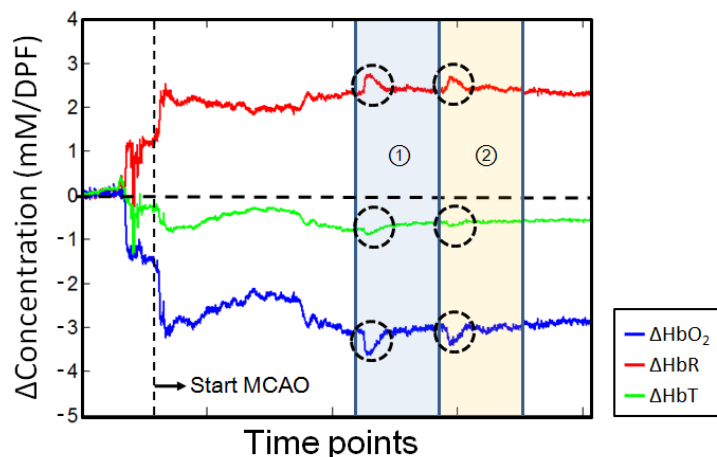


Figure 5.12 Temporal profiles of hemodynamic changes with two successive ICG injections (marked within light blue and light yellow blocks).

To investigate possible interference on changes of hemodynamic signals from ICG injection, hemodynamic changes taken from both animal groups of $G-I_{no-ICG}$ and $G-I_{ICG}$ are compared. Quantitative hemodynamic changes from these two groups were analyzed, using the same procedures as described above. The time points chosen to quantify temporal hemodynamic signals were interleaved with the time points for ICG administration (see section 5.2.7), so the inference from ICG absorption should be minimal. Pearson's correlation coefficients between the two groups (i.e., with and without ICG administration) were calculated for ΔHbO_2 , ΔHbR , ΔHbT , respectively, and are shown in Figure 5.13. The results demonstrate good positive correlations between $G-I_{no-ICG}$ and $G-I_{ICG}$ within ROI-2 in ΔHbO_2 ($r = 0.92$; $p < 0.05$), ΔHbR ($r = 0.90$; $p < 0.05$) and ΔHbT ($r = 0.84$; $p < 0.05$), as listed in Table 5.1. Relatively low correlations appear between the two groups within ROI-1 for all three parameters ($r = 0.52$ for ΔHbO_2 and 0.50 for ΔHbR ; $p > 0.05$) except ΔHbT . A high correlation of ΔHbO_2 and ΔHbR

between $G-I_{no-ICG}$ and $G-I_{ICG}$ in ROI-1 is not expected since ROI-1 was the no-injury side and had no consistent pattern of hemodynamic changes observed from each rat. Also, relative small hemodynamic fluctuations were found throughout entire measurements, but the changes were not significant as compared to the pre-MCAO baseline, as shown in Figure 5.11. Overall, the analysis on cerebral hemodynamic changes in the two animal groups with and without ICG injection confirmed that the injection of ICG did not significantly affect changes of hemodynamic signals.

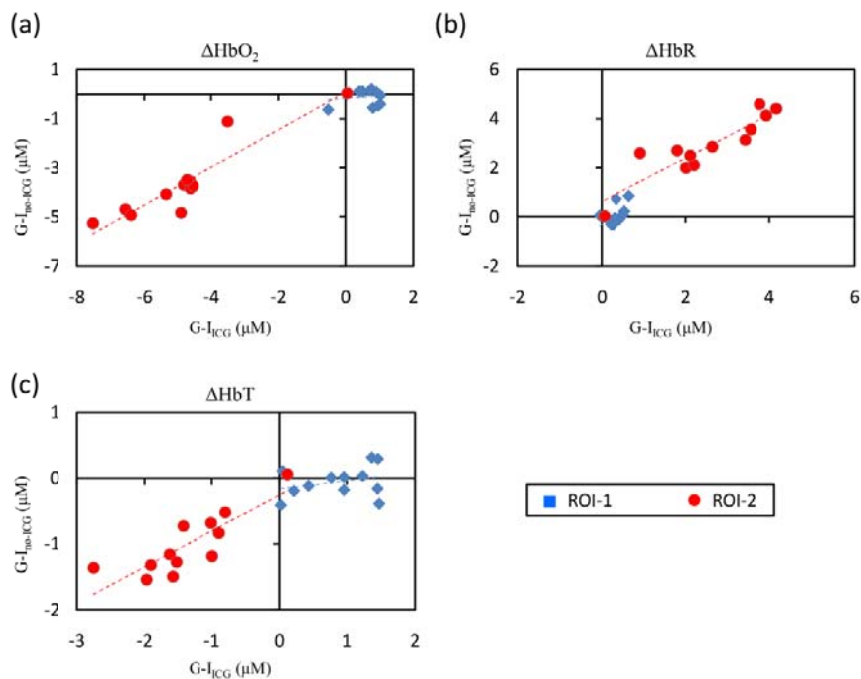


Figure 5.13 Scatter plots for comparison of (a) ΔHbO_2 , (b) ΔHbR and (c) ΔHbT between $G-I_{ICG}$ and $G-I_{no-ICG}$ in two ROIs.

Table 5.1 Correlation coefficients of the comparison between $G-I_{ICG}$ and $G-I_{no-ICG}$ in ROI-1 and ROI-II for ΔHbO_2 , ΔHbR , and ΔHbT .

	ROI-1		ROI-2	
	r	slope	r	slope
ΔHbO_2	0.52 (p = 0.59)	0.142	0.92 (p = 0.0001)*	0.770
ΔHbR	0.54 (p = 0.07)	1.091	0.90 (p = 0.0001)*	0.888
ΔHbT	0.27 (p = 0.39)	0.122	0.84 (p = 0.0007)*	0.547

* p < 0.05

5.3.3 Changes of cerebral hemodynamic for embolism-induced ischemic stroke model

The left panel in Figure 5.14 shows the quantitative time traces of hemodynamic changes from two embolism-induced ischemia animal groups of G-II_{ICG_no-rtPA} (control group, n=6) and G-II_{ICG_rtPA} (treatment group, n=6). After using the same data analysis procedures as given in Section 5.3.2.1, it can be seen that embolism-induced MCAO caused decreases of ΔHbO_2 on the ischemic side of the rat brain (ROI-2) after embolization in both groups (down to $-5.2\pm 1.1\mu\text{M}$ in G-II_{ICG_no-rtPA} and $-4.7\pm 1.3\mu\text{M}$ in G-II_{ICG_rtPA}), while increases of ΔHbR also occurred (up to $4.8\pm 1.2\mu\text{M}$ in G-II_{ICG_no-rtPA} and $3.7\pm 1.2\mu\text{M}$ in G-II_{ICG_rtPA}). Further statistical analysis on temporal profiles reveals that in ROI-2, there existed significant differences in ΔHbO_2 (see Figure 5.14a) and ΔHbR (see Figure 5.14b) between the pre-MCAO and post-MCAO readings during the three periods of occlusion, treatment, and reperfusion, respectively, for both treated and un-treated groups. In ROI-1, on the other hand, there was no statistically significant change of ΔHbO_2 (see Figure 5.14a) and ΔHbR (see Figure 5.14b) between pre- and post-MCAO signals.

In particular, for rtPA-treated rats, a trend of increases in ΔHbO_2 (from $-4.9\pm 1.3\mu\text{M}$ to $-3.3\pm 1.1\mu\text{M}$; see Figure 5.14a) and a trend of decreases in ΔHbR (from $4.9\pm 1.3\mu\text{M}$ to $3.3\pm 1.1\mu\text{M}$; see Figure 5.14b) were found in ROI-2 15-mins after rtPA administration; these trends of recovery continued throughout the entire reperfusion period. For untreated animals, however, there was no significant change before and after injection of saline in both ΔHbO_2 and ΔHbR signals. During the recovery period, we specially noticed that 45 min and 60 min after rtPA infusion, respectively, ΔHbR and ΔHbO_2 started to have statistically significant differences between treated and untreated animals, as marked in Figure 5.14a. While a similar increase trend of ΔHbT after rtPA infusion was also noticed in the treated group, ΔHbT remained insignificant between the treated and untreated groups, and between pre- and post- MCAO surgery.

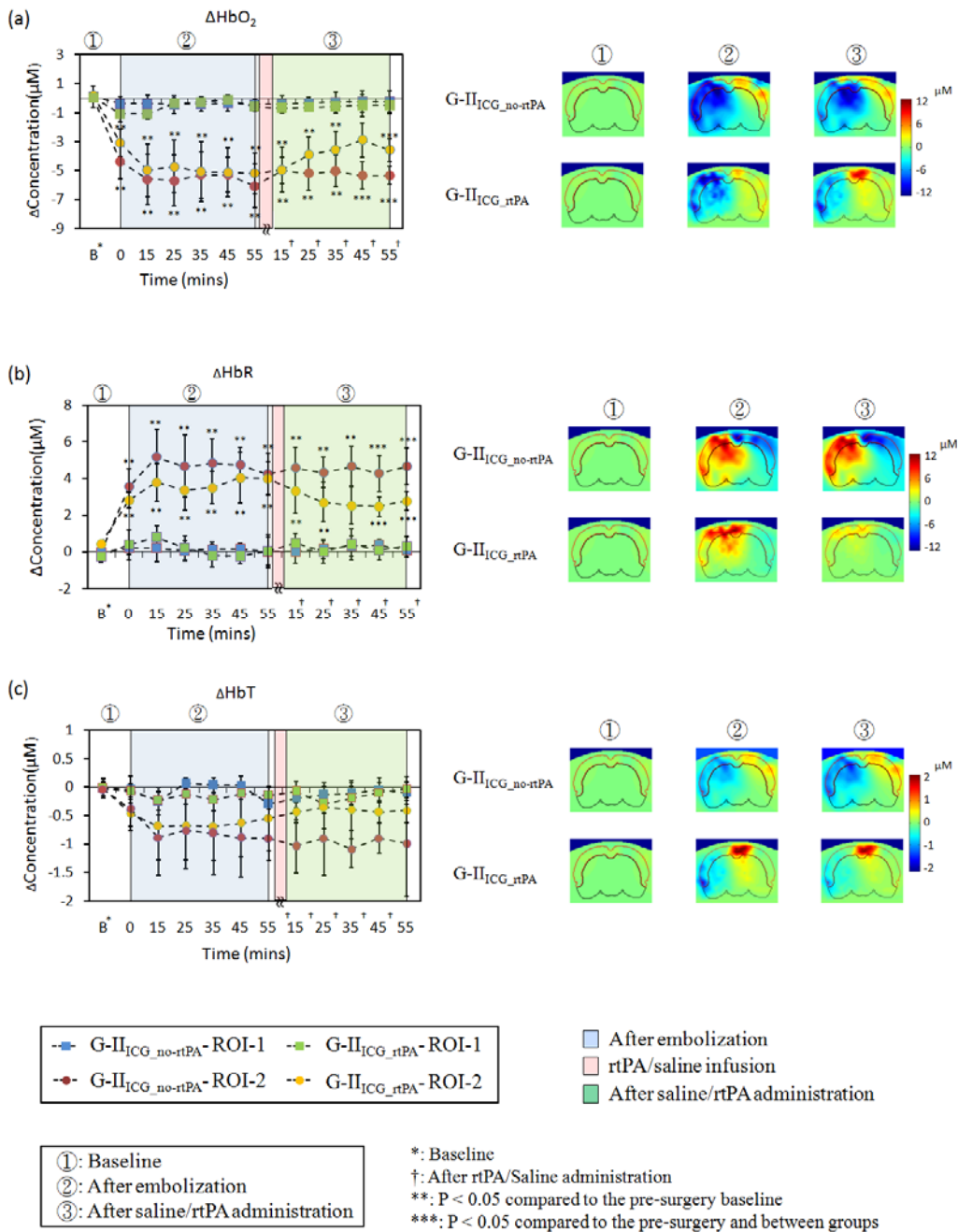


Figure 5.14. Left column shows the time tracers of (a) ΔHbO_2 , (b) ΔHbR and (c) ΔHbT in two ROIs for G-II_{ICG}_{no-rtPA} (control group) and G-II_{ICG}_{rtPA} (treatment group).

Every data point is presented as mean plus SD. Right column display the corresponding coronal reconstructed images at three time points, which are baseline, after embolization, and after rtPA/saline administration, respectively. Cortical region in Figure is marked with black dashed line while subcortical region is marked with red dashed line.

For spatial data analysis, the bottom panels of right column of Figure 5.16 show three characteristic, time-evolving coronal images averaged over 6 rats at the time points of before and during MCAO (i.e., baseline and 30 min after embolism was introduced), as well as 30 min after the 30-min rtPA/saline treatment. This set of coronal images consistently reveals that the treated animal group had a much better improvement in both ΔHbO_2 and ΔHbR recovery, about 45-60 min after rtPA administration, throughout the most of ROI-2 than the untreated group. However, within this period of time, the recoveries in both parameters were only partial within ROI-2.

5.3.4 Dynamic response of ICG bolus measured by NIRS

Figure 5.15 shows the dynamic response of ICG bolus measured by NIRS from normal rat (Figure 5.17a) and rat during MCAO (Figure 5.15b). The same pattern of change of optical density (ΔOD) due to ICG passenger is exhibited between right (contralateral control side) side and left (ipsilateral ischemic side) side of brain for normal rats (Figure 5.15a). However, Figure 5.15b shows higher amplitude in ΔOD on right side and also faster rise time compared to left side. Moreover, to visualize to ICG kinetics and allow results more easily comparison between ROIs, the spatial distribution maps of ΔICG , RT and BFI were generated by the steps described in section 5.2.6.

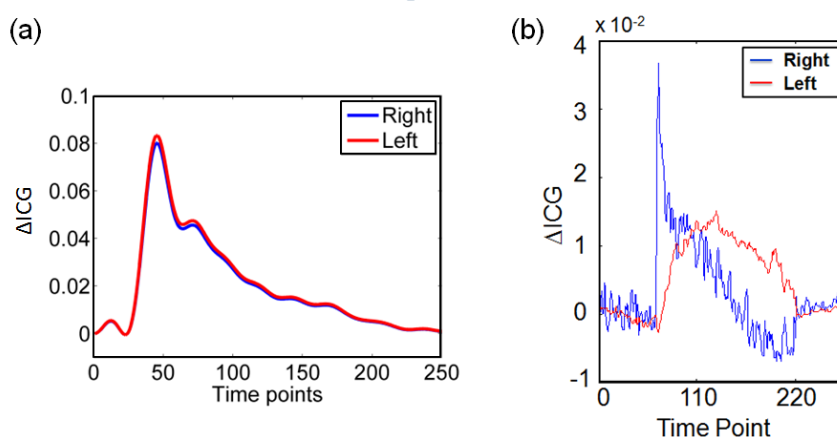


Figure 5.15 Profiles of ICG kinetics from (a) normal rat and (b) rat under MCAO.

Based on Figure 5.7 and Equation 5.5, values of Δ ICG, RT and thus BFI at each FEM-mesh-based node were quantified and formed volumetric images of respective ICG kinetic parameters after we obtained 3D reconstruction of DOT. Figure 5.16 shows coronal views, close to the middle of the animal brain (as marked in the left panel), of spatial distribution maps of Δ ICG, RT and BFI from normal rats without any occlusion (averaged over 6 rats) and the rats (n=6 rats) during embolism-induced MCAO. These spatial maps were smoothed using 3 x 3 uniform kernels. Figure 5.16a shows a relatively symmetric pattern between the two hemispheres in each of the Δ ICG, RT and BFI images/maps. Comparing to Figure 5.16a, in contrast, Figure 5.16b shows a lower Δ ICG distribution over the entire ischemic (left) side of rat brain due to the lack of ICG delivery caused by MCA occlusion. Moreover, the RT maps display increases in the transit time of ICG on the ischemic side of hemispheres during occlusion. No such differences between the two hemispheres were observed in the normal rats. Accordingly, the maps of BFI also indicate decreases of cerebral blood flow on the ischemic side of the rat brain.

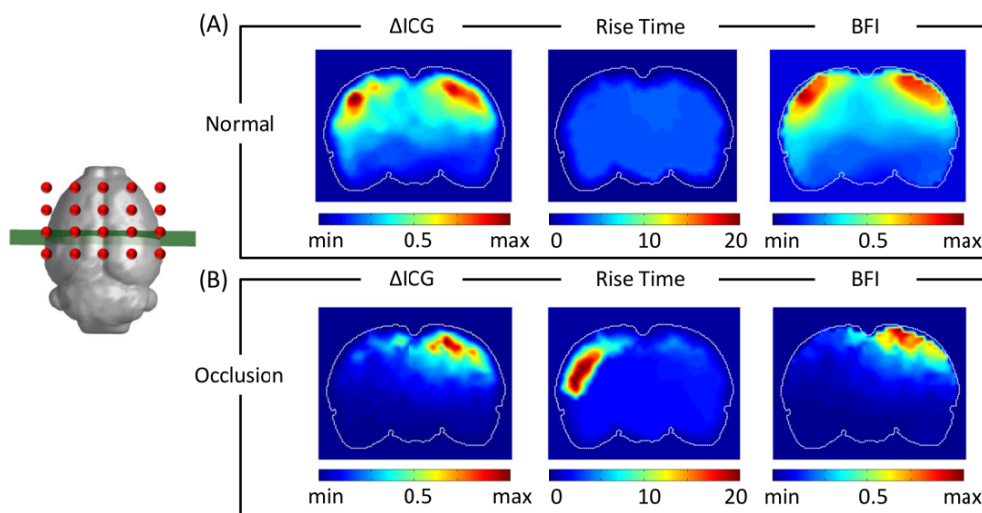


Figure 5.16 Coronal sectioned images of spatial distribution maps of Δ ICG, RT, and BFI from (a) normal rats, and (b) rats during MCAO. Color scale for Δ ICG and BFI are normalized between minimum (0) and maximum (1). Color in RT maps represent in second.

5.3.4.1 ICG kinetics for suture-induced ischemic model

Quantitatively, to calculate time-evolving dynamic changes of BFI throughout the entire measurements before, during and after the suture-induced MCAO was introduced; the spatial BFI maps at the chosen coronal plane (see the left panel in Figure 5.16) at different time points for G-I_{CG} rats were obtained and then normalized between their maximum and minimum values. Values of normalized BFI within ROI-1 and ROI-2 (as defined in Figure 5.10) were extracted at each node and spatially averaged, respectively. In general, BFI has been presented to be directly proportional to CBF. However, several studies have also reported that BFI can provide accurate, repeatable results only for intra-subject comparisons, but not for inter-subject comparisons because of the unknown proportionality or normalization factor among different subjects [93]. Therefore, we defined and utilized a BFI ratio between its changes in ROI-2 to

ROI-1, namely, $Ratio_{BFI} = \frac{BFI_{averaged_ROI-2}}{BFI_{averaged_ROI-1}}$, during the cerebral blood flow circulation in this

study.

Based on this definition, we obtained a temporal profile (top panel of Figure 5.17) of $Ratio_{BFI}$, expressed as relative reductions of BFI on the occlusion/stroke side with respect to the control side, at different time points (n=6). This trace clearly demonstrates that much less blood flow occurred on the ischemic hemisphere during MCAO, followed by an immediate increase after suture was withdrawn, indicating the recovery of blood reperfusion. Quantitatively, the time trace in Figure 5.17 illustrates that the ratio of BFIs between the ischemic and normal side dropped to about 14% ($14.2 \pm 11.3\%$) during MCAO, recovered to 77% ($77.3 \pm 12\%$) 10 min after MCAO, and then remained at an average of 79% ($79.2 \pm 13\%$) of that of ROI-1. The bottom panels of Figure 5.17 show the corresponding spatial maps of normalized BFI ratios during MCAO and reperfusion at times equal to 30 min. Consistently, these two images confirm gradual recovery of a spatial-symmetry pattern in $Ratio_{BFI}$, which was seen as a characteristic in BFI of normal rats (see Figure 5.19).

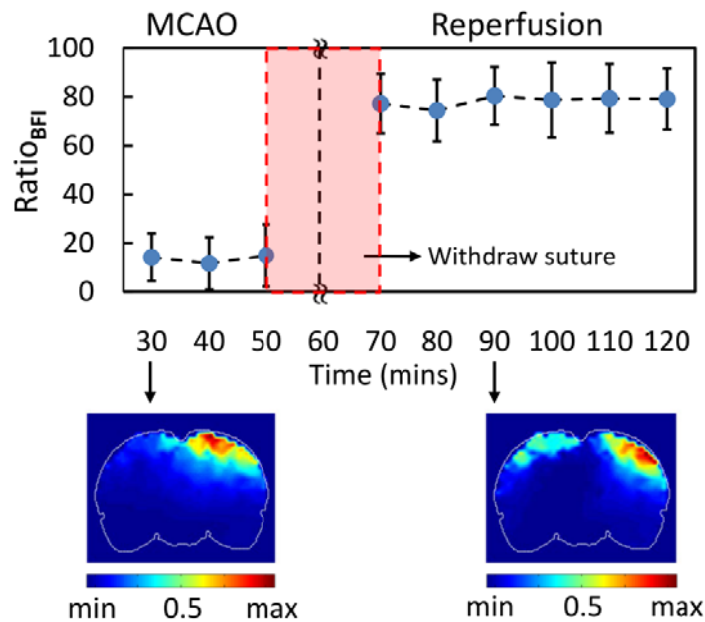


Figure 5.17 Time tracers of ratio of BFI between ROI-1 and ROI-II in G-I_{ICG}. Every data point represent mean plus SD. Bottom row show coronal section of BFI images during MCAO and after suture was withdrawn (reperfusion).

5.3.4.2 ICG kinetics for embolism-induced ischemic model

Using the same data processes, ICG kinetics of the two embolism-induced ischemic rat models: namely, G-II_{ICG_no-rtPA} and G-II_{ICG_rtPA} were analyzed. The corresponding temporal curves for the two animal groups are given in Figure 5.18a. Note that rtPA was injected at 60 min after MCAO started, followed by a 30-min treatment time and then the 1st ICG injection and measurement 10 minutes after the treatment (i.e., 100 min after MCAO or 40 min after rtPA). A trend of recovery in BFI on the left hemisphere is revealed in this figure for G-II_{ICG_rtPA} rats after rtPA administration while no obvious change was found for G-II_{ICG_no-rtPA} rats after saline injection. Specifically, for the untreated group, the normalized $Ratio_{BFI}$ in ROI-2 (the ischemic side) dropped to 40% (40.7 ± 11.6) with respect to the BFI over ROI-1 30 min after embolization, followed by no changes thereafter. For the rtPA-treated animals, the normalized $Ratio_{BFI}$ from ROI-2 decreased to 34% (34.3 ± 12.2) of the BFI over ROI-1 during occlusion, followed by gradual returns to 58% (58.7 ± 16.5) at 40 min after rtPA administrated (100 min after MCAO)

and to 82% (81.6 ± 17.8) at ~90 min after rtPA treatment (~150 min after MCAO). Statistical differences between the treated and un-treated groups were found 30 min after rtPA/saline injection and thereafter.

Moreover, the bottom left panels of Figure 5.18 show the corresponding spatial maps of normalized BFI ratios during embolic MCAO for both treated (Figure 5.18c) and un-treated (Figure 5.18b) rat groups, exhibiting a similar low $Ratio_{BFI}$ on the ischemic side. During reperfusion after rtPA intervention at times equal to 30 min after MCAO, values of $Ratio_{BFI}$ on the ischemic side of the treated rats appeared to recover throughout the lesion region and exhibited a spatial-symmetry pattern with respect to the distribution of $Ratio_{BFI}$ on the control side (Figure 5.18d). This recovery characteristic was very similar to that seen in the suture-induced MCAO rats (see Figure 5.17). In contrast, saline intervention did not induce any noticeable changes in $Ratio_{BFI}$ on the ischemic side of the untreated rats (Figure 5.18e).

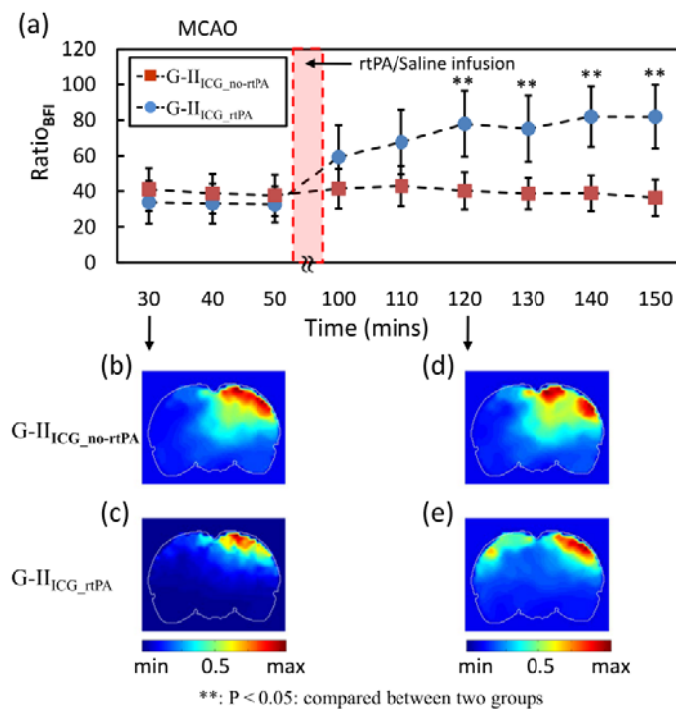


Figure 5.18. Time tracers of ratio of BFI between ROI-1 and ROI-II in G-II_{ICG}no-rtPA and G-II_{ICG}rtPA. Every data point represent mean plus SD. Bottom row displays coronal section of BFI images after embolization and after rtPA (G-II_{ICG}rtPA) or saline (G-II_{ICG}no-rtPA) administration.

5.4 Discussion

In this chapter, we presented an experimental study of ischemic stroke using rat MCAO models and high-density DOT measurements. After utilizing DCA and co-registering the optical probes on a rat brain template, we were able to obtain rat brain atlas-guided, volumetric DOT. In particular, an interleaved data acquisition and analysis process was planned and implemented so that we were able to obtain 3D visualization of hemodynamic changes and CBF index in the rat brain, with or without a thrombolytic treatment. Several special aspects of this study are summarized and discussed below:

5.4.1 Rat brain atlas-guided, volumetric DOT

While DOT suffers from lack of showing anatomical structures, we could calculate hemodynamic changes and compare corresponding differences between ROIs based on anatomical locations if MR images with *prior* structure information were cooperated. It is well known that reconstruction performances and spatial resolutions of DOT can be enhanced by using a priori structural information [100, 101], where imaging volumes could be divided into anatomical regions or contours, as ROIs, identified from *prior* images by MRI or CT. Accordingly, the identified ROIs can be assigned with heterogeneous optical properties so as to reduce the number of unknown optical properties in image reconstructions or in spatial constraint methods [37]. However, the key issue of these methods is that accurate subject-specific *prior* information needs to be acquired. In this study, we used the *prior* anatomical information to extract ROIs and to project reconstructed volumetric DOT images on a rat brain atlas. Since we did not have subject-specific MR images for each rat, the rat brain atlas-guided DOT matches appropriate anatomical locations only as a group-averaged approximation, but it still provides us with estimated anatomic views of *in vivo* ischemic rat brains non-invasively. Also, the image reconstruction process described in this study can be easily applied when subject-specific *prior* information is available.

Arrangement of optodes may affect the measurement sensitivity and quality of image reconstruction. Xu et al. [102] presented the improvement of sensitivity and image quality for deeper tissue structures by adding extra array-opposing fibers, which provided transmission measurements. In our animal measurements, fibers were placed on top of the animal's scalp, providing back-reflection optode arrangement. It has been also shown that mathematical compensation algorithms can help greatly improve accuracy of depth localization for deeper tissue structures. Such depth compensated methods have been reported to counterbalance the decrease in measurement sensitivity with increase in depth, thus benefiting the image quality of DOT. Most of the approaches have been developed to image human brain activities [103] or to detect human cancer [104, 105]. For animal study, on the other hand, Culver et al. [14] presented an approach using spatially variant regularization (SVR) to monitor rat brain activation. In present study, DCA was adopted to compensate the sensitivity in deeper layer and also decrease sensitivity on superficial layer near the optodes, leading the improvements of depth localization and resolution. Total sensitivity analysis shown in section 3.4.3 demonstrated higher measurement sensitivities (larger than 50%) covering cortical and subcortical regions. This reveals deeper measurement sensitivities coverage than regular DOT. Experimental animal data showed in Figure 5.10 demonstrate the improvement of depth localization of hemodynamic changes which were mostly observed in cortical and subcortical regions. Moreover, computer simulations introduced in sections 3.4.4 and 3.4.5 also show the improvement of image quality as well as the depth localization while performing the three dimensional reconstruction. Results indicate good improvement in depth localization for DOT with incorporating with depth compensation algorithm, providing good potential in studying brain activities in deeper tissues.

5.4.2 Effects of baseline optical properties and mesh densities on reconstructed DOT images

It is expected that different baseline optical properties lead to different values of reconstructed hemodynamic changes (i.e., ΔHbO and ΔHbR) since the measurement sensitivity

matrix, J , is generated accordingly based on baseline optical parameters (see Section 3.4.1). Since a large diversity in optical properties of a rat head has been reported by different research groups, we investigated in this sub-section the degree of deviation in reconstructed hemodynamic parameters induced by different baseline optical properties, which were published by several groups. Table 5.2 lists several sets of published optical properties of a rat head: Set 1 has been used earlier in Chapter 3 (see Section 3.4.1 and Ref. [42]) to obtain reconstructed hemodynamic images due to MCAO with (Figures 5.9 and 5.11) and without (Figure 5.13) rtPA treatment. The parameters of Set 2 were introduced by Pogue et al [100], having a larger absorption coefficient in the rat brain tissues than that in the skin/muscle, a somewhat different trend versus that in Set 1. Both of these sets list very similar reduced scattering coefficients.

Besides baseline optical properties, mesh distributions and densities may affect spatial reconstructions of hemodynamic parameters. To demonstrate this point, the baseline optical properties of a rat head in Set 3 had the same homogeneous values of absorption and reduced scattering coefficients, respectively, for each of the 3 layers that were seen in the three-layer model used in Sets 1 and 2. On the other hand, Set 4 assumed only a one-layer homogenous model, having the same optical properties as those in Set 3 [106].

Table 5.2 Optical properties of 3-layer and 1-layer homogeneous rat head model

	3-layer model; μ_a (mm⁻¹)			3-layer model; μ_s' (mm⁻¹)		
	skin/muscl	skull	brain	skin/muscle	skull	brain
Set 1 [42]	0.02	0.005	0.015	0.68	2.2	2.2
Set 2 [100]	0.01	0.015	0.02	0.5	2.0	2.0
Set 3 [106]	0.006	0.006	0.006	1.0	1.0	1.0
	homogeneous model; μ_a			homogeneous model; μ_s' (mm⁻¹)		
Set 4 [106]	0.006			1.0		

Figure 5.19a to 5.19d show cross-sectional contours of reconstructed ΔHbO_2 images during cerebral ischemia when 4 different sets of baseline optical properties or mesh

distributions were utilized to generate the MS matrix, J . Figure 5.19b shows a less dramatic decrease of ΔHbO_2 as compared to those in Figs. 5.19c and 5.19d. However, Figs. 5.19a to 5.19c reveal a similar pattern since most of hemodynamic changes are located on the left side of the rat brain. Figure 5.19d, on the other hand, shows a more diffused and symmetrical/spherical pattern of ΔHbO_2 on the left side of hemisphere.

More quantitatively, as compared to optical properties given by set 1 used in this study, we found averaged 38% of increase in ΔHbO_2 amplitude (~30 min after occlusion within ROI-2) when set 2 being used, 3% decrease in amplitude when set 3 being used, and 34% decrease in amplitude when set 4 being used. Comparing the time traces of ΔHbO_2 in ROI-2 for 4 sets of optical properties being used as the background properties, high correlations ($r= 0.97-0.99$; $p < 0.05$) were observed between set 1 and the other three sets (see Figure 5.19e). Overall, this Analysis demonstrates that baseline optical properties surely affect reconstructed changes in amplitudes of hemodynamic parameters, but not the trend of dynamic changes throughout the times.

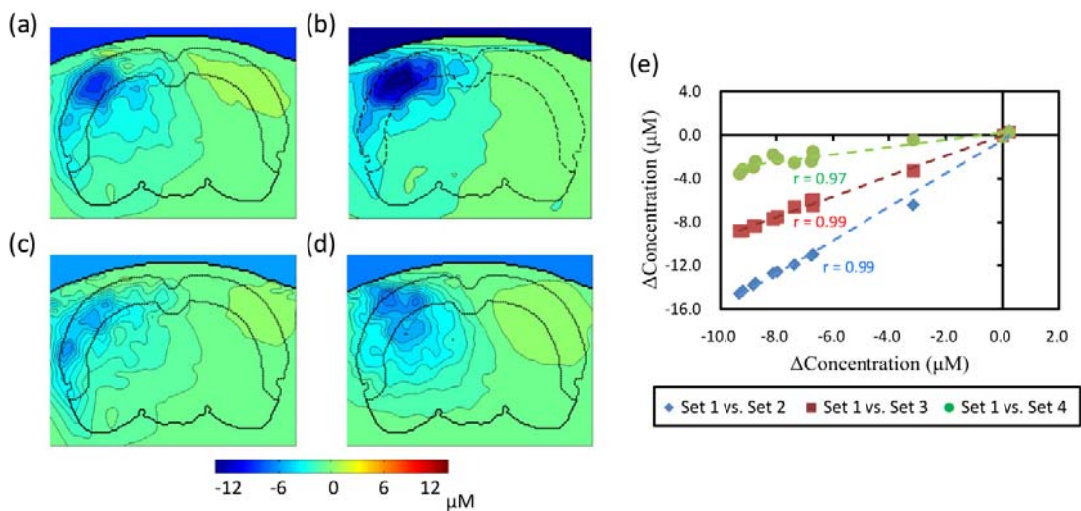


Figure 5.19 Reconstructed images of coronal sections of ΔHbO_2 from (a) to (d) are reconstructed by different sets of optical properties. Figures (c) and (d) were used the same optical properties but (d) was modeled with only one-layer. (e) Scatter plots for comparison of ΔHbO_2 among four sets of optical properties in ROI-2.

5.4.3 Two types of MCAO rat models

Two rat MCAO models have been measured and investigated in this study. The first model, where focal ischemia was carried out with suture-introduced intraluminal MCAO, has been well developed and widely used to investigate stroke physiology and intervention-related effects by fMRI, PET, as well as NIRS. Thus, we used it as a good calibration representation to validate our experimental setup of high-density DOT, to examine interleaved data acquisition and analysis process, as well as to confirm our volumetric reconstruction methodology. In this part of study, our results show statistically significant differences in a decrease of ΔHbO_2 and an increase of ΔHbR during the occlusion period across the injured brain side, ROI-2 (see Fig. 5.10). These significant changes started within the early ischemic period (10-15 min after suture was introduced), followed by the recovery of ΔHbO_2 and ΔHbR in the early period of reperfusion. An indicator of total blood volume (ΔHbT), however, did not show any statistical difference in its change as compared to that at the pre-surgery baseline. All the observations were consistent with previous publications [54, 78].

A newly developed embolism-induced ischemic model, which more closely mimics ischemic stroke in humans than the suture model, was also measured and investigated in this study. In general, this embolic stroke model provides more precise lodgment or simulation of clots at MCA bifurcation, thus improving the reproducibility and similarity of ischemic injury. Also, treatment of ischemic stroke with rtPA has been well documented, which helps restore blood flow and oxygen in the focal stroke region affected by embolism-induced cerebral ischemia in both humans [107] and animals [108-110]. In this chapter, I was able to demonstrate that time-evolving effects or longitudinal monitoring of thrombolytic therapy with rtPA could be achieved by non-invasive volumetric DOT using the embolic MCAO rat model. Specifically, the treated $G\text{-II}_{\text{ICG-rtPA}}$ animal group exhibited gradual recovery in both cerebral hemodynamics (Fig. 5.14) and blood reperfusion (Fig. 5.18), similar to those seen after withdrawal of the suture in the suture-induced MCAO model (Figs. 5.11 and 5.17). After recanalization, however, the recovery of

increasing ΔHbO_2 and decreasing ΔHbR were found to be slower as compared to those in the suture model since the process of clot breakdown took time, relatively much slower than withdrawing a suture. In order to validate our DOT results, we also performed histology analysis on the post-surgery animal brains and found small breaking-down clots at a couple of peripheral branches of MCA only in one of the six rtPA-treated rats (Fig. 5.20), but no significant effect seen on changes of hemodynamic parameters. Both temporal and spatial results from G-II_{ICG_{no}-rtPA} rats reveal the outcome of a permanent rat MCAO model, while the hemodynamic changes reconstructed from G-II_{ICG_{rtPA}} animals represent reversible retrieval of cerebral functions because of a timely therapeutic intervention, without causing obvious changes thereafter.



Figure 5.20 Brain sample removed from G-IV. Small breaking-down clot was found at peripheral branch of MCA (indicated by arrow).

5.4.4 Advantages of Interleaved Data Acquisition and Analysis

One novelty of this study was to develop and achieve interleaved data acquisition and analysis (see Figure 5.6) in order to obtain both hemodynamic parameters (ΔHbO_2 and ΔHbR) and BFI, or to obtain volumetric DOT images of ΔHbO_2 , ΔHbR , and BFI during and after ischemic stroke. Specifically, we determined and utilized a 10-min inter-injection interval based on our pilot study, which showed a rapid clearance time of ICG to be ~ 5 minutes or shorter in the blood stream of a living biological system (such as rats). Then, the measured optical density changes by multi-channel NIRS were temporally interleaved into two categories during data analysis: (1) the data taken 0-5 min right after ICG administration would be used to derive BFI; (2) the data collected 5-10 min after ICG injection would give rise to ΔHbO_2 and ΔHbR , with

small interference from ICG absorption. In this way, we were able to accomplish volumetric DOT images of ΔHbO_2 , ΔHbR , and BFI, before, during, and after MCAO in both ischemic stroke rat models.

It is known, however, that NIRS or DOT measurements would be perturbed by multiple ICG injections, potentially by a small amount of ICG residual, thus leading to possible errors in quantification of ΔHbO_2 and ΔHbR . To avoid such faulty outcomes, we carefully studied the effect of transit ICG injection on changes of hemodynamic parameters (see Sections 5.2.7, 5.3.2.2, and Fig. 5.15). We found that each of the hemodynamic parameters (i.e., ΔHbO_2 , ΔHbR , and ΔHbT) are highly correlated between $G-I_{\text{no-ICG}}$ and $G-I_{\text{ICG}}$ on the ischemic side, indicating no significant interference or effects due to ICG injection on trends of ΔHbO_2 , ΔHbR , and ΔHbT during and after suture-induced MCAO. Moreover, no obvious ICG accumulation or re-circulation (only one clear peak was found in temporal profiles of optical density changes per ICG injection) was observed since the body-weight-proportioned ICG concentration was precisely calculated and diluted several times for injection.

It is also noteworthy that NIRS measurements were perturbed by multiple ICG injections in this study, so that studying the effect of ICG transit on changes of hemodynamic was significantly important. According to characteristic of rapid clearance of ICG, we applied 10-mins inter-injection period based on the pilot studies. By avoiding the early period after ICG injections and comparing changes of hemodynamic at mid-point between injections, results between $G-I_{\text{no-ICG}}$ and $G-I_{\text{ICG}}$ show high correlations in ΔHbO_2 , ΔHbR and ΔHbT , indicating no significant interferences were observed due to the injection of ICG. Moreover, no obvious of ICG accumulation and re-circulation (only one clear peak was found in one ICG injection) was observed since only small volume of ICG was injected for each injection. Similar result was also reported by De Visscher et al. [111].

To investigate the reduction of CBF during cerebral ischemia, ICG-tracking technique was employed in our study. For suture-induced MCAO model, it has been well documented that

occlusion leads to a decrease in CBF to approximately 30% to 40% of the pre-ischemic baseline [112, 113]. CBF was recovered to approximate 80% of baseline after reperfusion [78]. Our results exhibited that BFI on the ischemic side dropped to approximately 14% of that on the control side during occlusion and then returned to 79%. In terms of the embolism-induced MCAO model, the study shows a relatively broader range of drop of CBF after embolization than the suture-induced MCAO model. rtPA-mediated recanalization also exhibited a different range of CBF recovery. The reason could be the complexity of embolic model itself, e.g. lengths of clot, types of clot, etc. Our results showed that BFI on the ischemic side dropped to approximately 34% of that on the control side in G-II_{ICG-rtPA} after embolization and then returned to about 82% after rtPA treatment. The BFI ratio decreased to 40% during the occlusion and remained no significant changes after saline injection in G-II_{ICG_no-rtPA}. Similar results were found in Haelewyn et al. [109] while rats only administered with saline after embolization.

Notice that a large standard deviation is shown in our analysis and may be caused by the inter-subject variation. Although the whole procedures were done by a well-trained surgeon, the differences among animals still could not be eliminated. Notice that the BFI ratios in this study were calculated based on the assumption that no significant changes occurred on the control regions during MCAO and reperfusion for both rat models. Culver et al. [54] showed that CBF on control side of brain remained relatively stable during occlusion and reperfusion in rats and suture-induced ischemic stroke model. Haelewyn et al. [109] also presented no significant changes on the non-ischemic side of rat brain when using the embolism-induced model. Although ICG-tracking techniques do not allow absolute quantification of CBF, our results demonstrated the feasibility of using continuous-wave NIRS measurement combined with ICG-tracking strategy to study the trend of dynamic changes of CBF due to cerebral ischemia.

5.4.5 Weakness of the study

While we illustrated a good correlation for each of ΔHbO_2 , ΔHbR , and ΔHbT between G-I_{no-ICG} and G-I_{ICG} rat groups during and after suture-induced MCAO, a close inspection on

these quantitative correlations (see Table 5.1) revealed non-identical or non-equal values of ΔHbO_2 , ΔHbR , and ΔHbT from the two groups with and without ICG injection. The mismatch is most likely due to after-clearance residuals of ICG. Table 1 lists that ΔHbR gave rise to the best consistency between two groups with a slope of 0.89, followed by ΔHbO_2 with a slope of 0.77, while all of the three quantities had somewhat offset caused by ICG residuals. Several possible ways to minimize the interference of ICG absorption, such as reduce the concentration of ICG solution or the injection volume, and increase the inter-injection period, may help in ICG clearance from the blood stream. However, reduce the concentration of ICG solution or the injection volume may cause the decrease of signal-to-noise ratio (SNR) for ICG kinetics, leading to the quantification errors during calculations. Also, increase inter-injection period will cause the loss of temporal resolution, i.e., less time points for monitoring the dynamic changes of CBF. Further investigation in selecting the time points for interleaved data analysis and the inter-injection period could help in optimized the proposed methodology. Moreover, by increasing the used wavelengths for measurement (>2), one should be able to differentiate absorption of ICG from that of hemoglobin species (HbO and HbR), and thus to simultaneously evaluate cerebral hemodynamics and perfusion.

5.5 Conclusion

Overall, in conclusion, we have utilized a continuous-wave DOT system to study and image the changes of hemodynamic parameters resulting from suture-induced and embolism-induced rat stroke models. In the meanwhile, using the same experimental setup with the ICG-tracking method, we were able to investigate dynamic changes in cerebral perfusion at multiple temporal points during and after cerebral ischemia without extra instrumentation and with little interference of measurements. Moreover, utilizing DCA to achieve volumetric image reconstruction has facilitated 3D hemodynamic (i.e., HbO_2 and Hb) and BFI imaging. The methodology developed in this study has also provided us with an excellent visualization and quantification tool to gain insight into cerebral changes at different sites of the rat brain

undergoing ischemic stroke or treatment. Our analyzed results have exhibited consistent patterns of changes in cerebral hemodynamics and perfusion from both rat models during occlusion and reperfusion, and they are also in good agreement with previous reported studies. This paper overall demonstrates that the interleaved imaging approach shown is a useful and feasible tool to study stroke physiology and can also be used in evaluating the effect of thrombolysis.

CHAPTER 6
DIFFUSE OPTICAL TOMOGRAPHY TO STUDY THE BILATERAL FUNCTION
CONNECTIVITY AFTER CEREBRAL ISCHEMIA WITH RESTING-STATE FUNCTIONAL
CONNECTIVITY

6.1 Introduction

Attentions in functional connectivity, defined as temporal correlations between neural or hemodynamic fluctuations between the distinct brain regions of cerebral cortex, have been significantly increased recently [114-116]. The hemodynamic fluctuations with low frequency (< 0.1Hz) were observed in the human brain even in absence of tasks (resting-state). These spontaneous low frequency fluctuations can be used in study of functional connections among different brain regions. Resting-state functional connectivity is a great tool to investigate brain networks in a variety of human brain diseases or conditions, such as Alzheimer's [117], depression [118], post-traumatic stress disorder (PTSD) [119], and the impact of lesions in brains affected by stroke.

Two most commonly applied techniques to analyze resting-state functional connectivity are component analysis and seed-based correlation. Seed-based approaches correlate the mean time course of the hemodynamic signal within a ROI (seed) with the time courses of all other brain areas. Resting-state functional connectivity (RSFC) in study of recovery or motor performance due to lesion-induced disruption by using functional magnetic resonance imaging (fMRI) have been studied and reported in human [117, 120] as well as in animal [121],

Functional near infrared spectroscopy (fNIRS) recently demonstrates the potential to investigate the RSFC in human [122]. Taking advantage of its portability, ease of implementation, and high temporal resolution, fNIRS is appropriate for measuring cases not suitable for fMRI measurements. Although several studies of using fMRI to study RSFC in acute

cerebral ischemia or in relation of recovery after ischemic stroke in animal models have been reported; however, similar studies still have not been extended to fNIRS.

Therefore, in this chapter, a seed-based resting-state functional connectivity based on the fNIRS measurement to investigate the tissue recovery after cerebral ischemia has been presented. Two widely-used middle cerebral artery occlusion (MCAO) animal models, which are suture-induced and embolism-induced ischemic models, respectively, were measured and used to assess the methodology. Moreover, study in embolism-induced ischemic model using resting-state functional connectivity can be used to evaluate the treatment effect of thrombolysis.

6.2 Materials and Methods

6.2.1 Animal preparation

Male Sprague-Dawley rats weighing 350-400 grams were purchased from Charles River (Wilmington, MA). Rats were housed in a 12 hr light and 12 hr dark cycle and had free access to water and food for at least 48 hours. All surgical procedures were approved by the Institutional Animal Care and Use Committee of the University of Texas at Arlington and the University of North Texas Health Science Center.

6.2.2 Middle cerebral artery occlusion (MCAO) models

Rats were received two major types of MCAO models, which are suture-induced and embolism-induced MCAO models, respectively. In suture-induced MCAO model, briefly, the monofilament suture coated with silicone on front-end was introduced into left external carotid artery (ECA) and advanced through internal carotid artery (ICA) to MCA bifurcation. Occlusion was performed for 60-mins and suture was withdrawn to allow reperfusion. For embolism-induced MCAO model, thrombin added clots were introduced into ECA via catheter with the tip of catheter close to the common carotid artery (CCA) bifurcation for delivering clots toward the brain to embolize the MCA. After 60-mins of embolization, rats were received thrombolytic therapy which recombinant tissue plasminogen activator (rtPA) was intravenously administrated with infusion for 30-mins.

6.2.3 Experimental groups

The experimental protocols were mainly divided by two groups based on two MCAO models, which are suture-induced ischemic model and embolic-induced ischemic model, respectively. The details are described as follows.

- (1) Suture-induced MCAO model (G-I): Rats received the suture-induced MCAO were then further divided into two subgroups. Lesions found in brain sample via 2,3,5-triphenyltetrazolium chloride (TTC) staining were grouped in G-I_{lesion} (n = 10) whereas no lesion was found in brain sample were assigned as G-I_{no_lesion} (n = 7).
- (2) Embolism-induced MCAO model (G-II): Rats introduced embolism-induced MCAO were also divided into two subgroups, which were treatment group (G-II_{rtPA}, rats administrated with rtPA 1-hr after embolization, n = 4) and control group (G-II_{control}, rat only received saline after embolization, n = 3).

6.2.4 Experimental setup

Two groups of rats were positioned in supine position (Figure 6.1a) and anesthetized with isoflurane (2%) in 80% of air/20% of O₂. On rat scalp, fibers were arranged in rectangular shape. The fiber array consisted of 20 bifurcated source–detector probes (4 rows x 5 columns) that were placed symmetrically on the scalp above the region of cerebrum with a nearest inter-optode distance of 5 mm (Figure 6.1b). The full tomographic dataset, involving 20 sources and 20 detectors, contained total 380 source-detector pairs/measurements (ignoring the co-location fiber pairs).

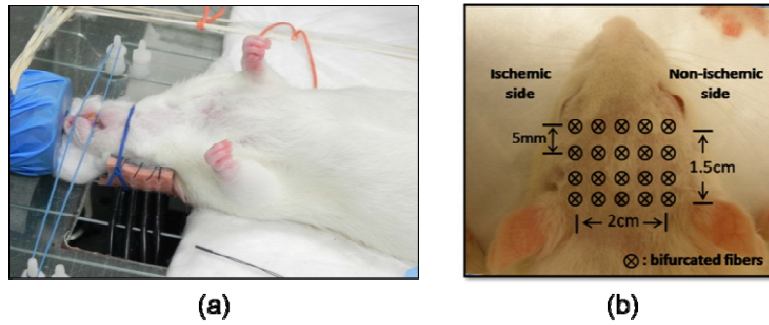


Figure 6.1 (a) Rat was positioned in supine position during the NIR measurement. (b) Optode array arrangement for NIR measurement.

NIRS measurements on rat head were performed non-invasively with tomographic imaging system, dynamic near-infrared optical tomographic instrument, DYNOT (NIRx Medical Technologies, LLC, NY, USA). The system operated in continuous-wave mode with a frame rate of 1.81 Hz. Laser light from each of two laser diodes, with wavelengths = 760nm and 830 nm, was sequentially coupled into different fiber bundles, which deliver the laser light to various positions on the rat head.

In terms of the measurement protocol, rats were measured 10-mins of pre-surgery baseline (resting-state) before performed the MCAO surgery. This data set was considered as the data for normal rats and can be used to validate the results since rats before receiving MCAO were assumed as normal rats. After MCAO operation, two groups of rats shown in section 6.2.3 were measured under resting-state for 10 min. The time points of measurements for two groups were listed in Table 6.1. Moreover, two sham-operated rats were also measured. For sham-operated rats, the operation procedure was the same as suture-induced MCAO model except the suture was removed right after suture was introduced. Sham rats were also considered as the normal rats in this study.

Table 6.1 Measurement protocol of resting-state NIRS measurement

	Pre-surgery	After MCAO operation
Suture-induced MCAO	10-mins	7 days after MCAO (10-mins)
Embolism-induced MCAO	10-mins	1,2,3, and 7 days after MCAO (10-mins)

6.2.5 Data pro-processing and correlation analysis

NIRS data were processed and analyzed using channel wise assessment; the channels with significant motion artifacts were excluded before data processing. Data were filtered by bandpass filter with frequencies between 0.009 - 0.08 Hz following previous human functional connectivity algorithms [122], and this band was also used to study resting-state functional connectivity in mouse [123]. Image changes of optical density (ΔOD) for two wavelengths of measurements and reconstruction of the spatial distribution of changes in hemoglobin concentration were performed following the same methodology as described in section 5.2.5. After reconstruction of hemoglobin concentration changes, time course of hemoglobin concentration changes for each voxel were obtained by extracting the value of each voxel from reconstructions which were reconstructed at different time points.

Resting-state functional connectivity methods were used to evaluate spatiotemporal correlation patterns in spontaneous brain activity. The connections of a given region (defined as a seed) were obtained by performing a Pearson's correlation analysis between the seed and other locations in the brain. Before performing the correlation analysis, time courses for seed and other regions were down-sampled from 1.81 Hz to 1 Hz. Correlation map/volume was then obtained by replacing values in each pixel or voxel with a correlation coefficient, which is usually denoted as r . Functional connectivity studies were done by using ΔHbO_2 , ΔHbR , or ΔHbT contrast. In this study, only ΔHbO_2 data was used for functional connectivity analysis.

Regarding the selection of seed, since this study mainly targeted lesion-induced disruption of bilateral functional connectivity, seed was selected on the contralesional (right) side of

hemisphere. Since lesion due to MCAO is mostly observed on the left outer side of the brain in MCA territory and also due to the limitation of spatial resolution of diffuse optical image, the location of seed was roughly selected with approximate location placed on the outer right cortical area, as shown in Figure 6.2.

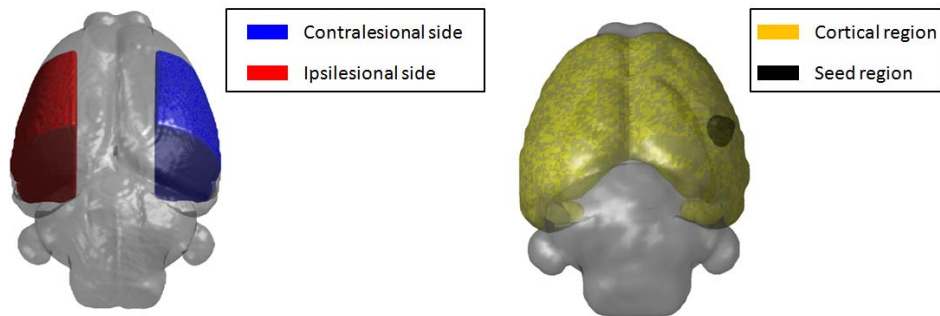


Figure 6.2 3D rendered plot of ischemic (red) and control (blue) side of hemispheres. Seed was located on outer right side of cortical area, as shown in figure in the right.

6.3 Results

In this section and subsection, the results from suture-induced and embolism-induced MCAO models are described.

6.3.1 Validation of methodology by normal and sham rats

Since the reconstruction was a three dimensional volumetric reconstruction, data analysis was only performed on one slice of the coronal-sectioned image which cut along the location at MCA territory shown in Figure 6.3a. Figure 6.3b shows the normalized temporal profiles of ΔHbO_2 for normal rats (data from pre-surgery baseline) from three regions of interest (ROIs): seed region, mirror region of seed, and central region. It clearly exhibits the similar pattern of low-frequency of fluctuation in ΔHbO_2 which can be observed on seed and in its mirror region whereas different patterns of low-frequency fluctuation are revealed in the central region.

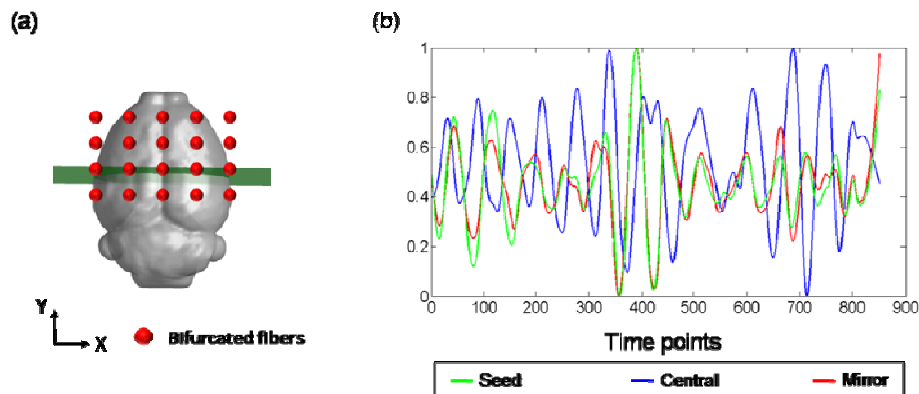


Figure 6.3 (a) Data analysis was performed on one slice of coronal-sectioned image which cut along the location at MCA territory. (b) Normalized temporal profiles from seed, mirror and central regions.

Figure 6.4a presents the coronal-sliced correction map sliced along the location shown in Figure 6.3a. The color scale on Figure 6.4a represents the correlation coefficient for each voxel. From Figure 6.4a, the high correlation values are shown on both outer sides of the hemisphere while low correlation values are shown in the central region. The same procedure of data analysis was done on sham-operated rats. Figure 6.4b shows the correlation map of a sham rat and a similar pattern can be observed in normal rats.

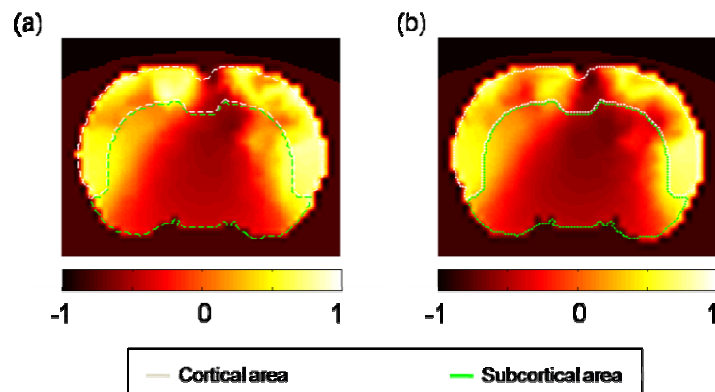


Figure 6.4 Resting-state functional connectivity correlation maps for (a) normal rats ($n = 12$) and (b) sham-operated rats ($n = 2$). Correlation maps showing here were averaged maps.

Moreover, to quantify the difference between seed and its mirror region, two ROIs were selected. ROI-1 was located on the ipsilesional (left) outer side of cortical area and ROI-2 was

selected on the contralesional (right) side of cortical area which contains the seed region, as shown in Figure 6.5.

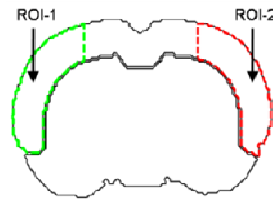


Figure 6.5 Two ROIs located on both outer side of brain

In order to stabilize the variance, the correlation coefficient r was transformed into z value by Fisher transformation [114], as:

$$z = \frac{1}{2} \log\left(\frac{1+r}{1-r}\right) \quad (6.1)$$

Correlation coefficient map (r map) was first transformed to z map and pixels within ROI-1 and ROI-2 and were then averaged individually. Notice that the ROI analysis was only performed on normal rats because there weren't enough sham-operated rats ($n = 2$) to perform experiment. Figure 6.6 shows the comparison between two ROIs and results, which show no statistically significant difference ($p > 0.05$) between the two ROIs as we expect to see bilateral functional connectivity on normal rats. Results from the normal rats and sham-operated rats demonstrate the feasibility of using the volumetric diffuse optical tomographic method to study resting-state functional connectivity for the rat brain.

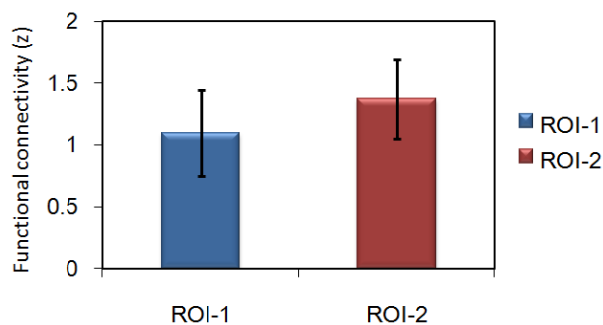


Figure 6.6 Comparison of functional connectivity between ROI-1 and ROI-2 for normal rats ($n=12$). Error bar represents the standard deviation of z .

6.3.2 Resting-state functional connectivity for suture-induced MCAO model

Figures 6.7a and 6.7b show the resting-state functional connectivity maps for $G-I_{\text{lesion}}$ (with lesion) and $G-I_{\text{no_lesion}}$ (without lesion) measured at 7 days after MCAO surgery. In $G-I_{\text{lesion}}$, Figure 6.7a clearly shows that the seed region has significant correlation with surrounding area. Unlike the correlation map of the normal rats (Figure 6.4a), functional connectivity between seed and its mirror region (ipsilesional side) was diminished at 7 days after MCAO.

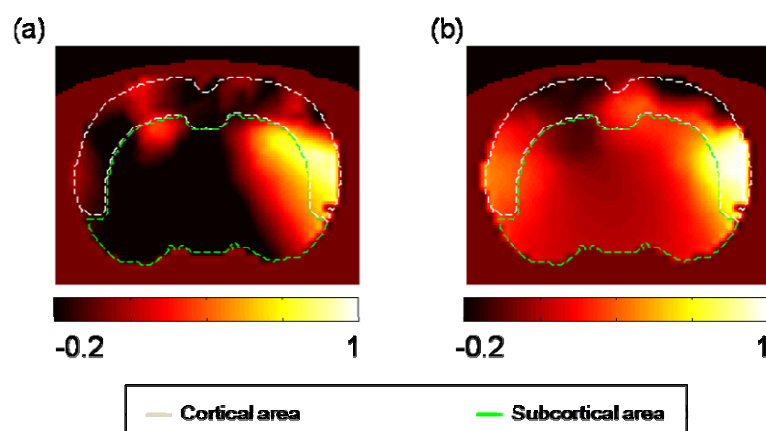


Figure 6.7 Resting-state functional connectivity correlation maps for (a) $G-I_{\text{lesion}}$ ($n = 10$) and (b) $G-I_{\text{no_lesion}}$ ($n = 7$). Correlation maps shown here were averaged maps. Notice that color shown here presents the correlation coefficient r and ranges between -0.2 and 1.

In $G-I_{\text{no_lesion}}$, high correlation can be observed around seed region. Correlation map still shows high intrahemispherical correlation around seed region at 7 days after MCAO. Unlike correlation map of $G-I_{\text{lesion}}$, the recovery of functional connectivity between contralesional and ipsilesional side of the brain 7 days after MCAO was observed. Moreover, the two ROIs shown in Figure 6.5 were compared. Figure 6.8 compares functional connectivity z between ROI-1 and ROI-2 for $G-I_{\text{lesion}}$ and $G-I_{\text{no_lesion}}$. The significance of differences between group means was determined using a Student's paired t -test. Functional connectivity for $G-I_{\text{no_lesion}}$ showed a relatively low z value in ROI-1 compared to that of ROI-2 but no statistical difference ($p > 0.05$) was found. In $G-I_{\text{lesion}}$, a statistically significant difference was observed between ROI-1 and ROI-2. The observation demonstrated the loss of functional connectivity due to lesion-induced disruption.

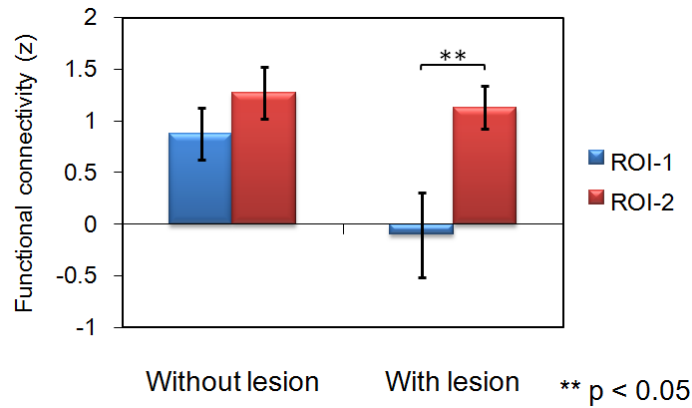


Figure 6.8 Comparison of functional connectivity between ROI-1 and ROI-2 for G-I_{lesion} (n = 10) and G-I_{no_lesion} (n = 7). Error bar represents the standard deviation of z.

6.3.3 Resting-state functional connectivity for embolism-induced MCAO model

Figures 6.9a and 6.9b demonstrates the functional connectivity correlation maps for G-II_{control} and G-II_{rtPA} after 1 day, 2 days, 3 days, and 7 days of embolism-induced MCAO. For G-II_{control}, rats only received saline after embolization, that is, clots stayed at MCA bifurcation and caused permanent occlusion for MCA territory. Lesions were found from the brain samples (not shown) via TTC staining and clots were observed at MCA observation at MCA bifurcation. Figure 6.9a shows the loss of functional connectivity between the contralesional and ipsilesional side of brain for all the measurements performed after 1 day, 2 days, 3 days and 7 days.

However, for G-II_{rtPA} in which rats were administrated the clot-busting drug rtPA, no lesions except for a small lesion (only found in one rat) were observed from brain samples. After 1 day of MCAO occlusion, the first plot Figure 6.9b shows low resting-state functional connectivity. From the second to fourth plots of Figure 6.9b, an increase of interhemispheric functional connectivity (represented by color and a correlation coefficient and value between -1 to 1) was observed on the ipsilesional side of brain.

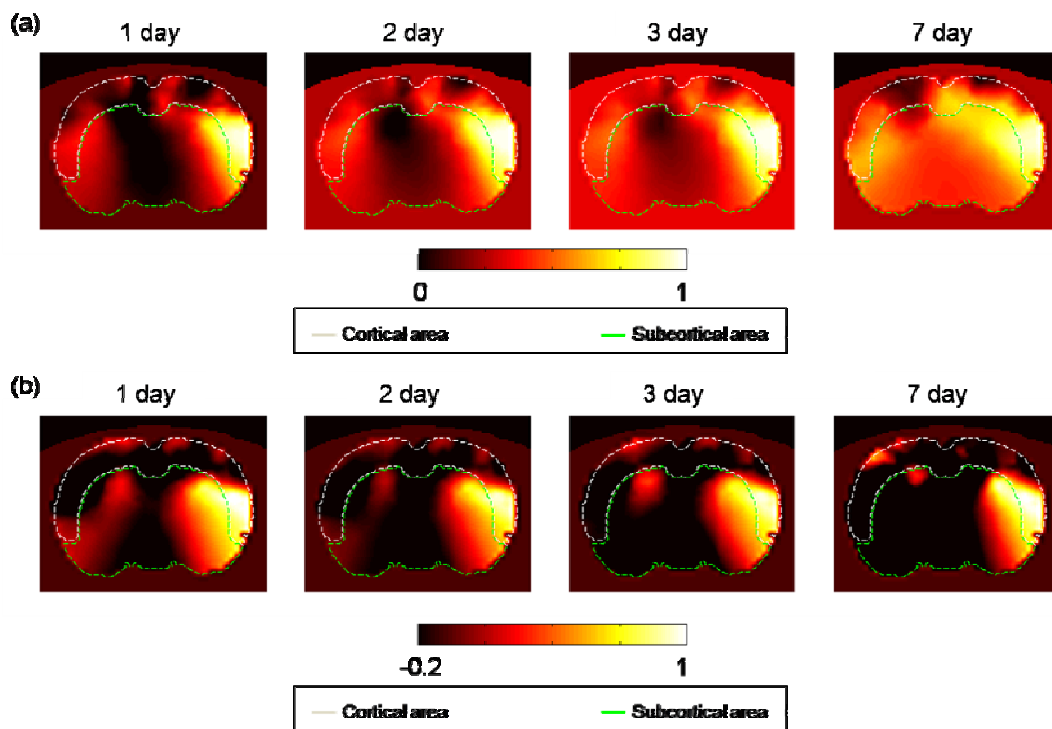


Figure 6.9 Resting-state functional connectivity correlation maps for (a) G-II_{rTPA} (n = 4) and (b) G-II_{control} (n = 7) obtained from different time point measurements. Correlation maps showing here were averaged maps. Notice that color shown here presents the correlation coefficient r . Figures in upper panel are scaled within range between 0 and 1 and -0.2 to 1 for bottom panel.

Quantitatively, Figure 6.10 shows the time tracer of functional connectivity (z) obtained from two ROIs for G-II_{control} and G-II_{rTPA} measured on different days. Similar contralesional intrahemisphere functional connectivity is shown in both G-II_{control} and G-II_{rTPA} and remains relatively unchanged during longitudinal measurements. For G-II_{control}, functional connectivity at ROI-1 dropped to -0.115 1 day after embolism-induced MCAO. A slightly decreased trend of functional connectivity was observed as functional connectivity decreased to -0.207 at 7 days after embolism-induced MCAO. The same decrease of functional connectivity was found 1 day after MCAO at ROI-1 for G-II_{rTPA}. However, a pattern of functional connectivity recovery was found thereafter up to 7 days after MCAO.

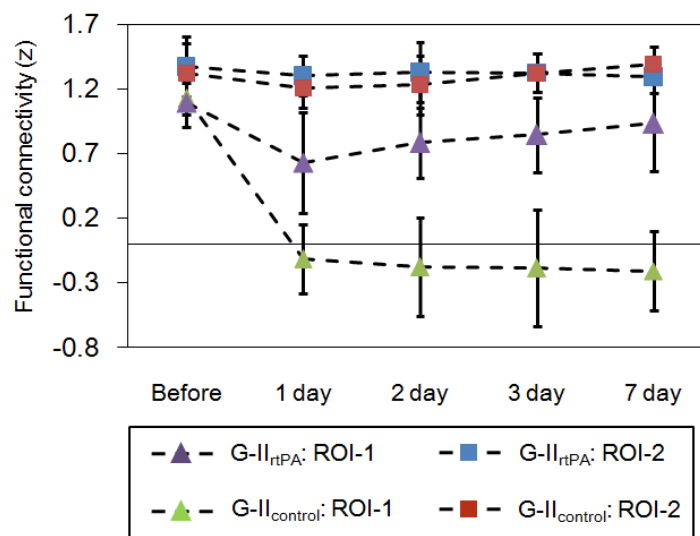


Figure 6.10 Time tracer of functional connectivity between ROI-1 and ROI-2 for G-II_{rtPA} (n = 4) and G-II_{control} (n = 3). Measurements were performed before MCAO surgery and also 1 day, 2 day, 3 day, and 5 day after MCAO. Each point represents the functional connectivity averaged for ROI. Error bar represents the standard deviation of z.

6.4 Discussion and conclusion

In this chapter, seed-based resting-state functional connectivity was used to investigate and study changes of bilateral functional connectivity after MCAO in rodent model. The spatial distributions of change of hemoglobin concentration were reconstructed by the methodology presented in Chapters 3 and 5. To study the rat's interhemispheric functional connectivity, seed was selected at the contralesional side of brain and the functional connectivity was obtained by using Pearson's correlation analysis. The spatial distributions of correlation coefficients were then generated by replacing the value of change of hemoglobin concentration for each voxel to correlation coefficient.

Utilization of fNIRS to study resting-state functional connectivity in human subjects has been presented with good reliability [124] and reproducibility [122]; however, validation for using fNIRS to study functional connectivity in rats was still needed at the beginning of this study. This study's end results from normal rats (measured from pre-surgery resting-state) and sham-

operated rats showed strong bilaterally symmetric functional connectivity in both temporal profiles as well as spatial maps. Similar findings have been presented in using functional magnetic resonance imaging (fMRI) [114], which proves the feasibility of using fNIRS to study resting-state connectivity in rat.

This study investigated the change of functional connectivity due to lesion-induced neuronal activity disruption. A similar study was presented using fMRI [121]. In the fMRI study, lesion was determined from T2-weighted MR images. A lesion region/mask was selected by the voxels in the ipsilesional hemisphere which has larger signal intensity compared to the mirror voxels in the contralesional hemisphere (usually >25% of intensity value). Since no anatomical structural images can be obtained by diffuse optical measurement, presence of lesion and its location could only be determined by TTC staining of brain samples removed from sacrificed rats.

Loss of bilateral functional connectivity for rats after MCAO has been clearly demonstrated, especially for rats where lesions were found in TTC staining brain samples. In suture-induced MCAO model, low bi-hemispherical functional connectivity was observed from spatial correlation map in lesion group while no statistical difference was found in terms of bilateral functional connectivity in the group without lesion.

For the embolism-induced MCAO model, which more closely mimics the human stroke, rtPA was administered. Treatment with rtPA has been well-documented in helping restore blood flow and oxygen to the brain affected by embolism-induced cerebral ischemia in both human [107] and animals [108-110]. Also, rtPA treatment of rats has been reported to reduce the lesion volume in brain [114]. From our experiment, no lesion or small lesion was found in brain samples removed from rtPA treatment group G-II_{rtPA} (not shown). Decrease of bilateral functional connectivity was observed for both control and treatment group at 1 day after MCAO although strong connectivity strength was shown in G-II_{rtPA} compared to that of G-II_{control}. Starting from 2 days after MCAO, increase of functional connectivity was visible in G-II_{rtPA} while

a decrease of connectivity strength was evident in $G-II_{\text{control}}$. Results suggest that changes of bilateral functional connectivity are highly relative to whether a lesion was formed.

Three different hemodynamic contrasts can be used to study the resting-state functional connectivity; they are ΔHbO_2 , ΔHbR , and ΔHbT , respectively. Figure 6.11 show the correlation map obtained by using (a) ΔHbO_2 , (b) ΔHbR and (c) ΔHbT . All figures in Figure 6.11 show a similar pattern of correlation coefficient distribution on the controllesional side (right) of brain. In terms of ipsilesional side (left), Figures 6.11a and 6.11c present a similar pattern of correlation coefficient distribution in using ΔHbO_2 and ΔHbT , and this finding has good agreement in Refs [49, 122]. Slightly strong connectivity strength is shown in Figure 6.11b, which may cause different quantification in ROI analysis but further investigations are needed. Additionally, using ΔHbO_2 as hemodynamic contrast to study the resting-state functional connectivity has been adopted in mice. Therefore, only ΔHbO_2 data as hemodynamic contrast was used in this work.

Resting-state functional connectivity measurements were based on the coherence of slow hemodynamic fluctuations, which indirectly represents synchronization of neuronal activities. Several factors, such as level of carbon dioxide (CO_2) and anesthesia levels [125], can influence the coherence of low-frequency hemodynamic fluctuations. Hemodynamic change not caused by resting-state low frequency spontaneous brain activity dramatically affected the results of seed-based correlation analysis in this study. Hence, to maintain the level of hemodynamic change, a small amount of pure O_2 (approximately 1ml/min) was administered during the measurement. Moreover, to preserve the temporal correlation of low frequency spontaneous hemodynamic fluctuations, we tried different levels of anesthesia. According to the results from our pre-run measurements on normal rats, rats were anesthetized with approximately 2% isoflurane. Although the level of anesthesia was higher than in a similar study involving fMRI, the weight range of rats used in this work was larger than that in van Meer et al. [121], which accounts for differences in level of anesthesia. [121] pointed out that coherence of bilateral low-frequency blood oxygenation level-dependent (BOLD) fluctuation diminished after

administering 2.9% isoflurane. Although the imaging modality for this dissertation's study was different, the selected anesthesia level was still in a reasonable range for studying bilateral resting-state functional connectivity.

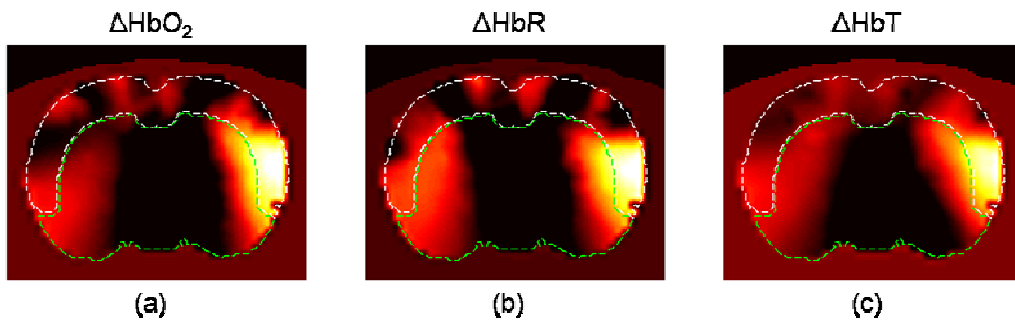


Figure 6.11 Resting-state functional connectivity correlation maps obtained by different hemodynamic contrast, which are (a) ΔHbO_2 , (b) ΔHbO_2 and (c) ΔHbT , respectively.

In conclusion, the feasibility of using diffuse optical measurement to study the loss of bilateral resting-state functional connectivity has been proven. The results show high temporal synchronization and a strong resting-state functional connectivity between hemispheres in normal and sham-operated rats. Spatial correlation maps presented loss of bilateral resting-state functional connectivity due to lesion-induced disruption. Overall, this chapter demonstrated the feasibility of using fNIRS-based resting-state functional connectivity to investigate tissue recovery after MCAO in suture-induced model. Also, the same methodology used herein can be extended to evaluate the treatment effect of thrombolysis for embolism-induced models.

CHAPTER 7
SUMMARY AND FUTURE WORK

7.1 Summary

This research focused on continuous-wave diffuse optical tomography to study focal cerebral ischemia in a pre-clinical rodent model. The objectives of the study were:

- i. To refine and validate the proposed image reconstruction algorithms with laboratory phantoms and animal measurements by using CCD-camera-based and fiber-based DOT system.
- ii. To investigate whether proposed algorithms can be used to study the widely-used rodent MCAO model.
- iii. To explore the difference and effect of therapeutic intervention after ischemic stroke.

To achieve the goals, three strategies were implemented:

1) State-of-the-art image reconstruction methods, DCA and GCM, were investigated via computer simulations and laboratory phantom experiments. DCA improved depth localization and resolution in three dimensional reconstructions which helped in visualization and relative quantification. GCM also improved the quality of reconstructed images and most importantly helped in absolute value quantification.

2) Construction and testing of CCD-camera-based DOT systems were used in laboratory phantom experiments. Both DCA and GCM were validated using a CCD-camera-based DOT system. In addition, a suture-induced rodent MCAO model was measured with the same system.

3) Measurement of Suture-induced and embolism MCAO rodent models was achieved by using a commercially available DOT system. A three-dimensional (3D) rat head model was

generated and DCA was applied in the 3D reconstruction of changes of hemoglobin during and after MCAO. Moreover, to study the changes of cerebral blood flow, an ICG-tacking technique was adopted. The effect of thrombolytic treatment in recovery of blood flow perfusion was also studied.

4) Study of changes in resting-state functional connectivity due to lesion-induced neuronal connection disruptions was facilitated by two MCAO models, which were measured by a CW-DOT system under resting state and longitudinal measurements for rats after MCAO.

The present study demonstrated that:

1. Computer simulation results show reconstruction with DCA improves depth localization and quality of reconstructed images. Results obtained from the MCAO measurements also demonstrated more accurate depth localization of changes of hemodynamic concentration, which helped quantify the hemodynamics in study the physiology of cerebral ischemia.

2. CCD-camera-based DOT system was built and validated with laboratory phantom experiments. After combining the image reconstruction with DCA application, convincing results became evident in the three dimensional reconstruction of embedded inclusions in tissue-like phantom showing good depth localization as well as depth resolution. Reconstruction using GCM also showed good localization and spatial resolution for embedded inclusions. Most importantly, it showed the good ability of the recovery of optical properties with acceptable error range through “black box” experiments. A suture-induced rat MCAO model was measured using developed CCD-camera-based DOT system. Results did not present the changes of optical density throughout MCAO intervention as I expected.

3. Two well-developed MCAO models were measured by commercially available fiber-based DOT system. In suture-induced MCAO model, results showed a decrease of ΔHbO_2 and ΔHbT during MCAO while increase of ΔHbR was observed. Reperfusion caused an increase of ΔHbO_2 and ΔHbT and a decrease of ΔHbR during the early period of reperfusion and then

remained relatively un-changed thereafter. Experiments in studying interference of ICG injection to hemodynamic changes showed that with small volume of ICG injection, only very early period hemodynamic changes were contaminated by ICG bolus traveling, showing the feasibility of a study focusing on changes of hemodynamic and cerebral blood flow with dual wavelengths measurement using interleaved time points analysis. Results from embolism-induced MCAO model measurements demonstrated a similar pattern of hemodynamic changes with suture-induced MCAO model (reperfusion followed by occlusion) while rats received rtPA thrombolytic treatment. Decrease of ΔHbO_2 and ΔHbT and increase of ΔHbR was revealed after embolization and remained relatively stable thereafter even after rats were administered saline.

4. Study changes of cerebral blood flow using ICG tracking showed a decrease of blood flow to approximately 14% in ischemic side compared to normal side of brain in suture-induced MCAO model and the blood flow rate dropped approximately 30-40% on normal side in embolism-induced MCAO model during occlusion. After reperfusion, blood flow on ischemic side recovered to about 79% on normal side for suture-induced MCAO model. Rats receiving thrombolytic treatment that presented the blood flow on ischemic side recovered to approximately 82% of normal side. Rats without any thrombolytic treatment showed no changes of cerebral blood flow after embolization.

5. Study of bilateral resting-state function connectivity using CW-DOT system showed a strong bilateral connectivity on normal and sham-operated rats. Loss of bilateral functional connectivity was observed after MCAO in rats in which lesions were shown from the TTC stained brain samples. For the rats receiving rtPA thrombolytic treatment, it showed a decrease of bilateral functional connectivity 1 day after MCAO operation, but recovered thereafter. Rats that only received saline treatment showed diminished bilateral functional connectivity due to lesion-induced neuronal connection disruptions from longitudinal measurements.

7.2 Future work

1. As mentioned in chapter 4, suture-induced rat MCAO model measured by CCD-

camera-based DOT system did not show the results we expected. However, several studies using CCD camera as a detector of DOT in animal studies have been presented [114], which proves that a CCD camera is a suitable detector for reducing the complexity of system setup. For future measurement, the CCD camera should have a larger dynamic range, e.g., 16 bits, to maximize achievable signal. As the dynamic range of a device is increased, the ability to quantitatively measure the dimmest or small changes of intensities in an image is improved.

Furthermore, the light source in this work was delivered by source fibers which were placed in direct contact with measurement tissue/medium. For achieving complete non-contact measurement, galvanometers can be utilized by using two orthogonal galvanometers (XY) for faster scanning of possible source positions.

2. In this study, the 3D rat head model was used for FEM forward calculation. Projection of optode location to the 3D rat head meshes is important in terms of localization. Because of the initial experimental design, the locations of the optodes on each rat head were not measured for co-registration with a rat head template atlas. Optode locations measured by a 3D digitizer were obtained from some of the rats. The co-registrations' optode locations were the averaged locations from the measured rats. However, the size and shape of a rat's head varies across different rats. Also, the exact locations of an optode for every measurement will also vary. For future studies, the projection of optodes location should be performed for each rat according to their own unique optode location to minimize location error.

3. The spatial resolution diffused optical image relays on the number of source-detector pairs/measurements. Although higher measurement density did not necessarily improve the spatial resolution significantly, it was still helpful in improving spatial resolution and image quality if denser optode geometry was used for measurement. As bifurcated fibers were used in this work, there is no necessity to study the arrangement of optodes. However, for other diffuse optical tomographic imaging systems with separate source and detector fibers, it is important to optimize the arrangement of source and detector fibers.

4. As described in chapter 5, distinguishing three compounds (HbO₂, HbR, and ICG) was a challenge due to distribution of the changes in optical density with dual wavelengths measurement. Future studies using multiple wavelengths (>2) will be considered to differentiate all the important chromophores (e.g., HbO₂, HbR, ICG, etc), thus providing simultaneous evaluation of cerebral hemodynamic and blood perfusion.

5. In the study of resting-state functional connectivity, hemodynamic signal in deeper brain tissues may be contaminated by the signal from tissue outside the brain area, which may have an unwanted effect in correlation analysis. Gregg et al. [126] presented the improvement of diffuse optical imaging by using superficial signal regression which eliminated the signal contaminated by superficial tissues. Also, in fMRI study, researchers also applied global mean signal regression and linear regression to enhance the detection of system-specific positive [127, 128]. For future study with denser optode geometry, similar superficial signal regression and global mean signal regression should be applied to improve the outcome of spatial correlation maps and quantification.

APPENDIX A
HUMAN HEAD ATLAS-GUIDE DOT

A.1 Modeling of standard human head template

In this study, the ICBM (International Consortium for Brain Mapping) 152 MNI (Montreal Neurological Institution) template was selected for our human head model as the ICBM152 template is the most common stereotaxic platform for tomographic functional brain mapping methods [112]. ICBM152 was obtained by averaging the scans of 152 normal subjects. Each MR scan was normalized to MNI space using nine parameter affine transformations. The ICBM152 MNI template is freely available at <http://www.bic.mni.mcgill.ca/ServicesAtlases/ICBM152NLin2009> with MNC or NTFI format. The ICBM 2009c Nonlinear Asymmetric template was selected to generate the head model. Files included T1-weighted, T2-weighted and *proton density-weighted* modalities. The resolution of the ICBM152 template is 229 x 193 x 193 with 1 mm x 1 mm x 1 mm voxel size. The T1-weighted sagittal, transverse, and coronal section of MR images are shown in Figure A.1.

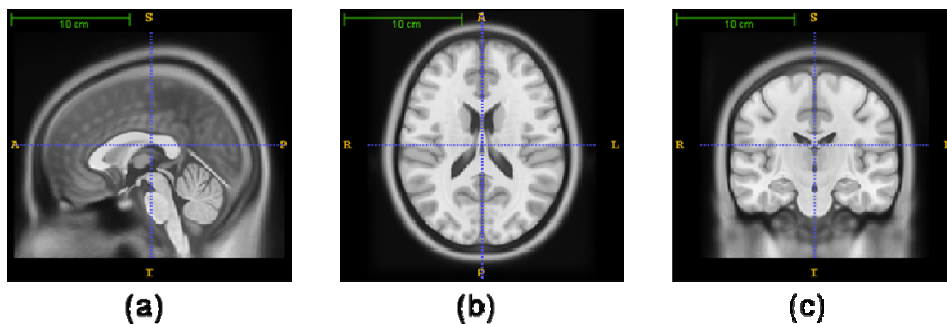


Figure A.1 T1-weighted MR images in (a) sagittal, (b) transverse, and (c) coronal view.

ICBM152 template was then converted to ANALYZED format using ITK-SNAP [43] which is also freely available (<http://www.itksnap.org/pmwiki/pmwiki.php>). Further image analysis was performed in MATLAB (2009a, The MathWorks, Inc., Natick, MA). In MR image sequence, four regions of interest (ROIs), which were scalp, skull, gray matter and white matter, respectively, were mainly identified and segmented. A binary mask of head was included in the ICBM template file so that the scalp boundary could be extracted. The other three boundaries were extracted from transverse MR sequence images, as shown in Figure A.2. Binary masks of skull,

gray matter and white matter were generated after boundaries of scalp, skull, gray and white matters were extracted from MR image sequence.

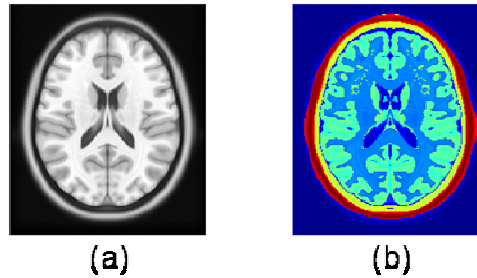


Figure A.2 T1 MR image and (a) Axial view of a T1-weighted MR image averaged over 152 normal subjects; (b) segmented layers and areas of the ICBM152 MNI template, corresponding to (a). Layer with red color shows scalp/muscle and yellow layer represents the skull. The light green areas represent gray matter and the light blue areas represent white matter.

After binary masks were obtained, the segmented two dimensional image sequences were then stacked together to generate three-dimensional volume models (see Figs. 5(a) to 5(d)). Three-dimensional finite element model (FEM) meshes (Figs. 5(e) to 5(h)) were then generated by MATLAB-based mesh generator iso2mesh, which can be found at <http://iso2mesh.sourceforge.net/cgi-bin/index.cgi>. This mesh model contained approximately 2×10^5 nodes, which corresponded to approximately 10^6 linear tetrahedral elements. Each node was labeled by one of three ROIs and the node locations were assigned the particular tissue optical properties. The optical properties were obtained from published literature [21] and listed in Table A.1.

Table A.1 Optical properties of head tissues for modeling

	Scalp		Skull		Gray Matter		White Matter	
	750nm	850nm	750nm	850nm	750nm	850nm	750nm	850nm
μ_a (mm ⁻¹)	0.017	0.019	0.012	0.014	0.018	0.019	0.017	0.021
μ_s' (mm ⁻¹)	0.740	0.640	0.940	0.840	0.836	0.673	1.191	1.011

The layer of cerebrospinal fluid (CSF), which is located between boundary of the inner skull and gray matter and also within some gray and white matter, was also extracted (not shown). The CSF layer was not considered in this study since the layer between the boundary

of the inner skull and gray matter is thin and CSF optical properties are relatively small in both absorption and scattering. Moreover, CSF within a deeper location of the brain did not affect the reconstruction results due to the penetration depth of light limitation.

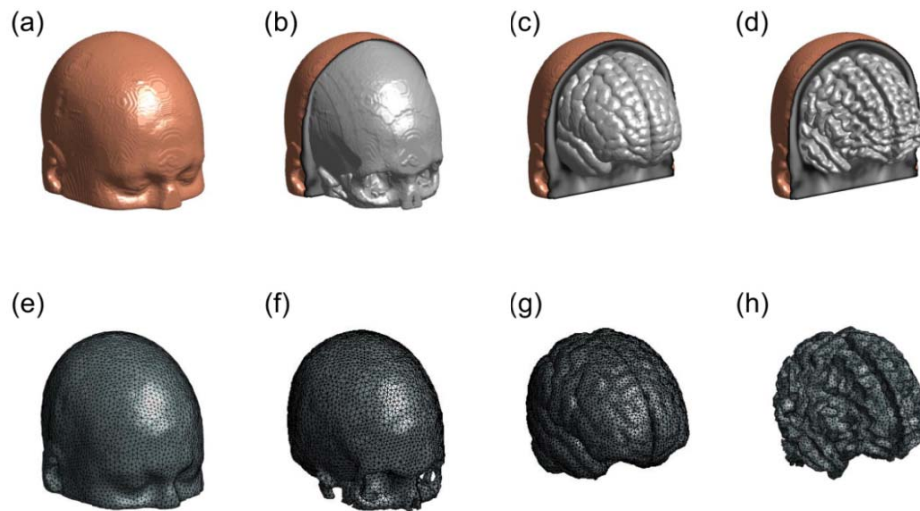


Figure A.3 Three dimensional rendered volume of ICBM152 template for four tissue types. Figures (a) to (e) depict (a) scalp, (b) skull, (c) gray matter, and (d) white matter. Figures (e) to (h) demonstrate the 3D FEM meshes of scalp, skull, gray matter and white matter, respectively.

A.1.1 Optodes arrangement

The sparse optode geometry was used in forward modeling. The optode array consisted of 12 sources and 18 detectors with a nearest inter-optode distance of 2.5 cm, as shown in Figure A.5. This geometry was used in our laboratory to measure brain activity functions. To simulate real measurement, only first nearest neighbor measurements were selected to calculate forward problem (Figure A.4). The full tomographic dataset contained a total of 40 source-detector pairs for one wavelength measurement.

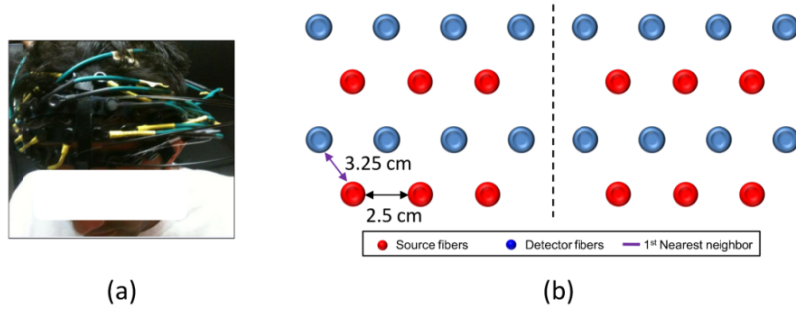


Figure A.4 (a) Photograph of optode arrangement. (b) Optode arrangement for forward modeling. First nearest neighbor was defined by source-detector separation of 3.25 cm.

For projection of optode locations measured from subject's head in real world (RW) coordinates to atlas template, an affine transformation was utilized [129, 130]. Briefly, optode positions on a subject's forehead were measured by the 3D Patriot™ digitizer (Polhemus Inc., Colchester, VT). Moreover, we selected several anatomical landmarks based on the EEG international 10-20 system of electrodes placement as anchors for co-registration. The landmarks were Nz (nasion), In (inion), AL (left ear), AR (right ear), and Cz (central position), which were also measured by a 3D digitizer. The MNI coordinates of 10-20 scalp position for ICBM152 were obtained from Cutini et al. [131]. Then the transformation matrix W was calculated. With the affine transformation matrix, the optode locations on the MNI head template can be obtained by:

$$P_{MNI_O} = P_{RW_O} \times W \quad (A.1)$$

where P_{RW_O} represents the coordinates of fNIRS optodes in the RW space; P_{MNI_O} represents the coordinates of fNIRS optodes in the MNI space; W is the transformation matrix. Coordinates of projected optode in z axis were then further adjusted by projecting the transformed optode locations in MNI space along the averaged norm of patches from the ICBM152 head model. The optode projected onto the surface of the head model is depicted in Figure A.5 (a and b). The region of interest (ROI) was determined as the volume covered by the optode array up to 40 mm in depth to minimize the complexity and computational expense, as shown in Figure A.5

c.

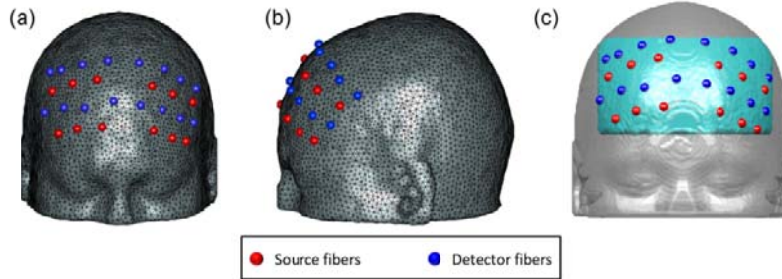


Figure A.5 Illustration of 3D FEM meshes co-registered with the fNIRS optodes used in our BART study in (a) frontal and (b) dorsal views. (c) The region of interest (ROI) was defined by the volume enclosed in the light blue region.

A.1.2 Forward light modeling, image reconstruction and DCA implementation

Forward light modeling in rat head model was performed using FEM based MATLAB package NIRFAST to obtain Jacobian/sensitivity matrix J . The forward problem for light propagation inside the head model using Rytov approximation [28] and can then be written as:

$$\Delta y = J_h \Delta x \quad (\text{A.2})$$

where Δy represents a matrix of measured changes in optical density at all source-detector pairs between initial baseline (y_0) and after a change of absorption due to brain response to tasks (y), i.e., $\Delta y = \log(y) - \log(y_0)$; J_h is the Jacobain matrix derived from the voxel-wise ICBM152 head model; and Δx represents a matrix of changes in absorption at each node within the 3D head coordinates system. DCA, which modified the sensitivity matrix J by counterbalancing the measurement sensitivity for deeper layer tissue, was then adopted. The implementation of DCA with image reconstruction is described in section 3.4.2 and spatial distribution of distance from ROI on scalp to node inside the head model is shown in Figure A.6.

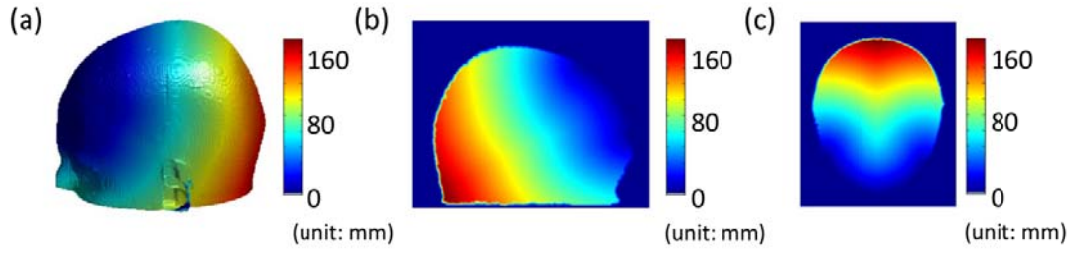


Figure A.6 (a) Three-dimensional view, (b) sagittal and (c) transverse view of spatial distribution of distance from ROI to nodes within head model.

Note that $\gamma = 1.4$ was used in this study. The adjusted sensitivity matrix $J_h^\#$ is defined as $J_h^\# = J_h M$ to be used in the inverse calculation. The image reconstruction equation with DCA applied can be expressed as:

$$\Delta x = J_h^{\#T} \left(J_h^\# J_h^{\#T} + \lambda S_{\max} I \right)^{-1} \Delta y \quad (\text{A.3})$$

where λ is the regularization factor and was chosen as 10^{-2} ; S_{\max} is the maximum of diagonal of the matrix $J_h J_h^T$ and I is the identity matrix.

A.1.3 Spatial distribution of total sensitivity

Figure A.7 demonstrates the spatial distribution of total measurement sensitivity for compensated (with DCA) and un-compensated (without DCA) sensitivity matrix. Figures shown here were normalized and scaled between minimum (0) and maximum (1) and were also smoothed by the $3 \times 3 \times 3$ Gaussian kernel. Figure A.7 (a and b) depict the sagittal and axial views of the spatial distribution of total measurement sensitivity. A slice was cut along the location shown on the left side of Figures A.7a and A.7b, which clearly shows that the region with higher measurement sensitivity (larger than 50% of maximum measurement sensitivity) is mainly located in the skull and CSF region. Furthermore, higher sensitivities are revealed close to the surface of scalp for uncompensated total measurement sensitivity. This distribution is not suitable to image the brain activation and may lead to large localization errors while recovering the activations that occurred on cortical regions.

On the other hand, when DCA was applied, the region of sensitivity extended downward throughout the cortical regions thereby accommodating higher sensitivity readings when measured. Moreover, Figure A.7 (c) shows a higher total sensitivity distribution for DCA-compensated sensitivity on the cortical surface while most low total sensitivity distribution (less than 50% of maximum measurement sensitivity) was observed in uncompensated (no DCA application) sensitivity. The results suggest that DCA could potentially benefit the cortical region's ability to recover activation with better localization and spatial resolution. It is noteworthy that Figure 8 exhibits a non-symmetric pattern of distribution of total sensitivity. Although it was assumed that the optode geometry for the right and left side of the brain was symmetric, Figure A.5 (a and b) clearly shows the positioning error and displacement due to variations of measurement by 3D digitizer. These results ran contrary to the expected results which anticipated a non-uniform and non-symmetric total sensitivity distribution pattern between hemispheres.

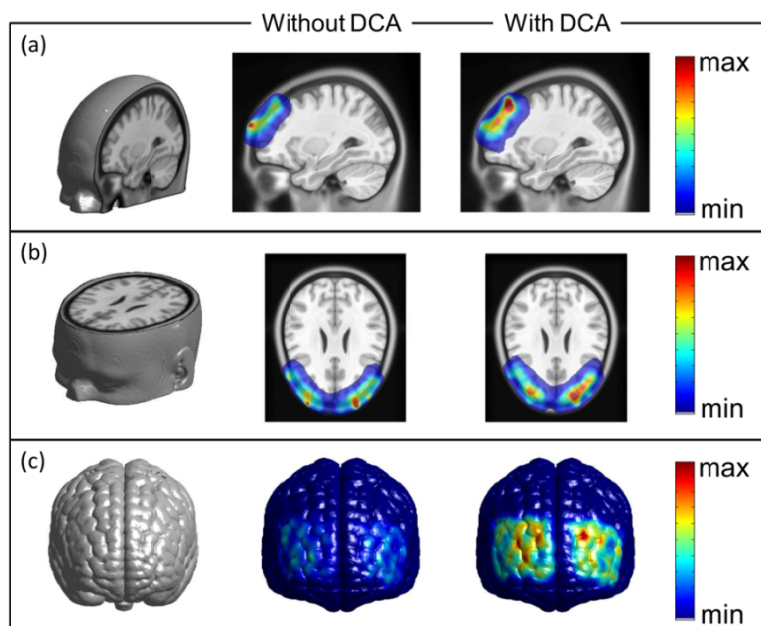


Figure A.7 Spatial distributions of compensated and uncompensated sensitivities are shown in (a) coronal view and (b) axial view, and also on (c) anterior view of cortical surface. Notice that color scale shown in figures reveals normalized to maximum values.

A.2 Computer simulation with ICBM152 head model

In order to evaluate image quality and improvement of depth localization, computer simulations were performed to simulate focal activation on brain. ICBM152 head model and probe geometry as shown in Figure A.7 were used in simulations. A small perturbation, located within left side of hemisphere with a 2:1 contrast in absorption compared with gray matter, was assigned to simulate the focal activation. Our computer simulation set up is shown in Figure A.8. We added 1% Gaussian random noise in simulations. Notice that the simulations presented here are limited to a single wavelength since the optical properties we selected were based on a wavelength at 750 nm. Furthermore, although the optode geometry used in this study assumed symmetry on both hemispheres (despite an optode location error due to a 3D digitizer measurement error), simulation was only performed on one side of hemisphere.

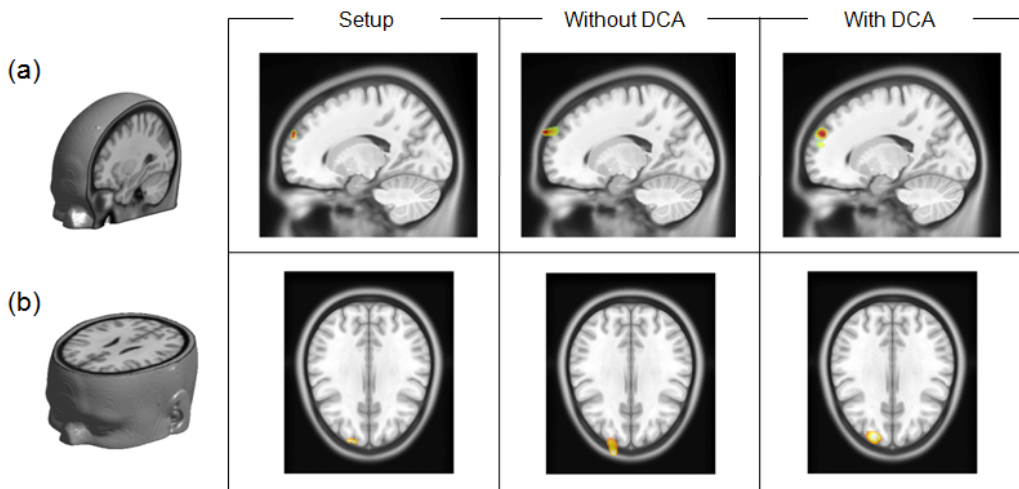


Figure A.8 Cross-section reconstructed images on rat brain's (a) sagittal and (b) transverse view. The reconstructed perturbation based on data from these images was defined as voxels with reconstructed value larger than 50% of the maximum value.

Figure A.8 shows the simulation results of cross-section reconstructed images on sagittal (Figure A.8a) and also gives a transverse view (Figure A.8b). Without applying DCA, the reconstructed perturbation was observed mostly in extracerebral region, as shown in the third

column of Figure A.8 (a and b). With DCA applied, the reconstructed perturbation was exhibited at relatively correct location (at area of gray matter, shown in fourth column of Figure A.8 (a and b) compared to the setup of simulation shown in the first column.

Moreover, a 3D rendering plot, as shown in Figure A9, was generated for observation. The reconstructed object/perturbation was defined as the voxel with the value larger than 50% of maximum value. Figure A.9a shows the location for actual perturbation, and objects for both reconstructions are essentially overlapped from the anterior view. However, a large difference can be observed in the lateral view (Figure A.9b) as the reconstructed perturbation resides outside the cerebral region (3D rendering with light gray color) without DCA application. With DCA application, the reconstruction shows relative correct localization. To quantify the error of localization, the location error was defined as:

$$location\ error = \sqrt{(x_{recon} - x_{actual})^2 + (y_{recon} - y_{actual})^2 + (z_{recon} - z_{actual})^2} \quad (A.4)$$

where the x_{recon} , y_{recon} , and z_{recon} are the centroid xyz coordinates of the reconstructed object and x_{actual} , y_{actual} , and z_{actual} are the centroid coordinates of simulated perturbation. The location error is reduced from 11 mm to 5.6 mm after DCA application, showing approximately 50% improvement of depth localization.

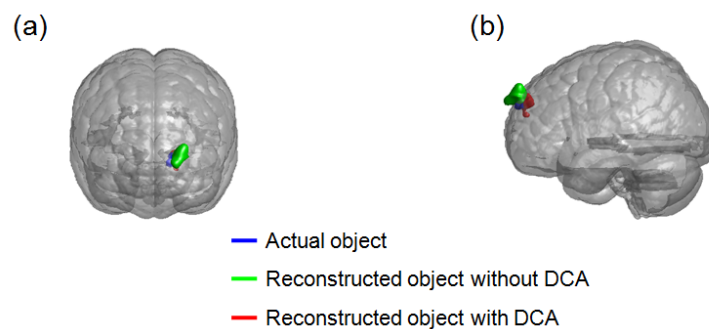


Figure A.9 (a) The anterior view and (b) lateral view of 3D reconstruction. The reconstructed objects were defined as the voxels with reconstructed value larger than 50% of the maximum value.

A.3 Approach of human brain activity measurement: risk decision-making study

In addition to computer simulation, to validate the proposed 3D reconstruction methodology combined with DCA application, we validated the atlas-guided DOT in real human brain activity measurement. The protocol we selected was the study of risk decision-making using Balloon Analogue Risk Task (BART) paradigm. The details of the whole protocol can be found in Cazzell et al. [132] and is briefly introduced in the following subsection. Also, we demonstrate the feasibility of combining the 3D-DOT and general linear model (GLM) based analysis, which is the conventional way to define the brain activation in the fMRI field as it pertains to fNIRS-derived functional brain imaging.

A.3.1 Participants and measurement protocol

A total of 40 healthy young adults (23 males and 17 females, from 25-44 years old) were recruited and measured. Subjects were asked to play the MATLAB-based BART paradigm which was modified from the BART paradigm used in fMRI study presented by Rao et al [133]. The protocol included two modes, which were active (voluntary) and passive (involuntary) modes. For both modes, the protocol started with a small balloon showed on monitor (Figure A.10a) with a balloon which was kept inflated during each iteration. Moreover, the game reward kept increasing when the number of iterations increased. There were two outcomes in the BART paradigm:

- (1) Win: The balloon stopped inflating and the sentence, "You win!!" was showed on monitor (Figure A.10b). Subject gained all the reward from the game in the win case.
- (2) Lose: The image of an exploded balloon was showed (Figure A.10c), followed by the sentence, "You lose!!" showed on the monitor. Subject lost all of the reward in this case.



Figure A.10 (a) Beginning of BART paradigm. The outcomes of BART task is shown in both modes in (a) the win case and (b) the lose case.

In the active mode, subject can decide whether he/she would like to keep playing BART task or not while computer automatically played the game for subjects when the start button was clicked in passive mode. Each BART paradigm included 15 repeated balloon tasks (Figure A.11), in either active or passive mode. Each subject was measured with the fNIRS brain imager in three temporal phases: (1) at the resting state for 5 min as baseline, (2) during ~5-sec BART performance, and (3) with 15-sec post-stimulation recovery. The last two phases were grouped as one block and repeated 15 times (Figure A.11).

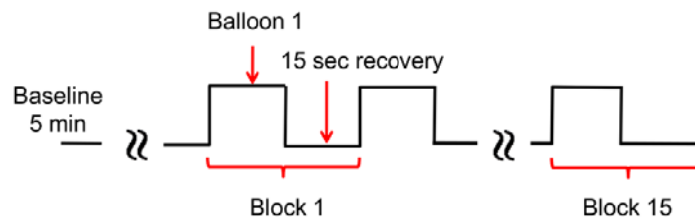


Figure A.11 Schematic diagram depicting 15 task blocks. Each block includes an activation period (5 s) and a 15-second recovery time.

A.3.2 fNIRS Data Acquisition and Data Pre-processing

The fNIRS data was measured using a commercially available multi-channel fNIRS brain imager NeuroDot (Cephalogics®). The brain imager used light-emitting (LED) sources at 750 nm and 850 nm. The source-detector arrangement was the same as described in 3.4.1.2 (Figure 3.6b). Sampling frequency for fNIRS data acquisition was 10.8 Hz. fNIRS data recorded by NeuroDot were pre-processed for each source-detector pair measurement. Bandpass filter, with pass band frequencies between 0.03 and 0.2 Hz, was applied to remove high frequency

instrument noise and low frequency baseline drift. The blocked average was over 15 blocks and was adopted to improve the signal-to-noise ratio (SNR).

For three dimensional image reconstructions, the perturbation approach was applied. The perturbation, which can be denoted as Δx and represents change of absorption, was generated when subject performed the BART task. The reconstructed $\Delta\mu_a$ for both measurement wavelengths can be obtained by Equation A.3. Consequently, determination of absorption changes at two wavelengths leads to reconstructed images of relative changes in HbO₂ (ΔHbO_2), HbR (ΔHbR), and HbT (ΔHbT) concentrations, which are based on spectral decomposition of the extinction coefficients for both wavelengths, as:

$$\begin{bmatrix} \Delta HbO_2 \\ \Delta HbR \end{bmatrix} = \begin{bmatrix} \epsilon_{HbO_2}^{750} & \epsilon_{HbR}^{750} \\ \epsilon_{HbO_2}^{850} & \epsilon_{HbR}^{850} \end{bmatrix}^{-1} \begin{bmatrix} \Delta\mu_a^{750} \\ \Delta\mu_a^{850} \end{bmatrix} \quad (A.5)$$

As described in the previous section, each subject was asked to perform 15 repeated balloon tasks. Filtered channel-wise fNIRS data was averaged by 15 blocks to enhance the signal-to-noise ratio and the averaged block time was about 20 sec.

A.3.3 Data analysis

Regarding the conventional diffuse optical image analysis, the classical way of defining the brain activation during the tasks uses the following steps: (1) defining the maximum activation period in a time series of fNIRS images; (2) using FWHM (full width of half maximum) to determine the region of brain activation; (3) comparing the HbO₂ values within the defined activation area between two states (e.g. “rest” versus “task”) with a paired t-test to determine if the changes between the two states are statistically significant. However, the major limitation of this method is that the maximum activation or post-activation period needs to be subjectively defined and could be highly affected by post-stimulation signals and noise. To overcome this limitation, several groups in the fNIRS field have followed an analysis method commonly utilized by fMRI researchers, namely, the general linear model (GLM) based analysis. The GLM-based method examines whether or not the experimental fNIRS data and a designed linear model are

matched over the experiment's entire time course. This approach rests on a physiology-based principle or model wherein hemodynamic signals are measured in response to brain stimulation resulting from a convoluted effect between the stimulation task and hemodynamic response function (HRF), where the latter two functions are already given. Thus, there is no need to subjectively select the activation and/or post-activation period in order to determine the activation regions in the brain.

The basic principle of GLM can be expressed as:

$$Y = X \times \beta + \varepsilon \quad (\text{A.6})$$

where Y is the data matrix which contains the observed signal at various time points at a single voxel; X is the designed hemodynamic response matrix with components explaining the observed data/signal; β is a parameter defining the contribution of the designed response matrix to the observed data; ε is the error matrix containing the difference between the observed data Y and predicted data by the model of $X \times \beta$. In the fNIRS study, the observed data/signals could be the changes of hemodynamic parameters, including ΔHbO_2 , ΔHbR , and ΔHbT . Only ΔHbO_2 was utilized as the observed data for further data analysis in this study since the magnitudes of ΔHbR were much smaller than those of ΔHbO_2 .

In general, a designed hemodynamic response matrix consists of a model (i.e., regressor) which is associated with brain activation in response to tasks or stimulations given. The design of the regressor is usually based upon experimental protocol including the timing and duration of the neuronal activity. According to this study's experimental protocol, the BART paradigm included approximately a 5-sec baseline, as shown in Figure A.12a (highlighted in blue color), a 5-sec performance or stimulation period, also seen in Figure A.12a (highlighted in red color), followed by a 5-sec response time after the outcome was seen (Figure A.12a, highlighted in green color), while the recovery time was 15 sec. In this study, we targeted on the brain response after participants observed the outcomes; thus, the event-related stimulation for

BART was designed to focus on the short period of time, using a boxcar of 1 sec, as illustrated by the dashed line in Figure A.12a. The regressor then included the convoluted effect between the stimulation function and hemodynamic response function (HRF) to represent hemodynamic response in the brain.

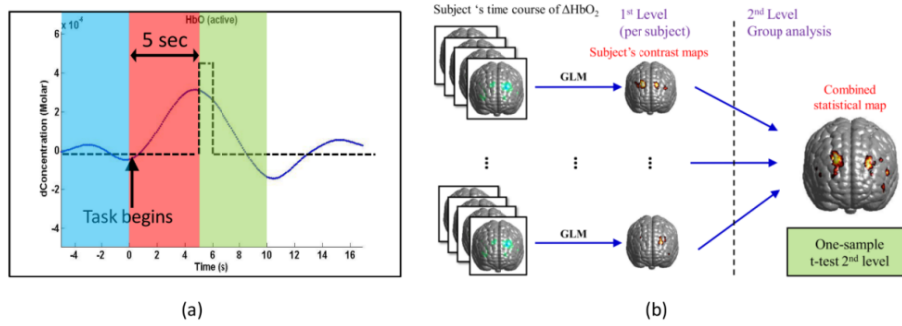


Figure A.12 (a) A time course of block-averaged ΔHbO_2 profile in response to BART. The time course contains a 5-sec baseline, a 5-sec BART performance, followed by a 15-sec recovery time. Boxcar marked with dashed line represents the event-related stimulation associated with outcomes. (b) Schematic diagram of a two-stage random-effects analysis.

After the regressor was constructed, the time course of ΔHbO_2 at each voxel within the human head template was fitted to Equation A6 using least squares estimation. Note that the human head template was reconstructed using atlas-guided DOT image reconstruction. Parameter β can be calculated by:

$$\beta = (X^T X)^{-1} X^T Y \quad (\text{A.7})$$

The t-statistics can then be calculated by:

$$t = c' \beta / \sqrt{\text{Var}(\varepsilon) c' (X' X)^{-1} c} \quad (\text{A.8})$$

where c represents the contrast vector and the denominator in Equation A.8 represents the standard error of $c' \beta$. This reconstruction process was performed voxel by voxel in order to identify the specific cortical regions which were activated by BART. Since this study involved multiple participants, inter-subject variation did exist. Thus, we further performed the random-effects analysis, which is a commonly used method in fMRI studies.

In principle, random-effects analysis contains two stages of analysis operation: single-subject analysis and group-level analysis, respectively, as demonstrated in Figure A.12b. In this study, for the first-level (i.e., single-subject) analysis, we generated a contrast map of β -values or t-statistics on the voxel-wise atlas template for each subject. For the second level (i.e., group-level) analysis, the one sample t-test was performed voxel by voxel over all the participants. The outcome of this group-level random-effects analysis gave rise to a combined statistically meaningful brain activation map in response to BART stimulation.

A.3.4 Results

In this section and affiliated subsection, the results of brain activation regions derived by voxel-wise GLM analysis for both active and passive modes are described.

A.3.4.1 Active versus Passive Mode in BART Paradigm

Figures A.13a and A.13b show the activation images generated at the group-level when performing the active and passive BART modes. To compare the results with those reported in an fMRI study [133] and fNIRS study [132], subjects were not divided by genders, that is, a total of 37 subjects were grouped and only outcomes of two modes were considered as the factor. Axial and coronal view of activation maps were sliced along the locations depicted on Figure A.13c. Two cross-sections were crossed near the dorsal lateral prefrontal cortex (DLPFC) where the activations related to BART were mostly revealed based on observations by Cazzell et al. [132].

To obtain the brain activation images, changes of HbO_2 concentrations in response to two modes were reconstructed by atlas-guided 3D-DOT. Group level of brain activation images (t-maps) were generated by random-effects analysis; a threshold of false discovery rate (FDR) corrected $p < 0.01$ was used to identify brain activation areas associated with the balloon task. No cluster size threshold was utilized in our study. For subjects who performed the active mode of BART paradigm, brain activations on both left and right hemispheres were exhibited on both DLPFC or Brodmann area (BA) 9 and 46 (see in Figure A.13a). In addition, in the axial and coronal slice views, activations mostly revealed within the cerebral region where brain activation

such as that associated with the balloon task should take place. Spatial results indicated that atlas guided 3D-DOT with DCA localized the brain activates reasonably. On the other hand, no brain activations were shown, as illustrated in bottom row of Figure A.13b, when subjects performed within the passive mode of BART. Also, no activations were observed in volumetric slice, including axial and coronal views.

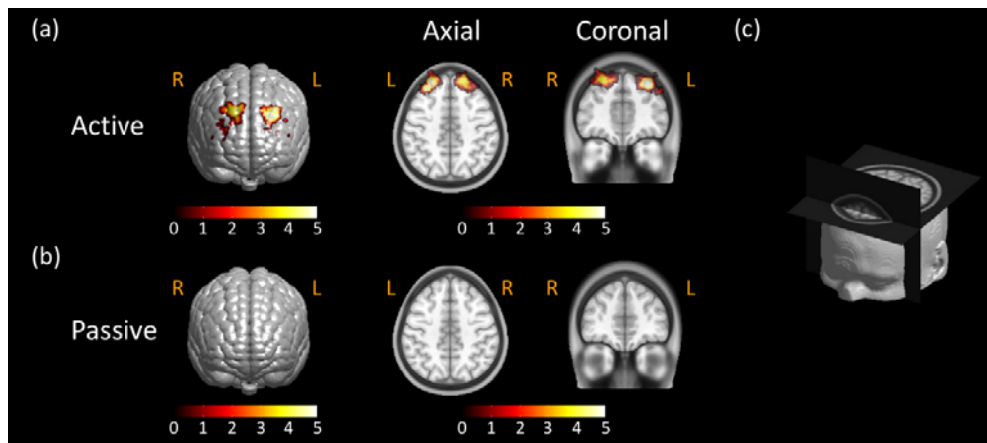


Figure A.13 Brain activation maps from subjects performing (a) active BART task and (b) passive BART task. Threshold was set as $p < 0.01$ (FDR corrected). Axial and coronal views of brain activations were sliced along the location shown in (c). Color scale in figures represented the t value. Notice that “R” represents right and “L” represents left side of the brain.

A.3.4.2 Gender Difference in Active Model

In order to further confirm our developed methodology, we also compared the differences of brain activation associated with risk-related decision making between male and female participants in the active mode. We targeted the active mode comparisons since there was no brain activation in the passive mode as shown in Fig. 9b. Voxel-wise GLM was performed after time-resolved volumetric ΔHbO_2 images for gender groups (male: $N = 21$; female: $N = 16$) were reconstructed. Regressors for GLM analysis were generated associated with the two different outcomes, which are “win” case and “lose” case, respectively. Random-effects analysis was then performed to identify the brain activations for different genders in group level; the activation threshold was set to be FDR corrected $p < 0.01$.

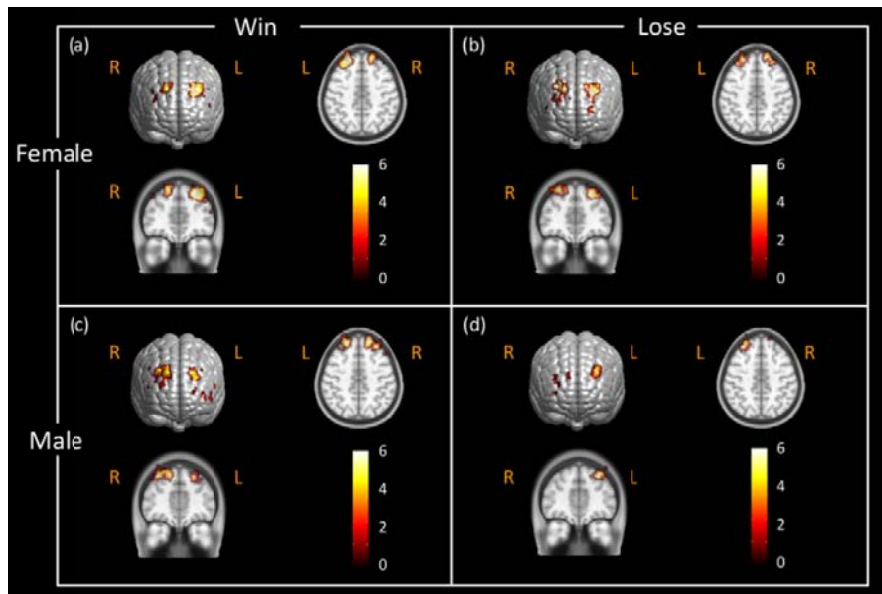


Figure A.14. Brain activation maps in response to active BART mode from (a) female group (N = 21) in the “win” case, (b) female group in the “lose” case, (c) male group (N = 16) in the “win” case, and (d) male group in the “lose” case. These activation maps had the statistical threshold of FDR corrected $p < 0.01$. Axial and coronal views of brain activations were sliced along the location shown in Fig. 9c. Color scale in figures represented the t value. Notice that “R” represents right and “L” represents left side of the brain.

In the “win” case, we observed strong bilateral brain activations on or near DLPFC in both male and female subjects (Figures A.14a and A.14c). In the “lose” case, bilateral brain activations on DLPFC are exhibited clearly in female participants (Figure A.14b), while male subjects displayed more unilateral brain activation on the left DLPFC (Figure A.14d). In contrast, very little brain activation was exhibited on the right DLPFC by “lose” outcome in male subjects (Figure A.14d). Moreover, it is noteworthy that the reasonable locations of brain activations were observed for four different cases in axial and coronal views, further proving the feasibility of visualizing brain activity in full 3D space.

A.3.5 Discussion

In this section, we presented the atlas-guided DOT combined with DCA to obtain the hemodynamic changes images which were associated with brain activations in 3D with improved 3D visualization and localization. Moreover, we combined 3D atlas-guided DOT with

GLM-based analysis to generate volumetric brain activation images under BART paradigms. 3D atlas-guided DOT techniques recently have been established by several research groups in the fNIRS field. Studies including computational simulations [36, 37] and in-vivo human data [134, 135] have demonstrated great improvements in resolution as well as quantification. In addition, a quantitative spatial comparison study between DOT and fMRI showed good correlation and match [21], indicating great capability of 3D-DOT in studying cortical brain activity.

The major issue of 3D-DOT technique is poor depth localization due to the exponential attenuation of measurement sensitivity with increase of penetration depth. While increasing the source-detector pair separations (i.e., increase maximizes separations of source-detector measurements) has been reported to enhance depth sensitivity [136], mathematical models have also been proposed to increase sensitivity in deep layer/tissue to benefit the image quality of DOT. Boas et al. [36] proposed the cortical (or brain) constraint method where voxels located outside the brain region were forced to have sensitivity of zero. This method implied that changes of absorptions only occurred within brain region including gray and white matter. The spatially variant regularization (SVR) technique, which spatially regularized the higher sensitivities near superficial layers and provided more homogenous spatial sensitivity distribution, has been utilized for human [134-136] as well as rat DOT studies [54]. Moreover, Zhan et al. [37] demonstrated the improvement of image quality when whole-brain spatial constraint and SVR were utilized simultaneously based on computational simulations. Our developed depth compensation algorithm utilizing DCA application, based on the mathematical compensation of the fast decay of sensitivity in deeper layers, was adopted in this study. Each method may have a different outcome and its own advantage; however, the comparison of different methods to improve the depth localization is not the scope of this study. We presented the improvement of spatially sensitivity distribution for deeper tissue in section A.1.3. and Figure A.7. Specifically, to demonstrate the improvement of depth localization when DCA was applied, we investigated the spatial distribution of activation voxels which were derived from voxel-wise

GLM analysis across all participants. Only active mode was analyzed since no activation was observed in passive mode, as described in Active versus Passive Mode in BART Paradigm section. For each subject, the brain activation voxels were defined by GLM analysis after which the activation image was then binarized, i.e.,

$$V_i = \begin{cases} 1 & \text{where voxel } i \text{ was activated} \\ 0 & \text{otherwise} \end{cases} \quad (\text{A.9})$$

where V_i represents the voxel after GLM analysis in 3-D domain. The binarized activation image for each subject was generated and all activation images were then added up, as shown in Figure A.15. Note that the color scale in Figure A.15 represented the times of overlapping for each voxel.

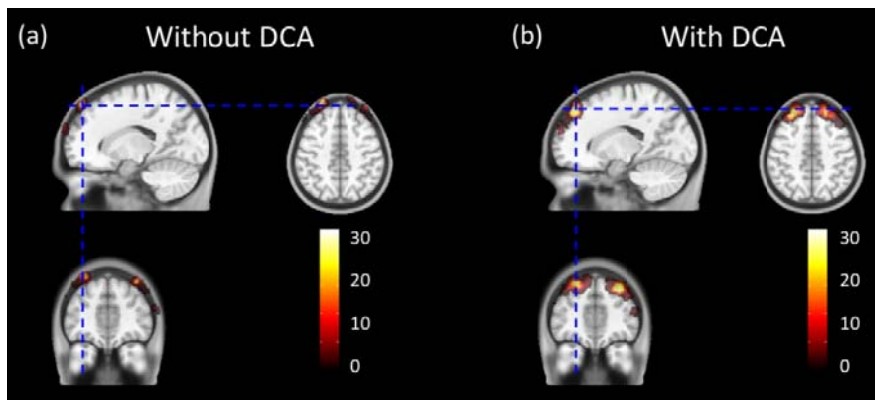


Figure A.15 Axial, coronal and sagittal views of brain activations across all participants using (a) uncompensated (without DCA) and (b) compensated (with DCA) methods during 3D-DOT reconstruction. Color shown in figure represents the times of overlapping.

Figure A.15a clearly shows that brain activations for all subjects were mostly located in the extracerebral region, from axial, sagittal and coronal view when DCA was not utilized during 3D-DOT reconstruction. No obvious activations located within the cerebral region were observed in any of the participants. These results projected wrong anatomical locations as the activation should happen within the cortical area while the subject performed BART. However, Figure A.15b clearly showed improvement of depth localization in most activations exhibited within brain region for all participants when DCA was applied for 3D-DOT reconstruction. These

improvements resulted the better visualization of 3D space and also potentially will lead to more accurate quantification in ROI analysis based on anatomical location selection.

Quantitatively, we performed the spatial voxel-wise comparisons between DCA and no-DCA GLM-derived activation images. The percentage of voxels, which represented brain activation was calculated and listed in Table A.2.

Table A.2 Activation overlapping ratio between brain and non-brain region

	Total activation voxels	Cerebral region	Extracerebral region
Without DCA	14668	495 (3.4%)	14173 (96.6%)
With DCA	22697	20701 (91.2%)	1996 (8.8%)

From Table A.2, we observed only 3.4% of total activated voxels were located within the cerebral region while 96.6% of total activated voxels were in the extracerebral region for the conventional 3D-DOT reconstruction (without DCA adoption). Dramatic improvement (from 3.4% to 91.2%) can be found when reconstruction with DCA application. It is noteworthy that approximate 9% (8.8%) of activated voxels were outside the brain region even DCA was applied during 3D-DOT reconstruction. The possible explanation is due to the selection of adjusted power factor γ since γ controlled the compensation power and the spatial distribution of sensitivity altered with changing of r . We expect the results to improve further if optimization of γ selection is employed.

Comparison with Previous Studies

We have used voxel-wise GLM analysis for fNIRS to study BART paradigm in this study. As previously stated, we modified the BART paradigm from Rao et al. [133] using in fMRI research. Our BART protocol closely followed Rao et al.'s design although we designed it with a slight difference in the passive mode. In Rao et al.'s design, participants merely pressed the button to keep the balloon inflated during the protocol while the computer decided the end points and outcomes including win or lose. In our BART paradigm, participants only pressed the button once at the beginning of each block and then observed the computer playing BART. The

balloon was automatically inflated until the computer stopped the task in a win case or the balloon exploded in a lose case. In terms of data analysis, we used the GLM analysis to determine brain activation which is similar to Rao et al.'s study; however, Rao et al. utilized the BOLD signal as contrast while we targeted on hemodynamic changes, especially ΔHbO_2 . Moreover, due to the limited interrogation depth for fNIRS, our study only focused on the hemodynamic changes in BA 9, 10 and 46 while fMRI was able to investigate the whole brain. Despite these differences, our results show strong bilateral activations on DLPFC in the active mode regardless of the gender of participants while no activation was observed on DLPFC in passive mode. These results are highly consistent with those of Rao et al. It is noteworthy that there were two major stimulations for BART, which were balloon inflation (action of playing BART) and outcomes as passively seen by participants. However, our study focused on the brain response while participants observed the outcomes by applying only one regressor in GLM analysis as described in the general linear model section. By adding one more regressor representing the action of playing BART, we were able to further validate our outcome.

A closer comparison was made between our study and Cazzell et al. [132] in fNIRS research. Cazzell et al. recently compared gender differences in brain activation maps and hemodynamic responses in HbO_2 when subjects responded to BART. Although brain activation maps in their study were determined by FWHM (full width half maximum) of HbO_2 spatial patterns, the study concluded strong bilateral brain activations on DLPFC in active mode which is consistent with our results as shown in Figure A.13a. In passive mode, we observed no activation on DLPFC in our results whereas slight brain activations were exhibited on DLPFC in Cazzell et al. although they were relatively weaker compared to those in active mode. For the comparison of different outcomes between genders, the study reported by Cazzell et al. concluded strong bilateral brain activations on DLPFC in both "win" and "lose" cases for female subjects and in win "case" for male. This conclusion is relatively consistent with our findings given here, as seen in Figures A.14a and A.14b. For male subjects, Cazzell et al.

demonstrated strong bilateral changes on DLPFC in the “win” case with a strong decrease (or deactivation) in ΔHbO_2 on the left DLPFC. However, the brain activation/deactivation maps obtained in the “lose” case for male subjects exhibited somewhat different patterns or distributions between the results of Cazzell et al. and the results reported in this dissertation, wherein FWHM-derived results revealed more diffuse deactivation patterns which were distributed closer to DLPFC (BA 46) bilaterally, while GLM-derived results exhibited more unilateral activation on the left frontal region, located near both BA 9 and 46 (see Figure A.14d).

The agreement and disagreement between the brain activation maps derived by two types of data analysis methods need to be understood in order to select a more accurate approach for improved DOT for brain imaging. The disagreement could result from the following factors: (1) Image reconstruction process in this study is based on human brain atlas-guided 3D DOT after depth-compensation and voxel-wise GLM analysis were performed, while the earlier study by Cazzell et al. utilized non-atlas-guided, 2D-DOT with no depth compensation or statistical parametric analysis. In Cazzell et al.’s study, 2D-DOT FWHM-based thresholded images were approximately projected onto the anatomical human brain template according to the approach given by Homan et al. [137]. Distinct differences of distribution of activation patterns exists because of different reconstruction algorithms, co-registration methods, and studies of an anatomical brain template used between two studies. (2) Due to the difference in image processing algorithms, the two methods rest on two hidden hypotheses: 1) the current method given in this paper utilizes the conventional GLM model commonly used in fMRI, assuming that voxel-wise HbO_2 signals can be modeled well by convolving the stimulation function with the hemodynamic response function (HRF), and 2) the FWHM-based image processing method by Cazzell et al. to determine the activation maps relied on the level of reconstructed maximum activation which made it subject to error due to the fact that any activation pattern can be highly affected by the level of maximum activation.

In order to perform a more comparative analysis, we re-analyzed data by using 3D-DOT reconstruction and then defined the activation by FWHM-based thresholding. The reconstructed ΔHbO_2 images were averaged from the time period of 5-sec of post decision-making.

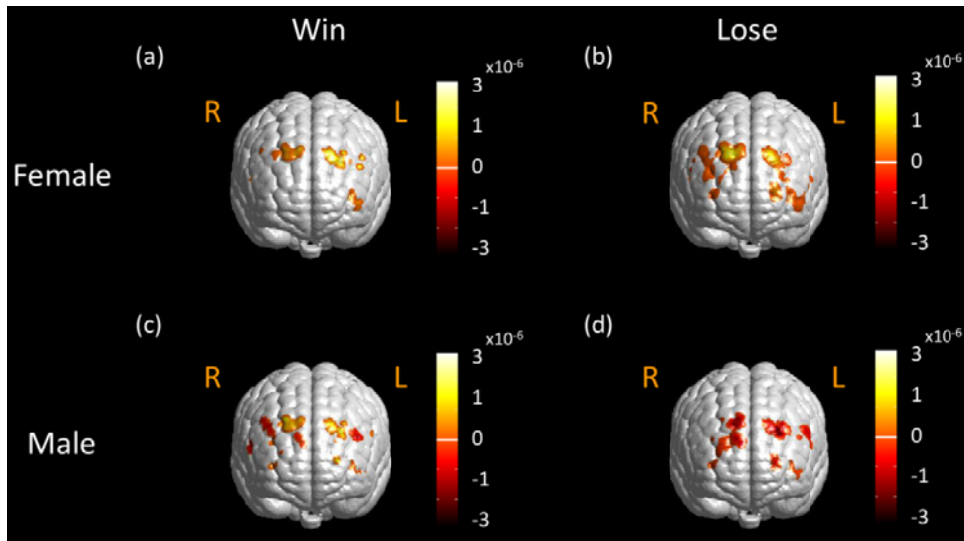


Figure A.16 Brain activation maps in response to active BART mode from (a) female group (N = 21) in the “win” case, (b) female group in the “lose” case, (c) male group (N = 16) in the “win” case, and (d) male group in the “lose” case. These activation maps were defined by FWHM. Axial and coronal views of brain activations were sliced along the location shown in Fig. 9c. Color scale in figures was the μM . Notice that “R” represents right and “L” represents left side of the brain.

Figure A.16 shows the FWHM-derived activation images for a female and male in “win” and “lose” cases. Activation images were averaged across female and male participants. In female and male “win” cases, compared to GLM-derived activation images (Figures A.14a and A.14c), we observed similar bilateral activation patterns on DLPFC (near both BA 9 and 46, see Figures A.16a and A.16c). In female “lose” case, strong bilateral brain activations also revealed near BA 9 and 46 bilaterally but more activations was exhibited near BA 10 while results by GLM-derived method revealed more localized activation pattern, as shown in Figure A.14b. Moreover, in male “lose” case, we observed strongest activation on left DLPFC from

FWHM-derived activation images (see Figure A.16d) whereas GLM-derived activation images also showed strong activation on left DLPFC. Similar observation was shown in Fig. 8a from Cazzell et al. [132]. Diffuse patterns of activation were also exhibited on FWHM-derived activation image (see Figure A.16d) while more localized activation was shown in GLM-derived activation images. Based on the comparative study, we demonstrated that our newly developed, brain-atlas guided, GLM-based 3D-DOT reconstruction algorithm should lead to more accurate brain activation maps with a better spatial resolution and stronger statistical power compared to the FWHM-derived method.

Atlas-guided DOT in brain research

In this study, we utilized the head atlas to anatomically guide the 3D-DOT reconstruction. Anatomically-guided DOT reconstruction has been used on brain research in fNIRS community to overcome the major drawback of DOT in lack of structural information. Two major approaches, including atlas anatomical-guided [138] or subject-specific anatomical-guided 3D-DOT [21, 44], have been intensely presented in the field recently. Subject-specific anatomical-guided 3D-DOT demonstrated accurate localization of brain activation compared with fMRI [21], and the expected errors in terms of the localization were revealed while using the atlas-guided DOT approach because of: (1) differences between subject specific anatomy and atlas anatomy; (2) the registration error between subject space and atlas space. Later delineation included variations or errors due to measurement of optode locations in subject space by a 3D digitizer. Studies of the comparisons between two approaches have been presented by Custo et al. [138] and Cooper et al. [44]. Custo et al. compared the reconstructions results from two approaches from three subjects. Their spatial and numerical results (overlapping between two reconstructions up to 93%; Dice' coefficient up to 0.86) concluded that accurate cortical activation can be obtained using an atlas-based head model. Further validation by Copper et al. also concluded that atlas-guided 3D-DOT could provide reasonable localization of brain activation based on the computational simulation studies. Based

on these conclusions, atlas-guided 3D-DOT was determined to be a useful tool in the study of brain activity and it provided us with estimated anatomic views for activation.

A.4 Conclusion

Overall in this work, we demonstrated the feasibility of using atlas-guided 3D-DOT to study brain activities occurring while participants performed mental tasks. To overcome the major error of localization or depth error for 3D image reconstruction due to sensitivity decay with increasing penetration depth, we applied DCA in 3D DOT image reconstruction. After applying the DCA, the regions with larger measurement sensitivities were compensated and moved toward the cerebral area, which is a more suitable distribution for imaging the cortical response to tasks. Also, results from computer simulations demonstrated that the better recoveries in terms of localization for simulated cortical activation can be observed with DCA adoption, i.e., the DCE compensated method. .

Besides computer simulations, we also validated the atlas-guided 3D DOT under BART stimulation. Moreover, unlike conventional methods used to determine brain activation in DOT (i.e., FWHM), GLM-based analysis was integrated with volumetric DOT, allowing us to determine brain activations with more statistical power and an improved spatial resolution. Based upon the experimental results under BART stimulation, voxel-wise GLM analysis was developed and utilized in 3D-DOT image reconstructions, demonstrating good agreement with a study by fMRI. Furthermore, results indicated that fNIRS measurement with voxel-wise GLM analysis showed good potential in the study of cognitive-related brain activity. Most importantly, this voxel-wise GLM-based DOT analysis method can be extended to reconstruct and analyze fNIRS or DOT images induced by different brain stimulation protocols. Also, reconstructed 3D DOT images seen on a brain atlas template can be more easily compared and confirmed with published literature in fMRI studies if further validation is desired. In conclusion, atlas-guided 3D DOT provides better visualization and can serve as a primary tool to localize brain activations in cortical areas. Proposed reconstruction procedures can be extended for subject-specific DOT

reconstructions if specific anatomical structure information is available. Possible future work would be to validate and evaluate the performances and quantifications for atlas-guided 3D DOT by using different existing stimulation protocols.

APPENDIX B

MATLAB CODE FOR CONVERTING COORDINATES IN RW SPACE TO MNI SPACE

```

%%%%%%%%%%%%%%%%%%%%%%%%%%%%%%%%%%%%%%%%%%%%%%%%%%%%%%%%%%%%%%%%%%%%%%%%
%%%%%%%%%%%%%%%%%%%%%%%%%%%%%%%%%%%%%%%%%%%%%%%%%%%%%%%%%%%%%%%%%%%%%%%%
%%--- Convert real world (RW) XYZ coordinates to MNI coordinates ---%%
%%%%%%%%%%%%%%%%%%%%%%%%%%%%%%%%%%%%%%%%%%%%%%%%%%%%%%%%%%%%%%%%%%%%%%%%
%%%%%%%%%%%%%%%%%%%%%%%%%%%%%%%%%%%%%%%%%%%%%%%%%%%%%%%%%%%%%%%%%%%%%%%%

```

```
function [x_mni y_mni z_mni] = xyzTomni (xr, yr, zr, vs, origin)
```

```
%%%%%%%%%%%%%%%%%%%%%%%%%%%%%%%%%%%%%%%%%%%%%%%%%%%%%%%%%%%%%%%%%%%%%%%%
```

```

% xr : x coordinates to convert in RW space in Nx1 dimension
% yr : y coordinates to convert in RW space in Nx1 dimension
% zr : z coordinates to convert in RW space in Nx1 dimension
% vs : voxel size in mm (default is 1mm)
% origin : 1x3 in dimension location of Anterior Commissure (AC) in MNI template

```

```
%%%%%%%%%%%%%%%%%%%%%%%%%%%%%%%%%%%%%%%%%%%%%%%%%%%%%%%%%%%%%%%%%%%%%%%%
```

```

if nargin < 3 || isempty(zr)
    [112] = ind2sub(y,x);
end

```

```

if nargin < 4 || isempty(vs)
    vs = 1; % default is 1mm
end

```

```

% MNI origin in voxel coordinates
% location of AC in MNI template

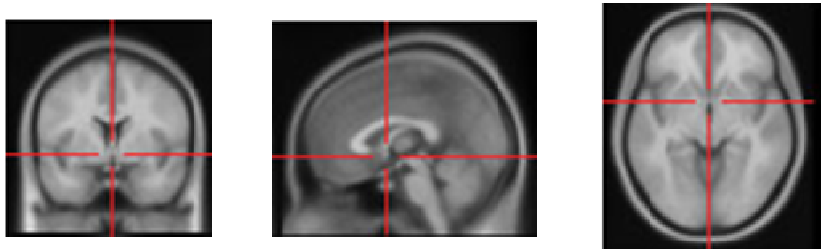
```

```

x_mni = ( origin(1) - xr ) * vs;
y_mni = ( yr - origin(2) ) * vs;
z_mni = ( zr - origin(3) ) * vs;

```

```
end
```



Anterior Commissure in ICBM152 (T1-weighted MRI)

APPENDIX C
RECIPE OF GELATIN PHANTOM

Materials:

1. Gelatin powder (G2500, Sigma-Aldrich Corporation, St. Louis, MO)
2. Scattering agent (20% Intralipid; Baxter Healthcare Corporation, Deerfield, IL)
3. Absorbing agent (Black non-waterproof India ink)
4. Water
5. Pipette dropper
6. Weigh scale

Preparation for making phantom:

In this example, the solid gelatin phantom ($\mu_a \approx 0.1\text{cm}^{-1}$ and $\mu'_s \approx 10\text{cm}^{-1}$) will be made. The recipe is as following.

1. 100g Gelatin powder
2. 80ml 20% Intralipid
3. Diluted India ink (5ml India ink + 45ml water) 200 μ l
4. 360ml water

Procedure:

1. Pour the gelatin powder into boiled water and keep stirring until the gelatin powder completely dissolved.
2. Cool down the gelatin solution to 40-45°C then pour Intralipid and diluted ink into gelatin solution.
3. Quickly mix gelatin solution, Intralipid and diluted ink and make sure they are completely mixed.
4. Pour the mixed solution into the mold and wait for 15-30mins in room temperature.

REFERENCES

- [1] [http://www.strokeassociation.org/STROKEORG/AboutStroke/Impact-of-Stroke-Stroke-statistics UCM 310728 Article.jsp](http://www.strokeassociation.org/STROKEORG/AboutStroke/Impact-of-Stroke-Stroke-statistics_UCM_310728_Article.jsp).
- [2] <http://floydmemorial.com/healthscope/understanding-stroke-the-basics/>.
- [3] S. Nakamura, T. Kano, K. Sakatani *et al.*, "Optical topography can predict occurrence of watershed infarction during carotid endarterectomy: technical case report," *Surgical Neurology*, 71(5), 540-542 (2009).
- [4] C. W. Pennekamp, M. L. Bots, L. J. Kappelle *et al.*, "The value of near-infrared spectroscopy measured cerebral oximetry during carotid endarterectomy in perioperative stroke prevention. A review," *Eur J Vasc Endovasc Surg*, 38(5), 539-45 (2009).
- [5] M. C. Taillefer, and A. Y. Denault, "Cerebral near-infrared spectroscopy in adult heart surgery: systematic review of its clinical efficacy," *Can J Anaesth*, 52(1), 79-87 (2005).
- [6] M. S. Damian, and R. Schlosser, "Bilateral near infrared spectroscopy in space-occupying middle cerebral artery stroke," *Neurocrit Care*, 6(3), 165-73 (2007).
- [7] T. Durduran, C. Zhou, B. L. Edlow *et al.*, "Transcranial optical monitoring of cerebrovascular hemodynamics in acute stroke patients," *Opt Express*, 17(5), 3884-902 (2009).
- [8] K. Yoshitani, M. Kawaguchi, K. Tatsumi *et al.*, "A comparison of the INVOS 4100 and the NIRO 300 near-infrared spectrophotometers," *Anesth Analg*, 94(3), 586-90; table of contents (2002).
- [9] I. Miyai, H. Yagura, I. Oda *et al.*, "Premotor cortex is involved in restoration of gait in stroke," *Annals of Neurology*, 52(2), 188-194 (2002).
- [10] M. Okamoto, H. Dan, K. Shimizu *et al.*, "Multimodal assessment of cortical activation during apple peeling by NIRS and fMRI," *Neuroimage*, 21(4), 1275-1288 (2004).
- [11] M. Suzuki, I. Miyai, T. Ono *et al.*, "Prefrontal and premotor cortices are involved in adapting walking and running speed on the treadmill: an optical imaging study," *Neuroimage*, 23(3), 1020-1026 (2004).
- [12] B. Khan, P. Chand, and G. Alexandrakis, "Spatiotemporal relations of primary sensorimotor and secondary motor activation patterns mapped by NIR imaging," *Biomed Opt Express*, 2(12), 3367-86 (2011).
- [13] F. Tian, M. R. Delgado, S. C. Dhamne *et al.*, "Quantification of functional near infrared spectroscopy to assess cortical reorganization in children with cerebral palsy," *Opt Express*, 18(25), 25973-86 (2010).
- [14] J. P. Culver, A. M. Siegel, J. J. Stott *et al.*, "Volumetric diffuse optical tomography of brain activity," *Opt Lett*, 28(21), 2061-3 (2003).
- [15] A. M. Siegel, J. P. Culver, J. B. Mandeville *et al.*, "Temporal comparison of functional brain imaging with diffuse optical tomography and fMRI during rat forepaw stimulation," *Phys Med Biol*, 48(10), 1391-403 (2003).
- [16] D. A. Boas, A. M. Dale, and M. A. Franceschini, "Diffuse optical imaging of brain activation: approaches to optimizing image sensitivity, resolution, and accuracy," *Neuroimage*, 23 Suppl 1, S275-88 (2004).
- [17] Z. Jiang, D. Piao, G. Xu *et al.*, "Trans-rectal ultrasound-coupled near-infrared optical tomography of the prostate, part II: experimental demonstration," *Opt Express*, 16(22), 17505-20 (2008).

- [18] G. Xu, D. Piao, C. H. Musgrove *et al.*, "Trans-rectal ultrasound-coupled near-infrared optical tomography of the prostate, part I: simulation," *Opt Express*, 16(22), 17484-504 (2008).
- [19] A. Corlu, R. Choe, T. Durduran *et al.*, "Three-dimensional in vivo fluorescence diffuse optical tomography of breast cancer in humans," *Opt Express*, 15(11), 6696-716 (2007).
- [20] V. Ntziachristos, A. G. Yodh, M. Schnall *et al.*, "Concurrent MRI and diffuse optical tomography of breast after indocyanine green enhancement," *Proc Natl Acad Sci U S A*, 97(6), 2767-72 (2000).
- [21] A. T. Eggebrecht, B. R. White, S. L. Ferradal *et al.*, "A quantitative spatial comparison of high-density diffuse optical tomography and fMRI cortical mapping," *Neuroimage*, 61(4), 1120-8 (2012).
- [22] B. R. White, S. M. Liao, S. L. Ferradal *et al.*, "Bedside optical imaging of occipital resting-state functional connectivity in neonates," *Neuroimage*, 59(3), 2529-38 (2012).
- [23] S. L. Jacques, "Light distributions from point, line and plane sources for photochemical reactions and fluorescence in turbid biological tissues," *Photochem Photobiol*, 67(1), 23-32 (1998).
- [24] L. Wang, S. L. Jacques, and L. Zheng, "MCML--Monte Carlo modeling of light transport in multi-layered tissues," *Comput Methods Programs Biomed*, 47(2), 131-46 (1995).
- [25] D. Boas, J. Culver, J. Stott *et al.*, "Three dimensional Monte Carlo code for photon migration through complex heterogeneous media including the adult human head," *Opt Express*, 10(3), 159-70 (2002).
- [26] T. J. Farrell, M. S. Patterson, and B. Wilson, "A diffusion theory model of spatially resolved, steady-state diffuse reflectance for the noninvasive determination of tissue optical properties in vivo," *Med Phys*, 19(4), 879-88 (1992).
- [27] M. S. Patterson, B. Chance, and B. C. Wilson, "Time resolved reflectance and transmittance for the non-invasive measurement of tissue optical properties," *Appl Opt*, 28(12), 2331-6 (1989).
- [28] S. R. Arridge, "Optical tomography in medical imaging," *Inverse Problems*, 15(2), R41-R93 (1999).
- [29] M. A. O'Leary, D. A. Boas, B. Chance *et al.*, "Experimental images of heterogeneous turbid media by frequency-domain diffusing-photon tomography," *Opt Lett*, 20(5), 426-8 (1995).
- [30] D. Sorger, M. Patt, P. Kumar *et al.*, "[¹⁸F]Fluoroazomycinarabinofuranoside (¹⁸FAZA) and [¹⁸F]Fluoromisonidazole (¹⁸FMISO): A comparative study of their selective uptake in hypoxic cells and PET imaging in experimental rat tumors," *Nuclear Medicine and Biology*, 30(3), 317-326 (2003).
- [31] H. Dehghani, M. E. Eames, P. K. Yalavarthy *et al.*, "Near infrared optical tomography using NIRFAST: Algorithm for numerical model and image reconstruction," *Commun Numer Methods Eng*, 25(6), 711-732 (2008).
- [32] S. R. Arridge, and M. Schweiger, "Photon-Measurement Density-Functions .2. Finite-Element-Method Calculations," *Applied Optics*, 34(34), 8026-8037 (1995).
- [33] A. D. Zacharopoulos, S. R. Arridge, O. Dorn *et al.*, "Three-dimensional reconstruction of shape and piecewise constant region values for optical tomography using spherical harmonic parametrization and a boundary element method," *Inverse Problems*, 22(5), 1509-1532 (2006).
- [34] P. K. Yalavarthy, "A generalized least-squares minimization method for near Infrared diffuse optical tomography," PhD Dissertation, (2007).
- [35] N. M. Technologies, [Dynot User Manual], (2006).

- [36] D. A. Boas, and A. M. Dale, "Simulation study of magnetic resonance imaging-guided cortically constrained diffuse optical tomography of human brain function," *Appl Opt*, 44(10), 1957-68 (2005).
- [37] Y. Zhan, A. T. Eggebrecht, J. P. Culver *et al.*, "Image quality analysis of high-density diffuse optical tomography incorporating a subject-specific head model," *Front Neuroenergetics*, 4, 6 (2012).
- [38] B. W. Pogue, T. O. McBride, J. Prewitt *et al.*, "Spatially variant regularization improves diffuse optical tomography," *Appl Opt*, 38(13), 2950-61 (1999).
- [39] H. Niu, F. Tian, Z. J. Lin *et al.*, "Development of a compensation algorithm for accurate depth localization in diffuse optical tomography," *Optics Letters*, 35(3), 429-31 (2010).
- [40] P. A. Valdes-Hernandez, A. Sumiyoshi, H. Nonaka *et al.*, "An in vivo MRI Template Set for Morphometry, Tissue Segmentation, and fMRI Localization in Rats," *Front Neuroinform*, 5, 26 (2011).
- [41] P.-S. Liao, T.-S. Chen, and P.-C. Chung, "A fast algorithm for multilevel thresholding," *J Inf Sci Eng* 17, 713-727 (2001).
- [42] A. Y. Bluestone, M. Stewart, J. Lasker *et al.*, "Three-dimensional optical tomographic brain imaging in small animals, part 1: hypercapnia," *J Biomed Opt*, 9(5), 1046-62 (2004).
- [43] A. Custo, D. A. Boas, D. Tsuzuki *et al.*, "Anatomical atlas-guided diffuse optical tomography of brain activation," *Neuroimage*, 49(1), 561-7 (2010).
- [44] R. J. Cooper, M. Caffini, J. Dubb *et al.*, "Validating atlas-guided DOT: a comparison of diffuse optical tomography informed by atlas and subject-specific anatomies," *Neuroimage*, 62(3), 1999-2006 (2012).
- [45] M. Herranz, and A. Ruibal, "Optical imaging in breast cancer diagnosis: the next evolution," *J Oncol*, 2012, 863747 (2012).
- [46] B. J. Tromberg, B. W. Pogue, K. D. Paulsen *et al.*, "Assessing the future of diffuse optical imaging technologies for breast cancer management," *Med Phys*, 35(6), 2443-51 (2008).
- [47] N. Iftimia, and H. Jiang, "Quantitative optical image reconstruction of turbid media by use of direct-current measurements," *Appl Opt*, 39(28), 5256-61 (2000).
- [48] A. Siegel, J. J. Marota, and D. Boas, "Design and evaluation of a continuous-wave diffuse optical tomography system," *Opt Express*, 4(8), 287-98 (1999).
- [49] B. R. White, A. Z. Snyder, A. L. Cohen *et al.*, "Resting-state functional connectivity in the human brain revealed with diffuse optical tomography," *Neuroimage*, 47(1), 148-56 (2009).
- [50] D. R. Leff, O. J. Warren, L. C. Enfield *et al.*, "Diffuse optical imaging of the healthy and diseased breast: a systematic review," *Breast Cancer Res Treat*, 108(1), 9-22 (2008).
- [51] J. P. Sacha, M. D. Cockman, T. E. Dufresne *et al.*, "Quantification of regional fat volume in rat MRI," *Medical Imaging 2003: Physiology and Function: Methods, Systems, and Applications*, 5031, 289-297 (2003).
- [52] A. Laib, O. Barou, L. Vico *et al.*, "3D micro-computed tomography of trabecular and cortical bone architecture with application to a rat model of immobilisation osteoporosis," *Medical & Biological Engineering & Computing*, 38(3), 326-32 (2000).
- [53] C. Vanhove, T. Lahoutte, M. Defrise *et al.*, "Reproducibility of left ventricular volume and ejection fraction measurements in rat using pinhole gated SPECT," *European Journal of Nuclear Medicine and Molecular Imaging*, 32(2), 211-220 (2005).

- [54] J. P. Culver, T. Durduran, D. Furuya *et al.*, "Diffuse optical tomography of cerebral blood flow, oxygenation, and metabolism in rat during focal ischemia," *J Cereb Blood Flow Metab*, 23(8), 911-24 (2003).
- [55] G. Gulsen, O. Birgul, M. B. Unlu *et al.*, "Combined diffuse optical tomography (DOT) and MRI system for cancer imaging in small animals," *Technol Cancer Res Treat*, 5(4), 351-63 (2006).
- [56] Q. Zhao, L. Ji, and T. Jiang, "Improving depth resolution of diffuse optical tomography with a layer-based sigmoid adjustment method," *Opt Express*, 15(7), 4018-29 (2007).
- [57] S. B. Howell, "Handbook of CCD Astronomy," (2000).
- [58] S. C. Kanick, U. A. Gamm, M. Schouten *et al.*, "Measurement of the reduced scattering coefficient of turbid media using single fiber reflectance spectroscopy: fiber diameter and phase function dependence," *Biomed Opt Express*, 2(6), 1687-702 (2011).
- [59] M. Johns, C. Giller, D. German *et al.*, "Determination of reduced scattering coefficient of biological tissue from a needle-like probe," *Opt Express*, 13(13), 4828-42 (2005).
- [60] G. Zonios, and A. Dimou, "Modeling diffuse reflectance from semi-infinite turbid media: application to the study of skin optical properties," *Opt Express*, 14(19), 8661-74 (2006).
- [61] T. Z. Jiang, Q. Zhao, and L. J. Ji, "Improving performance of reflectance diffuse optical imaging using a multicentered mode," *Journal of Biomedical Optics*, 11(6), (2006).
- [62] F. Tian, G. Alexandrakis, and H. Liu, "Optimization of probe geometry for diffuse optical brain imaging based on measurement density and distribution," *Appl Opt*, 48(13), 2496-504 (2009).
- [63] J. Su, M. V. Klibanov, Y. Liu *et al.*, "Optical imaging of phantoms from real data by an approximately globally convergent inverse algorithm," *Inverse Problems in Science and Engineering*, (2012).
- [64] J. Su, H. Shan, H. Liu *et al.*, "Reconstruction method with data from a multiple-site continuous-wave source for three-dimensional optical tomography," *J Opt Soc Am A Opt Image Sci Vis*, 23(10), 2388-95 (2006).
- [65] Z.-J. Lin, H. Niu, Y. Liu *et al.*, "CCD-camera-based diffuse optical tomography to study ischemic stroke in preclinical rat models," 78960R-78960R (2011).
- [66] M. V. Klibanov, and A. Timonov, "Numerical studies on the globally convergent convexification algorithm in 2D," *Inverse Problems*, 23(1), 123-138 (2007).
- [67] F. Liu, and L. D. McCullough, "Middle cerebral artery occlusion model in rodents: methods and potential pitfalls," *J Biomed Biotechnol*, 2011, 464701 (2011).
- [68] K. Uluc, A. Miranpuri, G. C. Kujoth *et al.*, "Focal cerebral ischemia model by endovascular suture occlusion of the middle cerebral artery in the rat," *J Vis Exp*(48), (2011).
- [69] D. Virley, J. S. Beech, S. C. Smart *et al.*, "A temporal MRI assessment of neuropathology after transient middle cerebral artery occlusion in the rat: correlations with behavior," *J Cereb Blood Flow Metab*, 20(3), 563-82 (2000).
- [70] M. J. O'Neill, and J. A. Clemens, "Rodent models of focal cerebral ischemia," *Curr Protoc Neurosci*, Chapter 9, Unit9 6 (2001).
- [71] X. Li, L. Xi, R. Jiang *et al.*, "Integrated diffuse optical tomography and photoacoustic tomography: phantom validations," *Biomed Opt Express*, 2(8), 2348-53 (2011).
- [72] S. Andersson-Engels, J. Johansson, and S. Svanberg, "Medical diagnostic system based on simultaneous multispectral fluorescence imaging," *Appl Opt*, 33(34), 8022-9 (1994).

- [73] R. Baumgartner, H. Fisslinger, D. Jocham *et al.*, "A fluorescence imaging device for endoscopic detection of early stage cancer--instrumental and experimental studies," *Photochem Photobiol*, 46(5), 759-63 (1987).
- [74] Y. Tan, and H. Jiang, "A Fluorescence Molecular Tomography In-vivo Imaging System for Macro/Meso-Scale Subjects," *J Biosens Bioelectron*, 4, (2011).
- [75] R. von Kummer, K. L. Allen, R. Holle *et al.*, "Acute stroke: usefulness of early CT findings before thrombolytic therapy," *Radiology*, 205(2), 327-33 (1997).
- [76] T. Neumann-Haefelin, H. J. Wittsack, F. Wenserski *et al.*, "Diffusion- and perfusion-weighted MRI. The DWI/PWI mismatch region in acute stroke," *Stroke*, 30(8), 1591-7 (1999).
- [77] M. Xia, S. Yang, J. W. Simpkins *et al.*, "Noninvasive monitoring of estrogen effects against ischemic stroke in rats by near-infrared spectroscopy," *Appl Opt*, 46(34), 8315-21 (2007).
- [78] L.-F. Liu, C.-K. Yeh, C.-H. Chen *et al.*, "Measurement of Cerebral Blood Flow and Oxygen Saturation Using Laser Doppler Flowmetry and Near Infrared Spectroscopy in Ischemic Stroke Rats," *Med. Biol. Eng.*, 28, 101-105 (2008).
- [79] W. Chen, G. Lu, and W. Lichty, "Localizing the focus of ischemic stroke with near infrared spectroscopy," *Chin Med J (Engl)*, 115(1), 84-8 (2002).
- [80] W. G. Chen, P. C. Li, Q. M. Luo *et al.*, "Hemodynamic assessment of ischemic stroke with near-infrared spectroscopy," *Space Med Med Eng (Beijing)*, 13(2), 84-9 (2000).
- [81] A. Y. Bluestone, M. Stewart, B. Lei *et al.*, "Three-dimensional optical tomographic brain imaging in small animals, part 2: unilateral carotid occlusion," *J Biomed Opt*, 9(5), 1063-73 (2004).
- [82] M. A. Soriano, O. Sanz, I. Ferrer *et al.*, "Cortical infarct volume is dependent on the ischemic reduction of perifocal cerebral blood flow in a three-vessel intraluminal MCA occlusion/reperfusion model in the rat," *Brain Res*, 747(2), 273-8 (1997).
- [83] L. Pavics, F. Grunwald, K. Reichmann *et al.*, "Regional cerebral blood flow single-photon emission tomography with 99mTc-HMPAO and the acetazolamide test in the evaluation of vascular and Alzheimer's dementia," *Eur J Nucl Med*, 26(3), 239-45 (1999).
- [84] R. Kwiatek, L. Barnden, R. Tedman *et al.*, "Regional cerebral blood flow in fibromyalgia: single-photon-emission computed tomography evidence of reduction in the pontine tegmentum and thalami," *Arthritis Rheum*, 43(12), 2823-33 (2000).
- [85] D. L. Johnson, J. S. Wiebe, S. M. Gold *et al.*, "Cerebral blood flow and personality: a positron emission tomography study," *Am J Psychiatry*, 156(2), 252-7 (1999).
- [86] S. Tuominen, Q. Miao, T. Kurki *et al.*, "Positron emission tomography examination of cerebral blood flow and glucose metabolism in young CADASIL patients," *Stroke*, 35(5), 1063-7 (2004).
- [87] Y. Shang, L. Chen, M. Toborek *et al.*, "Diffuse optical monitoring of repeated cerebral ischemia in mice," *Opt Express*, 19(21), 20301-15 (2011).
- [88] C. Zhou, G. Yu, D. Furuya *et al.*, "Diffuse optical correlation tomography of cerebral blood flow during cortical spreading depression in rat brain," *Opt Express*, 14(3), 1125-44 (2006).
- [89] J. Tonnesen, A. Pryds, E. H. Larsen *et al.*, "Laser Doppler flowmetry is valid for measurement of cerebral blood flow autoregulation lower limit in rats," *Exp Physiol*, 90(3), 349-55 (2005).
- [90] C. Terborg, S. Bramer, S. Harscher *et al.*, "Bedside assessment of cerebral perfusion reductions in patients with acute ischaemic stroke by near-infrared spectroscopy and indocyanine green," *J Neurol Neurosurg Psychiatry*, 75(1), 38-42 (2004).

- [91] W. M. Kuebler, A. Sckell, O. Habler *et al.*, "Noninvasive measurement of regional cerebral blood flow by near-infrared spectroscopy and indocyanine green," *J Cereb Blood Flow Metab*, 18(4), 445-56 (1998).
- [92] E. Keller, A. Nadler, H. Alkadhi *et al.*, "Noninvasive measurement of regional cerebral blood flow and regional cerebral blood volume by near-infrared spectroscopy and indocyanine green dye dilution," *Neuroimage*, 20(2), 828-39 (2003).
- [93] B. P. Wagner, S. Gertsch, R. A. Ammann *et al.*, "Reproducibility of the blood flow index as noninvasive, bedside estimation of cerebral blood flow," *Intensive Care Med*, 29(2), 196-200 (2003).
- [94] T. Kusaka, K. Isobe, K. Nagano *et al.*, "Estimation of regional cerebral blood flow distribution in infants by near-infrared topography using indocyanine green," *Neuroimage*, 13(5), 944-52 (2001).
- [95] E. Z. Longa, P. R. Weinstein, S. Carlson *et al.*, "Reversible middle cerebral artery occlusion without craniectomy in rats," *Stroke*, 20(1), 84-91 (1989).
- [96] M. Ren, Z.-J. Lin, H. Qiana *et al.*, "Embolic middle cerebral artery occlusion model using thrombin and fibrinogen composed clots in rat," *J Neurosci Methods.*, (2012).
- [97] S. R. Arridge, "Optical tomography in medical imaging " *Inverse Probl*, 15, R41-R93 (1999).
- [98] S. T. Carmichael, "Rodent models of focal stroke: size, mechanism, and purpose," *NeuroRx*, 2(3), 396-409 (2005).
- [99] A. Tamura, D. I. Graham, J. McCulloch *et al.*, "Focal cerebral ischaemia in the rat: 1. Description of technique and early neuropathological consequences following middle cerebral artery occlusion," *J Cereb Blood Flow Metab*, 1(1), 53-60 (1981).
- [100] B. W. Pogue, and K. D. Paulsen, "High-resolution near-infrared tomographic imaging simulations of the rat cranium by use of a priori magnetic resonance imaging structural information," *Opt Lett*, 23(21), 1716-8 (1998).
- [101] B. Brooksby, B. W. Pogue, S. Jiang *et al.*, "Imaging breast adipose and fibroglandular tissue molecular signatures by using hybrid MRI-guided near-infrared spectral tomography," *Proc Natl Acad Sci U S A*, 103(23), 8828-33 (2006).
- [102] H. Xu, H. Deghani, B. W. Pogue *et al.*, "Near-infrared imaging in the small animal brain: optimization of fiber positions," *J Biomed Opt*, 8(1), 102-10 (2003).
- [103] H. Niu, Z. J. Lin, F. Tian *et al.*, "Comprehensive investigation of three-dimensional diffuse optical tomography with depth compensation algorithm," *J Biomed Opt*, 15(4), 046005 (2010).
- [104] G. Xu, and D. Piao, [A Geometric-Differential-Sensitivity Based Reconstruction Algorithm Improves Target-Depth Localization for Trans-Luminal Outward-Imaging Diffuse Optical Tomography], Miami, Florida(2012).
- [105] B. Tavakoli, and Q. Zhu, "Depth-correction algorithm that improves optical quantification of large breast lesions imaged by diffuse optical tomography," *J Biomed Opt*, 16(5), 056002 (2011).
- [106] C. H. Schmitz, H. L. Graber, Y. Pei *et al.*, "Dynamic studies of small animals with a four-color diffuse optical tomography imager " *Rev. Sci. Instrum.*, 76(9), 094302 (2005).
- [107] J. Berrouschot, H. Barthel, S. Hesse *et al.*, "Reperfusion and metabolic recovery of brain tissue and clinical outcome after ischemic stroke and thrombolytic therapy," *Stroke*, 31(7), 1545-51 (2000).
- [108] Q. Jiang, R. L. Zhang, Z. G. Zhang *et al.*, "Diffusion-, T2-, and perfusion-weighted nuclear magnetic resonance imaging of middle cerebral artery embolic stroke and

- recombinant tissue plasminogen activator intervention in the rat," *J Cereb Blood Flow Metab*, 18(7), 758-67 (1998).
- [109] B. Haelewyn, J. J. Risso, and J. H. Abraini, "Human recombinant tissue-plasminogen activator (alteplase): why not use the 'human' dose for stroke studies in rats?," *J Cereb Blood Flow Metab*, 30(5), 900-3 (2010).
- [110] E. Busch, K. Kruger, P. R. Allegrini *et al.*, "Reperfusion after thrombolytic therapy of embolic stroke in the rat: magnetic resonance and biochemical imaging," *J Cereb Blood Flow Metab*, 18(4), 407-18 (1998).
- [111] G. De Visscher, K. van Rossem, J. Van Reempts *et al.*, "Cerebral blood flow assessment with indocyanine green bolus transit detection by near-infrared spectroscopy in the rat," *Comp Biochem Physiol A Mol Integr Physiol*, 132(1), 87-95 (2002).
- [112] N. J. Alkayed, I. Harukuni, A. S. Kimes *et al.*, "Gender-linked brain injury in experimental stroke," *Stroke*, 29(1), 159-65; discussion 166 (1998).
- [113] G. Yang, P. H. Chan, J. Chen *et al.*, "Human copper-zinc superoxide dismutase transgenic mice are highly resistant to reperfusion injury after focal cerebral ischemia," *Stroke*, 25(1), 165-70 (1994).
- [114] Q. Cao, Y. Zang, L. Sun *et al.*, "Abnormal neural activity in children with attention deficit hyperactivity disorder: a resting-state functional magnetic resonance imaging study," *Neuroreport*, 17(10), 1033-6 (2006).
- [115] M. D. Greicius, B. Krasnow, A. L. Reiss *et al.*, "Functional connectivity in the resting brain: a network analysis of the default mode hypothesis," *Proc Natl Acad Sci U S A*, 100(1), 253-8 (2003).
- [116] Y. Liu, C. Yu, M. Liang *et al.*, "Whole brain functional connectivity in the early blind," *Brain*, 130(Pt 8), 2085-96 (2007).
- [117] Y. I. Sheline, M. E. Raichle, A. Z. Snyder *et al.*, "Amyloid plaques disrupt resting state default mode network connectivity in cognitively normal elderly," *Biol Psychiatry*, 67(6), 584-7 (2010).
- [118] R. Bluhm, P. Williamson, R. Lanius *et al.*, "Resting state default-mode network connectivity in early depression using a seed region-of-interest analysis: Decreased connectivity with caudate nucleus," *Psychiatry and Clinical Neurosciences*, 63(6), 754-761 (2009).
- [119] R. L. Bluhm, P. C. Williamson, E. A. Osuch *et al.*, "Alterations in default network connectivity in posttraumatic stress disorder related to early-life trauma," *J Psychiatry Neurosci*, 34(3), 187-94 (2009).
- [120] T. Nakamura, F. G. Hillary, and B. B. Biswal, "Resting network plasticity following brain injury," *PLoS One*, 4(12), e8220 (2009).
- [121] M. P. van Meer, K. van der Marel, K. Wang *et al.*, "Recovery of sensorimotor function after experimental stroke correlates with restoration of resting-state interhemispheric functional connectivity," *J Neurosci*, 30(11), 3964-72 (2010).
- [122] H. Niu, S. Khadka, F. Tian *et al.*, "Resting-state functional connectivity assessed with two diffuse optical tomographic systems," *J Biomed Opt*, 16(4), 046006 (2011).
- [123] B. R. White, A. Q. Bauer, A. Z. Snyder *et al.*, "Imaging of functional connectivity in the mouse brain," *PLoS One*, 6(1), e16322 (2011).
- [124] H. Zhang, Y. J. Zhang, L. Duan *et al.*, "Is resting-state functional connectivity revealed by functional near-infrared spectroscopy test-retest reliable?," *J Biomed Opt*, 16(6), 067008 (2011).

- [125] H. Lu, Y. Zuo, H. Gu *et al.*, "Synchronized delta oscillations correlate with the resting-state functional MRI signal," *Proc Natl Acad Sci U S A*, 104(46), 18265-9 (2007).
- [126] N. M. Gregg, B. R. White, B. W. Zeff *et al.*, "Brain specificity of diffuse optical imaging: improvements from superficial signal regression and tomography," *Front Neuroenergetics*, 2, (2010).
- [127] G. Chen, C. Xie, B. D. Ward *et al.*, "A method to determine the necessity for global signal regression in resting-state fMRI studies," *Magn Reson Med*, 68(6), 1828-35 (2012).
- [128] I. E. Sommer, M. Clos, A. L. Meijering *et al.*, "Resting state functional connectivity in patients with chronic hallucinations," *PLoS One*, 7(9), e43516 (2012).
- [129] A. K. Singh, M. Okamoto, H. Dan *et al.*, "Spatial registration of multichannel multi-subject fNIRS data to MNI space without MRI," *Neuroimage*, 27(4), 842-51 (2005).
- [130] M. Okamoto, and I. Dan, "Automated cortical projection of head-surface locations for transcranial functional brain mapping," *Neuroimage*, 26(1), 18-28 (2005).
- [131] S. Cutini, P. Scatturin, and M. Zorzi, "A new method based on ICBM152 head surface for probe placement in multichannel fNIRS," *Neuroimage*, 54(2), 919-27 (2011).
- [132] M. Cazzell, L. Li, Z. J. Lin *et al.*, "Comparison of neural correlates of risk decision making between genders: An exploratory fNIRS study of the Balloon Analogue Risk Task (BART)," *Neuroimage*, 62(3), 1896-1911 (2012).
- [133] H. Rao, M. Korkczykowski, J. Pluta *et al.*, "Neural correlates of voluntary and involuntary risk taking in the human brain: an fMRI Study of the Balloon Analog Risk Task (BART)," *Neuroimage*, 42(2), 902-10 (2008).
- [134] B. R. White, and J. P. Culver, "Phase-encoded retinotopy as an evaluation of diffuse optical neuroimaging," *Neuroimage*, 49(1), 568-77 (2010).
- [135] B. R. White, and J. P. Culver, "Quantitative evaluation of high-density diffuse optical tomography: in vivo resolution and mapping performance," *J Biomed Opt*, 15(2), 026006 (2010).
- [136] H. Dehghani, B. R. White, B. W. Zeff *et al.*, "Depth sensitivity and image reconstruction analysis of dense imaging arrays for mapping brain function with diffuse optical tomography," *Appl Opt*, 48(10), D137-43 (2009).
- [137] R. W. Homan, J. Herman, and P. Purdy, "Cerebral location of international 10-20 system electrode placement," *Electroencephalogr Clin Neurophysiol*, 66(4), 376-82 (1987).
- [138] A. Custo, D. A. Boas, D. Tsuzuki *et al.*, "Anatomical atlas-guided diffuse optical tomography of brain activation," *Neuroimage*, 49(1), 561-567 (2010).

BIOGRAPHICAL INFORMATION

Zi-Jing Lin was born on August 3, 1979 in Taichung city, Taiwan. He received his Bachelor of Engineering degree in Automatic Control Engineering from Feng Chia University, Taichung city, Taiwan in June 2001. In Fall 2001, he started his graduate studies in Institution of Biomedical Engineering, National Cheng Kung University, Tainan city, Taiwan and graduated with a Master of Science in June 2003. After completion of his Master's degree, he served in Taiwan army as the medical corporal for one and half years. In Fall 2006, he started his Doctoral studies in bioengineering department, the University of Texas at Arlington, under the supervision of Dr. Hanli Liu. His plan is to complete his Doctor of Philosophy in Biomedical Engineering at the joint graduate program of the University of Texas at Arlington and the University of Texas Southwestern Medical Center at Dallas in December 2012. His research interests include Near Infrared diffuse optical spectroscopy and tomography and medical imaging techniques.